Modeling, Analysis, and Control of a Hypersonic Vehicle with Significant Aero-Thermo-Elastic-Propulsion Interactions: Elastic, Thermal and Mass Uncertainty

by

Jaidev Khatri

A Thesis Presented in Partial Fulfillment
of the Requirements for the Degree
Master of Science

Approved April 2011 by the
Graduate Supervisory Committee:

Armando A. Rodriguez, Chair
Konstantinos S. Tsakalis
Valana L. Wells

ARIZONA STATE UNIVERSITY

May 2011

ProQuest LLC
789 East Eisenhower Parkway
P.O. Box 1346
Ann Arbor, MI 48106-1346

ABSTRACT

This thesis examines the modeling, analysis, and control system design issues for scramjet powered hypersonic vehicles. A nonlinear three degrees of freedom longitudinal model which includes aero-propulsion-elasticity effects was used for all analyses. This model is based upon classical compressible flow and Euler-Bernouli structural concepts. Higher fidelity computational fluid dynamics and finite element methods are needed for more precise intermediate and final evaluations. The methods presented within this thesis were shown to be useful for guiding initial control relevant design. The model was used to examine the vehicle's static and dynamic characteristics over the vehicle's trimmable region. The vehicle has significant longitudinal coupling between the fuel equivalency ratio (FER) and the flight path angle (FPA). For control system design, a two-input two-output plant (FER - elevator to speed-FPA) with 11 states (including 3 flexible modes) was used. Velocity, FPA, and pitch were assumed to be available for feedback.

Aerodynamic heat modeling and design for the assumed TPS was incorporated to original Bolender's model to study the change in static and dynamic properties. De-centralized control stability, feasibility and limitations issues were dealt with the change in TPS elasticity, mass and physical dimension. The impact of elasticity due to TPS mass, TPS physical dimension as well as prolonged heating was also analyzed to understand performance limitations of de-centralized control designed for nominal model.

To my Family

ACKNOWLEDGEMENTS

I am very grateful for the cooperation and support of my advisor Dr. A. A. Rodriguez, who has shown a great deal of patience and confidence in my work.

Besides my advisor, I would like to thank the rest of my thesis committee: Drs. K. Tsakalis, and V. Wells.

There are several other faculty members who have widened my horizons considerably through their courses and guidance.

I would like to acknowledge the tremendous support and computing resources offered by the Ira A. Fulton School of Engineering High Performance Computing Initiative.

I would also like to acknowledge the help and guidance of Jeffrey J. Dickeson, Akshay Korad and Srikanth Sridharan.

This work has been supported by NASA grant NNX07AC42A.

TABLE OF CONTENTS

LIST OF TABLES

LIST OF FIGURES

1. INTRODUCTION

1.1 Motivation

With the historic 2004 scramjet-powered Mach 7 and 10 flights of the X-43A [17–20] , hypersonics research has seen a resurgence. This is attributable to the fact that air-breathing hypersonic propulsion is viewed as the next critical step towards achieving (1) reliable affordable access to space, (2) global reach vehicles. Both of these objectives have commercial as well as military applications. While rocket-based (combined cycle) propulsion systems [21] are needed to reach orbital speeds, they are much more expensive to operate because they must carry oxygen. This is particularly expensive when travelling at lower altitudes through the troposphere (i.e. below 36,152 ft). Current rocket-based systems also do not exhibit the desired levels of reliability and flexibility (e.g. airplane like takeoff and landing options). For this reason, much emphasis has been placed on two-stage-to-orbit (TSTO) designs which involve a turbo-ram-scramjet combined cycle in the first stage and a rocket-scramjet in the second stage. In this thesis, we focus on modeling and control challenges associated with scramjet-powered hypersonic vehicles. Such vehicles are characterized by significant aero-thermo-elastic-propulsion interactions and uncertainty [1, 2, 4, 6, 17–33].

1.2 Related Work and Literature Survey

1.2.1 Overview of Hypersonics Research

The 2004 scramjet-powered X-43A flights ushered in the era of air-breathing hypersonic flight. Hypersonic vehicles that have received considerable attention include the National AeroSpace Plane (NASP, X-30) [34–37], X-33 [26, 38, 39], X-34 [40, 41], X-43 [17, 19, 20, 42], X-51 [43], and Falcon (Force Application from CONUS) [38, 44–46]. A summary of hypersonics research programs prior to the

X-43A flights is provided within [47]. Some of this, and more recent, work is now described.

- *General Research on Scramjet Propulsion.* NASA has pursued scramjet propulsion research for over 40 years [47, 48]. During the mid 1960's, NASA built and tested a hydrogen-fueled and cooled scramjet engine that verified scramjet efficiency, structural integrity, and first generation design tools. During the early 1970's, NASA designed and demonstrated a fixed-geometry, airframe-integrated scramjet "flowpath" (capable of propelling a hypersonic vehicle from Mach 4 to 7) in wind tunnel tests.

- *NASP.* The NASP X-30 (1984-1996, $\$3B^{+}$) was a single-stage-to-orbit (SSTO) shovel-shaped (waverider) hydrogen fueled vehicle development effort involving DOD and NASA. At its peak, over 500 engineers and scientists were involved in the project [47, 49]. Despite the fact that no flights took place, much aero-thermo-elastic-propulsion research was accomplished through this effort [19, 34, 47, 50–53]. The program was unquestionably too ambitious [18] given the (very challenging) manned requirement as well as the state of materials, thermal protection, propulsion, computer-aided-design technology readiness levels (TRLs) and integration readiness levels (IRLs). Within [54], relevant cutting-edge structural strength/thermal protection issues are addressed; e.g. high specific strength (strength/density) that ceramic matrix composites (CMCs) offer for air-breathing hypersonic vehicles experiencing $2000^{\circ} - 3000^{\circ}F$ temperatures.

- *SSTO Technology Demonstrators.* The X-33 and X-34 would follow NASP.
  - The X-33 (Mach 15, 250 kft) [26, 38, 39] was a Lockheed Martin Skunk Works unmanned sub-scale (triangularly shaped) lifting body

(linear aerospike) rocket-engine powered technology demonstrator for their proposed VentureStar SSTO reusable launch vehicle (RLV).

  - The X-34 (Mach 8, 250 kft) [40, 41], much smaller than the X-33, was an unmanned sub-scale (shuttle shaped) Orbital Sciences (Fastrac) rocket-engine powered technology demonstrator intended to operate like the space shuttle.

- *HyShot Flight Program.* Supersonic combustion of a scramjet in flight was first demonstrated July 30, 2002 (designated HyShot II) by the University of Queensland Center for Hypersonics (HyShot program) [55, 56]. Another flight demonstration took place on March 25, 2006 (HyShot III). During each flight, a two-stage Terrier-Orion Mk70 rocket was used to boost the payload (engine) to an apogee of 330 km. Engine measurements took place at altitudes between 23 km and 35 km when the payload carrying re-entry Orion reached Mach 7.6. Gaseous hydrogen was used to fuel the scramjet. Flight results were correlated with the University of Queensland's T4 shock tunnel. Thus far, the center has been involved with five flights - the last on June 15, 2007 (HyCAUSE) [57].

- *Hyper-X.* In 1996, the Hyper-X Program was initiated to advance hypersonic air-breathing propulsion [48]. The goal of the program was to (1) demonstrate an advanced, airframe-integrated, air-breathing hypersonic propulsion system in flight and (2) validate the supporting tools and technologies [17–20, 42]. The Hyper-X program culminated with the (March 27, November 16) 2004 Mach 7, 10 (actually 6.83, 9.8) X-43A scramjet-powered flights [18–20]. Prior to these flights, the SR-71 Blackbird held the turbojet record of just above Mach 3.2 while missiles exploiting ramjets had reached about Mach 5 [49].

– *Flight 1.* The first X-43A flight was attempted on June 2, 2001. After being dropped from the B-52, the X-43A stack (Orbital Sciences Pegasus rocket booster plus X-43A) lost control. A "mishap investigation team" concluded that the (Pegasus) control system design was deficient for the trajectory selected due to inaccurate models [18, 58]. The trajectory was selected on the basis of X-43A stack weight limits on the B-52. The mishap report [58] (5/8/2003) said the (Pegasus) control system could not maintain stack stability during transonic flight. Stack instability was observed as a roll oscillation. This caused the rudder to stall. This resulted in the loss of the stack. Return to flight activities are summarized in [59].

– *Flight 2.* Results from Flight 2 (Mach 7, 95 kft, 1000 psf) are described within [22, 23, 60, 61]. The X-43A (Hyper-X research vehicle) was powered by an airframe-integrated hydrogen-fueled, dual mode scramjet. The fueled portion of the scramjet test lasted approximately 10 sec. The vehicle possessed 4 electromechanically actuated aerodynamic control surfaces: two (symmetrically moving) rudders for yaw control and two (symmetrically and differentially moving) all moving wings (AMWs) for pitch and roll control.

  Onboard flight measurements included [22] 1) three axis translation accelerations, 2) three axis rotational accelerations, 3) control surface deflections, 4) three space inertial velocities, 5) geometric altitude, 6) Euler angles (i.e. roll, pitch, and heading angles), and 7) wind estimates, 8) flush air data systems (FADS), amongst others (e.g. over 200 surface pressure measurements, over 100 thermocouples, GPS, weather balloon atmospheric measurements) [19, 62]. Body axis velocities, AOA, and

sideslip angle [22] were estimated using (4) and (6).

Control system design was based on sequential loop closure root locus methods [61]. Gains were scheduled on Mach and angle-of-attack (AOA) with dynamic pressure compensation. Gain and phase margins of 6 dB and 45° were designed into each loop for most flight conditions. Smaller margins were accepted for portions of the descent. Control system operated at 100 Hz, while guidance commands were issued at 25 Hz.

Scramjet engine performance was within 3% of preflight predictions. During powered flight, AOA was kept at $2.5^\circ \pm 0.2^\circ$. Pre-flight aeropropulsive database development for Flight 2 (based on CFD and available ground-test data) is discussed within [63]. Relevant X-43A preflight descent aero data, including experimental uncertainty, is discussed within [24]. The data suggests vehicle static stability (in all three axes) along the descent trajectory. Moreover, longitudinal stability and rudder effectiveness are diminished for AOA's above 8°.

– *Flight 3.* Flight 3 (Mach 10, 110 kft, 1000 psf) results are described within [64]. Scramjet development tests exploiting the NASA/HyPulse Shock Tunnel in support of Flight 3 are described within [65]. The X-43A was a very heavy, short, very rigid (3000 lb, 12 ft, 5 ft wide, 2 ft high, 42 Hz lowest structural frequency [66]) lifting body and hence thermo-elastic considerations were not significant.

Aerodynamic parameter identification results obtained from Flight 3 descent data at Mach 8, 7, 6, 5, 4, 3, based on multiple orthogonal phase-optimized sweep inputs applied to the control surfaces, are described within [67]. A linear aero model was used for fitting purposes.

The fitting method (which led to the best results) was an equation-error frequency domain method. In short, estimated data agreed well with preflight data based on wind tunnel testing and computational fluid dynamics (CFD).

It is instructive to compare the operational envelops of several modern hypersonic vehicles. This is done in [40]. Approximate altitude and Mach extremes for some vehicles are as follows:

X-30: 250 kft, Mach 25;

X-33: 250 kft, Mach 15;

X-34: 250 kft, Mach 8;

X-43A: 110 kft, Mach 10.

The associated envelop scale back is, no doubt, a direct consequence of the aggressive goals of NASP - goals, in part, motivated by the politics of gaining congressional and presidential approval [18]. More fundamentally, this scale back reflects the need for carefully planned demonstrations and flight tests.

- *HiFIRE.* The Hypersonic International Flight Research Experimentation (HiFIRE) is an ongoing collaboration between NASA, AFRL, Australian Defence Science and Technology Organization (DSTO), Boeing Phantom Works, and the University of Queensland [68]. It will involve 10 flights over 5 years. HiFIRE flights will focus on the goal of understanding fundamental hypersonic phenomena.

- *X-51A Scramjet Demonstrator Waverider.* The Boeing X-51A is an expendable hydrocarbon fueled scramjet engine demonstrator waverider vehicle (16 ft long, 1000 lb.) that is being developed by AFRL, Boeing, and Pratt & Whitney [43]. Multiple flight tests are scheduled for 2009. An X-51-booster stack will be carried via B-52 to a drop altitude. The Army tactical missile

system solid rocket booster will then propel the vehicle to Mach 4.5. At that point, the scramjet will take over and the vehicle will accelerate to Mach 7.

- *Falcon.* Aspects of the Falcon waverider project are described within [38, 44–46, 69, 70] . The project began in 2003 with the goal of developing a series of incremental hypersonic technology vehicle (HTV) demonstrators. It involves the United States Air Force (USAF) and DARPA. Initially, ground demonstrations (HTV-1) were conducted. HTV-3X will involve a reusable launch vehicle with a hydrocarbon-fueled turbine-based combined-cycle (TBCC) propulsion system that takes off like an airplane, accelerates to Mach 6, and makes a turbojet powered landing. These demonstrations are designed to develop technologies for a future reusable hypersonic cruise vehicle (HCV) designed for prompt global reach missions.

- *Aero-Thermo-Elastic-Propulsion CFD-FE Tools.* The design of subsonic, transonic, and supersonic vehicles have benefited from extensive ground testing. Such testing is much more difficult for hypersonic vehicles. As such, the use of state-of-the-art CFD-FE-based aero-thermo-elasticity-propulsion modeling tools is particularly crucial for the development of hypersonic vehicles. While much has been done at the component level (e.g. wings, surfaces), relatively little has been done that addresses the entire vehicle (at least in the published literature). This, of course, is due to the fact that accurate CFD studies often require the nation's most advanced supercomputing resources. Relevant work in this area is described within the following and the associated references [38, 49, 71, 72]. A major contribution of the 2004 X-43A flights was the validation of design tools [17, 18]. It should be noted that CFD is often applied in conjunction with or after applying classic engineering methods (e.g. panel methods) as described within [1, 28, 73]. Widely used pro-

grams that support such methods include (amongst many others) HABP (Hypersonic Arbitrary Body Program), APAS (Aerodynamic Preliminary Analysis System), and CBAERO (Configuration Based Aerodynamics prediction code) [1, 28, 37, 73]. Given the above, it is useful to know what was used for the X-43A. The primary CFD tool used for preflight performance analysis of the X-43A is GASP [63] - a multiblock, structured grid, upwind-based, Navier-Stokes flow solver which addresses (1) mixtures of thermally perfect gases via polynomial thermodynamic curve fits, (2) frozen, equilibrium, or finite-rate chemistry, (3) turbulent flow via Baldwin-Lomax algebraic turbulence model with Goldberg backflow correction. The SRGULL (developed by NASA's Zane Pinckney) and SHIP (supersonic hydrogen injection program) codes were used to predict scramjet performance for the X-43A [19, 62, 63]. SRGULL uses a 2D axis-symmetric Euler flow solver (SEAGULL). This was used [63] to address the forebody, inlet, and external nozzle regions of the X-43A lower surface flowpath. SRGULL also includes a 1D chemical equilibrium analysis code (SCRAM) which was used to approximate the combustor flowfield. X-43A CFD flow field solutions may be visualized in [19]. Extensive databases exist for designing engines which exhibit good performance in the range Mach 4-7 [19].

1.2.2 Controls-Relevant Hypersonic Vehicle Modeling

The following describes control-relevant hypersonic vehicle models addressing aero-thermo-elastic-propulsion effects.

- In support of NASP research, the work within [37] describes a 6DOF model for a 300,00 lb, 200 ft, horizontal-takeoff winged-cone SSTO hypersonic vehicle. The model was generated using a (1) subsonic/supersonic panel code

(APAS [73]), (2) hypersonic local surface inclination code (HABP [73]), (3) 2D forebody, inlet, nozzle code, and a (4) 1D combustor code. This model/vehicle has been used to guide the work of many controls researchers [74–81]. A significant short coming of the above model is that it cannot be used for control-relevant vehicle configuration design studies (at least not without repeating all of the work that went into generating the model); e.g. examining stability and coupling as vehicle geometry is varied. Efforts to address this are described below.

- Within [82] the authors describe the development of one of the first control-relevant first principles 3-DOF models for a generic hypersonic vehicle. Aerodynamic forces and moments are approximated using classical 2D Newtonian impact theory [1] . A simple static scramjet model is used. The flow is assumed to be quasi-one-dimensional and quasi-steady. Scramjet components include an isentropic diffuser, a combustor modeled via Rayleigh flow (1D compressible flow with heat addition) [83], and an isentropic internal nozzle. The aft portion of the fuselage serves as the upper half of an external nozzle. The associated free-stream shear layer forms the lower half of the external nozzle. This layer is formed by the equilibration of the static pressure of the exhaust plume and that of the free-stream flow. A simplifying aft nozzle-plume-shear layer assumption is made that smoothly transitions the aft body/nozzle pressure from an exit pressure value p_e to the downstream free-stream value p_∞. Implicit in the assumption is the idea that Mach and AOA perturbations do not change the location of the shear layer and that aft pressure changes are determined solely by exit pressure changes and elastic motion [82, pg. 1315]. Controls include an elevator, increase in total temperature across the combustor, and diffuser area ratio. A single body bending

mode was included based on a NASTRAN derived mode shape and frequency for a vehicle with a similar geometry. This model is a big step toward permitting control-relevant vehicle configuration design studies.

- The following significant body of work (2005-2007) [3, 4, 12, 15] examines aero-thermo-elastic-propulsion modeling and control issues using a first principles nonlinear 3-DOF longitudinal dynamical model which exploits inviscid compressible oblique shock-expansion theory to determine aerodynamic forces and moments, a 1D Rayleigh flow scramjet propulsion model with a variable geometry inlet, and an Euler-Bernoulli beam based flexible model. The model developed in this work will be used as the basis for this thesis - one which describes important control system design issues; e.g. importance of FER margin as it relates to the control of scramjet powered vehicles.
- Within [84] the authors describe the development of a nonlinear 3-DOF longitudinal model using oblique shock-expansion theory and a Rayleigh scramjet (as above) for the winged-cone vehicle described within [37]. Euler-based (inviscid) computational fluid dynamics (CFD) is used to validate the model. A related line of work has been pursued in [85]. Within [74], wind-tunnel-CFD based nonlinear and linear longitudinal and lateral models are obtained for the above winged-cone vehicle.
- X-43A related 6-DOF Monte-Carlo robustness work is described within [17]. Results obtained from conducting closed loop simulations in the presence of uncertainty are presented (as permitted). Limited comparisons between flight data and simulation data are made in an effort to highlight modeling shortfalls.

The above demonstrates the need for (mathematically tractable) parameterized control system design models that can be used for configuration design studies as well

as higher fidelity control system evaluation models.

1.2.3 Modeling and Control Issues/Challenges

Lifting Body and Waverider Phenomena/Dynamics. Much attention has been given in the literature to integrated-airframe air-breathing propulsion [21] lifting body designs; e.g. X-30 [34–36], X-33 [26, 38, 39], X-34 [40, 41], X-43 [17, 19, 20, 42], X-51 [43]. Waverider designs [1, 86–89] - a special subclass of lifting body designs - have received particular attention; e.g. X-30, X-51 [43], Falcon [44–46, 69, 70, 90] . Relevant phenomena/dynamics are now discussed.

Why Waveriders? Generally, lift-to-drag (L/D) decreases with increasing Mach and is particularly poor for hypersonic vehicles (flat plate: $(L/D)_{max} = 6.5$; Boeing 707: $(L/D)_{max} = 20$ cruising near Mach 1) [1, page 251]. Conventional hypersonic vehicles typically have a detached shock wave along the leading edge and a reduced $(L/D)_{max}$. This is particularly true for blunt lifting body designs. In contrast, waveriders are hypersonic vehicles that (if properly designed and controlled) have an attached shock wave along the leading (somewhat sharp) edge [1, pp. 251-252] and "*appear to ride the bow shock wave*." Moreover, the high pressure flowfield underneath the vehicle remains somewhat contained with little leakage over the top in contrast to conventional hypersonic vehicles. As such, waveriders can exhibit larger L/D ratios, a larger lift for a given angle-of-attack (AOA), and can be flown at lower AOAs. A maximum L/D is desirable to maximize range [1]. It follows, therefore, that *waveriders are ideal for global reach cruise applications*. A major design advantage associated with waveriders is that their associated flow fields are generally (relatively speaking) easy to compute [1]. This can be particularly useful during the initial design phase where it is critical to explore the vehicle pa-

rameter design space in order to address the inherent multidisciplinary optimization [90, 91].

Aero-Thermo. Drag can be reduced by making the body more slender (increased fineness) [92]. While this can reduce drag, it increases structural heating [1]; e.g. nose (stagnation point) heating, is inversely proportional to the nose radius. For this reason, *most hypersonic vehicles possess blunt noses*; e.g. Space Shuttle [1, page 200]. The needle-nosed coned-wing studied in [77, 80] and other studies may generate excessive heat for the first stage of a TSTO solution. Despite this, the authors strongly recommend that the reader examine the work described within [77, 80]. The point here is that fundamentally, hypersonic vehicle design is heat-driven, not drag-driven. This is because within the hypersonic regime *heating varies cubicly with speed, while drag varies quadratically* [1, pp. 347-348].

Scramjet Propulsion. The *entire underbelly of a waverider is part of the scramjet propulsion system*. Waveriders rely on bow shock and forebody design to provide significant *compression lift*, while the aftbody acts as the upper half of an expansion nozzle. Hypersonic vehicles generally possess long forebody compression surfaces to make the effective free-stream capture area as large as possible relative to the engine inlet area [21, pp. 40-41]. Generally, multiple compression ramps are used to achieve the desired conditions at the inlet. The X-43A, for example, used three compression ramps.

In contrast to rockets, air-breathing propulsion systems need not carry an oxidizer. This significantly reduces take-off-gross-weight (TOGW) [93]. Roughly, for a given payload weight $W_{payload}$, $\frac{W_{rocket}}{W_{payload}} \approx 25$ while $\frac{W_{airplane}}{W_{payload}} \approx 6.5$ [21, page 16]. Moreover, air-breathing systems offer increased safety, flexibility, robustness, and

reduced operating costs [48, 94]. Scramjet propulsion specifically offers the potential for significantly increased specific impulse I_{sp} in comparison to rocket propulsion - hence lower cost-per-pound-to-orbit [59] (I_{sp} for hydrogen is much greater than that for hydrocarbon fuels). Scramjet operation is roughly Mach 5-16 [21], while air-breathing propulsion operation is roughly below 200kft [21, page 44]. In contrast to regular jets which have a compressor, scramjets (which rely on forebody compression) have no moving parts. When fuelled with hydrogen, they can (in theory) operate over a large range of Mach numbers (Mach 5-24) [95]. Scramjets are typically optimized at a selected design Mach number (e.g. Mach 7) to satisfy a shock-on-lip condition. At off-design speeds, a cowl door can be used to minimize air mass flow spillage. Cowl doors are generally scheduled open-loop [95]. For a very flexible vehicle, however, feedback may be required in order to reduce sensitivity to modeling errors.

Trajectories. Likely vehicle trajectories will lie within the so-called air-breathing corridor corresponding to dynamic pressures in the range $\overline{q} \in [500, 2000]$ psf - lower bound dictated by lifting area limit, upper bound dictated by structural limits. At Mach 16, the lower $\overline{q} = 500$ bound will require flight below 150kft [21, page 39]. Generally speaking, scramjet-powered vehicles will fly at the highest allowable (structure permitting) dynamic pressure in order to maximize free-stream mass airflow per unit area to the engine. It should be noted, however, that accelerating vehicles would have to increase dynamic pressure in order to maintain mass flow per unit area to the engine [21, page 41]. For this reason, we may wish to fly the vehicle being considered at $\doteq 1500 - 1750$ psf (see Figure 1) so that it has room to increase dynamic pressure by moving toward larger Mach numbers while avoiding thermal choking at the lower Mach numbers (e.g. Mach 5). Within [21,

page 39], we see that the air-breathing corridor is about 30 kft wide vertically (see Figure 1). Assuming that the vehicle is flying along the center of the corridor, a simple calculation shows that if the flight path angle (FPA) deviates by about 2.86° ($\gamma \geq \sin^{-1}\left(\frac{\Delta h/\Delta t}{v}\right) \approx \sin^{-1}\left(\frac{15000/30}{10(1000)}\right)$) for 30 sec at Mach 10, then the vehicle will leave the corridor. (This simple calculation, of course, does not capture the potential impact of dynamics.) This unacceptable scenario illustrates the need for FPA control - particularly in the presence of uncertain flexible modes.

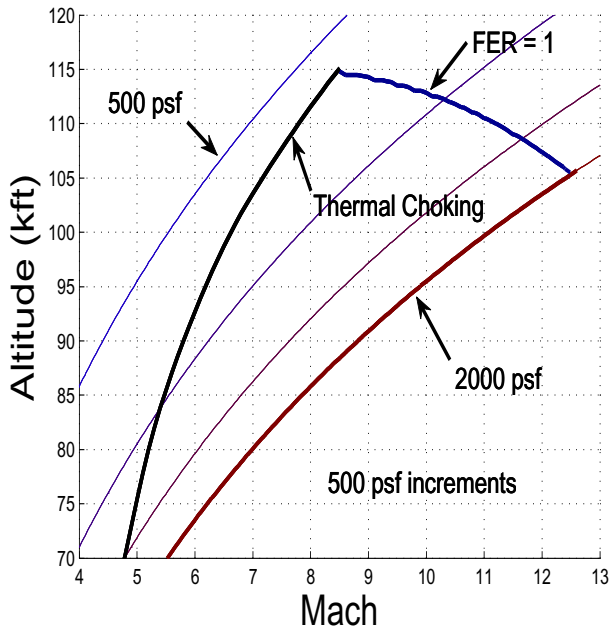

Figure 1: Air-Breathing Corridor Illustrating Constant Dynamic Pressure (Altitude vs Mach) Profiles, Thermal Choking Constraint, and FER Constraint; Notes: (1) Hypersonic vehicle considered in this thesis cannot be trimmed above the thermal choking line; (2) An FER $\leq$ 1 constraint is enforced to stay within validity of model; (3) Constraints in figure were obtained using viscous-unsteady model for level flight [2–15]

Figure 1 shows the constant dynamic pressure "trajectories" (or profiles) of altitude versus Mach. (It should be noted that the term trajectory is used loosely here since time is not shown in the figure.) With that said, Figure 1 demonstrates the

permissible "air-breathing flight corridor" or "flight envelope" for air-breathing hypersonic vehicles. In addition to the dynamic pressure constraints discussed above, the figure also indicates a constraint associated with thermal choking and one due to unity stoichiometrically normalized fuel equivalency ratio (FER=1). Additional air-breathing corridor constraints are discussed within [96].

Aero-Propulsion Coupling. In contrast to sub- and supersonic vehicles, hypersonic vehicles are uniquely characterized by *unprecedented aero-propulsion coupling*; i.e. the components providing lift, propulsion, and volume are strongly coupled [1, pp. 11-12]. More specifically, *aero performance cannot be decoupled from engine performance* because external forebody and nozzle surfaces are part of the engine flowpath [97]. For this reason, the integrated airframe-engine is sometimes referred to as an "engineframe." More specifically, vehicle aerodynamic properties impact the bow shock - detached for blunt leading edges, attached for sharp leading edges. This influences the engine inlet conditions which, in turn, influences thrust, lift, drag, external nozzle conditions, and pitching moment. More specifically, while forebody compression results in lift and a nose-up pitching moment aftbody expansion results in lift and a nose-down pitching moment. With the engine thrust situated below the c.g., this produces a nose-up pitching moment that must be countered by some control effector. Finally, it must be noted that scramjet air mass capture area, spillage, engine performance, as well as overall vehicle stability and control properties depend upon Mach, angle-of-attack (AOA), side-slip-angle (SSA), and engine power setting.

Hypersonic Flow Phenomena. Hypersonic flow is characterized by certain physical variables becoming progressively important as Mach is increased [1, 28, 30].

The boundary layer (BL), for example, grows as $\frac{M_\infty^2}{\sqrt{Re_{local}}}$. This causes the body to appear thicker than it really is. Viscous interactions refers to BL mixing with the inviscid far field. This impacts pressure distribution, lift, drag, stability, skin friction, and heat transfer. Shock layer variability is observed to start at around Mach 3 [1, page 13].

Aero-Thermo-Elastic-Propulsion. Hypersonic vehicles are generally unstable (long forebody, rearward engine, cg aft of ac) [4, 82]. As such, such vehicles generally require a *minimum control bandwidth (BW) for stabilization* [4, 98, 99]. The achievable BW, however, can be limited by flexible (structural) dynamics, actuator dynamics, right half plane zeros, other high frequency uncertain dynamics, and variable limits (e.g. control saturation level) [99]. High Mach numbers can induce significant heating and flexing (reduction of flexible mode frequencies) [34, 38, 100]. Carbon-Carbon leading edge temperatures on the X-43A Mach 10 flight, for example, reached nearly $2000^\circ F$ [19]. During the Pegasus boost (100 sec), surface temperatures reached nearly $1500^\circ F$ [19].

Heat induced forebody flexing can result in bow shock wave and engine inlet oscillations. This can impact the available thrust, stability, and achievable performance – a major control issue if the vehicle is too flexible (light) and open loop unstable. A thermal protection system (TPS) is important to reduce heat-induced flexing; i.e. *prevent lowering of structural mode frequencies* [6, 10, 54, 60]. Designers must generally tradeoff vehicle lightness (permissible payload size) for increased thermal protection and vice versa. Type IV shock-shock interactions (e.g. bow shock interaction with cowl shock, results in supersonic jet impinging on cowl) - can cause excessive heating [1, page 226] that leads to structural damage. Within [54], relevant cutting-edge structural strength/thermal protection is-

sues are addressed; e.g. high specific strength (strength/density) that ceramic matrix composites (CMCs) offer for air-breathing hypersonic vehicles experiencing $2000^\circ - 3000^\circ F$ temperatures. Materials for leading edges, aeroshells, and control surfaces are also discussed.

Non-minimum Phase Dynamics. Tail controlled vehicles are characterized by a non-minimum phase (right half plane, RHP) zero which is associated with the elevator to flight path angle (FPA) map [15]. This *RHP zero limits the achievable elevator-FPA BW* [98, 99, 101].

High Temperature Gas Effects. Relevant high temperature gas effects include [1] caloric imperfection (temperature dependent specific heats and specific heat ratio), vibrational excitation, O_2 dissociation, N_2 dissociation, plasma/ionization, radiation, rarefied gas effects [1, 21]. A more detailed description of these effects (and the conditions at which they are manifested) is provided in this thesis (see section 3.1, page 35).

The above hypersonic phenomena are accurately modeled by suitable partial differential equations (PDEs); e.g. Navier-Stokes, Euler, Euler-Bernoulli, Timoshenko, and heat transfer PDEs. This, together with the above interactions and associated uncertainty [1, 2, 4, 6, 17–23, 25–33], highlights the relevant modeling and control challenges.

Model Limitations. The limitations of the model used in this thesis are listed here by functional section

1. **Aero.** the inviscid flow does not properly feed the viscid flow. In this model

the Inviscid flow is computed over the skin of the vehicle and the viscous effects are added into the drag and lift forces. In reality the inviscid flow is dependent on the viscid flow over the body. Boundary Layer/Shock interactions are not captured in the model, as well as Shock/Shock interactions

2. **Propulsion.** The scramjet engine is modeled as having 1-Dimensional Rayliegh flow, this gives algebraic equations for the temperature inside the engine, rather that ODE's which would account for the finite chemistry rate that is actually taking place.

3. **Elastics.** TPS masses are not modeled in determining the aero-thermo-flexibility for the vehicle. The model uses 1 free free beam with the center of gravity behind the center of pressure to model the vibrations. This is an more accurate depiction as this leads to deflection at the center of gravity based on its mass and structural properties.

This motivates the following control-relevant questions:

- When do each of the above become significant for controls?
- How can each of the above phenomena be modeled with a desired level of user-specified fidelity in an effort to capture control needs?

1.3 Outline

The rest of this thesis is organized as follows. Chapter 3 describes the mathematical models of the HSV aircraft for the longitudinal dynamics. Chapter 4 describes how the properties of the nominal nonlinear HSV change as a function of flight condition, when trimmed at a zero flight path angle (FPA). Chapter 5 describes the linearization process and investigates in detail how the linear dynamics of the trimmed HSV model change as a function of flight condition. In Chapter 6, structural TPS high speed aero heating concepts calculations and solutions are presented. Effect

of TPS formulation and its effects over static and dynamic properties of vehicle are also discussed. Chapter 7 presents a simple inner-outer loop control architecture, and the changes in the controller for different vehicle configurations(namely related to heat, mass and flexibility) is presented. Finally, Chapter 8 summarizes the results of this thesis, and suggests possible directions for future research.

1.4 Table of Definitions

The following is a list of variables with units which are used throughout the thesis.

v	Speed	(k ft/sec)
α	Angle of Attack	(deg)
q	Pitch Rate	(deg/sec)
Θ	Pitch Angle	(deg)
h	Altitude	(ft)
η_1	First Flexible Mode	(rad)
$\dot{\eta_1}$	First Flexible Mode Rate	(rad/s)
η_2	Second Flexible Mode	(rad)
$\dot{\eta_2}$	Second Flexible Mode Rate	(rad/s)
η_3	Third Flexible Mode	(rad)
$\dot{\eta_3}$	Third Flexible Mode Rate	(rad/s)
δ_e	Elevator Deflection	(deg)
FER	Fuel Equivalence Ratio	(-)
N_i	i^{th} Generalized Modal Force	(rad/s^2)
Φ_i	i^{th} mode shape	(-)
$\bar{q}$	Dynamic Pressure	(lbs/ft^2)
M_∞	Speed of freestream flow	(Mach)
V_∞	Speed of freestream flow	(ft/s)
p_∞	Freestream pressure	(lbs/ft^2)
T_∞	Freestream temperature	$(^\circ R)$
p_f	Pressure acting on the lower forebody	(lbs/ft^2)
$F_{x,f}$	Lower body forces in the x direction	(lbs)
$F_{z,f}$	Lower body forces in the z direction	(lbs)
M_f	Moment acting on the lower forebody	(lbs-ft)

p_u	Pressure acting on the upper forebody	(lbs/ft^2)
$F_{x,u}$	Upper body forces in the x direction	(lbs)
$F_{z,u}$	Upper body forces in the z direction	(lbs)
M_u	Moment acting on the upper forebody	(lbs-ft)
p_b	Pressure acting on the bottom of the engine	(lbs/ft^2)
$F_{z,b}$	Forces on the bottom of the engine in the z direction	(lbs)
M_b	Moment acting on the bottom of the engine	(lbs-ft)
M_1	Speed of flow in the engine inlet, behind the shock	(Mach)
V_1	Speed of flow in the engine inlet, behind the shock	(ft/s)
p_1	Pressure at the engine inlet, behind the shock	(lbs/ft^2)
T_1	Temperature at the engine inlet, behind the shock	$(^\circ R)$
$F_{x,inlet}$	forces at the engine inlet in the x direction	(lbs)
$F_{z,inlet}$	forces at the engine inlet in the z direction	(lbs)
M_2	Speed of flow in the engine diffuser	(Mach)
p_2	Pressure at the engine diffuser	(lbs/ft^2)
T_2	Temperature at the engine combustor entrance	$(^\circ R)$
M_3	speed of flow in the engine combustor	(Mach)
p_3	pressure at the engine combustor	(lbs/ft^2)
T_3	temperature at the engine combustor exit	$(^\circ R)$
ΔT_c	change in total temperature in the combustor	$(^\circ R)$
H_f	specific heat of LH2	(-)
c_p	specific heat of air	(-)
T^*	reference temperature	$(^\circ R)$
R_e	Reynolds number	(-)
$\dot{m}_f$	Massflow of fuel	(slugs/s)
M_e	Speed of flow in the engine exit	(Mach)

V_e	Speed of flow in the engine exit	(ft/s)
p_e	Pressure at the engine exit	(lbs/ft^2)
T_e	Temperature at the engine exit	$(^\circ R)$
$F_{x,e}$	exhaust forces on the aftbody in the x direction	(lbs)
$F_{z,e}$	exhaust forces on the aftbody in the z direction	(lbs)
$Lift_{viscous}$	Lift due to viscous effects	(-)
$Drag_{viscous}$	Drag due to viscous effects	(-)
$Normal_{viscous}$	Normal force due to viscous effects	(lbs)
$Tangent_{viscous}$	Tangent force due to viscous effects	(lbs)
$M_{viscous}$	Moment due to viscous effects	(-)
$F_{x,cs}$	elevator force in the x direction	(lbs)
$F_{x,cs}$	elevator force in the z direction	(lbs)
$F_{x,unsteady}$	forces due to unsteady pressure distribution in the x direction	(lbs)
$F_{z,unsteady}$	forces due to unsteady pressure distribution in the z direction	(lbs)
$M_{unsteady}$	Moment due to unsteady pressure distribution	(lbs-ft)
F_x	sum of the forces in the x direction	(lbs)
F_z	sum of the forces in the z direction	(lbs)
h_i	Engine Inlet Hieght	(ft)
A_d	Diffuser Area Ratio	(-)
A_n	exit nozzle area ratio	(-)

2. CONTRIBUTIONS

2.1 Contributions

A nonlinear 3DOF (degree of freedom) longitudinal model which includes aero-propulsion-elasticity effects is used for all analysis. The model is used to examine the vehicle's static and dynamic characteristics over the vehicle's trimmable region. The vehicle is characterized by unstable non-minimum phase dynamics with significant (approximately lower triangular) longitudinal coupling between fuel equivalency ratio (FER) or fuel flow and flight path angle (FPA). For control system design purposes, the plant is a two-input two-output plant (FER-elevator to speed-FPA) 11 state system (including 3 flexible modes). Speed, FPA, and pitch are assumed to be available for feedback.

The new model captures realistic heating for the provided TPS structure. 1D heat equation for the vehicle provides the temperature profile. This calculated temperature profile is then used to determine the viscous effects.

TPS modeling issues related to heat and mass are addressed and their effects on the elasticity is shown for Bolender's basic model with new engine and after shock pressure for the plume calculation. De-centralized control design and its performance is studied for change in elasticity due to change in added heat, mass.

Design and Analyses

1. *Developed an aerodynamic heating model based off of the methods described within [6]. The model generated time dependent temperature profiles for use within the HSV Dynamic Model.*

2. *Aerodynamic heating model can be used to simulate heating interactions for up to 3 different materials each with varying degrees of thickness. A time dependent temperature profile is generated for each material.*

3. *Aerodynamic heating model has been used to simulate heating profiles for the following cases at Mach8, Altitude 85kft, 2-20hrs of sustained flight. a. Aerodynamic heating by flight dependent net heat flux input. b. Constant net flux input of 15Btu/ft2s .*
4. *Aerodynamic heating model can be used to generate additional time dependent temperature profiles. Roughly 800 number of computational seconds are required to simulate 2 hours of flight time.*
5. *The HSV Dynamic Model has been modified to use the temperature of the outermost material layer as the boundary condition for viscous pressure model (Eckert's Temperature Reference Method).*
6. *The time dependent temperatures have been applied to the HSV Dynamic Model in order to capture flexibility (Elasticity), static and dynamic behavior*

7. *Nominal Control is designed for nominal model (mach8, altitude 85kft, flight dependent heat flux, 2hour of sustained flight, PM2K 3, SiO2 0.1, Titanium 9.6)*
8. *This controller is tested for all the cases of time of flight, Mass, Elasticity and TPS dimension variation.*
   (a) *2hr sustained flight for two different scenarios of heat input namely (1) flight dependent net heat flux and (2) constant heat flux input for following geometry*
      i. *PM2000 (3 inches), Si02 (.1 inches), Ti(9.6 to 4 inches) i.e. including TPS*
      ii. *Si02(0.1 inches), Ti (9.6 inches) without PM2000*
      iii. *Ti (9.6 to 4 inches) without TPS*
   (b) *20hr of flight for nominal model.*
   (c) *Mass variation (Mass ratio of 0.6 to 1.4)*
   (d) *Elasticity Variation (EI ratio of 0.3 to 1.5)*

Test Cases

This thesis addresses a myriad of issues that are of concern to both vehicle and control system designers,and represents a step toward answering the critical control-relevant vehicle design questions for scenarios involving Elasticity, TPS mass, TPS physical dimension and prolonged heat of the structures's TPS impact static and dynamic properties of the linearized model of HSV.

1. Cause- Structural Elasticity (EI) Changes:
   (a) For EI ratio of 0.3 to 1.5, after 2hr of sustained flight at Mach8, Altitude 85kft with flight dependent heat flux input.
2. Cause- Structure Mass Changes:
   (a) Cases for different masses of Structure namely MR 0.6 to 1.4 after 2hr of sustained flight at Mach8, Altitude 85kft with flight dependent heat flux input.
3. Cause- Aerodynamic Heating: Cases for 2 to 20hr of aerodynamic heating for PM2k 3, SiO2 0.1, Titanium 9.6:
   (a) With TPS, Flight dependent heat flux input.
   (b) Without TPS, Flight dependent heat flux input.
   (c) With TPS, constant heat flux input (15BTU/ft^2s).
   (d) Without TPS, constant heat flux input (15BTU/ft^2s).
4. Cause- TPS Structural dimension changes: Cases for reduced Titanium Thicknesses [9.6,9,8, 7,6,5,4] after 2hr of sustained flight:
   (a) With TPS (PM2k, SiO2, Titanium together), Flight dependent heat flux input.
   (b) Without TPS (only Titanium), Flight dependent heat flux input.

The outcome of the research work is described below sectioned in the form of fundamental questions and answers for the cases established above.

Fundamental Questions-Answers

2.1.1 Fundamental Questions; Answers - Elasticity Effects

Case1: With TPS (PM2k 3, SiO2 0.1Titanium 9.6), Flight dependent heat flux input : [Elasticity Ratio varied from 0.3 to 1.5 , 2hr of sustained flight, Mach-8, Altitude-85kft.

1. How do skin temperature, average Titanium temperature , EI elasticity and fundamental freq change for Elasticity (EI) Ratio change ?
   (a) Surface temperature of PM2000 is constant at 2035 R,
   (b) Average Titanium temperature is also constant at 654R
   (c) First Fundamental frequency (w1) varies linearly with Elasticity (EI) Ratio.
      i. For 50% rise in EI, w1 rises by 22.5% ;
      ii. 68% reduction in EI cause w1 to reduce by 43.3%.
   (d) So =6.0 db, To=4.15dB for 56% drop in EI, w1 is reduced by 33.7%.
   (e) To =6.0db, So=7.74dB for 59% drop in EI, w1 is reduced by 36%.
2. When does average titanium temperatures and Skin temperature reach their maximum operating temperature?
   (a) Average Titanium temperature and Skin temperature are always under their maximum operating temperatures for all EI Ratio after 2hr of flight. They remain unaltered for any change in EI (Avg. Titanium Temp= 654R, PM2000 External Surface Temp. = 2036 R)
3. Static and Dynamic changes?
   (a) Static properties are not affected for EI Ratio changes. Other than the flexible modes, other dynamic properties are not affected for EI Ratio changes.

4. When does controller fails? Q. How does Controller performance changes?
    (a) Controller for nominal model is able to stabilize plants generated for EIR 0.32 (68% reduction),
    (b) Below EI Ratio of 0.32 nominal controller fails to stabilize the plant.
    (c) Singular values observe increased peaking with decreasing EI Ratio, for EIR 0.32 (To=16.33dB So=17.12dB).

2.1.2 Fundamental Questions; Answers - Mass Effects

Case1: With TPS (PM2k 3, SiO2 0.1Titanium 9.6), Flight dependent heat flux input : [Mass Ratio varied from 0.6 to 1.4 , 2hr of sustained flight, Mach-8, Altitude-85kft.

1. How do skin temperature, average Titanium temperature , EI elasticity and fundamental freq change for Mass Ratio change ?
    (a) Surface temperature of PM2000 is constant at 2035 R,
    (b) Average Titanium temperature is also constant at 654R
    (c) Elasticity EI is independent of system mass. Hence, it does not change.
    (d) First Fundamental frequency (w1) is independent of system mass. Hence, it does not change.
2. When does average titanium temperatures and Skin temperature reach their maximum operating temperature?
    (a) Average Titanium temperature and Skin temperature are lower than their maximum operating temperatures for all MR after 2hr of flight. They remain unaltered for any change in MR (Avg. Titanium Temp= 654R, PM2000 External Surface Temp. = 2035 R)
3. Static and Dynamic changes?
    (a) Static and Dynamic properties change for MR changes.

4. When does controller fails? Q. How does Controller performance changes?
    (a) Controller for nominal model is able to stabilize plants generated for MR 0.9,
    (b) MR of 0.8 and below, controller fails to stabilize the plant.
    (c) Singular values observe increased peaking with decreasing MR, for MR 0.9 (To=5.31dB, So=9.04dB).

2.1.3 Fundamental Questions; Answers - Prolonged Heating

Case1: With TPS(PM2k 3, SiO2 0.1, Titanium 9.6), Flight dependent heat flux input, Mach-8, Altitude-85kft.(NOMINAL MODEL CASE)

1. How do skin temperature, average Titanium temperature , EI elasticity and fundamental freq change after 20hr of flight?
    (a) Surface temperature of PM2000 rises to 2083 R,
    (b) Average Titanium temperature rises to 1419 R (at t=0, Temperatures = 559 R)
    (c) Elasticity (EI) reduces by 27.77%
    (d) Structural fundamental frequency(w1) drops by 14.74%
2. When does average titanium temperatures and Skin temperature reach their maximum operating temperature?
    (a) SiO2, PM2k remain well within their maximum operating temperature ranges (even after 20hr flight),
    (b) Average titanium temperature reaches its maximum operating temperature after 15hrs (EI reduces by 22.57%, w1 reduces by 11.79%).
3. Fundamental frequency changes?
    (a) -2% after 2.52hrs; -5% after 6hrs; -10% after 12.27hrs;

4. Static and Dynamic changes?
    (a) Little impact static and dynamic properties
5. When does controller fails? Q. How does Controller performance changes?
    (a) Controller for nominal model is able to stabilize plants generated even after 20hr.
    (b) Singular values do no observe peaking even after 20hr of sustained flight. After 20hr heating (To=2.67dB, So=5.25dB).

Case2: Without TPS(only Titanium 9.6), Flight dependent heat flux input, Mach-8, Altitude-85kft.

1. How do skin temperature, average Titanium temperature , EI elasticity and fundamental freq change after 20hr of flight?
    (a) Surface temperature of PM2000 rises to 2173 R,
    (b) Average Titanium temperature rises to 2173 R (at t=0, Temperatures = 559 R)
    (c) Elasticity (EI) reduces by 52%
    (d) Structural fundamental frequency(w1) drops by 30.15%
2. When does average titanium temperatures and Skin temperature reach their maximum operating temperature?
    (a) Titanium Skin temperature reaches its operating limit after 0.37hr(EI reduces by 5.57%, w1 reduces by 2.95%).
    (b) Average titanium temperature reaches its maximum operating temperature after 1.35hrs (EI reduces by 20.35%, w1 reduces by 10.75%).
3. Fundamental frequency changes?
    (a) -2% after 0.25hrs; -5% after 0.62hrs; -10% after 1.25hr; -20% after 3.07hr; -30% after 13.65hr; -29.92% after 12 hrs

4. Static and Dynamic changes?
    (a) Little impact static and dynamic properties
5. When does controller fails? Q. How does Controller performance changes?
    (a) Controller for nominal model is able to stabilize plants generated even after 20hr.
    (b) Singular values do no observe peaking even after 20hr of sustained flight. After 20hr heating (To=3.03dB, So=4.51dB).

Case3: With TPS (PM2k 3, SiO2 0.1, Titanium 9.6), Constant heat flux input of 15BTU/ft^2s, Mach-8, Altitude-85kft.

1. How do skin temperature, average Titanium temperature , EI elasticity and fundamental freq change after 20hr of flight?
    (a) Surface temperature of PM2000 rises to 2568 R,
    (b) Average Titanium temperature rises to 1698 R (at t=0, Temperatures = 559 R)
    (c) Elasticity (EI) reduces by 36%
    (d) Structural fundamental frequency(w1) drops by 20%
2. When does average titanium temperatures and Skin temperature reach their maximum operating temperature?
    (a) SiO2, PM2k Never reach its maximum operation temperature.
    (b) Average titanium temperature reaches its maximum operating temperature after 10.6hrs (EI reduces by 22.19%, w1 reduces by 11.81%).
3. Fundamental frequency changes?
    (a) -2% after 1.94hrs; -5% after 4.37hrs; -10% after 8.82hrs; -15% after 14hrs; -20% after 20hrs

4. Static and Dynamic changes?
    (a) Little impact static and dynamic properties
5. When does controller fails? Q. How does Controller performance changes?
    (a) Controller for nominal model is able to stabilize plants generated even after 20hr.
    (b) Singular values do no observe peaking even after 20hr of sustained flight. After 20hr heating (To=2.73dB, So=4.92dB).

Case4: Without TPS (Titanium 9.6), Constant heat flux input of 15BTU/ft^{2}s, Mach-8, Altitude-85kft.

1. How do skin temperature, average Titanium temperature , EI elasticity and fundamental freq change after 20hr of flight?
    (a) Surface temperature of PM2000 rises to 2692 R,
    (b) Average Titanium temperature rises to 2692 R (at t=0, Temperatures = 559 R)
    (c) Elasticity (EI) reduces by 67.46%
    (d) Structural fundamental frequency(w1) drops by 42.95%
2. When does average titanium temperatures and Skin temperature reach their maximum operating temperature?
    (a) Titanium skin temperature reach its operating limit after 0.26hr(EI reduces by 5.4%, w1 reduces by 3.06%).
    (b) Average titanium temperature reaches its maximum operating temperature after 0.8hrs (EI reduces by 16.6%, w1 reduces by 9.41%).
3. Fundamental frequency changes?
    (a) -2% after 0.17hrs; -5% after 0.425hrs; -10% after 0.85hrs; -20% after 1.7hrs; -30% after 3.16; -40% after 7.05hrs; -42.76% after 12 hrs and

then its constant

4. Static and Dynamic changes?
   (a) Little impact static and dynamic properties
5. When does controller fails? Q. How does Controller performance changes?
   (a) Controller for nominal model is able to stabilize plants generated even after 20hr.
   (b) Singular values observe peaking after 20hr of sustained flight. After 20hr heating (To=12.69dB, So=13.84dB).

2.1.4 Fundamental Questions; Answers - Titanium Dimension Variation

Case1: With TPS (PM2k 3, SiO2 0.1, Titanium 9.6 to 4), Flight dependent heat flux input : [Titanium Thickness is reduced], 2hr of sustained flight, Mach-8, Altitude-85kft.

1. How do skin temperature, average Titanium temperature , EI elasticity and fundamental freq change for Reduced Titanium thickness ?
   (a) Surface temperature of PM2000 is constant at 2036 R,
   (b) Average Titanium temperature rises linearly to 771 R (at t=0, Temperature = 559 R, for 9.6 average temperature was 654R after 2hr)
   (c) Elasticity (EI) reduces to -6.9% at 4 wrt t=0sec at 9.6 (% EI drop after 2hr at 9.6 was -3.08%)
   (d) Structural fundamental frequency(w1) drops to -3.41% (% w1 drop after 2hr at 9.6 was -1.51%)
2. When does average titanium temperatures and Skin temperature reach their maximum operating temperature?
   (a) Average Titanium temperature and Skin temperature are larger than their maximum operating temperatures for all titanium thicknesses after

2hr of flight. For 4 of Titanium (Avg. Titanium Temp.= 771R, External Surface Temp. = 2036R)

3. Static and Dynamic changes?
   (a) Static and Dynamic properties decrease with decreasing Titanium thickness.
4. When does controller fails? Q. How does Controller performance changes?
   (a) Controller for nominal model is able to stabilize plants generated for 8 titanium,
   (b) Titanium 7 and below, controller fails to stabilize the plant.
   (c) Singular values do no observe peaking even after reducing the Titanium by more than 50%. For 8 Titanium (To=2.94dB, So=4.39dB).

Case2: Without TPS (Titanium 9.6 to 4), Flight dependent heat flux input: [Titanium Thickness is reduced], 2hr of sustained flight, Mach-8, Altitude-85kft.

1. How do skin temperature, average Titanium temperature , EI elasticity and fundamental freq change for Reduced Titanium thickness ?
   (a) Surface temperature of Titanium is reduced from 1871 R to 2118 R,
   (b) Average Titanium temperature rises linearly to 771 R (at t=0, Temperature = 559 R, for 9.6 average temperature was 654R after 2hr)
   (c) Elasticity (EI) reduces to -49.4% at 4 wrt t=0sec at 9.6 (% EI drop after 2hr at 9.6 was -30.15%)
   (d) Structural fundamental frequency(w1) drops to -28.21% (% w1 drop after 2hr at 9.6 was -15.94%)
2. When does average titanium temperatures and Skin temperature reach their maximum operating temperature?

(a) Average Titanium temperature and Skin temperature are larger than their maximum operating temperatures for all titanium thicknesses after 2hr of flight. For 4 of Titanium (Avg. Titanium Temp= 2086R, External Surface Temp. = 2118R)

3. Static and Dynamic changes?
   (a) Static and Dynamic properties decrease with decreasing Titanium thickness.
4. When does controller fails? Q. How does Controller performance changes?
   (a) Controller for nominal model is able to stabilize plants generated for 7 titanium,
   (b) Titanium 6 and below, controller fails to stabilize the plant.
   (c) Singular values observe tremendous peaking after reducing the Titanium by 2.6 . For 7 Titanium (To=21.21dB, So=21.69dB).

Publications:Control-Relevant Modeling, Analysis, and Design for Scramjet-Powered Hypersonic Vehicles,16th AIAA/DLR/DGLR International Space Planes and Hypersonic Systems and Technologies Conference, Germany, October 19-22, 2009

3. OVERVIEW OF HYPERSONIC VEHICLE MODEL

3.1 Overview

In this chapter, we consider a first principles nonlinear 3-DOF dynamical model for the longitudinal dynamics of a generic scramjet-powered hypersonic vehicle developed by Bolender et. al. [2–14]. The vehicle is 100 ft long with weight 6,154 lb per foot of depth and has a bending mode at about 21 rad/sec. The controls include: elevator, stoichiometrically normalized fuel equivalency ratio (FER), diffuser area ratio (not considered in our work), and a canard (not considered in our work). The vehicle may be visualized as shown in Figure 2 [2]. Nominal model parameter values for the vehicle are given in Table 3.4 (page 46).

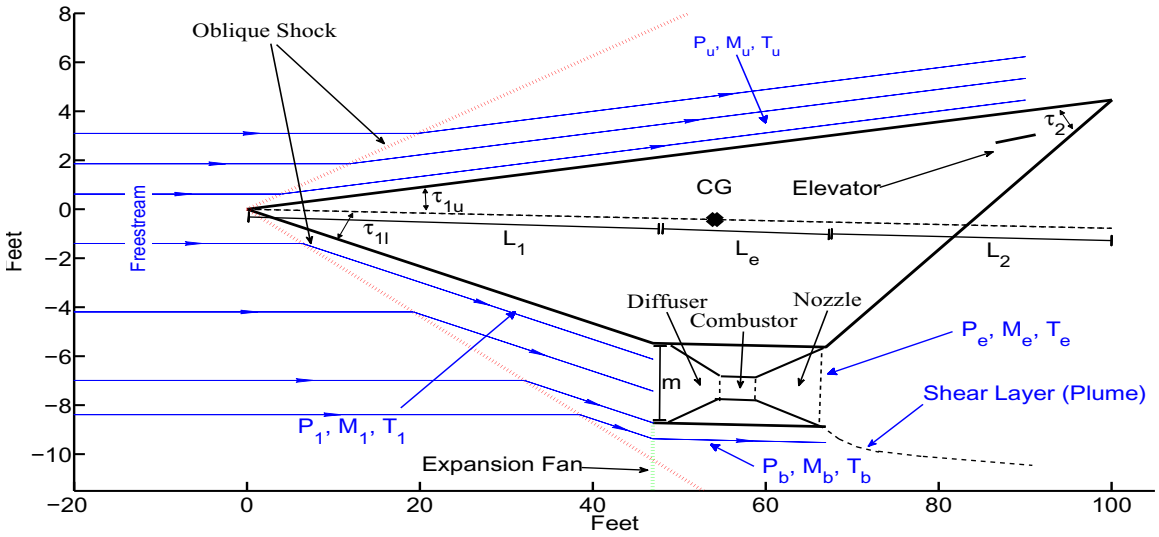

Figure 2: Schematic of Hypersonic Scramjet Vehicle

Modeling Approach. The following summarizes the modeling approach that has been used. Details are given in sections 3.3, 3.4, 3.7, 3.8.

- *Aerodynamics.* Pressure distributions are computed using inviscid compressible oblique-shock and Prandtl-Meyer expansion theory [1, 14, 28, 83]. Air

is assumed to be calorically perfect; i.e. constant specific heats and specific heat ratio $\gamma \stackrel{\text{def}}{=} \frac{c_p}{c_v} = 1.4$ [1, 83]. A standard atmosphere model is used (see section 3.4.1, page 46).

Viscous drag effects (i.e. an analytical skin friction model) are captured using Eckerts temperature reference method [1, 2]. This relies on using the incompressible turbulent skin friction coefficient formula for a flat plate at a reference temperature (see section 3.4.2, page 49). Of central importance to this method is the so-called wall temperature used.

Earlier version of the model assumes a steady state wall temperature of $2500°R$ after 1800 seconds of flight [2, page 12]. This is examined further in this thesis. [102]. The wall temperature depends upon the flight condition being examined. As such, modeling heat transfer to the vehicle via parabolic heat equation partial differential equations (pdes) as well as modeling a suitable thermal protection system is essential for obtaining insight into wall temperature selection [6]. This is be addressed more comprehensively in chapter 6.3

Unsteady effects (e.g. due to rotation and flexing) are captured using linear piston theory [2, 103]). The idea here is that flow velocities induce pressures just as the pressure exerted by a piston on a fluid induces a velocity (see section 3.4.3, page 51, or [104]).

- *Propulsion.* A single (long) forebody compression ramp provides conditions to the rear-shifted scramjet inlet. The inlet is a variable geometry inlet (variable geometry is not exploited in our work).

  The model assumes the presence of an (infinitely fast) cowl door which uses AOA to achieve shock-on-lip conditions (assuming no forebody flexing - i.e. FTA is precisely known). Forebody flexing, however, results in air mass flow

spillage [14]. At the design cruise condition, the bow shock impinges on the engine inlet (assuming no flexing). At speeds below the design-flight condition and/or larger flow turning angles, the shock angle is large and the cowl moves forward to capture the shock. At larger speeds and/or smaller flow turning angles, the shock angle is small and the bow shock is swallowed by the engine. In either case, there is a shock reflected from the cowl or within the inlet (i.e. we have a bow shock reflection - Figure 6, page 61). This reflected shock further slows down the flow and steers it into the engine. It should be noted that shock-shock interactions are not modeled. For example, at larger speeds and smaller flow turning angles there is a shock off of the inlet lip. This shock interacts with the bow shock. This interaction is not captured in the model. Such interactions are discussed in [1, page 225].

The model uses liquid hydrogen (LH2) as the fuel. It is assumed that fuel mass flow is negligible compared to the air mass flow. Thrust is linearly related to FER for all expected FER values. For large FER values, the thrust levels off. In practice, when FER $>$ 1, the result is decreased thrust. This phenomena [14] is not captured in the model. As such, control designs based on this nonlinear model (or derived linear models) should try to maintain FER below unity (see section 3.7.5, page 63). The model also captures thermal choking (i.e. unity combustor exit Mach - see section 3.7.5, page 63, or [105]). In what follows, we show how to compute the FER required to induce thermal choking as well as the so-called *thermal choking FER margin*. The above will lead to a useful FER margin definition - one that is useful for the design of control systems for scramjet-powered hypersonic vehicles.

Finally, it should be noted that the model offers the capability for addressing linear fuel depletion that can be exploited for nonlinear simulations.

- *Structural.* A single free-free Euler-Bernoulli beam partial differential equation model is used to capture vehicle elasticity. As such, out-of-plane loading, torsion, and Timoshenko effects are neglected. The assumed modes method (based on a global basis) is used to obtain natural frequencies, mode shapes, and finite-dimensional approximants. This results in a model whereby the rigid body dynamics influence the flexible dynamics through generalized forces. This is in contrast to the model described within [14] which uses fore and aft cantilever beams (clamped at the center of gravity) and leads to the rigid body modes being inertially coupled to the flexible modes (i.e. rigid body modes directly excite flexible modes). Within the current model, forebody deflections influence the rigid body dynamics via the bow shock which influences engine inlet conditions, thrust, lift, drag, and moment [10]. Aftbody deflections influence the AOA seen by the elevator. As such, flexible modes influence the rigid body dynamics.

  The nominal vehicle is 100 ft long. The associated beam model is assumed to be made of titanium. It is 100 ft long, 9.6 inches high, and 1 ft wide (deep). This results in the nominal modal frequencies $\omega_1 = 21.02$ rad/sec, $\omega_2 = 50.87$ rad/sec, $\omega_3 = 100.97$ rad/sec. When the height is reduced to 6 inches, we obtain $\omega_1 = 11.70$ rad/sec, $\omega_2 = 27.59$ rad/sec, $\omega_3 = 54.20$ rad/sec. Future work will examine vehicle mass-flexibility-control trade studies [3].

- *Actuator Dynamics.* Simple first order actuator models (contained within the original model) were used in each of the control channels: elevator - $\frac{20}{s+20}$, FER - $\frac{10}{s+10}$, canard - $\frac{20}{s+20}$ (Note: canard not used in our study). These dynamics did not prove to be critical in our study. An elevator saturation of $\pm 30^\circ$ was used [8, 106]. It should be noted, however, that these limits were never reached in our studies [105, 107–109]. A (state dependent) saturation

level - associated with FER (e.g. thermal choking and unity FER) - was also directly addressed [105]. This (velocity bandwidth limiting) nonlinearity is discussed in this chapter (section 3.7.5, page 63).

Generally speaking, the vehicle exhibits unstable non-minimum phase dynamics with nonlinear aero-elastic-propulsion coupling and critical (state dependent) FER constraints. The model contains 11 states: 5 rigid body states (speed, pitch, pitch rate, AOA, altitude) and 6 flexible states.

Unmodeled Phenomena/Effects. All models possess fundamental limitations. Realizing model limitations is crucial in order to avoid model misuse. Given this, we now provide a (somewhat lengthy) list of phenomena/effects that are not captured within the above nonlinear model. (For reference purposes, flow physics effects and modeling requirements for the X-43A are summarized within [63].)

- *Dynamics.* The above model does not capture longitudinal-lateral coupling and dynamics [110] and the associated 6DOF effects.
- *Aerodynamics.* Aerodynamic phenomena/effects not captured in the model include the following: boundary layer growth, displacement thickness, viscous interaction, entropy and vorticity effects, laminar versus turbulent flow, flow separation, high temperature and real gas effects (e.g. caloric imperfection, electronic excitation, thermal imperfection, chemical reactions such as 0_2 dissociation) [1], non-standard atmosphere (e.g. troposphere, stratosphere), unsteady atmospheric effects [22], 3D effects, aerodynamic load limits.

  Figure 3 shows the shuttle trajectory during re-entry. The angle-of-attack was fairly constant, ranging from 41 degrees at entry to 38 degrees at 10kft/s [111, page 3]. As can be seen, the vehicle passes through regions where

the vibrational excitation and chemical reactions are significant. The 10% and 90% markers denote the approximate regions where particular effects start/are completed. Some of the relevant high temperature gas effects include (see figure 3)[1]

1. Caloric imperfection (temperature dependent specific heats and specific heat ratio $\gamma \stackrel{\text{def}}{=} \frac{c_p}{c_v}$) begins at about 800K or about Mach 3.5 [1, page 18]
2. Vibrational excitation is observed around Mach 3 and fully excited around Mach 7.5 [1, page 460]
3. O_2 dissociation occurs at around 2000K and is observed at about Mach 7.5-8.5. It is complete at around 4000K or about Mach 15-17.[1], pp. 460-461

For the scramjet Mach ranges under consideration (5-15), the following phenomena are likely not to be relevant: N_2 dissociation, plasma/ionization, radiation, rarefied gas effects [1, 21]. It should be noted that onset temperatures for molecular vibrational excitation, dissociation, and ionization decrease when pressure is increased.

- *Propulsion.* Propulsion phenomena/effects not captured in the model include the following: cowl door dynamics, multiple forebody compression ramps (e.g. three on X-43A [112, 113]), forebody boundary layer transition and turbulent flow to inlet [112, 113], diffuser losses, shock interactions, internal shock effects, diffuser-combustor interactions, fuel injection and mixing, flame holding, engine ignition via pyrophoric silane [19] (requires finite-rate chemistry; cannot be predicted via equilibrium methods [90]), finite-rate chemistry and the associated thrust-AOA-Mach-FER sensitivity effects [114], internal and external nozzle losses, thermal choking induced phenomena (2D and 3D) and unstart, exhaust plume characteristics, combined cycle

issues [21].

Within [114], a higher fidelity propulsion model is presented which addresses internal shock effects, diffuser-combustor interaction, finite-rate chemistry and the associated thrust-AOA-Mach-FER sensitivity effects. While the nominal Rayleigh-based model (considered here) exhibits increasing thrust-AOA sensitivity with increasing AOA, the more complex model in [114] exhibits reduced thrust-AOA sensitivity with increasing AOA - a behavior attributed to finite-chemistry effects.

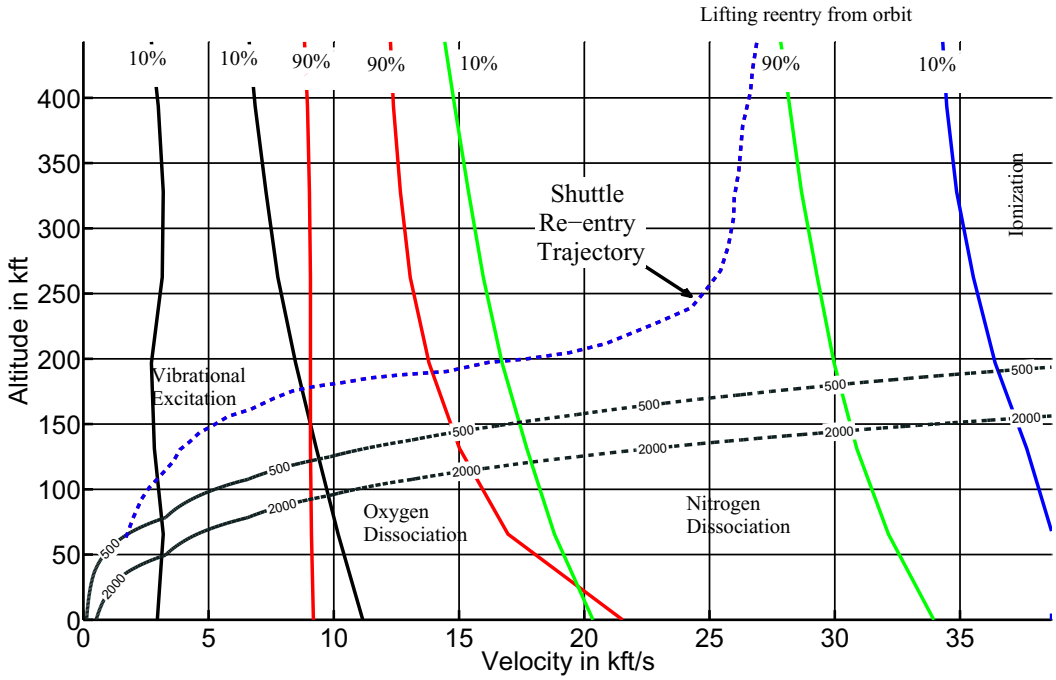

Figure 3: Visualization of High Temperature Gas Effects Due - Normal Shock, Re-Entry Vehicle (page 460, Anderson, 2006; Tauber-Menees, 1986) Approx: 1 Mach $\approx$ 1 kft/s

- *Structures.* Structural phenomena/effects not captured in the model include the following: out of plane and torsional effects, internal structural layout, unsteady thermo-elastic heating effects, aerodynamic heating due to shock im-

pingement, distinct material properties [54], and aero-servo-elasticity [115, 116].

– *Heating-Flexibility Issues.* Finally, it should be noted that Bolender and Doman have addressed a variety of effects in their publications. For example, within [6, 10] the authors address the impact of heating on (longitudinal) structural mode frequencies and mode shapes.

  Within [6], the authors consider a sustained two hour straight and level cruise at Mach 8, 85 kft. It is assumed that no fuel is consumed (to focus on the impact of heat addition). The paper assumes the presence of a thermal protection system (TPS) consisting of a PM2000 honeycomb outer skin followed by a layer of silicon dioxide (SiO_2) insulation. The vehicle - modeled by a titanium beam - is assumed to be insulated from the cryogenic fuel. The heat rate is computed via classic heat transfer equations that depend on speed (Mach), altitude (density), and the thermal properties of the TPS materials as well as air - convection and radiation at the air-PM2000 surface, conduction within the three TPS materials. The initial temperature of all three TPS materials was set to $559.67°R = 100°F$). The maximum heat rate (achieved at the flight's inception) was approximately $8.14\frac{BTU}{ft^2 sec}$ (50 foot aft of the nose).

  Suppose that the TPS has dimensions: Titanium = 6", SiO_2 = 0.1", PM2000 = 3." By the end of the two hour level flight, the average temperature within the titanium increased by $108°R$ and it was observed that the vehicle's (longitudinal) structural frequencies did not change appreciably ($< 2\%$) [6, page 18].

  When one assumes a constant $15\frac{BTU}{ft^2 sec}$ heat rate at the air-PM2000 surface (same initial TPS temperature of $559.67°R = 100°F$), then after

two hours of level flight the average temperature within the titanium increased by $200^{\circ}R$ [6, page 19]. In such a case, it can be shown that the vehicle's (longitudinal) structural frequencies do not change appreciably (3%). This high heat rate scenario gives one an idea by how much the flexible mode frequencies can change by. Such information is critical in order to suitably adapt/schedule the flight control system.

- *Actuator Dynamics.* Future work will examine the impact of actuators that are rate limited; e.g. elevator, fuel pump.

It should be emphasized that the above list is only a partial list. If one needs fidelity at high Mach numbers, then many other phenomena become important.

3.2 Vehicle Layout

In [10, page 9, Figure 2], the authors provide a notional layout for the internal volume of the model. In section 3.8 (page 74), the assumed modes method, based on Lagrange's equations (see section 3.8, page 74 or [10, page 9]) is used to calculate the natural frequencies and mode shapes for the flexible structure. The potential and kinetic energy calculations require the mass distribution for the vehicle. Below, we present the mass distributions used for the model considered in this thesis. The load of a subsystem is assumed to be uniformly distributed over the interval specified in the column 'Range'.

It should be noted that the model can account for fuel depletion. The fraction of oxygen and hydrogen consumed is used to recalculate the mass of left within the tanks. It is assumed that the fraction of fuel depleted in the fore and aft hydrogen tanks is the same.

Table 3.1: Mass Distribution for HSV Model

Subsystem	Mass (lbs)	Range (ft)
Beam	75000	[0 100]
Fore system	5000	[8 12]
Fore H_2 tank	114000	[30 50]
O_2 tank	155000	[48 62]
Payload	2500	[50 60]
Propulsion system	10000	[53 67]
Aft H_2 system	86000	[67.5 82.5]
Aft system	7500	[88 92]
Structure	50000	[40 70]

3.3 Equations of Motion

Longitudinal Dynamics. The equations of motion for the 3DOF flexible vehicle are given as follows:

$$\dot{v} = \left[\frac{T\cos\alpha - D}{m}\right] - g\sin\gamma \tag{3.1}$$

$$\dot{\alpha} = -\left[\frac{L + T\sin\alpha}{mv}\right] + q + \left[\frac{g}{v} - \frac{v}{R_E + h}\right]\cos\gamma \tag{3.2}$$

$$\dot{q} = \frac{\mathcal{M}}{I_{yy}} \tag{3.3}$$

$$\dot{h} = v\sin\gamma \tag{3.4}$$

$$\dot{\theta} = q \tag{3.5}$$

$$\ddot{\eta}_i = -2\zeta\omega_i\dot{\eta}_i - \omega_i^2\eta_i + N_i \qquad i = 1, 2, 3 \tag{3.6}$$

$$\gamma \stackrel{\text{def}}{=} \theta - \alpha \tag{3.7}$$

$$g = g_0\left[\frac{R_E}{R_E + h}\right]^2 \tag{3.8}$$

where L denotes lift, T denotes engine thrust, D denotes drag, $\mathcal{M}$ is the pitching moment, N_i denotes generalized forces, ζ demotes flexible mode damping factor, ω_i denotes flexible mode undamped natural frequencies, m denotes the vehicle's total mass, I_{yy} is the pitch axis moment of inertia, g_0 is the acceleration due to

gravity at sea level, and R_E is the radius of the Earth.

- *States.* The states consist of five classical rigid body states and six flexible modes states: the rigid states are velocity v, FPA γ, altitude h, pitch rate q, pitch angle θ, and the flexible body states $\eta_1, \dot{\eta}_1, \eta_2, \dot{\eta}_2, \eta_3, \dot{\eta}_3$. These eleven (11) states are summarized in Table 3.2.

Table 3.2: States for Hypersonic Vehicle Model

♯	**Symbol**	**Description**	**Units**
1	v	speed	kft/sec
2	γ	flight path angle	deg
3	α	angle-of-attack (AOA)	deg
4	q	pitch rate	deg/sec
5	h	altitude	ft
6	η_1	1^{st} flex mode	-
7	$\dot{\eta}_1$	1^{st} flex mode rate	sec^{-1}
8	η_2	2^{nd} flex mode	-
9	$\dot{\eta}_2$	2^{nd} flex mode rate	sec^{-1}
10	η_3	3^{rd} flex mode	-
11	$\dot{\eta}_3$	3^{rd} flex mode rate	sec^{-1}

- *Controls.* The vehicle has three (3) control inputs: a rearward situated elevator δ_e, a forward situated canard δ_c (not considered), and stoichiometrically normalized fuel equivalence ratio (FER). These control inputs are summarized in Table 3.3. In this research, we will only consider elevator and FER; i.e. the canard has been removed.

Table 3.3: Controls for Hypersonic Vehicle Model

♯	**Symbol**	**Description**	**Units**
1	FER	stoichiometrically normalized fuel equivalence ratio	-
2	δ_e	elevator deflection	deg
3	δ_c	canard deflection	deg

Nominal model parameter values for the vehicle under consideration are given in Table 3.4. Additional details about the model may be found in sections 3.4, 3.3,

3.7, 3.8, and within the following references [2–14].

Table 3.4: Vehicle Nominal Parameter Values

Parameter	Nominal Value	Parameter	Nominal Value
Total Length (L)	**100 ft**	Lower forebody angle (τ_{1L})	6.2^o
Forebody Length (L_1)	47 ft	Tail angle (τ_2)	14.342^o
Aftbody Length (L_2)	33 ft	Mass per unit width	$191.3024 \frac{slugs}{ft}$
Engine Length	20 ft	Weight per unit width	**6,154.1 lbs/ft**
Engine inlet height h_i	3.25 ft	Mean Elasticity Modulus	8.6482×10^7 psi
Upper forebody angle (τ_{1U})	3^o	Moment of Inertia I_{yy}	$86{,}723 \frac{slugs ft^2}{ft}$
Elevator position	(-85,-3.5) ft	Center of gravity	(-55,0) ft
Diffuser exit/inlet area ratio	1	Elevator Area	17 ft^2
Titanium Thickness	9.6 in	Nozzle exit/inlet area ratio	6.35
First Flex. Mode (ω_{n_1})	**21.02 rad/s**	Second Flex. Mode (ω_{n_2})	**50.87 rad/s**
Third Flex. Mode (ω_{n_3})	**101.00 rad/s**	Flex. Mode Damping (ζ)	**0.02**

3.4 Aerodynamic Modeling

The U.S. Standard Atmosphere (1976) is a commonly used atmospheric model that extends previous models (1962, 1966) from 5 up to 1000 km [117]. Above 100 kilometers, solar and geomagnetic activity cause significant variations in temperature and density [118].

3.4.1 U.S. Standard Atmosphere (1976)

Key assumptions associated with the model are as follows:

1. Sea level pressure is $2116.2\ \mathrm{lb/ft^2}$ ($14.6958\ \mathrm{lb/in^2}$, 29.92" Hg)
2. Sea level temperature is 59° F
3. Acceleration due to gravity at sea level is $g = 32.17\ \mathrm{ft/s^2}$

   - decreasing with increasing altitude as inverse of (distance from earth's center)^2
4. Molecular composition is sea level composition
5. Air is dry and motionless
6. Air obeys ideal gas law

7. Temperature decreases linearly with increasing altitude within troposphere ($-3.566°$F/1000 ft)

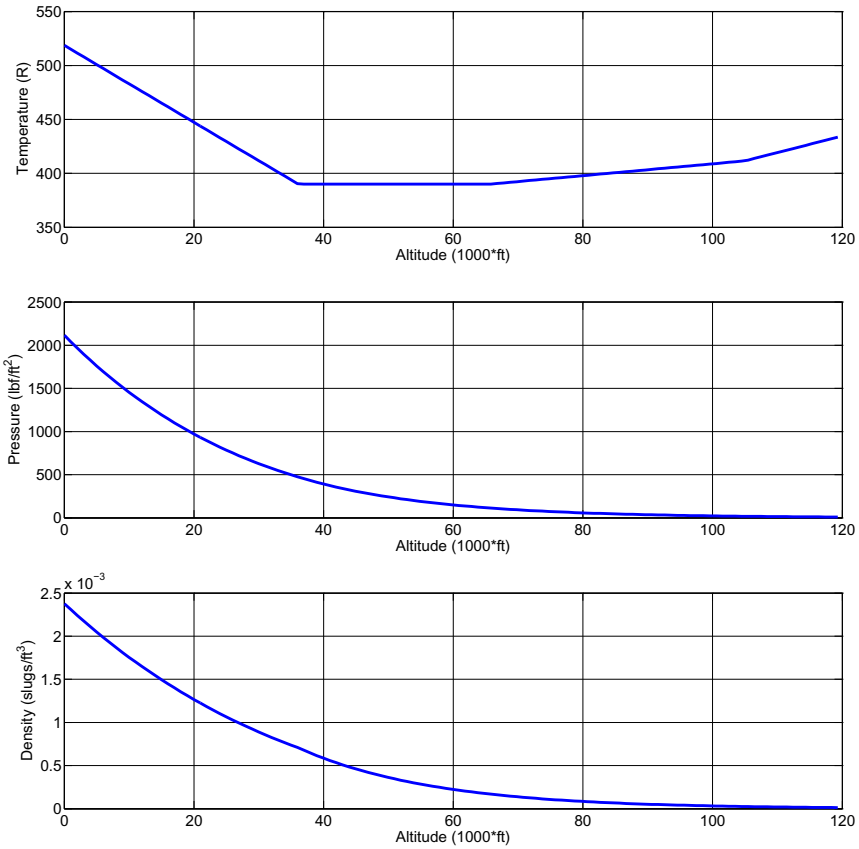

Figure 4: Atmospheric Properties vs. Altitude

- $0 \leq h < 36,089$ ft (6.835 miles)

$$t_r = 518.67 - .0036h \tag{3.9}$$

$$p = 2116 \left[\frac{t_r}{518.6}\right]^{-5.256} \tag{3.10}$$

$$\rho = 0.0024 \left[\frac{t_r}{518.6}\right]^{-4.256} \tag{3.11}$$

- $36,089$ ft $\leq h < 65,617$ ft (6.835 to 12.427 miles)

$$t_r = 389.97 \tag{3.12}$$

$$p = 472.68e^{-0.000048(h-36,069)} \tag{3.13}$$

$$\rho = \frac{p}{1416} \tag{3.14}$$

- $65,617$ ft $\leq h < 104,987$ ft (12.427-19.884 miles)

$$t_r = 389.97 + .000549(h - 65,617) \tag{3.15}$$

$$p = 114.34 \left[\frac{t_r}{389.97}\right]^{-34.16} \tag{3.16}$$

$$\rho = .0001708 \left[\frac{t_r}{389.97}\right]^{-35.16} \tag{3.17}$$

- $104,987$ ft $\leq h < 154,199$ ft (19.884-29.204 miles)

$$t_r = 411.57 + .0015(h - 104,987) \tag{3.18}$$

$$p = 18.128 \left[\frac{t_r}{411.57}\right]^{-12.2} \tag{3.19}$$

$$\rho = .0000257 \left[\frac{t_r}{411.57}\right]^{-13.2} \tag{3.20}$$

t_r - temperature (°Rankine) h - altitude above sea level (ft)

p - pressure (lbs/ft^2) ρ - density (slug/ft^3)

Limitations of 1976 U.S. Standard Atmosphere Model.

The atmosphere model does not capture fact that

- Air properties depend on latitude and are impacted by moisture,

- Air is not motionless (e.g. North-South, East-West, and vertical winds - the X-43A team assumed min-max limits at
  - 80 kft: $[-30.94, 24.46]$, $[-76.32, 70.40]$, 10 ft/sec
  - 120 kft: $[-64.34, 83.94]$, $[-78.24, 258.6]$, 10 ft/sec

3.4.2 Viscous Effects

The viscous effects [119] add a substantial amount of drag to the vehicle through the skin friction of the fluid moving around the vehicle. In this model, Eckert's Reference Temperature Method [2] is used to compute the viscous skin friction.

1. The method starts with the computation of the reference temperature which is a function of the Mach number (M_e) and temperature (T_e) at the edge of the boundary layer as well as the wall (skin) temperature T_w.

$$T^* = T_e \left[1 + M_e^2 + 0.58 \left(\frac{T_w}{T_e} - 1 \right) \right] \tag{3.21}$$

   where the wall temperature was given in ref [2] to be $2500^\circ R$. For simplicity we assume a constant wall temperature for all surfaces (see Table 3.5 for the surfaces for which viscous interaction are considered).

2. Using the perfect gas law, the density at the reference temperature ρ^* can be found from the following equation:

$$\rho^* = \frac{p}{RT^*} \tag{3.22}$$

   where p is the static pressure of the fluid.

3. The viscosity at the reference temperature μ^* can then be computed using

Sutherland's Formula, which is known to be valid up to $3500°R$.

$$\mu^* = 2.27 * 10^{-8} \frac{(T^*)^{3/2}}{T^* + 198.6} \tag{3.23}$$

4. Once the viscosity μ^* and the pressure are computed the Reynolds number at the reference temperature can be computed using:

$$Re^* = \frac{\rho^* V L}{\mu^*} \tag{3.24}$$

where V and L are the fluid velocity and the length, respectively.

5. Once the Reynolds number (Re) is calculated at the reference temperature, the skin friction coefficient for turbulent, supersonic flow over a flat plate can be computed as follows:

$$c_f = \frac{0.0592}{(Re^*)^{1/5}} \tag{3.25}$$

6. Now the shear stress at the wall τ_w can be computed by the following equation:

$$\tau_w = c_f((1/2)\rho_\infty V_\infty^2) \tag{3.26}$$

where Equation 3.26 gives the local skin friction.

7. Once τ_w is computed, integration over each surface is done to calculate the skin friction drag for each surface on the vehicle. This yields

$$F_{viscous} = \frac{5}{4}\tau_w L_s \tag{3.27}$$

When the local skin coefficient (c_f)is found for each surface of the vehicle, the normal and tangential forces are computed for each surface. The normal

Table 3.5: Viscous Interaction Surfaces

Surface	Inclination to body axis (β)
Upper forebody	τ_{1u}
Lower forebody	$-\tau_{1l}$
Engine base	0
Aftbody	$\tau_{1U}+\tau_2$
Elevator (upper surface)	$-\delta_e$
Elevator (lower surface)	$-\delta_e$

and tangential forces are obtained as follows:

$$Normal_{viscous} = F_{viscous}\sin(\beta) \tag{3.28}$$

$$Tangential_{viscous} = F_{viscous}\cos(\beta) \tag{3.29}$$

where $F_{viscous}$ is calculated as above, and β is the surface inclination to the body axis (refer Table 3.5, page 51)

The lift and drag contribution of the viscous effects are computed using these normal and tangential forces, and are given as:

$$Lift_{viscous} = Normal_{viscous}\cos(\alpha) - Tangential_{viscous}\sin(\alpha) \tag{3.30}$$

$$Drag_{viscous} = Normal_{viscous}\sin(\alpha) - Tangential_{viscous}\cos(\alpha) \tag{3.31}$$

3.4.3 Unsteady Effects

The unsteady effects are calculated using linear piston theory [2, 5, 103]. This unsteady pressure distribution is a direct result of the interactions between the flow and the structure, as well as the unsteady, rigid body motion of the vehicle. The pressure acting on the face of a piston moving in a (supersonic) perfect gas is:

$$\frac{P}{P_i} = \left(1 + \frac{V_{n,i}}{5a_i}\right)^7 \tag{3.32}$$

where P_i is the local static pressure behind the bow shock, P is the pressure on the piston face, $V_{n,i}$ is the velocity of the surface normal to the flow, and a_i ($= \sqrt{\gamma RT}$)is the local speed of sound. Using first order binomial expansion of equation 3.32:

$$\frac{P}{P_i} = 1 + \frac{7V_{n,i}}{5a_i} \tag{3.33}$$

$$P = P_i + \rho_i a_i V_{n,i} \tag{3.34}$$

The infinitesimal force acting on the face of the piston is given by:

$$d\mathbf{F}_i = (PdA)\,\mathbf{n}_i \tag{3.35}$$

$$\implies d\mathbf{F}_i = \left[-\left(P_i + \rho_i a_i V_{n,i}\right) dA\right] \mathbf{n}_i \tag{3.36}$$

The unsteady effects are computed by integrating 3.36 over each surface of the vehicle.

3.5 Properties Across a Shock

Properties Across Bow Shock. Let (M_∞, T_∞, p_∞) denote the free-stream Mach, temperature, and pressure. Let $\gamma \overset{\text{def}}{=} \frac{c_p}{c_v} = 1.4$ denote the specific heat ratio for air - assumed constant in the model; i.e. air is calorically perfect [1]. The shock wave angle $\theta_s = \theta_s(M_\infty, \delta_s, \gamma)$ can be found as the middle root (weak shock solution) of the following shock angle polynomial [14, 83]:

$$sin^6\theta_s + bsin^4\theta_s + csin^2\theta_s + d = 0 \tag{3.37}$$

where

$$
\begin{aligned}
b &= -\frac{M_\infty^2+2}{M_\infty^2} - \gamma sin^2\delta_s \\
c &= \frac{2M_\infty^2+1}{M_\infty^4} + \left[\frac{(\gamma+1)^2}{4} + \frac{\gamma-1}{M_\infty^2}\right] sin^2\delta_s \\
d &= -\frac{cos^2\delta_s}{M_\infty^4}
\end{aligned}
$$

The above can be addressed by solving the associated cubic in $sin^2\theta_s$. A direct solution is possible if Emanuel's 2001 method is used [83]:

$$\tan\theta_s = \frac{M_\infty^2 - 1 + 2\lambda\cos\left[\frac{1}{3}(4\pi\delta + \cos^{-1}\chi)\right]}{3\left(1+\frac{\gamma-1}{2}M_\infty^2\right)\tan\delta_s} \tag{3.38}$$

$$\lambda = \left[(M_\infty^2-1)^2 - 3\left(1+\frac{\gamma-1}{2}M_\infty^2\right)\left(1+\frac{\gamma+1}{2}M_\infty^2\right)\tan^2\delta_s\right]^{\frac{1}{2}} \tag{3.39}$$

$$\chi = \frac{(M_\infty^2-1)^3 - 9\left(1+\frac{\gamma-1}{2}M_\infty^2\right)\left(1+\frac{\gamma-1}{2}M_\infty^2+\frac{\gamma+1}{4}M_\infty^4\right)\tan^2\delta_s}{\lambda^3} \tag{3.40}$$

where $\delta = 1$ corresponds to desired weak shock solution; $\delta = 0$ yields strong solution.

After determining the shock wave angle θ_s, one can determine properties across the bow shock using classic relations from compressible flow [83]; i.e. M_s, T_s, p_s - functions of $(M_\infty, \delta_s, \gamma)$:

$$\frac{T_s}{T_\infty} = \frac{(2\gamma M_\infty^2\sin^2\theta_s + 1 - \gamma)((\gamma-1)M_\infty^2\sin^2\theta_s + 2)}{(\gamma+1)^2 M_\infty^2\sin^2\theta_s} \tag{3.41}$$

$$\frac{p_s}{p_\infty} = 1 + \frac{2\gamma}{\gamma+1}\left(M_\infty^2\sin^2\theta_s - 1\right) \tag{3.42}$$

$$M_s^2 sin^2(\theta_s - \delta_s) = \frac{M_\infty^2\sin^2\theta_s(\gamma-1)+2}{2\gamma M_\infty^2\sin^2\theta_s - (\gamma-1)} \tag{3.43}$$

It should be noted that for large M_∞, the computed temperature T_s across the shock

will be larger than it should be because our assumption that air is calorically perfect (i.e. constant specific heats) does not capture other forms of energy absorption; e.g. electronic excitation and chemical reactions [1, page 459].

Properties Across Prandtl-Meyer Expansion. An expansion fan occurs when there is a flow over a convex corner; i.e. flow turns away from itself. More specifically to the bow, if $\delta_s < 0$ a Prandtl-Meyer expansion will occur. To determine the properties across the expansion, let (M_∞, T_∞, p_∞) denote the free-stream (supersonic) Mach, temperature, and pressure, respectively. If we let $\delta = -\delta_s > 0$ denote the expansion ramp angle (in radians), the properties across the expansion fan (M_e, T_e, p_e) can be calculated as follows[14, 83]:

$$\nu_1 = \sqrt{\frac{\gamma+1}{\gamma-1}}\tan^{-1}\left(\sqrt{\frac{\gamma-1}{\gamma+1}(M_\infty^2-1)}\right) - \tan^{-1}\left(\sqrt{M_\infty^2-1}\right) \quad (3.44)$$

$$\nu_2 = \nu_1 + \delta \quad (3.45)$$

$$\nu_2 = \sqrt{\frac{\gamma+1}{\gamma-1}}\tan^{-1}\left(\sqrt{\frac{\gamma-1}{\gamma+1}(M_e^2-1)}\right) - \tan^{-1}\left(\sqrt{M_e^2-1}\right) \quad (3.46)$$

$$\frac{p_e}{p_\infty} = \left[\frac{1+\frac{\gamma-1}{2}M_\infty^2}{1+\frac{\gamma-1}{2}M_e^2}\right]^{\frac{\gamma}{\gamma-1}} \quad (3.47)$$

$$\frac{T_e}{T_\infty} = \left[\frac{1+\frac{\gamma-1}{2}M_\infty^2}{1+\frac{\gamma-1}{2}M_e^2}\right] \quad (3.48)$$

ν_1 is the angle for which a Mach 1 flow must be expanded to attain the free stream Mach.

3.6 Force and Moment Summations

While the above equations of motion (equations 3.1-3.6) apply to any 3-DOF aircraft, the force and moment summations (Lift, Drag, Thrust, Moment, N_i) which are summed below are specific to the scramjet powered HSV. These forces and mo-

ments are comprised of the breakdown of pressures in the body x and z directions. Some of these forces are shown in Figure 5.

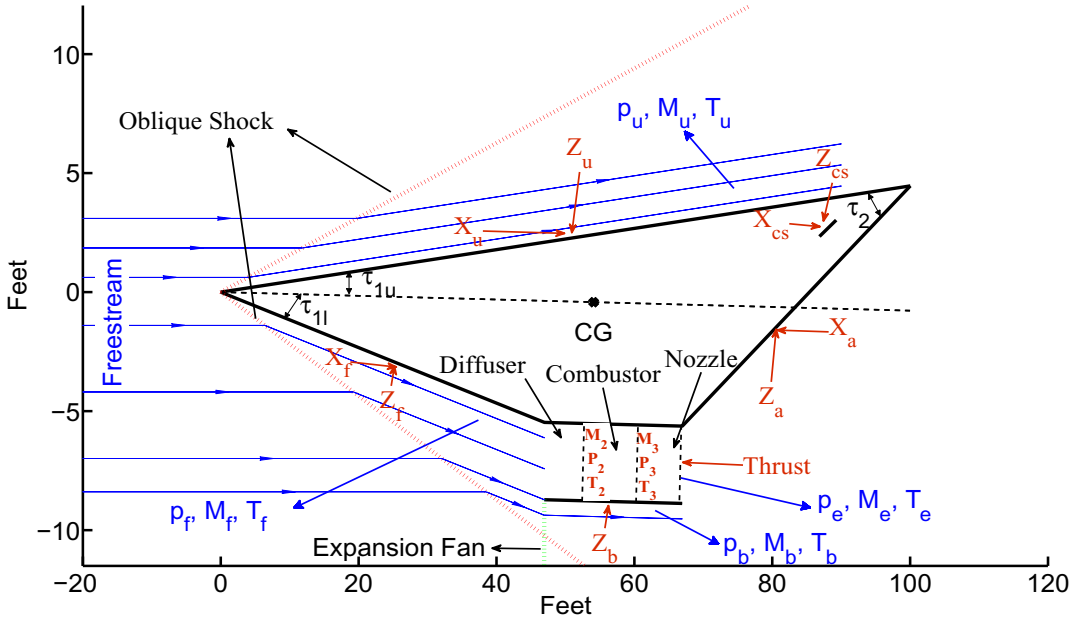

Figure 5: Free Body Diagram for the Bolender model

The equations for these forces and moments were given in [14]:

$$Lift = F_x \sin(\alpha) - F_z \cos(\alpha) + Lift_{viscous} \tag{3.49}$$

$$Drag = -(F_x \cos(\alpha) - F_z \sin(\alpha)) + Drag_{viscous} \tag{3.50}$$

$$Thrust = \dot{m}_a(V_e - V_\infty) + (p_e - p_\infty)A_e \tag{3.51}$$

$$\begin{aligned} Moment &= M_f + M_e + M_{inlet} + M_{cs} + M_u + M_b + M_{unsteady} \\ &\quad +(L_1 \tan(\tau_{1l})\frac{h_i}{2} - cg_z)Thrust + M_{viscous} \end{aligned} \tag{3.52}$$

$$N_i = \int p(x,t)\Phi_i(x)dx + \Sigma_j F_j(t)\Phi_i(x_j) \tag{3.53}$$

where n_i is the i^{th} modal coordinate of the flexible dynamics, $\Phi_i(x)$ is the i^{th} mode shape, V_e is the speed of flow exiting the engine, V_∞ is the freestream speed, p_e is the pressure at the exit of the internal nozzle, p_∞ is freestream pressure, $\dot{m}_a$ is the

mass airflow into the engine, A_e is engine exit area per unit span, F_x and F_z are the sum of forces in the x and z direction respectively, and α is the angle of attack of the vehicle. The forces and moments are summarized in Table 3.6.

Body Forces. The sum of the forces in the x and z directions (excluding viscosity, thrust) are given as

$$F_x = F_{x,f} + F_{x,u} + F_{x,e} + F_{x,inlet} + F_{x,cs} + F_{x,unsteady} \quad (3.54)$$

$$F_z = F_{z,f} + F_{z,u} + F_{z,b} + F_{z,e} + F_{z,inlet} + F_{z,cs} + F_{z,unsteady} \quad (3.55)$$

Table 3.6: HSV - Forces and Moments

Symbol	**Description**
N_i	i^{th} generalized force
$F_j(t)$	j^{th} point load acting at point x_j on the vehicle
F_x, F_z	sum of forces in x and z direction
$Lift_{viscous}$	lift due to viscous effects
$Drag_{viscous}$	drag due to viscous effects
$F_{x,f}, F_{z,f}$	lower forebody forces, x and z direction
$F_{x,u}, F_{z,u}$	upper forebody forces, x and z direction
$F_{x,inlet}, F_{z,inlet}$	forces in the engine inlet, x and z direction
$F_{x,e}, F_{z,e}$	exhaust forces on aftbody, x and z direction
$F_{x,cs}, F_{z,cs}$	elevator forces, x and z direction
$F_{x,unsteady}, F_{z,unsteady}$	unsteady forces, x and z direction
$F_{z,b}$	pressure on bottom of vehicle, z direction
$M_{unsteady}$	moment due to unsteady pressure distribution
$M_{viscous}$	moment due viscous effects
M_f	moment due to lower forebody forces
M_u	moment due to upper forebody forces
M_{inlet}	moment due to turning force at engine inlet
M_{cs}	moment due to control surface (elevator) forces
M_b	moment due to engine base forces

Forebody Forces and Moments. The forces acting on the upper and lower forebody are computed using the pressures acting on the upper and lower forebody (p_u, p_f). These pressures are computed using one of two methods depending on the

angle of the shock wave created by the nose of the vehicle. These methods are now summarized.

- If the flow over the forebody is flowing over a concave corner, use oblique shock theory
- If the flow over the forebody is flowing over a convex corner, use Prandtl-Meyer theory

Once the Mach, pressure and temperature after the shock have been calculated the pressures on the forebody are divided up into the upper forebody, the lower forebody and the x and z directions of each. The resulting moment acting on the lower forebody and upper forebody is also calculated.

The forces and moment acting on the lower forebody are given as:

$$F_{x,f} = -p_f L_f \tan \tau_{1l} \tag{3.56}$$

$$F_{z,f} = -p_f L_f \tag{3.57}$$

$$M_f = z_f F_{x,f} - x_f F_{z,f} \tag{3.58}$$

where (x_f, z_f) is the location of the lower forebody mid point w.r.t. the cg (L_f is the length of the lower forebody - see figure 2).

The pressures and moment acting on the upper forebody are given as:

$$F_{x,u} = -p_u L_u \tan \tau_{1u} \tag{3.59}$$

$$F_{x,u} = -p_u L_f \tag{3.60}$$

$$M_u = z_u F_{x,u} - x_u F_{z,u} \tag{3.61}$$

where (x_u, z_u) is the location of the upper forebody mid point w.r.t. the cg (L_u is the length of the upper forebody - see figure 2).

Engine Inlet Forces. The flow is parallel to the forebody after the shock at the nose. It must turn parallel to the body axis at the engine. This is achieved by an oblique shock with flow turn angle of $\tau_1 L$. The conditions behind the oblique shock gives the inlet conditions for the engine. The forces and moments imparted on the aircraft are given by:

$$F_{x,inlet} = \gamma M_f^2 p_f \left(1 - \cos\left(\tau_{1l} + \alpha\right)\right) \frac{A_e}{b} \frac{1}{A_d A_n} \tag{3.62}$$

$$F_{z,inlet} = \gamma M_f^2 p_f \sin\left(\tau_{1l} + \alpha\right) \frac{A_e}{b} \frac{1}{A_d A_n} \tag{3.63}$$

$$M_{inlet} = z_{inlet} F_{x,inlet} - x_{inlet} F_{z,inlet} \tag{3.64}$$

where (M_f, p_f) are the Mach and pressure after the lower forebody shock, and (x_{inlet}, z_{inlet}) is the location of the engine inlet w.r.t. the cg.

Engine Base Forces. Depending on spillage at the engine inlet, the pressure on the lower forebody is calculated:

- Spillage - Expansion fan (shock angle = τ_l, upstream conditions - lower forebody stream)
- No spillage - Oblique shock (shock angle = α, upstream conditions - freestream)

The forces and moment due to the base are:

$$F_{z,b} = -p_b L_e \tag{3.65}$$

$$M_b = -F_{z,b} x_b \tag{3.66}$$

where $F_{z,b}$ is the force on the engine base, x_b is the location of the center of the engine base w.r.t. the cg (L_e is the length of the engine base - see figure 2).

Aftbody Forces. Due to the physical configuration of this vehicle the exhaust from the scramjet engine creates pressure acting on the aftbody (we use the plume assumption in calculating this pressure - see section 3.7.7). The upper section of the exit nozzle makes up the lower aftbody, consequently the external expansion of the exhaust from the scramjet engine results in an aftbody pressure. The lower section of the exit nozzle in comprised of the resulting shear layer from the interaction of the exhaust with the freestream flow under the vehicle. The position of this shear layer dictates the pressure along the aftbody of the vehicle.

The pressure at any point on the aftbody is given by [82] as follows:

$$p_a = \frac{p_e}{1 + \frac{s_a}{L_a}(p_e/p_\infty - 1)} \tag{3.67}$$

where s_a is the location of the point along the aftbody (varies from 0 at the internal nozzle exit to L_a at the tip of the aftbody).

The contribution of the aftbody pressure in the z direction results in additional lift, and an offset to the drag in the x direction.

$$F_{x,e} = p_\infty L_a \frac{p_e}{p_\infty} \left[\frac{ln\frac{p_e}{p_\infty}}{\frac{p_e}{p_\infty} - 1} \right] \tan(\tau_2 + \tau_{1,u}) \tag{3.68}$$

$$F_{z,e} = -p_\infty L_a \frac{p_e}{p_\infty} \left[\frac{ln\frac{p_e}{p_\infty}}{\frac{p_e}{p_\infty} - 1} \right] \tag{3.69}$$

The aftbody pressure also creates a pitching moment centered around the point where the mean value of the pressure distribution occurs, with x_{exit}, and z_{exit} are the x and z coordinates of the effective aftbody pressure point w.r.t the cg respectively.

$$M_e = z_{exit} F_{x,e} - x_{exit} F_{z,e} \tag{3.70}$$

Control Surfaces. The elevator control surface is modeled here as flat plates, therefore to determine the pressures generated Prandtl-Meyer flow will be used on one side of the control surface and by oblique shock theory on the other. These pressures are centered around the mid-chord of the control surface. The elevator forces in the x and z direction and moment are given by equations 3.71-3.73

$$F_{x,cs} = -(p_{cs,l} - p_{cs,u}) \sin \delta_{cs} S_{cs} \tag{3.71}$$

$$F_{z,cs} = -(p_{cs,l} - p_{cs,u}) \cos \delta_{cs} S_{cs} \tag{3.72}$$

$$M_{cs} = z_{cs} F_{x,cs} - x_{cs} F_{z,cs} \tag{3.73}$$

where δ_{cs} is the deflection in the elevator, S_{cs} is the surface area of the elevator, x_{cs} and z_{cs} refer to the x and z location of the elevator w.r.t the cg (S_{cs} is the area of the elevator).

3.7 Propulsion Modeling

Scramjet Model. The scramjet engine model is that used in [14, 82]. It consists of an inlet, an isentropic diffuser, a 1D Rayleigh flow combustor (frictionless duct with heat addition [83]), and an isentropic internal nozzle. A single (long) forebody compression ramp provides conditions to the rear-shifted scramjet inlet. Although the model supports a variable geometry inlet, we will not be exploiting variable geometry in this research; i.e. diffuser area ratio $A_d \stackrel{\text{def}}{=} \frac{A_2}{A_1}$ will be fixed (see Figure 6.)

3.7.1 Shock Conditions.

A bow shock will occur provided that the flow deflection angle δ_s is positive; i.e.

$$\delta_s \stackrel{\text{def}}{=} \text{AOA} + \text{forebody flexing angle} + \tau_{1l} > 0^\circ \tag{3.74}$$

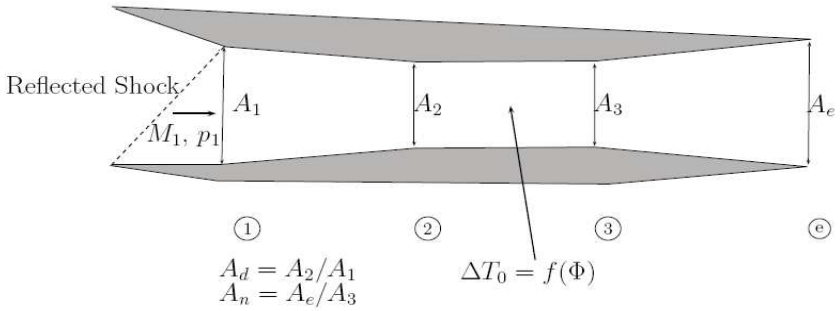

Figure 6: Schematic of Scramjet Engine

where $\tau_{1l} = 6.2°$ is the lower forebody wedge angle (see Figure 2). An expansion fan occurs when there is a flow over a convex corner; i.e. flow turns away from itself. More specifically to the bow, if $\delta_s < 0$ a Prandtl-Meyer expansion will occur.

3.7.2 Translating Cowl Door.

The model assumes the presence of an (infinitely fast) translating cowl door which uses AOA to achieve shock-on-lip conditions (assuming no forebody flexing). Forebody flexing, however, results in an oscillatory bow shock and air mass flow spillage [14]. A bow shock reflection (off of the cowl or inside the inlet) further slows down the flow and steers it into the engine. Shock-shock interactions are not modeled.

Impact of Having No Cowl Door. Associated with a translating cowl door are potentially very severe heating issues. For our vehicle, the translating cowl door can extend a great deal. For example, at Mach 5.5, 70kft, the trim FTA is $1.8°$ and the cowl door extends 14.1 ft. Of particular concern, due to practical cowl door heating/structural issues, is what happens when the cowl door is over extended through the bow shock. This occurs, for example, when structural flexing results in a smaller FTA (and hence a smaller bow shock angle) than assumed by the rigid-body shock-on-lip cowl door extension calculation.

3.7.3 Inlet Properties.

The bow reflection turns the flow parallel into the scramjet engine [14]. The oblique shock relations are implemented again, using M_s as the free-stream input, $\delta_1 = \tau_{1l}$ as the flow deflection angle to obtain the shock angle $\theta_1 = \theta_1(M_s, \delta_1, \gamma)$ and the inlet (or diffuser entrance) properties: M_1, T_1, p_1 - functions of (M_s, θ_1, γ).

3.7.4 Diffuser Exit-Combustor Entrance Properties.

The diffuser is assumed to be isentropic. The combustor entrance properties are therefore found using the formulae in [14, 83] - $M_2 = M_2(M_1, A_d, \gamma)$, $T_2 = T_2(M_1, M_2, \gamma)$, $p_2 = p_2(M_1, M_2, \gamma)$:

$$\frac{\left[1 + \frac{\gamma-1}{2}M_2^2\right]^{\frac{\gamma+1}{\gamma-1}}}{M_2^2} = A_d^2 \frac{\left[1 + \frac{\gamma-1}{2}M_1^2\right]^{\frac{\gamma+1}{\gamma-1}}}{M_1^2} \tag{3.75}$$

$$T_2 = T_1 \left[\frac{1 + \frac{1}{2}(\gamma-1)M_1^2}{1 + \frac{1}{2}(\gamma-1)M_2^2}\right] \tag{3.76}$$

$$p_2 = p_1 \left[\frac{1 + \frac{1}{2}(\gamma-1)M_1^2}{1 + \frac{1}{2}(\gamma-1)M_2^2}\right]^{\frac{\gamma}{\gamma-1}} \tag{3.77}$$

where $A_d \stackrel{\text{def}}{=} \frac{A_2}{A_1}$ is the diffuser area ratio. Also, one can determine the total temperature $T_{t_2} = T_{t_2}(T_2, M_2, \gamma)$ at the combustor entrance can be found using [83]:

$$T_{t2} = \left[1 + \frac{\gamma-1}{2}M_2^2\right] T_2. \tag{3.78}$$

Since $A_d = 1$ in the model, it follows that $M_2 = M_1$, $T_2 = T_1$, $p_2 = p_1$, and $T_{t2} = \left[1 + \frac{\gamma-1}{2}M_1^2\right] T_1 = T_{t_1}$.

3.7.5 Combustor Exit Properties.

The model uses liquid hydrogen (LH2) as the fuel. If f denotes fuel-to-air ratio and f_{st} denotes stoichiometric fuel-to-air ratio, then the stoichiometrically normalized fuel equivalency ratio is given by $FER \stackrel{\text{def}}{=} \frac{f}{f_{st}}$ [14, 21]. FER is the engine control. While FER is primarily associated with the vehicle velocity, its impact on FPA is significant (since the engine is situated below vehicle cg). This coupling will receive further examination in what follows.

In this model, we have a constant area combustor where the combustion process is captured via heat addition. To determine the combustor exit properties, one first determines the change in total temperature across the combustor [14]:

$$\Delta T_c = \Delta T_c(T_{t_2}, FER, H_f, \eta_c, c_p, f_{st}) = \left[\frac{f_{st} FER}{1 + f_{st} FER}\right]\left(\frac{H_f \eta_c}{c_p} - T_{t_2}\right) \quad (3.79)$$

where $H_f = 51,500$ BTU/lbm is the heat of reaction for liquid hydrogen (LH2), $\eta_c = 0.9$ is the combustion efficiency, $c_p = 0.24$ BTU/lbm°R is the specific heat of air at constant pressure, and $f_{st} = 0.0291$ is the stoichiometric fuel-to-air ratio for LH2 [21]. Given the above, the Mach M_3, temperature T_3, and pressure p_3 at the combustor exit are determined by the following classic 1D Rayleigh flow relationships [14, 83]:

$$\frac{M_3^2\left[1 + \frac{1}{2}(\gamma - 1)M_3^2\right]}{(\gamma M_3^2 + 1)^2} = \frac{M_2^2\left[1 + \frac{1}{2}(\gamma - 1)M_2^2\right]}{(\gamma M_2^2 + 1)^2} + \left[\frac{M_2^2}{(\gamma M_2^2 + 1)^2}\right]\frac{\Delta T_c}{T_2} \quad (3.80)$$

$$T_3 = T_2\left[\frac{1 + \gamma M_2^2}{1 + \gamma M_3^2}\right]^2\left(\frac{M_3}{M_2}\right)^2 \quad (3.81)$$

$$p_3 = p_2\left[\frac{1 + \gamma M_2^2}{1 + \gamma M_3^2}\right]. \quad (3.82)$$

Given the above, one can then try to solve equation (3.80) for $M_3 = M_3\left(M_2, \frac{\Delta T_c}{T_{2,}}, \gamma\right)$.

This will have a solution provided that M_2 is not too small, ΔT_c is not too large (i.e. FER is not too large or T_2 is not too small).

Thermal Choking FER ($M_3 = 1$). Once the change in total temperature $\Delta T_c = \Delta T_c(T_{t_2}, FER, H_f, \eta_c, c_p, f_{st})$ across the combustor has been computed, it can be substituted into equation (3.80) and one can "try" to solve for M_3. Since the left hand side of equation (3.80) lies between 0 (for $M_3 = 0$) and 0.2083 (for $M_3 = 1$), it follows that if the right hand side of equation (3.80) is above 0.2083 then no solution for M_3 exists. Since the first term on the right hand side of equation (3.80) also lies between 0 and 0.2083, it follows that this occurs when ΔT_c is too large; i.e. too much heat is added into the combustor or too high an FER. In short, a solution M_3 will exist provided that FER is not too large, T_2 is not too small (i.e. altitude not too high), and the combustor entrance Mach M_2 is not too small (i.e. FTA not too large). When $M_3 = 1$, a condition referred to as *thermal choking* [21, 83] is said to exist. The FER that produces this we call the *thermal choking FER* - denoted FER_{TC}. In general, FER_{TC} will be a function of the following: M_∞, T_∞, and FTA.

Physically, the addition of heat to a supersonic flow causes it to slow down. If the thermal choking FER (FER_{TC}) is applied, then we will have $M_3 = 1$ (i.e. sonic combustor exit). When thermal choking occurs, it is not possible to increase the air mass flow through the engine. Propulsion engineers want to operate near thermal choking for engine efficiency reasons [21]. However, if additional heat is added, the upstream conditions can be altered and it is possible that this may lead to engine unstart [21]. This is highly undesirable. For this reason, operating near thermal choking has been described by some propulsion engineers as "operating near the edge of a cliff."

When Does Thermal Choking Occur? Within Figure 8, the combustor exit Mach M_3 is plotted versus the free-stream Mach M_∞ for level-flight with zero FTA at 85 kft. It should be noted from Figure 11 that at 85 kft, the vehicle can be trimmed between the shown thermal choking and dynamic pressure barriers for ∼Mach 5.5-8 (where Mach 8, 85 kft corresponds to 2076 psf - slightly more than the "standard" structural constraint of 2000 psf). For $M_\infty = 8.5$, the thermal choking FER is unity. As M_∞ decreases, the thermal choking FER is reduced. When $M_\infty = 1.54$ (well below trimmable Mach at 85kft), $M_2 = 1$, and the thermal choking FER reduces to zero. In general, thermal choking will occur if FER is too high, M_∞ is too low, altitude is too high (T_∞ too low), FTA is too high. We now examine the above engine relations as they relate to thermal choking.

M_3 **versus** M_2**.** Figure 7 shows the relationship between the speed of the flow at the combustor exit Mach M_3 versus that at the combustor entrance M_2 for different values of FER (at 85 kft, level-flight, zero flow turning angle). The figure shows the following:

$M_2 = 7$	$FER = 1$	$M_3 = 2.06$
$M_2 = 6$	$FER = 1$	$M_3 = 1.27$
$M_2 = 5.85$	$FER = 1$	$M_3 = 1$
$M_2 = 5$	$FER_{TC} = 0.62$	$M_3 = 1$
$M_2 = 4$	$FER_{TC} = 0.33$	$M_3 = 1$
$M_2 = 3$	$FER_{TC} = 0.14$	$M_3 = 1$
$M_2 = 2$	$FER_{TC} < 0.1$	$M_3 = 1$
$M_2 = 1$	$FER_{TC} = 0$	$M_3 = 1$

For $M_2 = 6$ and $FER = 1$, we get $M_3 = 1.27$; i.e. we are nearly choking and the thermal choking FER is greater than unity. For $M_2 = 5.85$, the thermal choking FER becomes unity. As M_2 is reduced further, the thermal choking FER decreases.

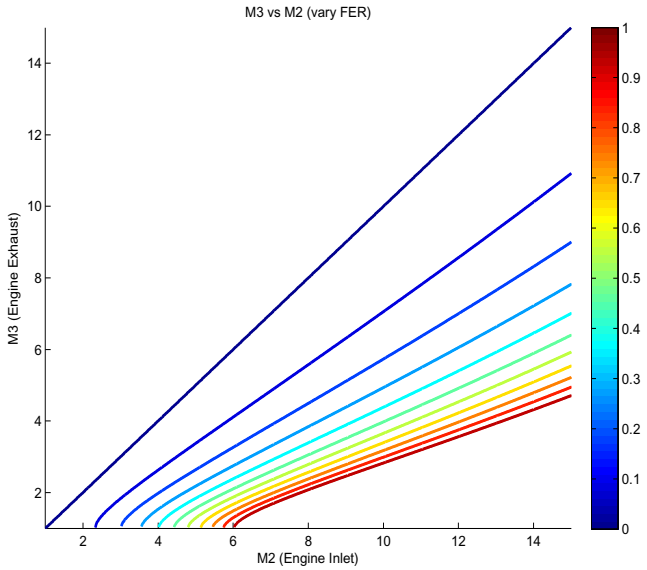

Figure 7: Combustor Exit Mach M_3 vs. Combustor Entrance Mach M_2 (85 kft, level-flight, zero FTA)

It decreases to zero as M_2 is reduced toward unity.

M_3 versus M_∞. Now consider Figure 8. In this figure, the combustor exit Mach M_3 is plotted versus the free-stream Mach M_∞ (at 85 kft, level-flight, zero flow turning angle). It should be noted from Figure 11 that at 85 kft, the vehicle can be trimmed within the shown thermal choking and dynamic pressure constraints for ∼Mach 5.5-8 (where Mach 8, 85 kft corresponds to slightly more than the "standard" structural constraint 2000 psf). The figure shows the following:

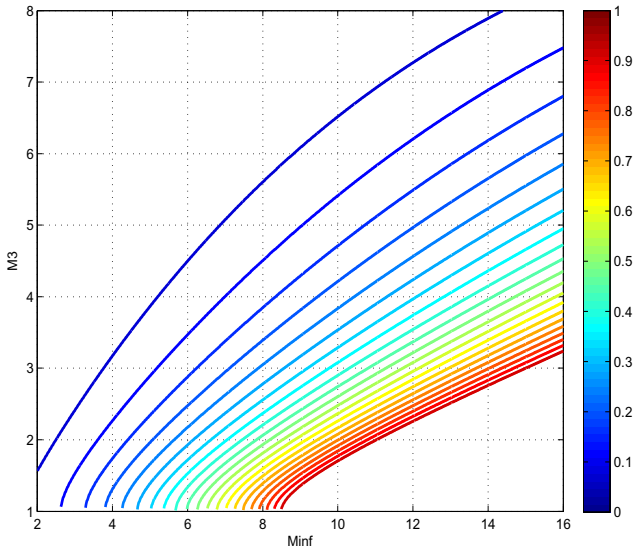

Figure 8: Combustor Exit Mach M_3 vs. Free-Stream Mach M_∞ (85 kft, zero FTA)

$M_\infty = 10$	$FER = 1$	$M_3 = 1.71$
$M_\infty = 8.5$	$FER = 1$	$M_3 = 1$
$M_\infty = 8$	$FER_{TC} = 0.88$	$M_3 = 1$
$M_\infty = 7$	$FER_{TC} = 0.64$	$M_3 = 1$
$M_\infty = 6$	$FER_{TC} = 0.45$	$M_3 = 1$
$M_\infty = 4$	$FER_{TC} = 0.17$	$M_3 = 1$
$M_\infty = 3.28$	$FER_{TC} = 0.1$	$M_3 = 1$
$M_\infty = 1.54$	$FER_{TC} = 0$	$M_3 = 1$

For $M_\infty = 8.5$ the thermal choking FER is unity. As M_∞ is reduced, the thermal choking FER is reduced. When $M_\infty = 1.54$ (well below trimmable Mach numbers at 85 kft, see Figure 11), $M_2 = 1$, and the thermal choking FER is reduced to zero. The analysis will be used to define an FER margin that will be useful for control system design.

Thermal Choking FER Properties. Figure 9 demonstrates FER margin properties that are characteristic of hypersonic vehicles. Figure 9 shows FER_{TC} for

$FTA \in [-5°, 5°]$ (red curves). The solid red curve corresponds to a zero FTA. The lower (upper) dashed red curve corresponds to FTA of $5°$ (-$5°$). Consequently, FER_{TC} depends on the FTA. To summarize, FER_{TC} is (nearly) independent of altitude (for constant FTA, not shown in figure), decreases with decreasing Mach (for constant FTA), decreases (increases) with increasing (decreasing) FTA (for constant Mach).

Thermal Choking and Unity FER Margins. Next, we define FER margins that are useful for control system design. While the patterns revealed are based on the simple 1D Rayleigh flow model discussed above, the FER margin framework introduced is useful for designing control systems that suitably tradeoff scramjet authority and efficiency.

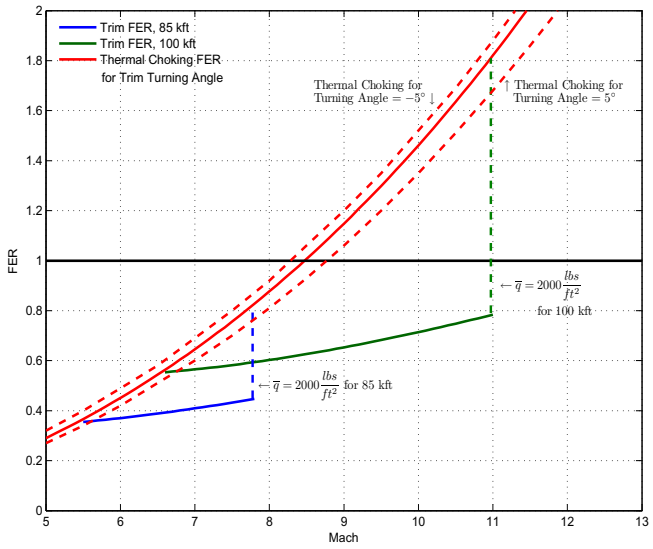

Figure 9: Visualization of FER Margins, Trim FER vs Mach for different altitudes, FER_{TC} vs Mach for different flow turning angles (FTAs)

Thermal Choking FER Margin. The *thermal choking margin* at an instant in time

is defined as follows:

$$FERM_{TC} \stackrel{\text{def}}{=} FER_{TC} - FER. \tag{3.83}$$

Since FER_{TC} depends upon altitude (free-stream temperature), free-stream Mach, and the FTA (hence vehicle state), so does $FERM_{TC}$. $FERM_{TC}$ measures FER control authority (or saturation margin) at a given time instant. It also measures the scramjet's ability to accelerate the vehicle. While an accurate FTA measurement may not be available, the $FERM_{TC}$ concept - when combined with measurements, models, and uncertainty bounds - could be very useful for controlling how close the scramjet gets to thermal choking; i.e. "to the edge of the cliff."

Trim FERM Properties. For a fixed FER, $FERM_{TC}$ exhibits behavior similar to the FER_{TC} (see above). Now suppose that FER is maintained at some trim FER and that the FTA is nearly constant; e.g. constant AOA and little flexing. For a nearly constant FTA and trim FER, $FERM^{FTA}_{TC_{trim\ fer}}$ decreases with decreasing Mach (altitude fixed), decreases with increasing altitude (Mach fixed), decreases with decreasing altitude and Mach along a constant $\bar{q}$ profile. Why is this? $FERM^{FTA}_{TC_{trim\ fer}}$ decreases with decreasing Mach because as Mach decreases, the FER_{TC} decreases faster than the trim FER; both decrease quadratically, but FER_{TC} decreases faster (Figure 9). It decreases with increasing altitude because as altitude increases, FER_{TC} remains constant while the trim FER increases. It decreases with decreasing altitude and Mach along a constant dynamic pressure profile because the trim FER decreases more slowly than FER_{TC} along such profiles. If one uses trim values, then one obtains $trim\ FERM_{TC} = \text{trim FER}_{\text{TC}} - \text{trim FER}$. Its dependence on the flight condition is more difficult to analyze since the trim FTA changes with the flight condition.

Unity FER Margin. Within the model, thrust is linearly related to FER for all expected FER values - leveling off at (unrealistically) large FER values. In practice, when $FER > 1$, the result is decreased thrust. This phenomena is not captured in the model [4]. As such, control designs based on this model (or derived linear models) should try to maintain FER below unity. This motivates the instantaneous FER unity margin:

$$FERM_{unity} \stackrel{\text{def}}{=} 1 - \text{ FER}. \tag{3.84}$$

Figure 11 shows that if FER is set to a trim FER, then $FERM_{unity}^{trim\ fer}$ decreases with increasing Mach or increasing altitude because trim FER increases with Mach and altitude.

FER Margin ($FERM$). Given the above, it is reasonable to define the *instantaneous FER margin* $FERM$ as follows:

$$FERM \stackrel{\text{def}}{=} \min \{ FERM_{TC}, FERM_{unity} \}. \tag{3.85}$$

Alternatively, $FERM \stackrel{\text{def}}{=} \min \{ FER_{TC}, 1 \} - FER$. It should be emphasized that at any time instant the FERM depends on the system state (i.e. M_∞, altitude via T_∞, FTA). The trim FERM also depends on p_∞. The static nonlinear FERM map has been determined for our simple Rayleigh-based model. This "saturation" map is used when applying control laws to the nonlinear model to ensure that $FER > FER_{TC}$ is never applied. This is important because the simulation "crashes" if too large an FER is issued; i.e. hypersonic vehicles have low thrust

margins [120].

Limitations of Analysis. The above is based on the simple 1D Rayleigh scramjet model being used. Thermal choking, strictly speaking, is not a 1D phenomena. Given this, the impact of 2D effects and finite-rate chemistry on estimating FERM will be examined in future work.

3.7.6 Internal Nozzle.

The exit properties $M_e = M_e(M_3, A_n, \gamma), T_e = T_e(M_3, M_e, \gamma), p_e = p_e(M_3, M_e, \gamma)$ of the scramjet's isentropic internal nozzle are founds as follows:

$$\frac{\left[1+\frac{\gamma-1}{2}M_e^2\right]^{\frac{\gamma+1}{\gamma-1}}}{M_e^2} = A_n^2 \frac{\left[1+\frac{\gamma-1}{2}M_3^2\right]^{\frac{\gamma+1}{\gamma-1}}}{M_3^2} \tag{3.86}$$

$$T_e = T_3 \left[\frac{1+\frac{1}{2}(\gamma-1)M_3^2}{1+\frac{1}{2}(\gamma-1)M_e^2}\right] \tag{3.87}$$

$$p_e = p_3 \left[\frac{1+\frac{1}{2}(\gamma-1)M_3^2}{1+\frac{1}{2}(\gamma-1)M_e^2}\right]^{\frac{\gamma}{\gamma-1}} \tag{3.88}$$

where $A_n \overset{\text{def}}{=} \frac{A_e}{A_3}$ is the internal nozzle area ratio (see Figure 6). $A_n = 6.35$ is used in the model.

Thrust due to Internal Nozzle. The purpose of the expanding internal nozzle is to recover most of the potential energy associated with the compressed (high pressure) supersonic flow. The thrust produced by the scramjet's internal nozzle is given by [83]

$$\text{Thrust}_{\text{internal}} = \dot{m}_a(v_e - v_\infty) + (p_e - p_\infty)A_e \tag{3.89}$$

where $\dot{m}_a$ is the air mass flow through the engine, v_e is the exit flow velocity, v_∞

is the free-stream flow velocity. p_e is the pressure at the engine exit plane, A_1 is the engine inlet area, A_e is the engine exit area, $v_e = M_e sos_e$, $v_\infty = M_\infty sos_\infty$, $sos_e = \sqrt{\gamma RT_e}$, $sos_\infty = \sqrt{\gamma RT_\infty}$, and R is the gas constant for air. Because we assume that the internal nozzle to be symmetric, this internal thrust is always directed along the vehicle's body axis. The mass air flow into the inlet is given as follows:

$$\dot{m}_a = \begin{cases} p_\infty M_\infty \sqrt{\frac{\gamma}{RT_\infty}} \left[L_1 \frac{sin(\tau_{1l} - \alpha)}{tan(\tau_{1l})} + h_i cos(\alpha) \right] & \text{Oblique bow shock (swallowed by engine)} \\ p_\infty M_\infty \sqrt{\frac{\gamma}{RT_\infty}} h_i \left[\frac{sin(\theta_s) cos(\tau_{1l})}{sin(\theta_s - \alpha - \tau_{1l})} \right] & \text{Oblique bow shock - shock on lip} \\ p_\infty M_\infty \sqrt{\frac{\gamma}{RT_\infty}} h_i cos(\tau_{1l}) & \text{Lower forebody expansion fan} \end{cases} \tag{3.90}$$

3.7.7 External Nozzle.

The purpose of the expanding external nozzle is recover the rest of the potential energy associated with the compressed supersonic flow. A nozzle that is too short would not be long enough to recover the stored potential energy. In such a case, the nozzle's exit pressure would be larger than the free stream pressure and we say that it is under-expanded [83]. The result is reduced thrust. A nozzle that is too long would result in the nozzle's exit pressure being smaller than the free stream pressure and we say that it is over-expanded [83]. The result, again, is reduced thrust. When the nozzle length is "properly selected," the exit pressure is equal to the free stream pressure and maximum thrust is produced.

Plume Assumption. The engine's exhaust is bounded above by the aft body/nozzle and below by the shear layer between the gas and the free stream atmosphere. The two boundaries define the shape of the external nozzle, and the pressure distribution

along the aftbody (Equation 3.67, page 59). Within [4, 82], a critical assumption is made regarding the shape of the external nozzle-and-plume in order to facilitate (i.e. speed up) the calculation of the aft body pressure distribution. The so-called "plume assumption" implies that the external nozzle-and-plume shape does not change with respect to the vehicle's body axes. This implies that the plume shape is independent of the flight condition. Our (limited) studies to date show that this assumption is suitable for preliminary trade studies but a higher fidelity aft body pressure distribution calculation is needed to understand how properties change over the trimmable region. This assumption is considered in more detail in [121]. In short, our fairly limited studies suggest that the plume assumption impacts static properties significantly while dynamic properties are only mildly impacted. The contribution of the external nozzle to the forces and moments acting on the vehicle have been discussed in section 3.4. In figure 10, we see how the actual pressure distribution along the aftbody compares to the plume approximation (vehicle trimmed at Mach 8, 85kft)

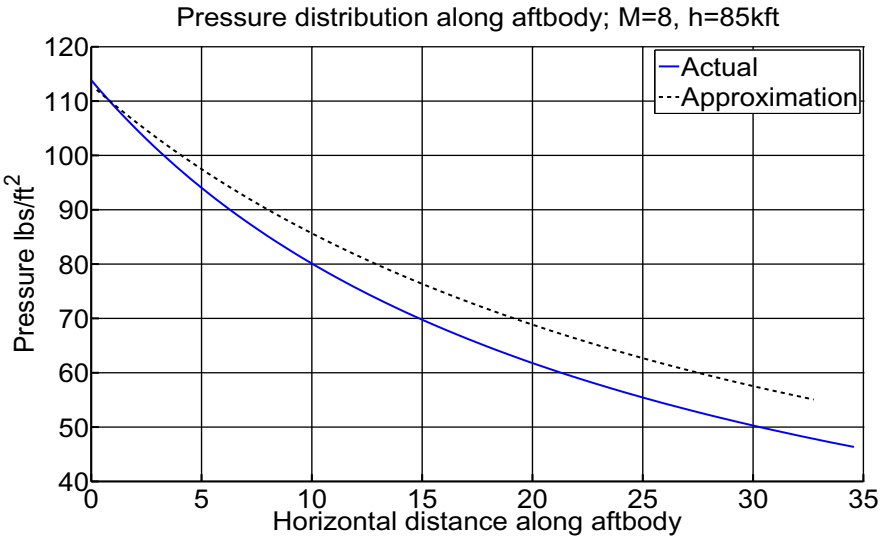

Figure 10: Aftbody pressure distribution: Plume vs. Actual

Within [122, 123] the authors say that the optimum nozzle length is about 7

throat heights. This includes the internal as well as the external nozzle. For our vehicle, the internal nozzle has no assigned length. This becomes an issue when internal losses are addressed. For the Bolender, et. al. model, the external nozzle length is 10.15 throat heights (with throat height $h_i = 3.25$ ft). For the new engine design presented later on in this research, the external nozzle length is 7.33 throat heights (with throat height $h_i = 4.5$ ft). The external nozzle contributes a force on the upper aft body. This force can be resolved into 2 components - the component along the fuselage water line is said to contribute to the total thrust. This component is given by the expression:

$$\text{Thrust}_{\text{external}} = p_\infty L_a \left(\frac{p_e}{p_\infty}\right) \left[\frac{\ln\left(\frac{p_e}{p_\infty}\right)}{\frac{p_e}{p_\infty} - 1}\right] \tan(\tau_2 + \tau_{1U}). \tag{3.91}$$

Total Thrust. The total thrust is obtained by adding the thrust due to the internal and external nozzles.

3.8 Structure Modeling

Flexible Body Dynamics The natural frequencies and modes shapes for the flexible structure are computed using the assumed modes method. The assumed modes utilizes basis functions ω_i for the modes shapes of the vehicle that correspond to the analytical solution to the transverse vibration of a uniform free-free beam [2]. The assumed modes method is based on the following Lagrange equation

$$\frac{d}{dt}\left(\frac{\partial}{\partial \dot{q}_i}\right) - \frac{\partial T}{\partial q_i} = f_i, i = 1, \ldots, n \tag{3.92}$$

where T is the total kinetic energy of the system and V is the potential energy. Displacement along the structure is given by the following expansion

$$w(x,t) = \sum_{i=1}^{n} \Phi_i(x)\eta_i(t) \tag{3.93}$$

where $\eta_i(t)$ is the generalized modal coordinate.

The kinetic energy is given by

$$T = \frac{1}{2}\,\dot{\mathbf{w}}^T M \dot{\mathbf{w}} \tag{3.94}$$

where $\mathbf{w} = [w_1 \dots w_n]^T$ and

$$M = \begin{bmatrix} m_{11} & \dots & m_{1n} \\ \vdots & \ddots & \\ m_{n1} & & m_{nn} \end{bmatrix} \tag{3.95}$$

with

$$m_{ij} = \int_0^L \rho A(x)\Phi_i(x)\Phi_j(x)dx \tag{3.96}$$

where $\rho A(x)$ denotes the mass per unit length of the structure.

$$V = \frac{1}{2}\int_0^L EI(x)\left(\frac{\partial^2 w}{\partial x^2}\right)^2 dx \tag{3.97}$$

gives the matrix-vector expression

$$V = \frac{1}{2}\,\mathbf{w}^T K \mathbf{w} \tag{3.98}$$

where

$$K = \begin{bmatrix} k_{11} & \dots & k_{1n} \\ \vdots & \ddots & \\ k_{n1} & & k_{nn} \end{bmatrix} \tag{3.99}$$

with

$$k_{ij} = \int_0^L EI(x) \frac{\partial^2 \Phi_i(x)}{\partial x^2} \frac{\partial^2 \Phi_j(x)}{\partial x^2} dx \tag{3.100}$$

$$f_i(t) = \int_0^L p(x,t)\Phi_i(x)dx + \sum_{j=1}^{m} u_j(x_{sj},t)\Phi_j(x_{sj}) \tag{3.101}$$

Forming the generalized force vector $\mathbf{f} = [f_1 \dots f_n]^T$, the n Langrange's Equations result in

$$M\ddot{\mathbf{w}} + K\mathbf{w} = \mathbf{f} \tag{3.102}$$

The natural frequencies and mode shapes of the structure are obtained by setting $\mathbf{f} = \mathbf{0}$ and $\ddot{u} = -w^2 u$. The resulting eigenvalue problem is given as

$$\left(w^2 I - M^{-1}K\right)\mathbf{w} = \mathbf{0} \tag{3.103}$$

the square roots of the eigenvalues of $M^{-1}K$ are the resulting natural frequencies of the structure, while the corresponding mode shapes are just linear combinations of the assumed modes (Φ) with the coefficients given by the eigenvectors of $M^{-1}K$.

3.9 Summary and Conclusion

In this chapter, we considered a first principles nonlinear 3-DOF dynamical model for the longitudinal dynamics of a generic scramjet-powered hypersonic vehicle. The model attempted to capture interactions between the aerodynamics, the propul-

sion system and the flexible dynamics.

Simplifying assumptions (such as neglecting high-temperature gas dynamics, infinitely fast cowl door, out-of-plane loading, torsion, Timoshenko effects etc.) were made. The limitations of the model were discussed.

In subsequent chapters we shall consider trimming (section 4.2, page 79) and linearization (section 5.2, page 79) of the vehicle to analyze the static and dynamic properties of this model. A redesign of the engine will also be considered in order to improve performance and address geometric feasibility issues.

4. Static Properties of Vehicle

4.1 Overview

This chapter provides a trimming overview for the HSV, as well as an analysis on the static properties of the HSV over a range of flight conditions. Specifically what is shown is the equilibrium values required to trim the vehicle as Mach and altitude are varied throughout the air-breathing corridor.

Fundamental questions.

- Over what range of flight conditions can vehicle be trimmed? i.e. What is vehicles trimmable region?
- How do static trim properties vary over trimmable region?

Observations.

- Trimmable region limited by 3 effects:
  - Structural loading due to high dynamic pressure q = 2000 psf.
  - Thermal choking within engine (section 3.7.5, page 63, or [105]).
  - FER = 1 (section 3.7.5, page 63, or [105]).
- Many static properties are constant (or fairly constant) along lines of constant dynamic pressure (section 4.4, page 83).

Equilibrium of a general nonlinear system.

For a general nonlinear system, we have the following state space representation:

$$\dot{x}(t) \quad = \quad f(x(t), u(t)) \qquad\qquad x(0) = x_o \tag{4.1}$$

where

- $f = [\, f_1(x_1, \ldots, x_n, u_1, \ldots, u_m), \ldots, f_n(x_1, \ldots, x_n, u_1, \ldots, u_m)\,]^T \in \mathcal{R}^n$ - vector of n functions

- $u = [\ u_1, \ldots, u_m\ ]^T \in \mathcal{R}^m$ - vector of m input variables
- $x = [\ x_1, \ldots, x_n\ ]^T \in \mathcal{R}^n$ - vector of n state variables
- $x_o = [\ x_{1_o}, \ldots, x_{n_o}\ ]^T \in \mathcal{R}^n$ - vector of n initial conditions

(x_e, u_e) is an *equilibrium* or *trim* of the nonlinear system at t = 0 if

$$f(x, u) = 0 \qquad \text{for all } t \geq 0 \tag{4.2}$$

Trimming refers to finding system equilibria; i.e. state-control vector pairs (x_e, u_e) st

$f(x_e, u_e) = 0$

4.2 Trimming

1. Choose Mach and altitude (within trimmable region).
2. Set pitch rate, flexible state derivatives to zero.
3. Set $\theta = \alpha$ (level flight or $\gamma = \theta - \alpha = 0°$).
4. Solve for AOA, flexible states, controls (elevator, FER).

Trim Existence and Uniqueness Issues

- 2 controls, Rigid: given existence, trim solution is unique.
- 2 controls, Flexible: given existence, trim solution need not be unique.

Optimization-Based Approach

$$\min\ \dot{\mathbf{x}}^T\mathbf{Q}\dot{\mathbf{x}} + \mathbf{u}^T\mathbf{R}\mathbf{u} + \mathbf{F}^T\mathbf{Z}\mathbf{F} \tag{4.3}$$

where $\dot{x}$ is the derivatives of the state (we want them to be small at trim), u are the controls and F are the resultant forces in the x and z directions.

1. Entries within Q and Z control trim accuracy.

2. Entries within R used to control size of u.

3. Selection of (Q,R,Z) and initial guess (x, u) impacts convergence.

[Numerical Issues - (1) convergence, (2) solution steering under non-uniqueness]

Terminology

fmincon is a MATLAB routine used to solve nonlinear minimization problem in Equation (4.3) The routine employs a Trust Region Reflective Algorithm that uses finite differences to calculate search gradients/Hessians.

- Function Evaluation

  each time right hand side of Equation (4.3) is called

  - Requires one evaluation of nonlinear model.
  - Takes approx 0.005 seconds on 3 GHz Intel processor.

- Iteration

  process during which routine moves minimizer from x_n to x_{n+1}

  - Requires between 10 to 20 function evaluations per iteration.
  - Takes average of 0.1 seconds per iteration on a 3 GHz Intel processor.

4.2.1 Trim - Steps and Issues

Pros:

- Does not require analytic knowledge of gradient/Hessians
- Rapid convergence to solution (typically less than 30 iterations)
- Coded to handle multi-processor systems for increased computational speed
  - Gridding flight corridor every 0.1 Mach and 500 ft in altitude (10^4 points) requires ~8 CPU hours.
  - Gridding flight corridor while studying 100 point parametric variation (10^6 points) requires ~800 CPU hours.

  - Easily handled by Arizona State University High-Performance Computing Cluster (400 processors).

Cons:

- Many function evaluations are necessary to calculate gradient/Hessian for each iteration
  - Not a problem so long as nonlinear model is computationally "cheap" to evaluate
    * Suitable for control-relevant models based on algebraic equations and look-up tables.
    * Not suitable for models containing iterative methods (ODE/PDE solvers, CFD).
- Even initial guess that is close to minimizer does not guarantee convergence!
  - General problem with nonlinear minimization.
  - Easily handled by terminating routine after more than 50 iterations; then perturbing initial guess.
- Numerical Accuracy:
  - Increasing numerical accuracy by an order of magnitude increases number of function evaluations/iterations.
  - Relationship between numerical accuracy and total evaluations is still being investigated.
  - All previously listed specifications allow for an accuracy smaller than 10^{-3} for state derivatives.

4.3 Static Analysis: Trimmable Region

Within this work trim refers to a non-accelerating state; i.e. no translational or rotational acceleration. Moreover, all trim analysis has focused on level flight.

Figure 11 shows the level-flight trimmable region for the nominal vehicle being considered [3, 4, 12, 105, 108] (using the original nominal engine parameters). We are interested in how the static and dynamic properties of the vehicle vary across this region. Static properties of interest include: trim controls (FER and elevator), internal engine variables (e.g. temperature and pressure), thrust, thrust margin, AOA, L/D. Dynamic properties of interest include: vehicle instability and RHP transmission zero associated with FPA. Understanding how these properties vary over the trimmable region is critical for designing a robust nonlinear (gain-scheduled/adaptive) control system that will enable flexible operation. For example, consider a TSTO flight. The mated vehicles might fly up along $\overline{q} = 2000$ psf to a desired altitude, then conduct a pull-up maneuver to reach a suitable staging altitude [109].

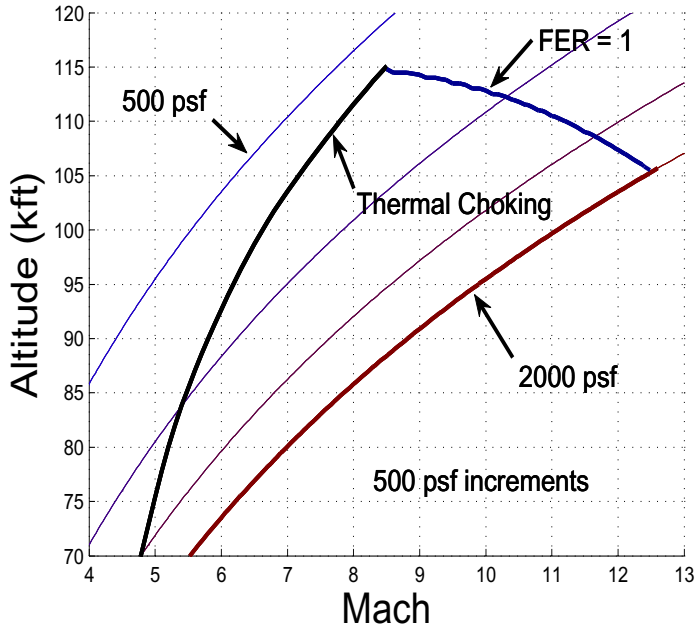

Figure 11: Visualization of Trimmable Region: Level-Flight, Unsteady-Viscous Flow, Flexible Vehicle

4.4 Static Analysis: Nominal Properties

4.4.1 Static Analysis: Trim FER

The following figures show the variations in the trim FER across the flight envelope, and for different Mach and altitudes.

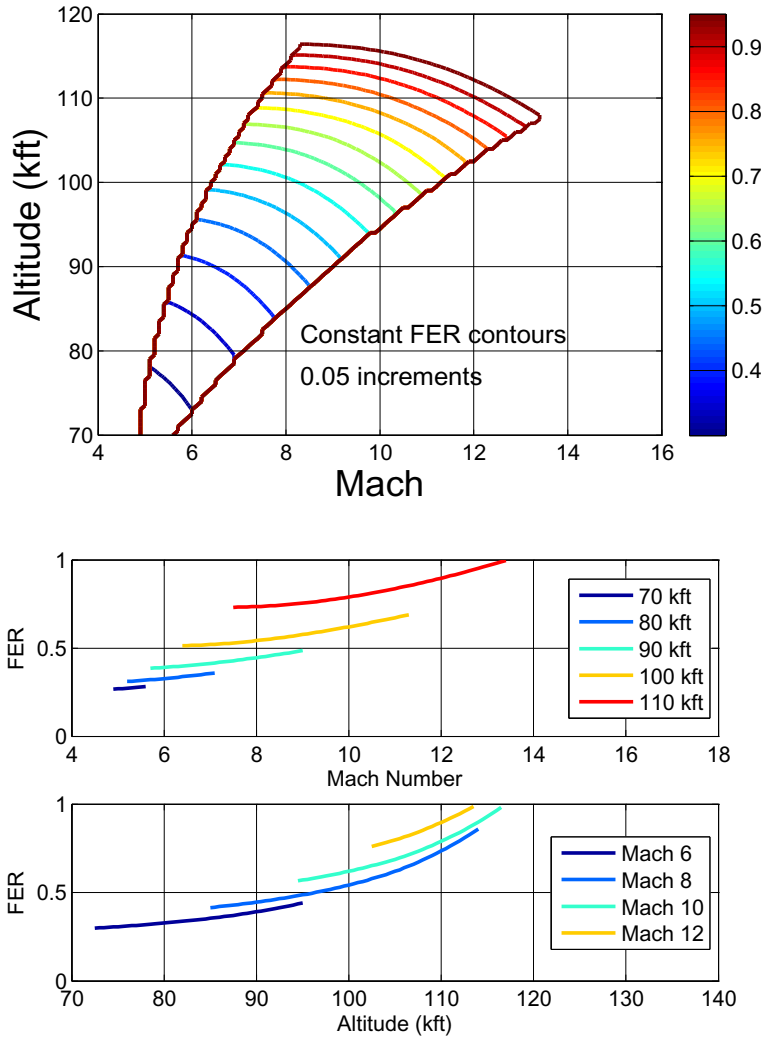

Figure 12: Trim FER: Level Flight, Unsteady-Viscous Flow, Flexible Vehicle

- FER increases monotonically with increasing mach/altitude

4.4.2 Static Analysis: Trim Elevator

The following figures show the variations in the trim elevator across the flight envelope, and for different Mach and altitudes.

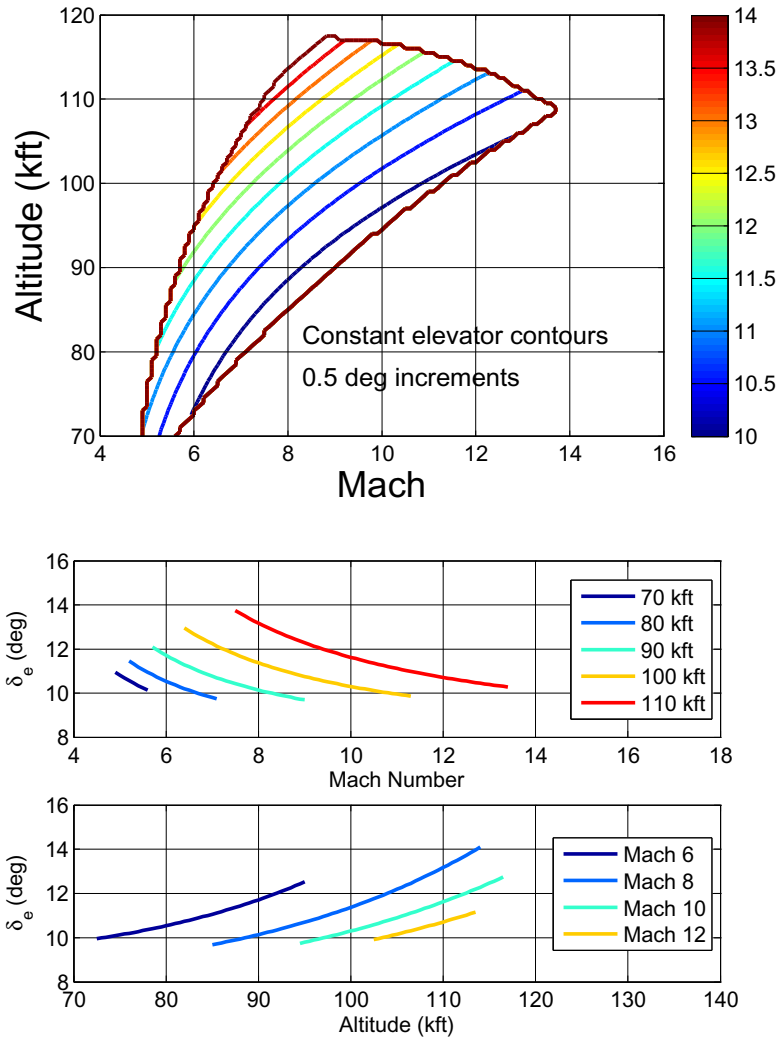

Figure 13: Trim Elevator: Level Flight, Unsteady-Viscous Flow, Flexible Vehicle

- Elevator deflection is fairly constant for constant dynamic pressures
- Elevator deflection decreases monotonically with increasing mach
- Elevator deflection increases monotonically with increasing altitude

4.4.3 Static Analysis: Trim Angle-of-Attack

The following figures show the variations in the trim angle-of-attack across the flight envelope, and for different Mach and altitudes.

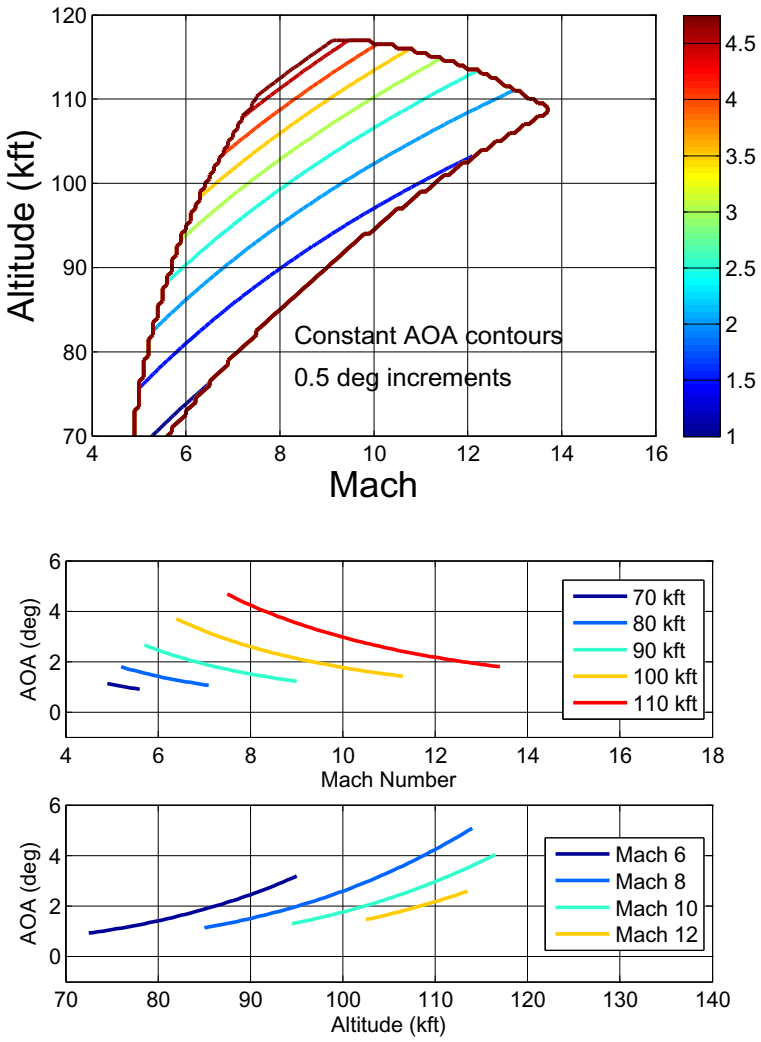

Figure 14: Trim AOA: Level Flight, Unsteady-Viscous Flow, Flexible Vehicle

- AOA is fairly constant for constant dynamic pressures
- AOA decreases monotonically with increasing mach
- AOA increases monotonically with increasing altitude

4.4.4 Static Analysis: Trim Forebody Deflection

The following figures show the variations in the trim forebody deflection across the flight envelope, and for different Mach and altitudes.

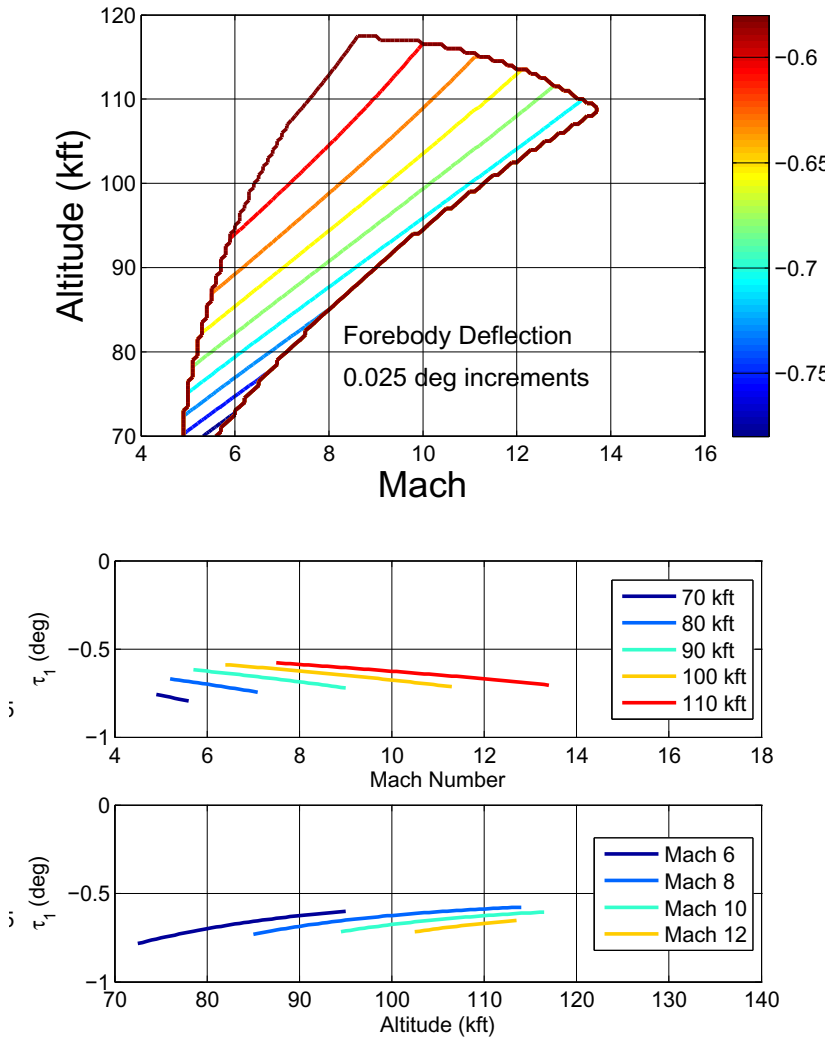

Figure 15: Trim Forebody Deflections: Level Flight, Unsteady-Viscous Flow, Flexible Vehicle

- Forebody deflections $< 1°$ across the flight envelope
- Forebody deflections increase with increasing mach/decreasing altitude

4.4.5 Static Analysis: Trim Aftbody Deflection

The following figures show the variations in the trim aftbody deflection across the flight envelope, and for different Mach and altitudes.

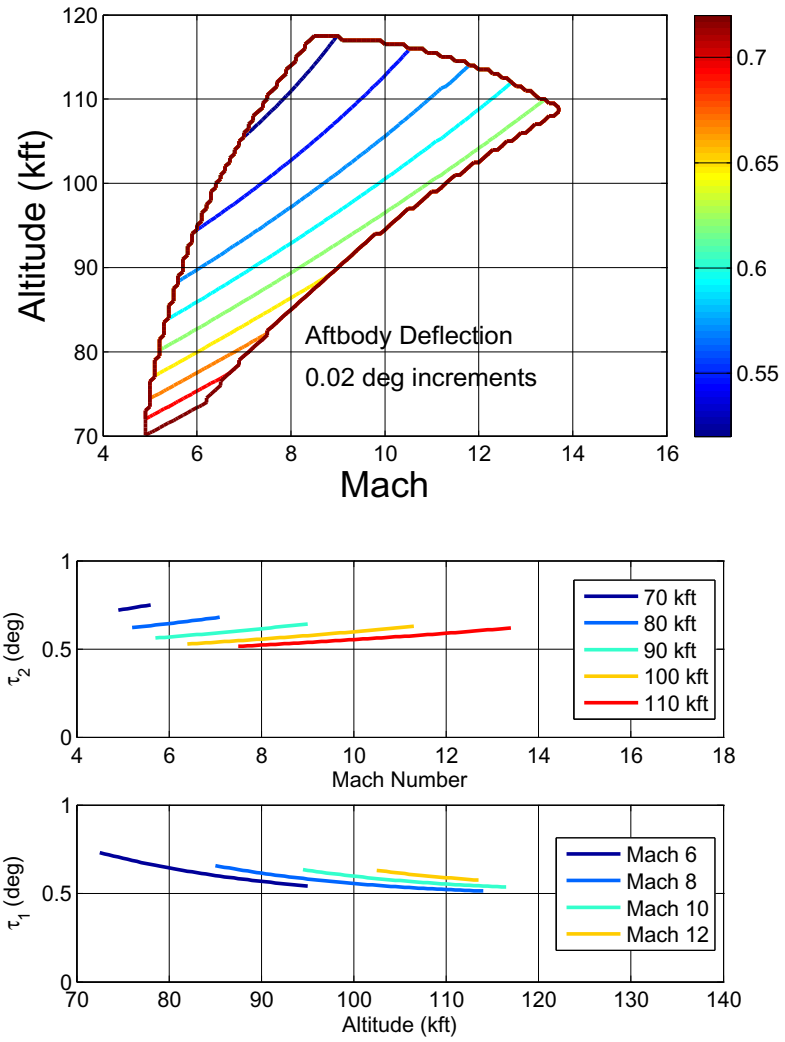

Figure 16: Trim Aftbody Deflections: Level Flight, Unsteady-Viscous Flow, Flexible Vehicle

- Aftbody deflections $< 1°$ across the flight envelope
- Aftbody deflections increase with increasing mach/decreasing altitude

4.4.6 Static Analysis: Trim Drag

The following figures show the variations in the trim drag across the flight envelope, and for different Mach and altitudes.

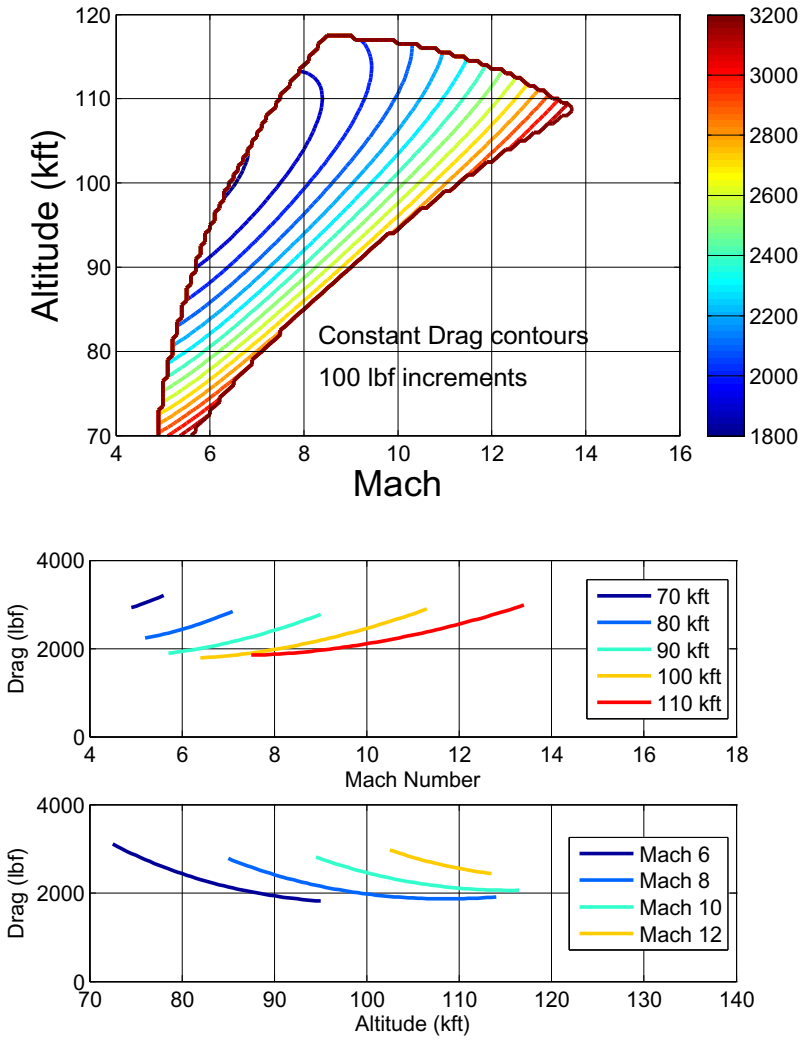

Figure 17: Trim Drag: Level Flight, Unsteady-Viscous Flow, Flexible Vehicle

- Drag increases with increasing mach
- Drag decreases with increasing altitude

4.4.7 Static Analysis: Trim Drag (Inviscid)

The following figures show the variations in the trim inviscid drag across the flight envelope, and for different Mach and altitudes.

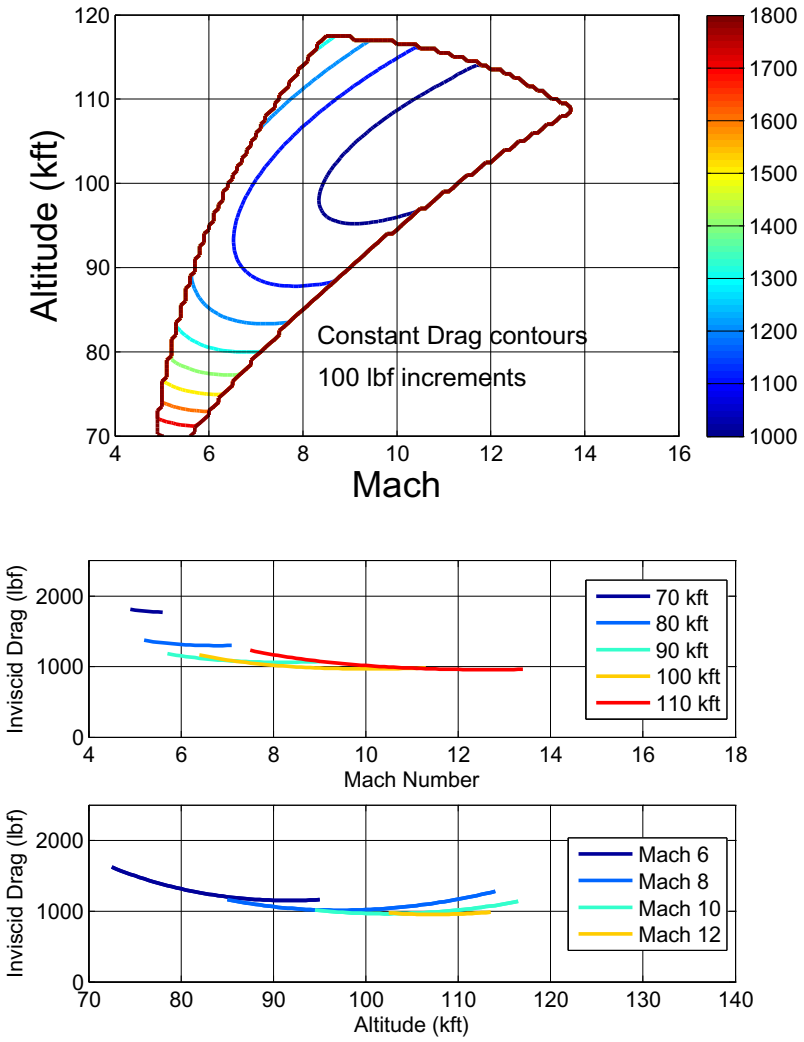

Figure 18: Trim Drag (Inviscid): Level Flight, Unsteady-Viscous Flow, Flexible Vehicle

- Inviscid drag decreases with increasing mach (due to decreasing AOA)
- Inviscid drag behaves nonlinearly with increasing altitude

4.4.8 Static Analysis: Trim Drag (Viscous)

The following figures show the variations in the trim viscous drag across the flight envelope, and for different Mach and altitudes.

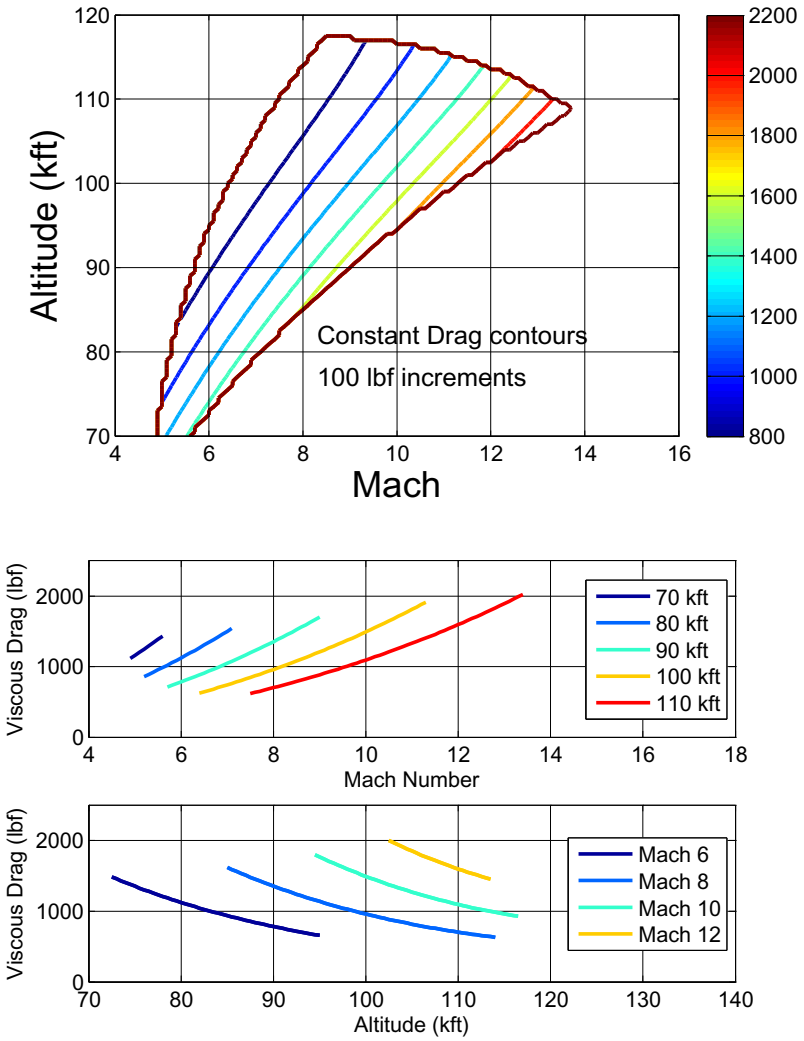

Figure 19: Trim Drag (Viscous): Level Flight, Unsteady-Viscous Flow, Flexible Vehicle

- Viscous drag increases with increasing mach
- Viscous drag decreases with increasing altitude

4.4.9 Static Analysis: Trim Drag Ratio (Viscous/Total)

The following figures show the variations in the ratio of the viscous drag to total drag across the flight envelope (at trim), and for different Mach and altitudes.

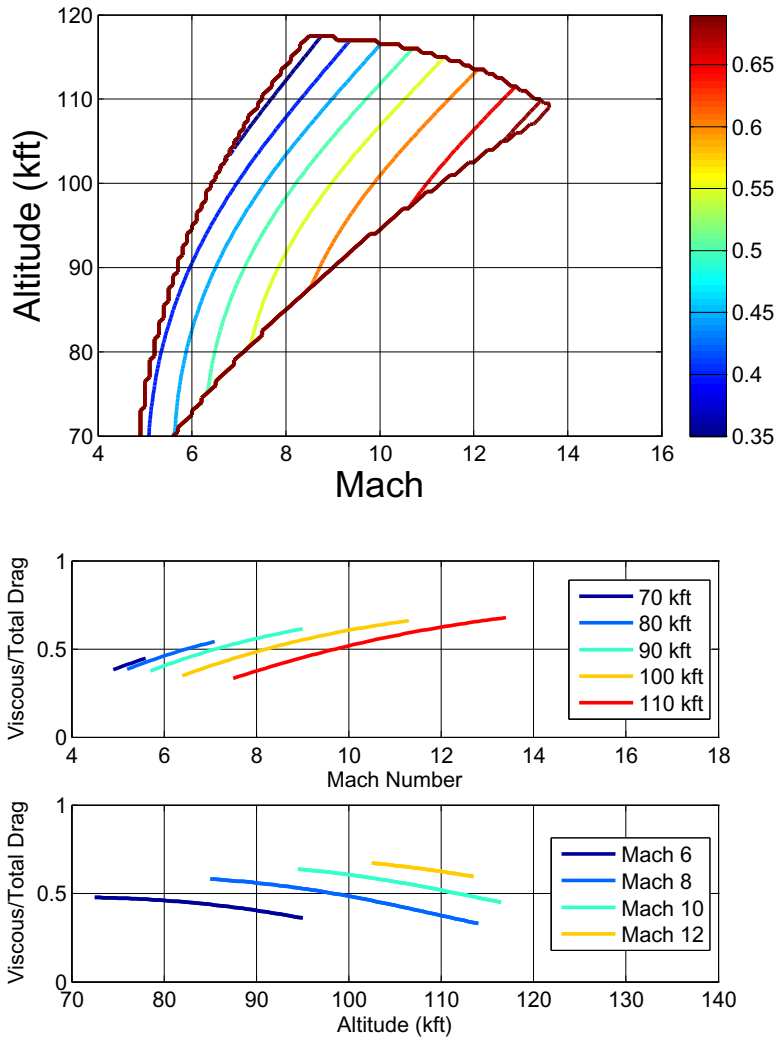

Figure 20: Trim Drag Ratio (Viscous/Total): Level Flight, Unsteady-Viscous Flow, Flexible Vehicle

- Drag ratio increases with increasing mach
- Drag ratio decreases with increasing altitude

4.4.10 Static Analysis: Trim L/D Ratio

The following figures show the variations in the trim lift-to-drag ratio across the flight envelope, and for different Mach and altitudes.

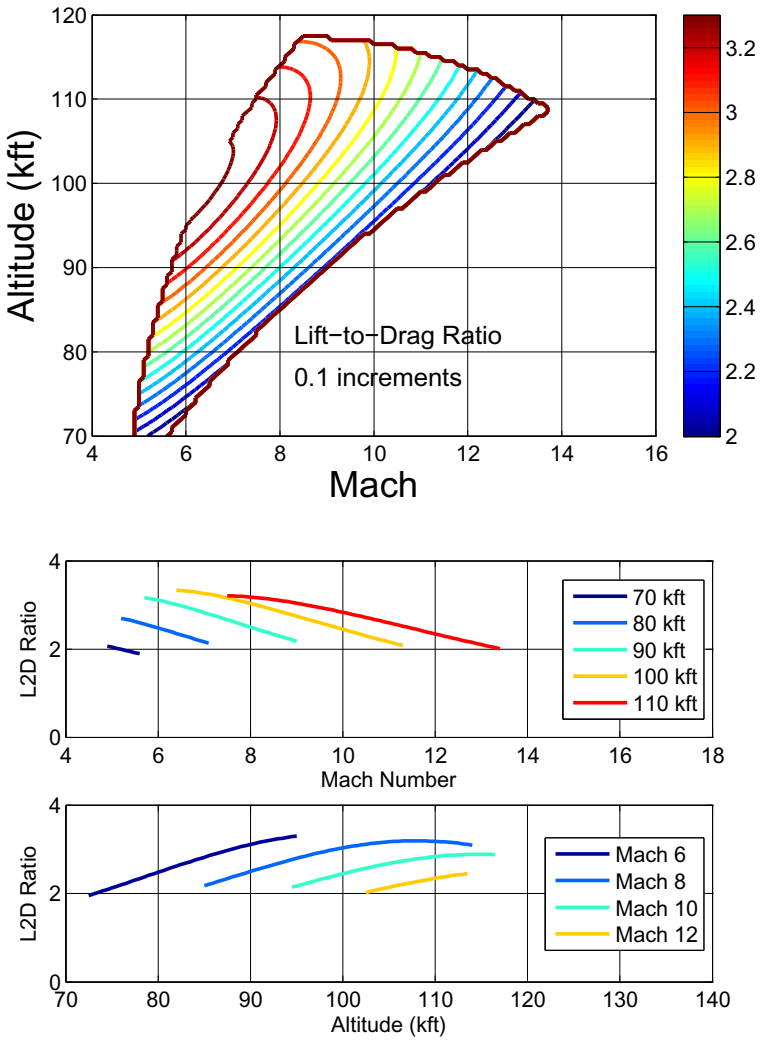

Figure 21: Trim L/D Ratio: Level Flight, Unsteady-Viscous Flow, Flexible Vehicle

- Lift-to-Drag decreases with increasing mach
- Lift-to-Drag generally increases with increasing altitude
- Lift-to-Drag is maximized at Mach 6.4, 100 kft

4.4.11 Static Analysis: Trim Elevator Force

The following figures show the variations in the trim force on the elevator across the flight envelope, and for different Mach and altitudes.

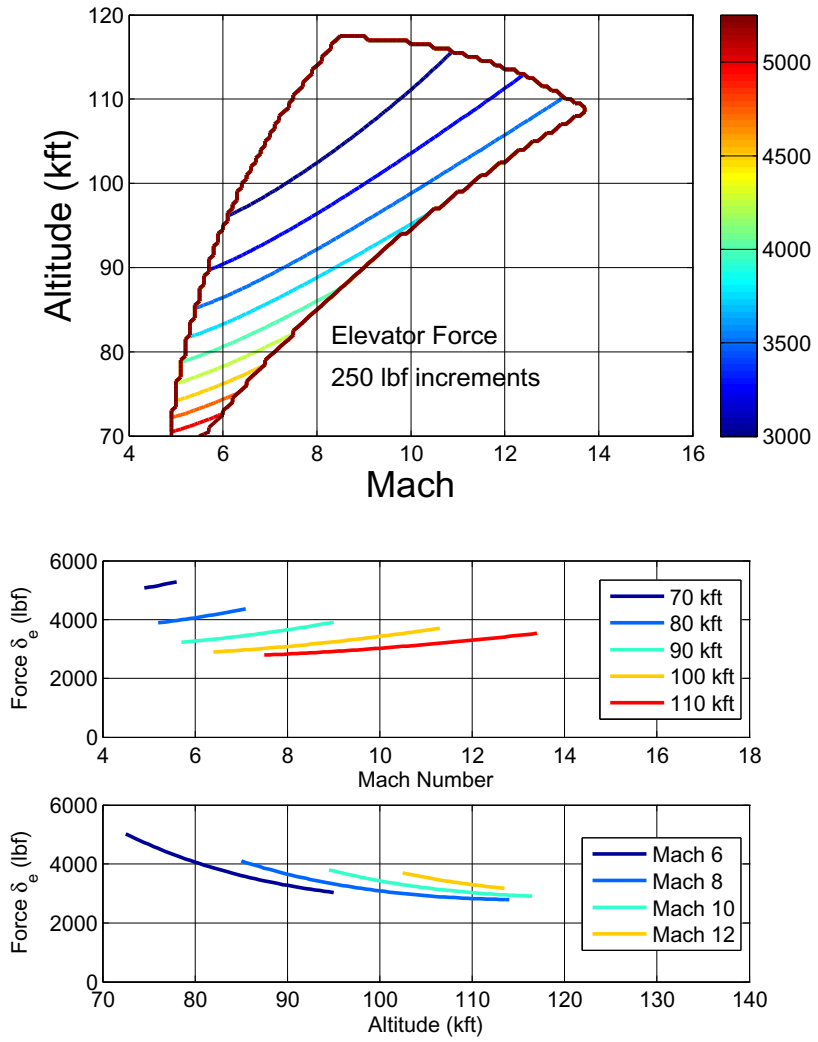

Figure 22: Trim Elevator Force: Level Flight, Unsteady-Viscous Flow, Flexible Vehicle

- Elevator resultant force increases linearly with increasing mach
- Elevator resultant force decreases with increasing altitude

4.4.12 Static Analysis: Trim Combustor Mach

The following figures show the variations in the trim Mach at the combustor exit across the flight envelope, and for different Mach and altitudes.

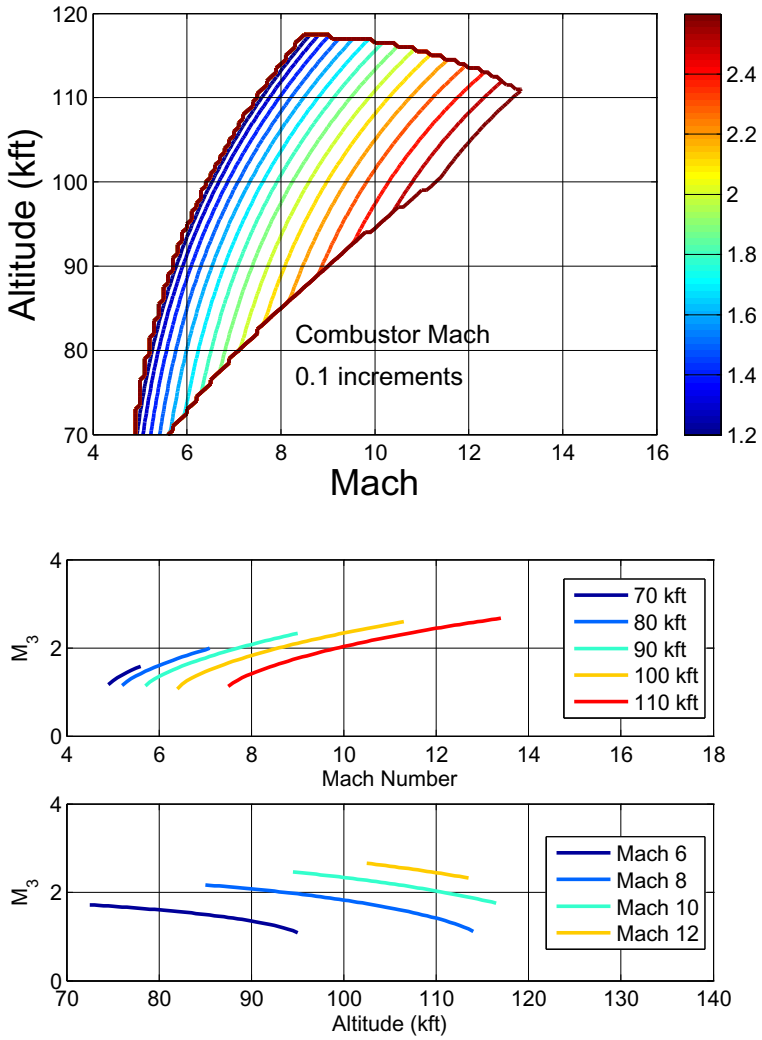

Figure 23: Trim Combustor Mach: Level Flight, Unsteady-Viscous Flow, Flexible Vehicle

- M_3 never goes below 1
- M_3 increases with increasing Mach
- M_3 decreases with increasing altitude

4.4.13 Static Analysis: Trim Combustor Temp.

The following figures show the variations in the trim temperature at the combustor exit (after fuel addition) across the flight envelope, and for different Mach and altitudes.

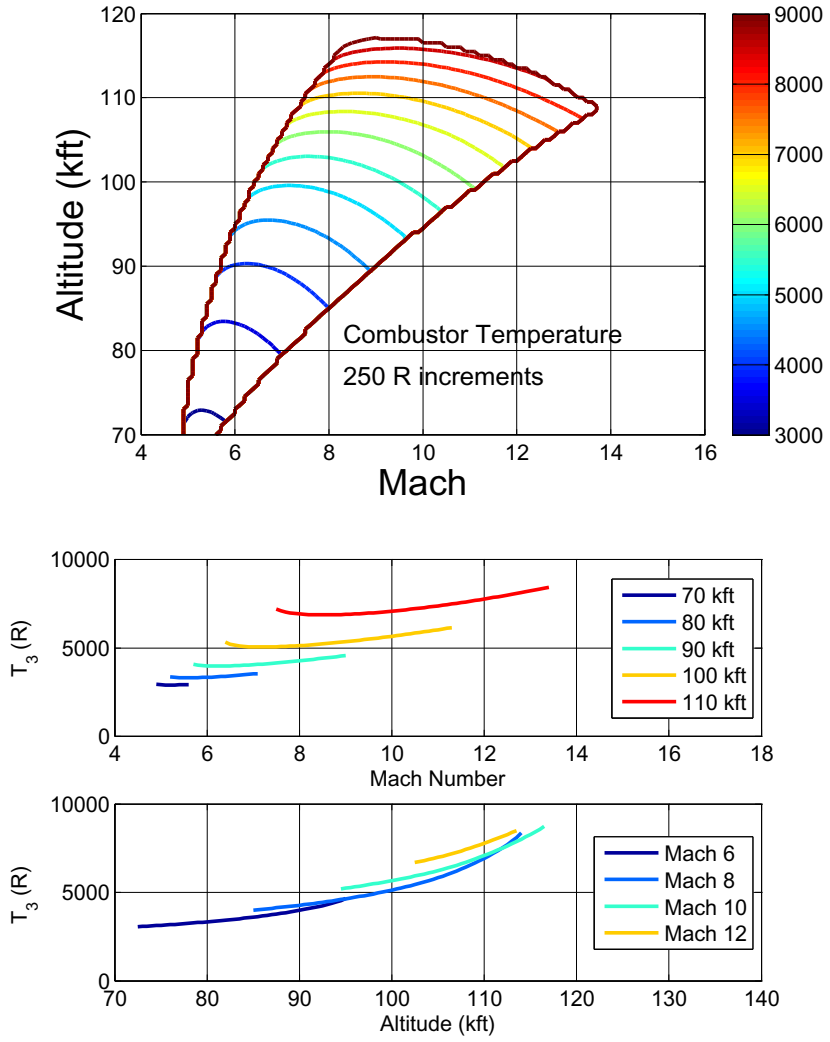

Figure 24: Trim Combustor Temp.: Level Flight, Unsteady-Viscous Flow, Flexible Vehicle

- T_3 displays similar behavior to the FER
- T_3 decreases slightly, then increases with increasing Mach
- T_3 increases with increasing altitude

4.4.14 Static Analysis: Trim Fuel Mass Flow

The following figures show the variations in the trim fuel mass flow across the flight envelope, and for different Mach and altitudes.

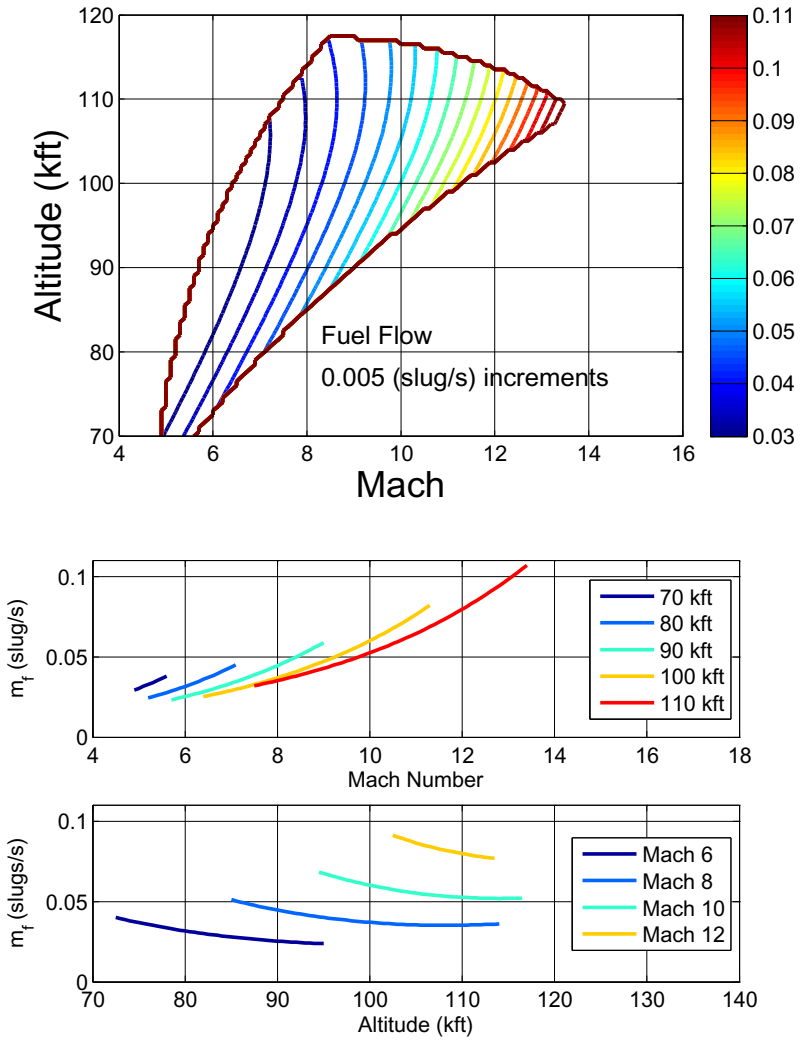

Figure 25: Trim Fuel Mass Flow: Level Flight, Unsteady-Viscous Flow, Flexible Vehicle

- $\dot{m}_f$ increases with increasing Mach
- $\dot{m}_f$ generally decreases with increasing altitude

4.4.15 Static Analysis: Trim Internal Nozzle Mach

The following figures show the variations in the trim Mach at the internal nozzle exit across the flight envelope, and for different Mach and altitudes.

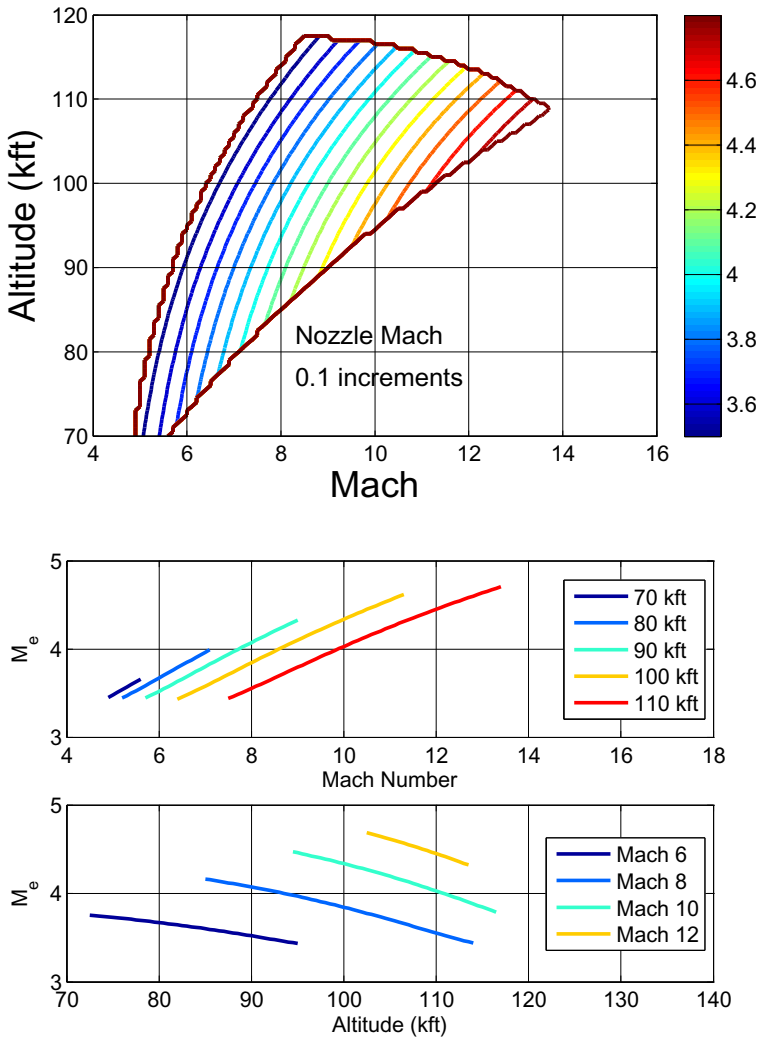

Figure 26: Trim Internal Nozzle Mach: Level Flight, Unsteady-Viscous Flow, Flexible Vehicle

- M_e increases fairly linearly with increasing Mach
- M_e decreases with increasing altitude

4.4.16 Static Analysis: Trim Internal Nozzle Temp.

The following figures show the variations in the trim temperature at the internal nozzle exit across the flight envelope, and for different Mach and altitudes.

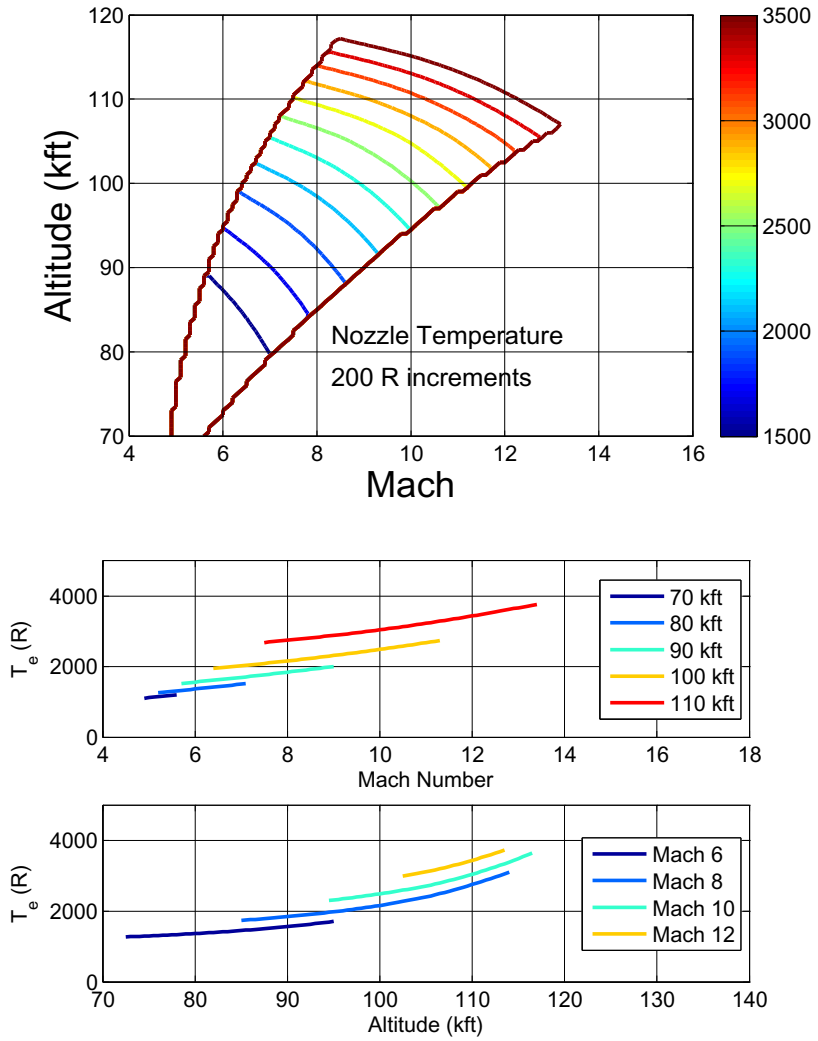

Figure 27: Trim Internal Nozzle Temp.: Level Flight, Unsteady-Viscous Flow, Flexible Vehicle

- T_e increases slightly with increasing Mach
- T_e increases with increasing altitude

4.4.17 Static Analysis: Trim Reynolds Number

The following figures show the variations in the trim Reynolds number across the flight envelope, and for different Mach and altitudes.

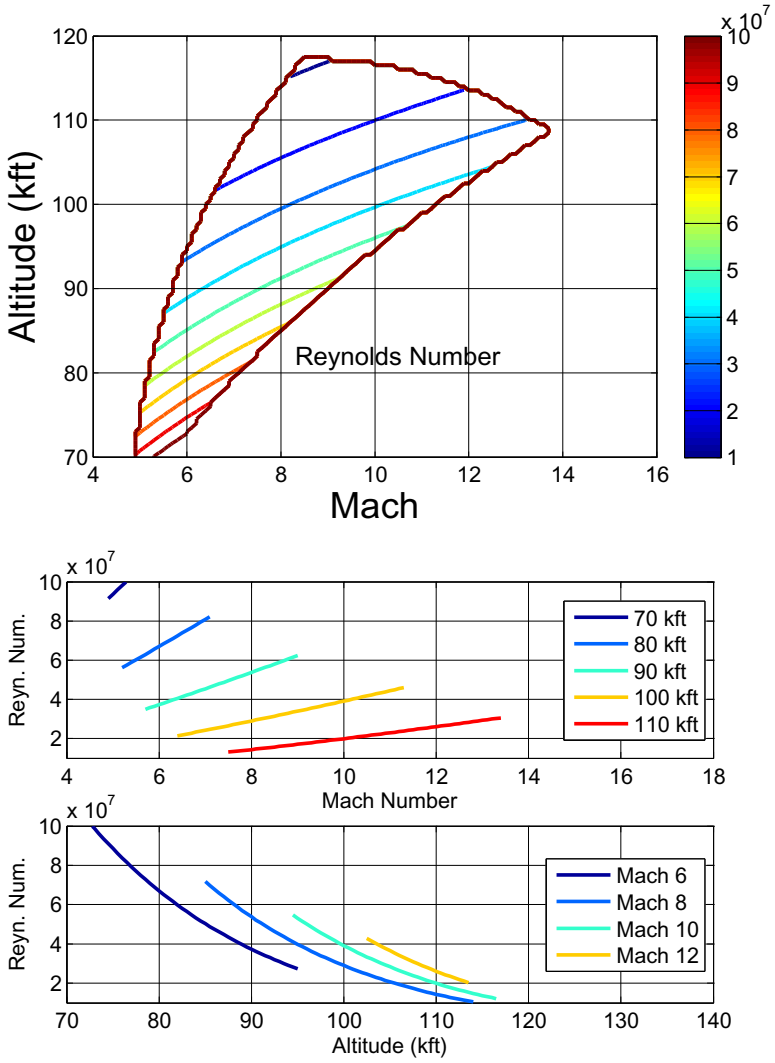

Figure 28: Trim Reynolds Number: Level Flight, Unsteady-Viscous Flow, Flexible Vehicle

- Reynolds Number increases linearly with increasing Mach
- Reynolds Number decreases with increasing altitude

4.4.18 Static Analysis: Trim Absolute Viscosity

The following figures show the variations in the trim absolute viscosity across the flight envelope, and for different Mach and altitudes.

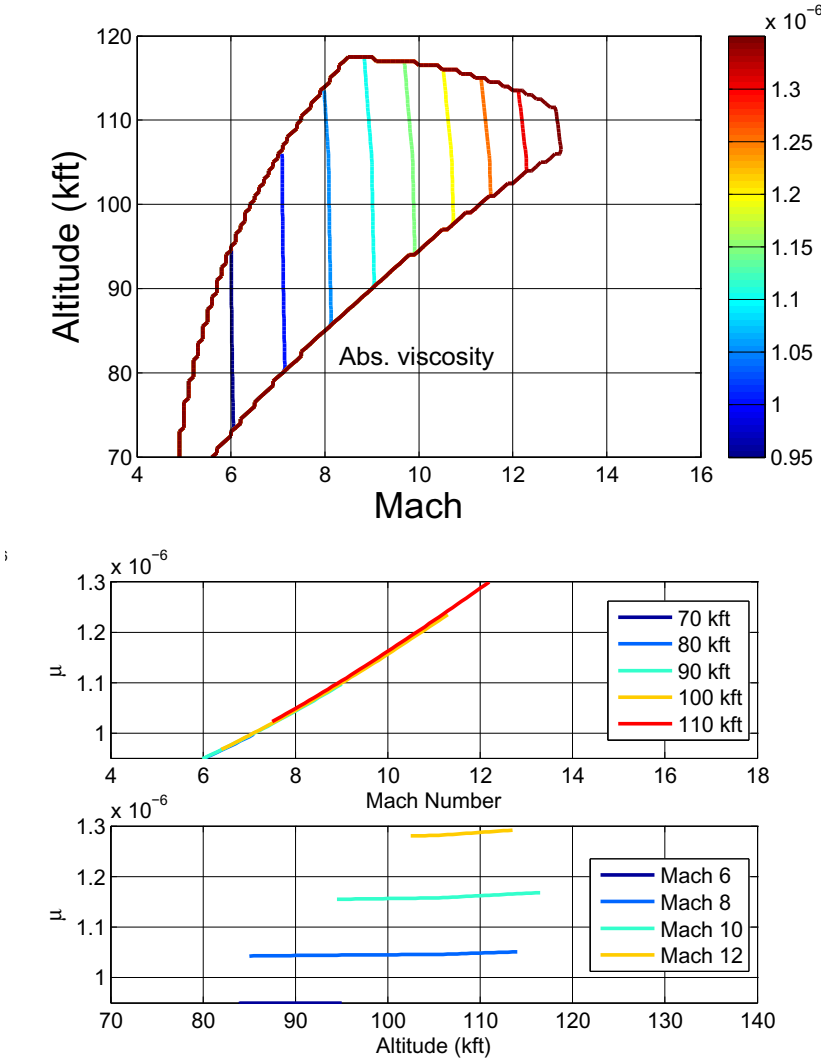

Figure 29: Trim Absolute Viscosity: Level Flight, Unsteady-Viscous Flow, Flexible Vehicle

- Absolute viscosity increases with increasing Mach
- Absolute viscosity is fairly constant w.r.t. increasing altitude

4.4.19 Static Analysis: Trim Kinematic Viscosity

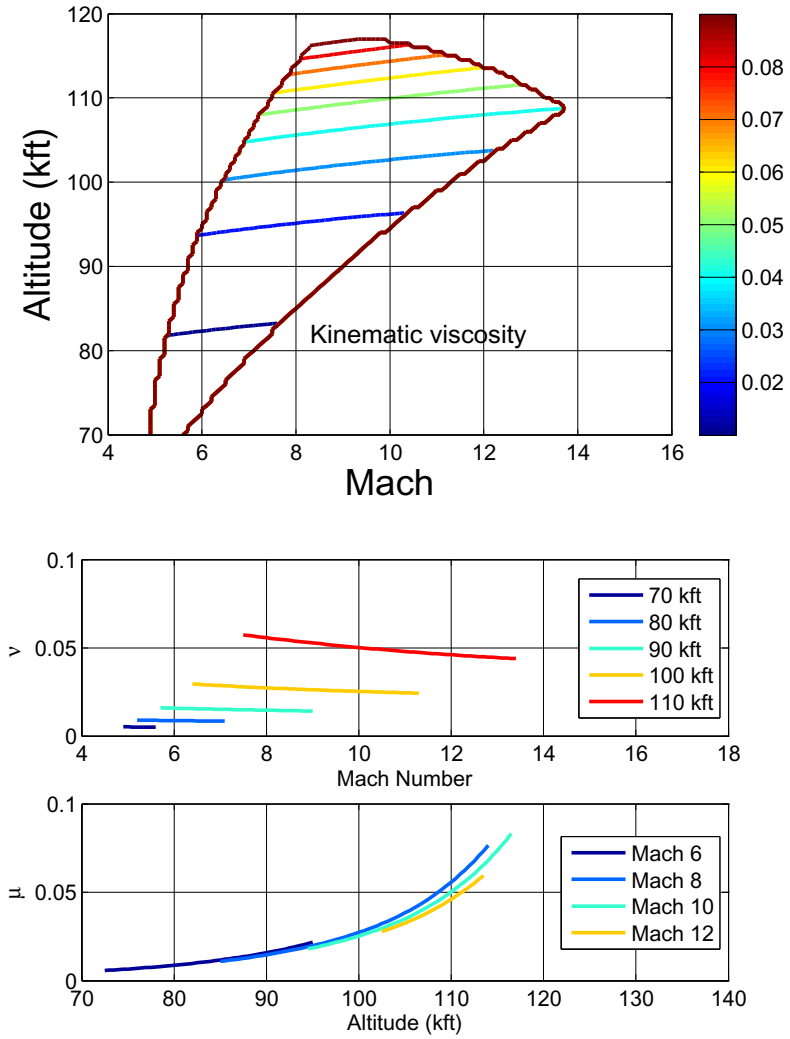

Figure 30: Trim Kinematic Viscosity: Level Flight, Unsteady-Viscous Flow, Flexible Vehicle

- Kinematic viscosity is fairly constant with increasing Mach (slight decrease at higher altitudes)
- Kinematic viscosity increases exponentially with increasing altitude

4.5 Summary and Conclusion

In this chapter the trimming algorithm was presented (a constrained optimization was used), and implementation of the algorithm (and its limitations) were discussed. Additionally the range of flight conditions over which the nominal vehicle can be trimmed was presented, and the variation in the trim properties in the region were presented.

The trimming algorithm will subsequently be used for performing trade studies in later chapters, and for vehicle optimization. The robustness of the algorithm is hence of importance, as it must be able to handle a variety of vehicle configurations and flight conditions.

Once the vehicle is trimmed at a given flight condition, lineaization at the equilibrium provides a model that can be used for linear system control design. The next chapter considers the linearization algorithm and the various dynamic properties of the system at different operating points.

5. Dynamic Properties

5.1 Overview

In this chapter, the linearization procedure for the HSV model is presented. Variations in the dynamic properties over the envelope are then examined. The following properties are examined:

- RHP Pole, RHP Zero, RHP Zero/Pole ratio variations
- Bode magnitude, phase responses
- Modal analysis
- Singular value decompositions

Fundamental questions.

- How do dynamic properties of vehicle vary over trimmable region?

Observations.

- Both instability and RHP zero tend to be constant along lines of constant dynamic pressure.

Linearization of a general dynamic system.

For a general nonlinear system, we have the following state space representation:

$$\dot{x}(t) = f(x(t), u(t)) \qquad x(0) = x_o \tag{5.1}$$

$$y(t) = g(x(t), u(t)) \tag{5.2}$$

where

- $f = [\, f_1(x_1, \ldots, x_n, u_1, \ldots, u_m), \ldots, f_n(x_1, \ldots, x_n, u_1, \ldots, u_m) \,]^T \in \mathcal{R}^n$ - vector of n functions
- $g = [\, g_1(x_1, \ldots, x_n, u_1, \ldots, u_m), \ldots, g_p(x_1, \ldots, x_n, u_1, \ldots, u_m) \,]^T \in \mathcal{R}^p$ - vector of p functions

- $u = [\ u_1, \ldots, u_m\ ]^T \in \mathcal{R}^m$ - vector of m input variables
- $x = [\ x_1, \ldots, x_n\ ]^T \in \mathcal{R}^n$ - vector of n state variables
- $x_o = [\ x_{1_o}, \ldots, x_{n_o}\ ]^T \in \mathcal{R}^n$ - vector of n initial conditions.
- $y = [\ y_1, \ldots, y_n\ ]^T \in \mathcal{R}^p$ - vector of p outputs

(x_e, u_e) is an *equilibrium* or *trim* of the nonlinear system at t = 0 if

$$f(x_e, u_e) = 0 \qquad \forall\ t \geq 0 \tag{5.3}$$

Trimming refers to finding system equilibria; i.e. state-control vector pairs (x_e, u_e) st $\dot{x}_e = f(x_e, u_e) = 0$

A linear state space representation (ssr) which approximates the nonlinear system near (x_e, u_e) is obtained:

$$\delta\dot{x}(t) = A\delta x(t) + B\delta u(t) \qquad \delta x(0) = \delta x_o \tag{5.4}$$

$$\delta y(t) = C\delta x(t) + D\delta u(t) \tag{5.5}$$

where

$$A = \left[\begin{array}{ccc} \frac{\partial f_1}{\partial x_1} & \cdots & \frac{\partial f_1}{\partial x_n} \\ \vdots & \vdots & \vdots \\ \frac{\partial f_n}{\partial x_1} & \cdots & \frac{\partial f_n}{\partial x_n} \end{array}\right]_{(x_e,u_e)} \qquad B = \left[\begin{array}{ccc} \frac{\partial f_1}{\partial u_1} & \cdots & \frac{\partial f_1}{\partial u_m} \\ \vdots & \vdots & \vdots \\ \frac{\partial f_n}{\partial u_1} & \cdots & \frac{\partial f_n}{\partial u_m} \end{array}\right]_{(x_e,u_e)} \tag{5.6}$$

$$C = \left[\begin{array}{ccc} \frac{\partial g_1}{\partial x_1} & \cdots & \frac{\partial g_1}{\partial x_n} \\ \vdots & \vdots & \vdots \\ \frac{\partial g_p}{\partial x_1} & \cdots & \frac{\partial g_p}{\partial x_n} \end{array}\right]_{(x_e,u_e)} \qquad D = \left[\begin{array}{ccc} \frac{\partial g_1}{\partial u_1} & \cdots & \frac{\partial g_1}{\partial u_m} \\ \vdots & \vdots & \vdots \\ \frac{\partial g_p}{\partial u_1} & \cdots & \frac{\partial g_p}{\partial u_m} \end{array}\right]_{(x_e,u_e)} \tag{5.7}$$

$$\delta u(t) \stackrel{\text{def}}{=} u(t) - u_e \qquad \delta x(t) \stackrel{\text{def}}{=} x(t) - x_e \qquad \delta x_o \stackrel{\text{def}}{=} x_o - x_e$$

$$\delta y(t) \stackrel{\text{def}}{=} y(t) - y_e \qquad y_e \stackrel{\text{def}}{=} g(x_e, u_e)$$

5.2 Linearization - Steps and Issues

Since analytic expressions for the partial derivatives listed in equation 5.1 are not available, they must be approximated numerically using finite differences.

The standard centralized finite difference has been implemented:

$$\frac{df}{dx} = \frac{f(x + \Delta x) - f(x - \Delta x)}{2\Delta x} \tag{5.8}$$

Consider the simple example where

$$f = sin(x) \tag{5.9}$$

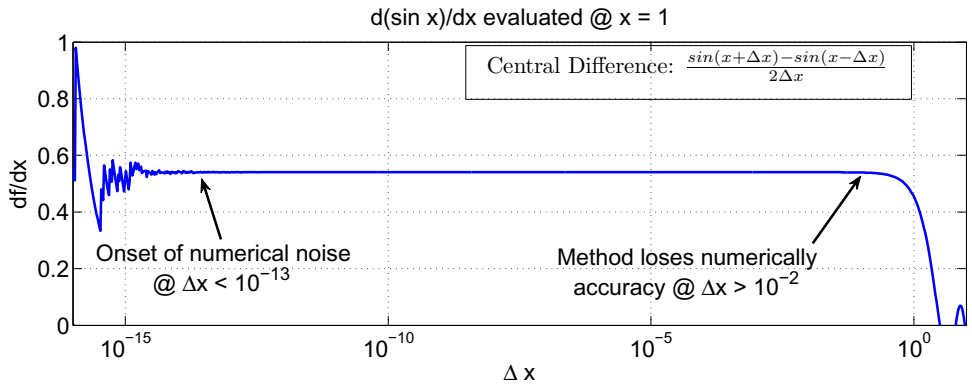

Figure 31: Simple Linearization Example

- For the simple example, step size bounds must be between $[10^{-13}\ 10^{-2}]$
- In general, for the complex nonlinear model the bounds are small: $[10^{-5}\ 10^{-3}]$

– Bounds may vary for each element of equation 5.1.

– Bounds may vary based on operating point.

– Blind implementation of MATLAB *linmod* command will not take this into account.

Based on the equations of motion (3.1-3.6), we define the following accelerations:

$$X = \frac{T\cos(\alpha) - D}{m} \tag{5.10}$$

$$Z = -\frac{T\sin(\alpha) + L}{m} \tag{5.11}$$

$$\mathscr{M} = \frac{M}{I_{yy}} \tag{5.12}$$

where L is the lift, D is the drag, T is the thrust, M is the moment, α is the angle of attack, m is the mass of the vehicle and I_{yy} is the moment of inertia.

We construct a model with the following states and controls

- $\mathbf{x} = [V_t \;\; \alpha \;\; Q \;\; h \;\; \theta \;\; \eta \;\; \dot{\eta} \;\; \cdots]^T$ (we may extend the vector x to include as many flexible modes as required. Below we use three flexible states and their derivatives)
- $\mathbf{u} = [\delta_e \;\; \delta_\phi]^T$ (we are considering a two control model with only the elevator and the FER as inputs)

Below, we provide a ssr for the linearized model [10]

$$\mathbf{A} = \begin{bmatrix}
X_v & X_\alpha & 0 & X_h & -g & X_{\eta_1} & 0 & \dots & X_{\eta_3} & 0 \\
\frac{Z_v}{V_{T_0}} & \frac{Z_\alpha}{V_{T_0}} & 1-\frac{Z_Q}{V_{T_0}} & \frac{Z_h}{V_{T_0}} & 0 & \frac{Z_{\eta_1}}{V_{T_0}} & 0 & \dots & \frac{Z_{\eta_3}}{V_{T_0}} & 0 \\
\mathscr{M}_v & \mathscr{M}_\alpha & \mathscr{M}_Q & \mathscr{M}_h & 0 & \mathscr{M}_{\eta\, h} & 0 & \dots & \mathscr{M}_{\eta\, h} & 0 \\
0 & -V_0 & 0 & 0 & V_0 & 0 & 0 & \dots & 0 & 0 \\
0 & 0 & 1 & 0 & 0 & 0 & 0 & \dots & 0 & 0 \\
0 & 0 & 0 & 0 & 0 & 0 & 1 & \dots & 0 & 0 \\
N_{1,v} & N_{1,\alpha} & 0 & N_{1,h} & 0 & -\omega_1^2+N_{1,\eta_1} & -2\zeta\omega_1+N_{1,\dot{\eta_1}} & \dots & N_{1,\eta_3} & 0 \\
0 & 0 & 0 & 0 & 0 & 0 & 0 & \dots & 0 & 0 \\
N_{2,v} & N_{2,\alpha} & 0 & N_{2,h} & 0 & N_{2,\eta_1} & 0 & \dots & N_{1,\eta_3} & 0 \\
0 & 0 & 0 & 0 & 0 & 0 & 0 & \dots & 0 & 1 \\
N_{3,v} & N_{3,\alpha} & 0 & N_{3,h} & 0 & N_{3,\eta_1} & 0 & \dots & -\omega_3^2+N_{3,\eta_3} & -2\zeta\omega_3+N_{3,\dot{\eta_3}}
\end{bmatrix} \tag{5.13}$$

$$\mathbf{B} = \begin{bmatrix} X_{\delta_e} & X_{\delta_\phi} \\ \frac{Z_{\delta_e}}{V_{T_0}} & \frac{Z_{\delta_\phi}}{V_{T_0}} \\ \mathscr{M}_{\delta_e} & \mathscr{M}_{\delta_\phi} \\ 0 & 0 \\ 0 & 0 \\ 0 & 0 \\ N_{1,\delta_e} & N_{1,\delta_\phi} \\ 0 & 0 \\ N_{2,\delta_e} & N_{2,\delta_\phi} \\ 0 & 0 \\ N_{3,\delta_e} & N_{3,\delta_\phi} \end{bmatrix} \tag{5.14}$$

For completeness, the dimensional derivatives equations for the rigid body modes are given below.

$$X_v = \frac{1}{m}\left(\frac{\partial T}{\partial V_T}\cos(\alpha_0) + \frac{\partial D}{\partial V_T}\right) \tag{5.15}$$

$$X_\alpha = \frac{1}{m}\left(\frac{\partial T}{\partial \alpha}\cos(\alpha_0) + \frac{\partial D}{\partial \alpha} + L_0\right) \tag{5.16}$$

$$X_h = \frac{1}{m}\left(\frac{\partial T}{\partial h}\cos(\alpha_0) + \frac{\partial D}{\partial h}\right) \tag{5.17}$$

$$Z_v = -\frac{1}{m}\left(\frac{\partial T}{\partial V_T}\sin(\alpha_0) + \frac{\partial L}{\partial V_T}\right) \tag{5.18}$$

$$Z_\alpha = -\frac{1}{m}\left(\frac{\partial T}{\partial \alpha}\sin(\alpha_0) + \frac{\partial L}{\partial \alpha} + D_0\right) \tag{5.19}$$

$$Z_Q = -\frac{1}{m}\left(\frac{\partial T}{\partial h}\sin(\alpha_0) + \frac{\partial L}{\partial h}\right) \tag{5.20}$$

$$Z_h = -\frac{1}{m}\left(\frac{\partial T}{\partial h}\sin(\alpha_0) + \frac{\partial L}{\partial h}\right) \tag{5.21}$$

$$\mathscr{M}_{V_T} = \frac{1}{I_{yy}}\frac{\partial M}{\partial V_T} \tag{5.22}$$

$$\mathscr{M}_\alpha = \frac{1}{I_{yy}}\frac{\partial M}{\partial \alpha} \tag{5.23}$$

$$\mathscr{M}_Q = \frac{1}{I_{yy}}\frac{\partial M}{\partial Q} \tag{5.24}$$

$$\mathscr{M}_h = \frac{1}{I_{yy}}\frac{\partial M}{\partial h} \tag{5.25}$$

$$X_{\delta_e} = \frac{1}{m}\left(\frac{\partial T}{\partial \delta_e}\cos(\alpha_0) + \frac{\partial D}{\partial \delta_e}\right) \tag{5.26}$$

$$Z_{\delta_e} = -\frac{1}{m}\left(\frac{\partial T}{\partial \delta_e}\sin(\alpha_0) + \frac{\partial L}{\partial \delta_e}\right) \tag{5.27}$$

$$\mathscr{M}_{\delta_e} = \frac{1}{I_{yy}}\frac{\partial M}{\partial \delta_e} \tag{5.28}$$

$$X_{\delta_\phi} = \frac{1}{m}\left(\frac{\partial T}{\partial \delta_\phi}\cos(\alpha_0) + \frac{\partial D}{\partial \delta_\phi}\right) \tag{5.29}$$

$$Z_{\delta_\phi} = -\frac{1}{m}\left(\frac{\partial T}{\partial \delta_\phi}\sin(\alpha_0) + \frac{\partial L}{\partial \delta_\phi}\right) \tag{5.30}$$

$$\mathscr{M}_{\delta_\phi} = \frac{1}{I_{yy}}\frac{\partial M}{\partial \delta_\phi} \tag{5.31}$$

5.3 Dynamic Analysis: Nominal Properties - Mach 8, 85kft

In this section, we consider the nominal plant's dynamic properties (linearized at Mach 8, 85kft). Below, we have the pole-zero map for the HSV model.

5.3.1 Nominal Pole-Zero Plot

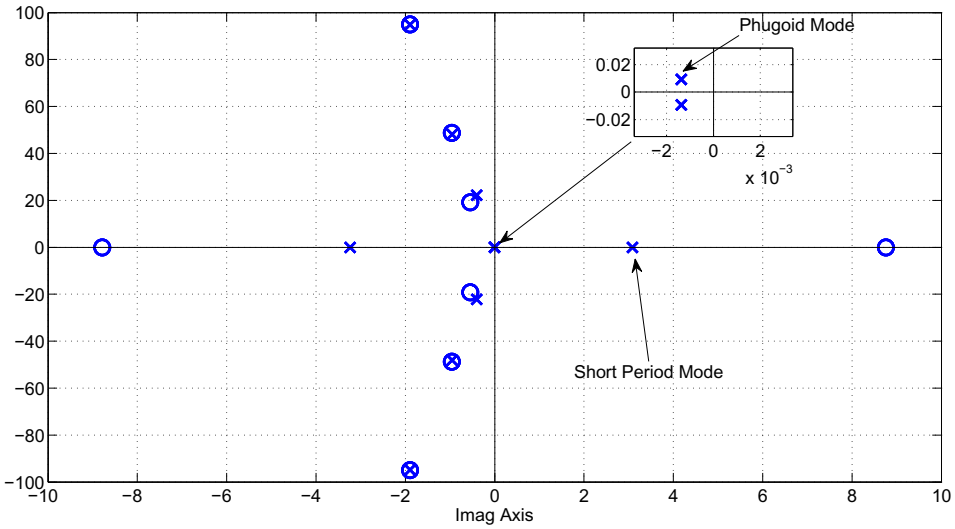

Figure 32: Pole Zero Map at Mach 8, 85kft: Level Flight, Flexible Vehicle

We note that the short period mode comprises of a stable and an unstable pole. The long lower forebody of typical hypersonic waveriders combined with a rearward shifted center-of-gravity (CG), results in a pitch-up instability. Hence, we need

a minimum bandwidth for stabilization [98]. Also, the flexible modes are lightly damped, and limit the maximum bandwidth [107–109].

Table 5.1: Poles at Mach 8, 85kft: Level Flight, Flexible Vehicle

Pole	Damping	Freq. (rad/s	Mode Name
3.21	-1	3.21	Unstable Short Period
-3.28	1	3.28	Stable Short Period
$-1.10 \cdot 10^{-3} \pm j5.75 \cdot 10^{-3}$	1.88	$5.85 \cdot 10^{-3}$	Phugoid Mode
$-0.41 \pm j22.1$	$2 \cdot 10^{-2}$	22.1	1^{st} Flex
$-0.96 \pm j48.1$	$2 \cdot 10^{-2}$	48.1	2^{nd} Flex
$-1.9 \pm j94.8$	$2 \cdot 10^{-2}$	94.8	3^{rd} Flex

Table 5.2 lists the zeros of the linearized model. We notice that the plant is non-minimum phase. This is a common characteristic for tail-controlled aircrafts, unless a canard is used [124, 125]. It is understood, of course, that any canard approach would face severe heating, structural, and reliability issues.

Table 5.2: Zeros at Mach 8, 85kft: Level Flight, Flexible Vehicle

Pole	Damping	Freq. (rad/s
8.54	-1	8.54
-8.55	1	-8.55
$-0.39 \pm j19.1$	$2 \cdot 10^{-2}$	19.1
$-0.96 \pm j48.7$	$1.96 \cdot 10^{-2}$	48.7
$-1.9 \pm j94.9$	$2.04 \cdot 10^{-2}$	94.9

5.3.2 Modal Analysis

Table 5.3 shows the eigenvectors for the modes given earlier. This subsection examines the natural tendencies of the linearized system. To examine the natural modes of a system, the input is set to zero and the initial conditions are chosen to excite only one mode. To examine a mode s_i, we let the initial condition be any linear combination of the real and complex components of a right eigenvector of the mode [126]. Eigenvectors to excite individual modes of the linearized model are given in table 5.3.

Table 5.3: Eigenvector Matrix at Mach 8, 85kft: Level Flight, Flexible Vehicle

State	Phugoid	Unstable short period	Stable Short Period
Velocity	-1.54e-2±-9.39e-2i	-1.95e-5	2.26e-5
AOA	-4.30e-3±2.61e-2i	-2.62e-1	-2.69e-1
Pitch Rate	-1.09e-3±5.72e-3i	-8.67e-1	8.61e-1
Pitch	9.95e-1	-2.71e-1	-2.61e-1
η_1	-4.96e-3±3.01e-2i	-9.69e-2	-1.00e-1
$\dot{\eta_1}$	-1.68e-4±6.16e-5i	-3.10e-1	3.30e-1
η_2	1.32e-4±8.02e-4i	9.93e-4	1.02e-3
$\dot{\eta_2}$	4.46e-6±1.64e-6i	3.18e-3	-3.36e-3
η_3	4.51e-5±2.74e-4i	-3.44e-4	-3.53e-4
$\dot{\eta_3}$	1.53e-6±5.61e-7i	-1.10e-3	1.17e-3
State	Flexible Mode 1	Flexible Mode 2	Flexible Mode 3
Velocity	-3.59e-6±1.32e-7i	-5.44e-7±2.22e-8i	-3.98e-7±1.61e-8i
AOA	-1.44e-4±5.05e-4i	-3.14e-5±1.94e-4i	-1.41e-5±9.50e-6i
Pitch Rate	1.13e-2±3.39e-4i	9.40e-3±3.68e-4i	9.51e-4±3.66e-5i
Pitch	-2.47e-5±5.08e-4i	-1.15e-5±1.95e-4i	-5.87e-7±1.00e-5i
η_1	-8.31e-4±4.51e-2i	-3.08e-5±6.79e-4i	-1.34e-5±2.56e-4i
$\dot{\eta_1}$	9.99e-1	3.27e-2±8.31e-4i	2.42e-2±7.83e-4i
η_2	-3.46e-6±1.36e-4i	-4.12e-4±2.08e-2i	1.26e-6±2.73e-5i
$\dot{\eta_2}$	3.00e-3±2.12e-5i	9.99e-1	-2.59e-3±6.77e-5i
η_3	-5.79e-7±1.61e-5i	2.68e-7±9.50e-6i	-2.11e-4±1.05e-2i
$\dot{\eta_3}$	3.57e-4±6.24e-6i	-4.57e-4±3.84e-6i	1.00

Phugoid Mode. The long-period or phugoid mode represents an interchange of potential and kinetic energy about the equilibrium operating point at nearly constant AOA [127, page 148, 152]. The mode is stable and lightly damped for our model. Low phugoid damping becomes objectionable for pilots flying under instrument flight rules [127, page 153]; automatic stabilization systems should be designed to provide adequate damping. Figure 33 shows variations in the velocity, FPA (equivalently altitude) when this mode is excited. Stability derivatives based approximations for this mode, and longitudinal flying qualities based on phugoid-damping, can be found in [127, page 153] (the phugoid mode may be approximated by a double integrator for our vehicle).

Short Period Mode. For conventional aircrafts, the short-period mode is typically

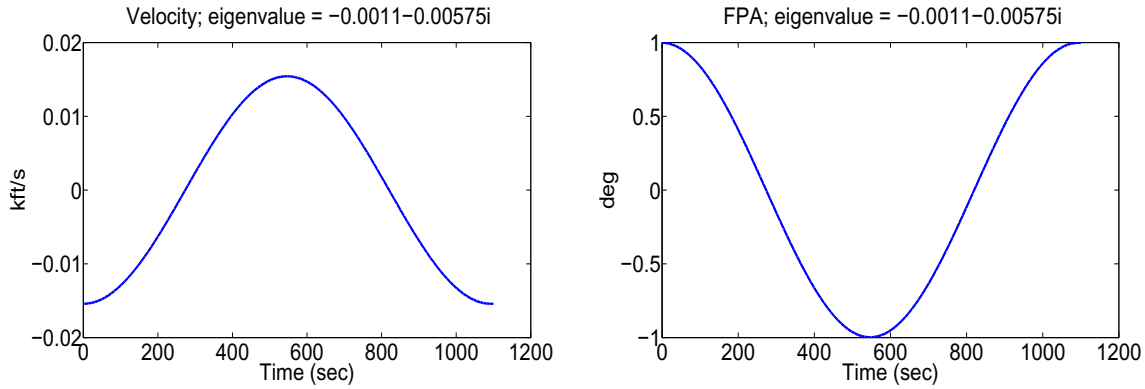

Figure 33: Phugoid mode excitation

heavily damped and has a short period of oscillation; the motion occurs at nearly constant speed [127, page 148]. High frequency and heavy damping are desirable for rapid response to elevator commands without undesirable overshoot [127, page 162]. For our model, the short period mode is not a complex conjugate pair; instead it is a stable and unstable pole pair. In section 5.4.1 the variations in the unstable mode are considered. Stability derivatives based approximations (see Appendix **??**, page **??**) and longitudinal flying qualities based on this mode can be found in [127, page 153].

Flexible Modes. The flexible modes of the HSV have very little impact on the outputs.

5.4 Dynamic Analysis - RHP Pole, Zero variations

5.4.1 Dynamic Analysis: RHP Pole

Figure 34 illustrates variations in the RHP pole with Mach, altitude and dynamic pressure.

- RHP pole fairly constant along constant dynamic pressure profiles;
  - increases with increasing dynamic pressure
  - Designing a minimum BW at the plant input for stabilization should be done at larger dynamic pressures to ensure sufficient control authority

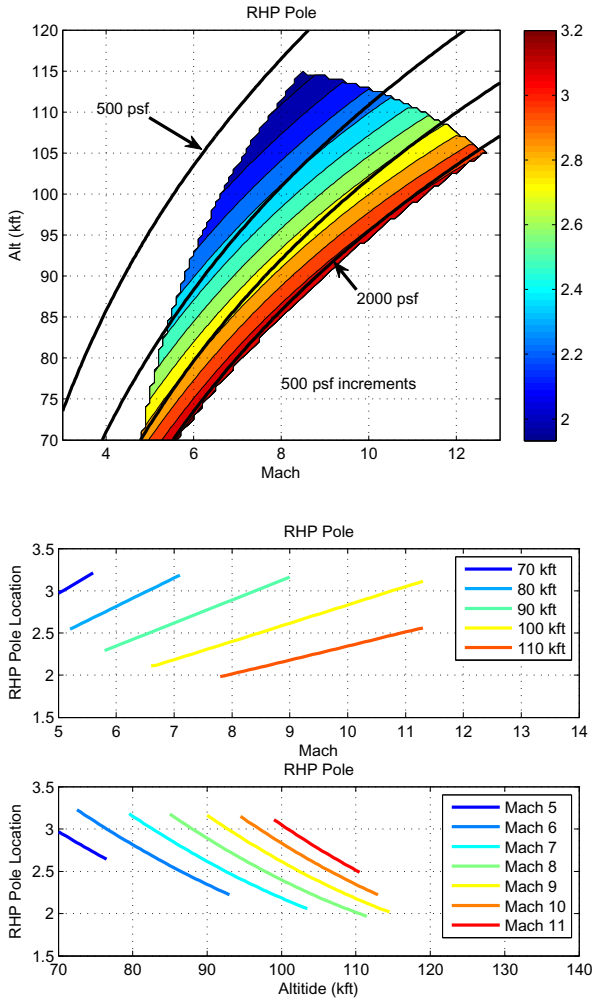

Figure 34: Right Half Plane Pole: Level Flight, Flexible Vehicle

across the flight envelope

- RHP pole increases linearly with increasing mach
- RHP pole decreases monotonically with increasing altitude

5.4.2 Dynamic Analysis: RHP Zero

Figure 35 illustrates variations in the RHP zero with Mach, altitude and dynamic pressure.

- RHP zero decreases with decreases dynamic pressure
- RHP zero increases linearly with increasing mach

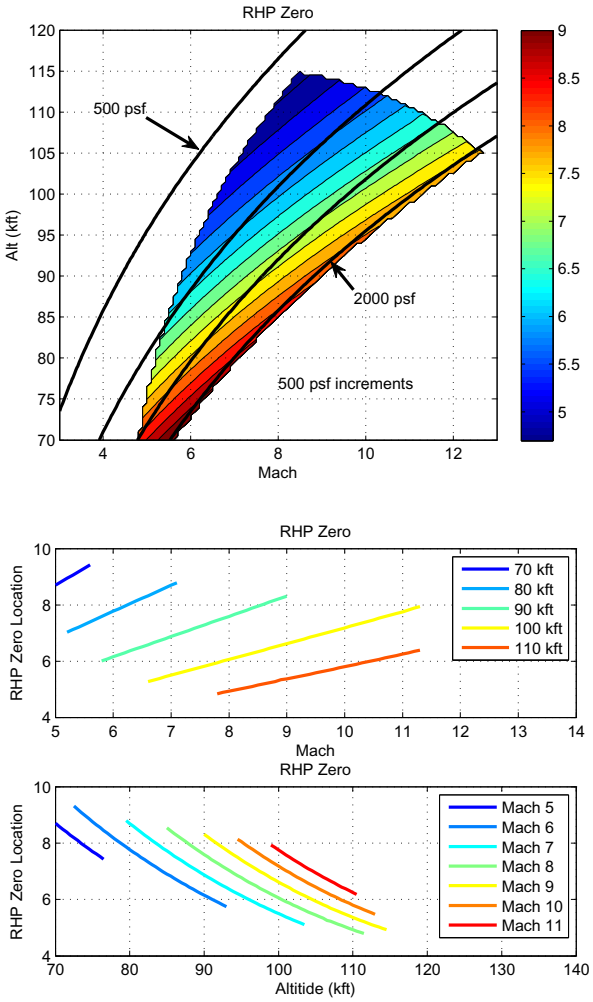

Figure 35: Right Half Plane Zero: Level Flight, Flexible Vehicle

- RHP zero decreases monotonically with increasing altitude
  - RHP zero determines maximum BW at FPA (plant output/error)
  - $z_{min} = 4.8$, occurs at Mach 8.5, 115 kft, determines worst case maximum BW

5.4.3 Dynamic Analysis: RHP Zero-Pole ratio

Figure 36 illustrates variations in the RHP zero/pole ratio with Mach, altitude and dynamic pressure.

- Z-P ratio decreases with increasing altitude

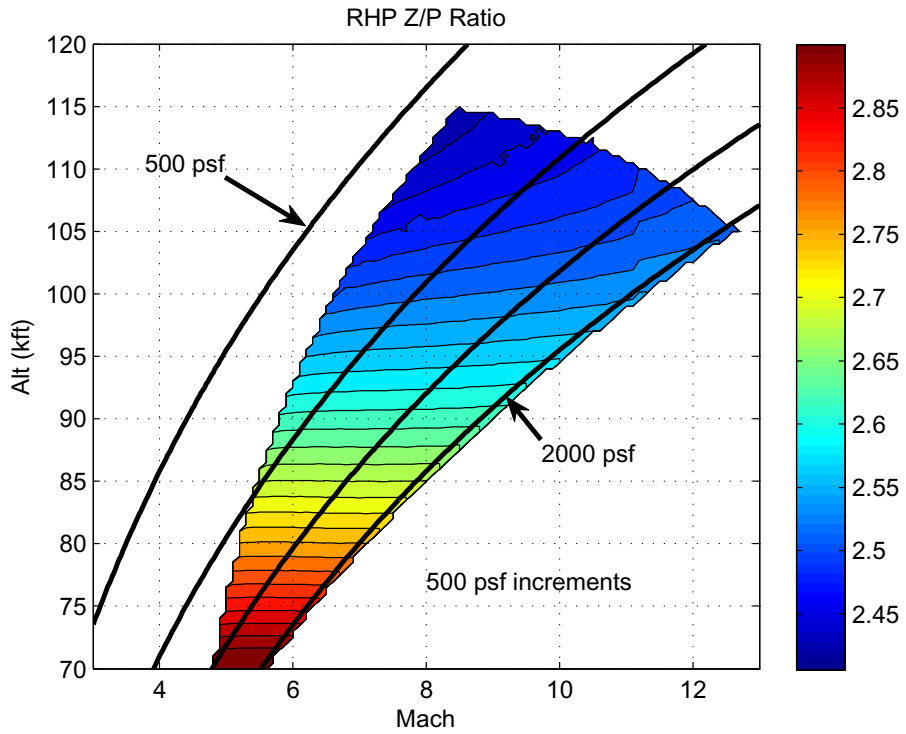

Figure 36: Right Half Plane Zero/Pole Ratio Contour: Level Flight, Flexible Vehicle

- Worst ratio at altitude = 113 kft, Mach = 8.5

5.5 Dynamic Analysis - Frequency Responses

5.5.1 Dynamic Analysis - Bode Magnitude Response

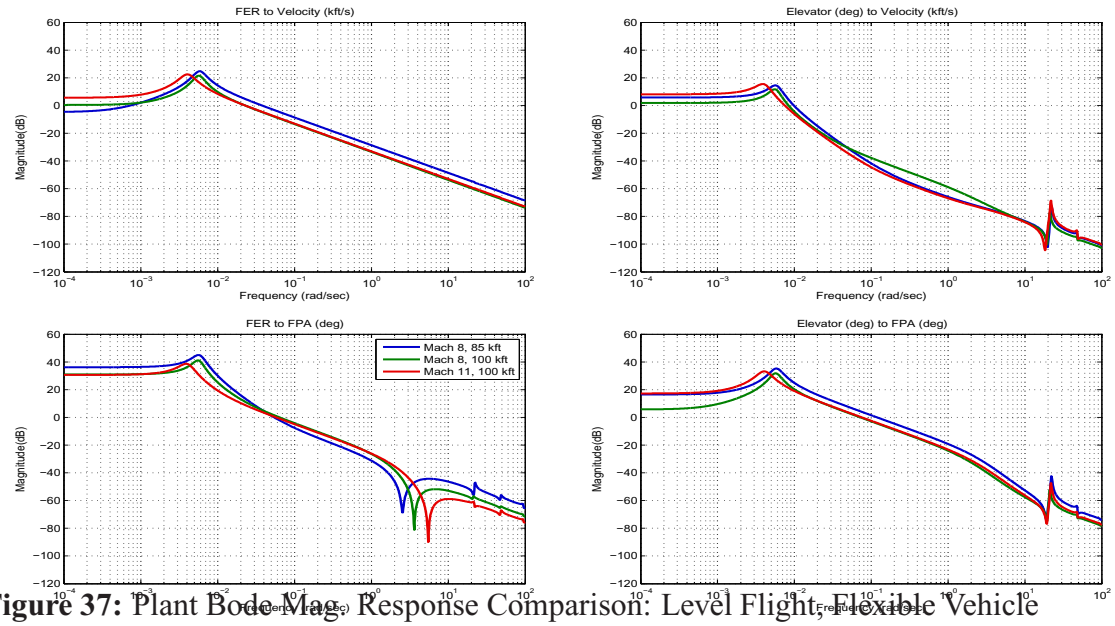

Figure 37: Plant Bode Mag. Response Comparison: Level Flight, Flexible Vehicle

5.5.2 Dynamic Analysis - Bode Phase Response

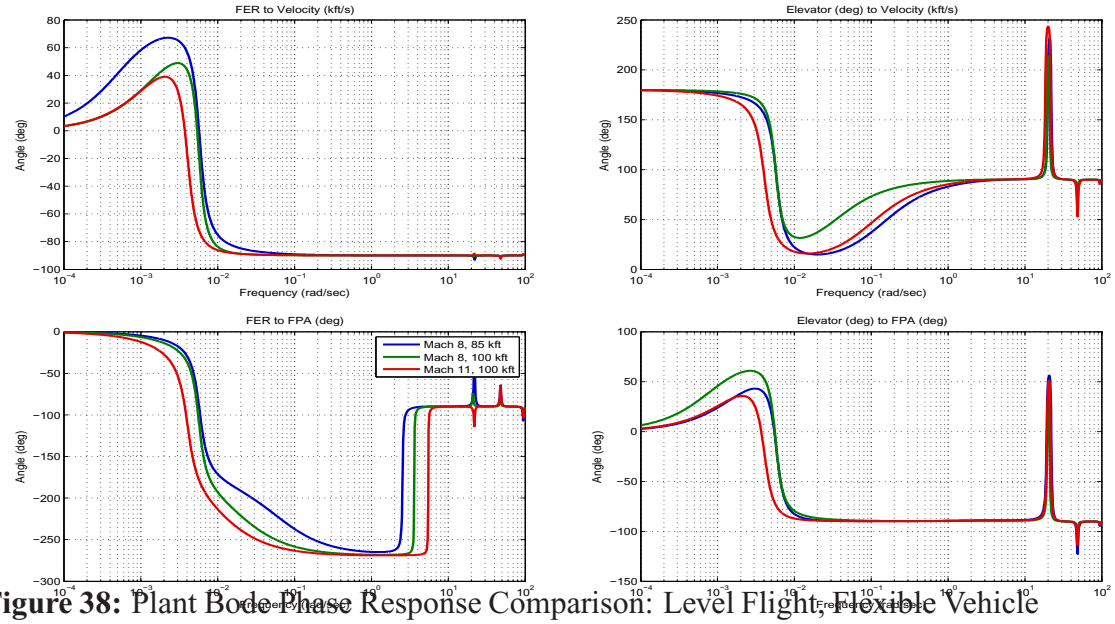

Figure 38: Plant Bode Phase Response Comparison: Level Flight, Flexible Vehicle

5.6 Dynamic Analysis - Singular Values

The figures 39 and 40 show the variation in the singular values with frequency, for the nominal plant.

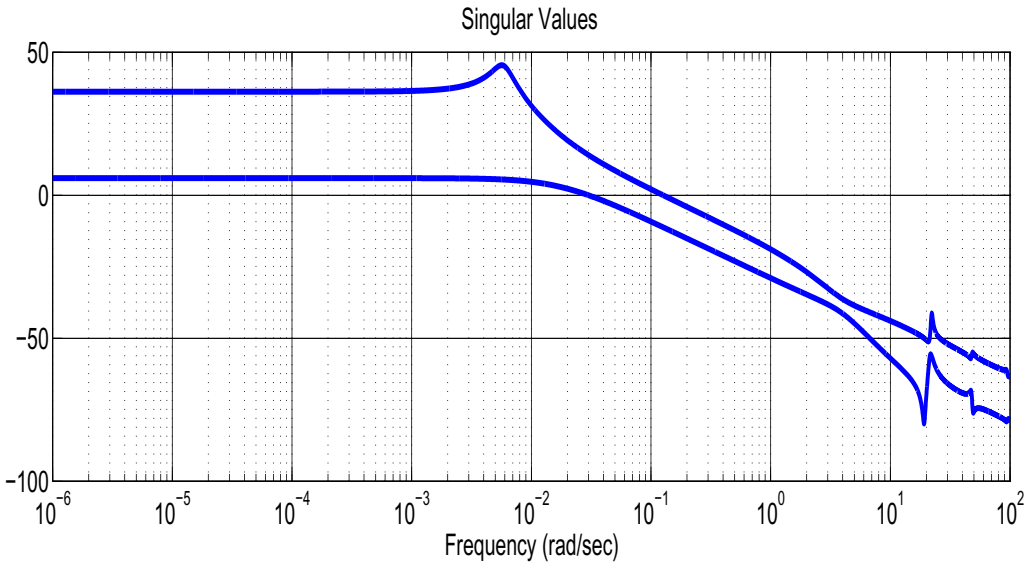

Figure 39: Singular Values: Level Flight, Flexible Vehicle, Mach 8, h=85 kft

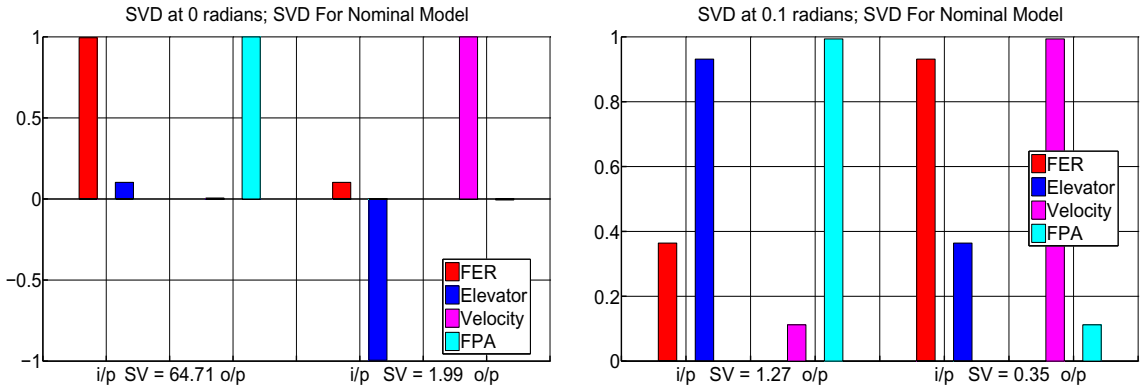

Figure 40: Singular Value Decomposition, Mach 8, h=85 kft

- At dc, FER (elevator) has greatest impact FPA (velocity).
- However, at low frequencies FER (elevator) should be used to command velocity (FPA).

5.7 FPA Control Via FER

The figure below shows the bode magnitude response for the nominal plant at Mach 8, 85kft (level flight).

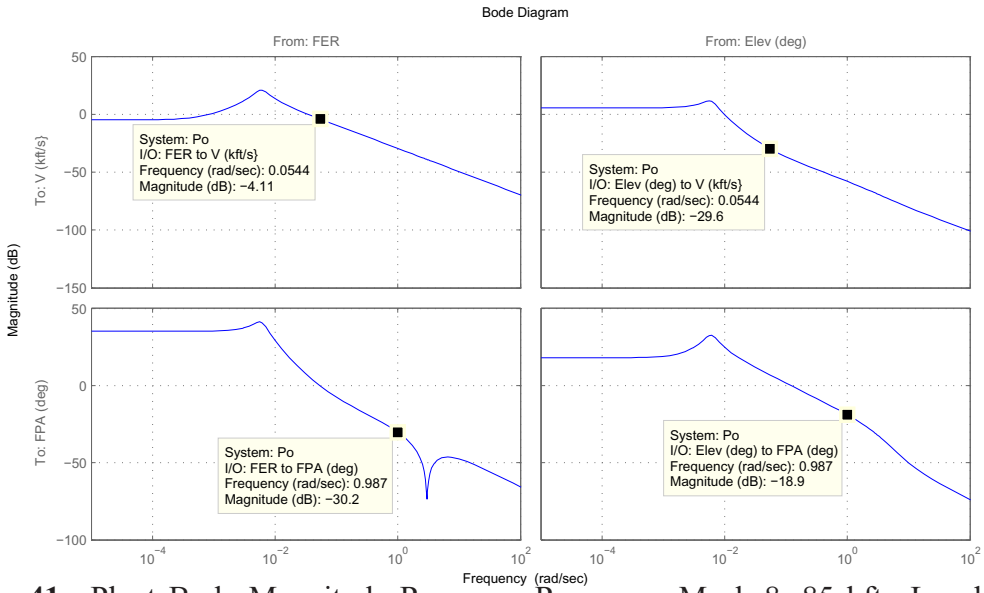

Figure 41: Plant Bode Magnitude Response Response, Mach 8, 85 kft: Level Flight, Flexible Vehicle

What is the feasibility of using FER to control FPA?

- At frequencies of 1 rad/sec (roughly corresponding to a 5 second settling time)
  - Each degree of FPA corresponds to 8.81 degrees (18.9 dB) of elevator
  - Each degree of FPA corresponds to an FER of 32.4 (30.2 dB)!!
- At frequencies of 0.05 rad/sec (roughly corresponding to a 100 second settling time)
  - Each degree of FPA corresponds to 0.5 degrees (-6.95 dB) of elevator
  - Each degree of FPA corresponds to an FER of 1 (0.05 dB)

5.8 Summary and Conclusions

In this chapter, the linearization algorithm and the dynamic properties of the nominal plant were presented. The vehicle is open loop unstable (due to cg rear of ac - long forebody serves as a compression ramp). There exists a RHP zero associated with a tail-controller aircraft (unless a canard is used [124, 125]). The RHP pole and RHP zero increase with dynamic pressure. The RHP zero-pole ratio increases with altitude.

For classical controllers, the RHP zero limits the achievable bandwidth (i.e. there exists a finite upward gain margin); the RHP pole requires a minimum controller bandwidth (i.e. there is a positive downward gain margin). The lightly damped flexible modes present additional control challenges and limit the bandwidth (it is desirable to avoid exciting them). The dynamic properties at trim influence controller design and must be considered during the vehicle design process. In the following chapter, we shall consider how these properties change with different vehicle configurations.

6. Heat Modeling TPS Considerations

6.1 Overview

The HSV model under consideration consists of an integrated airframe and engine [82]. The vehicle is open loop unstable [15]), and has a non-minimum RHP zero (unless a canard is present [15]). The model also has lightly damped flexible modes [10]. Due to the complexity of control, a multidisciplinary approach is required in the design of air-breathing hypersonic vehicles [128, 129]. The impact of parameters on control-relevant static properties (e.g. level-flight trimmable region, trim controls, AOA) and dynamic properties (e.g. instability and right half plane zero associated with flight path angle) must be considered at the design stage. In this chapter trade studies associated with vehicle TPS parameters are examined. Trade studies and control design are broadly categorized based on

- Elasticity (EI) effect for the vehicle.
- Effect of aerodynamic heating over vehicle properties.
- TPS sizing and mass effect along with heating.

TPS slows/stops the airframe structure from reaching its critical temperature when the structural material begins to loose its material characteristics. The thesis considers the effect of TPS size and mass effects in aerodynamic heating environment and to keep the structural temperature within acceptable limits.

TPS are very critical for high speed performance of the vehicle. Compromise over the weight and cost is always there, reduction in weight could lead to lower operable temperature limits.

Fundamental Questions. The following fundamental questions are examined during trade studies

- What are the impacts of TPS heating on Elasticity (fundamental frequencies),

static and dynamic properties of the vehicle?

- What are the impacts of TPS mass on Elasticity (fundamental frequencies), static and dynamic properties?
- What are the impacts of TPS physical dimension on Elasticity (fundamental frequencies), static and dynamic properties?
- What are the impact on control design for heating of TPS with mass and structure variations?
- What percentage change in flexibility,mass forces need of new control design?

6.2 Aerodynamic Heating.

Radiation equilibrium temperature and exposure times dictate the design of TPS[130]. NASP X series planes are designed considering their usage for high speed long duration flight. Greatest aerodynamic heating rates are anticipated during ascent rather than descent, [1, page 263] aerospace plane ascent maximum heat flux ($\dot{q}$) 650 W/cm^2 (572.5 BTU/ft^2s),for aerospace plane entry, maximum heat flux ($\dot{q}$) 100 W/cm^2 (88.07 BTU/ft^2s),for shuttle entry, maximum heat flux ($\dot{q}$) 50 W/cm^2 (44.03 BTU/ft^2s),

For the purpose of simplicity only sustained flight condition is studied in the thesis.

Viscous heating for high speed flow is discussed within [6, 131]. Skin friction is captured using Eckert's reference temperature method [131, 132]. Sutherland's formula is then used to calculate the associated reference viscosity of air at the reference temperature [133, page 292],[28, page 60]. Two scenarios are considered:

1. a constant heat flux (not typical but simplifies computations) and
2. a flight dependent heat flux (more realistic albeit computationally more in-

volved).

Relevant one-dimensional heat partial differential equations (pdes) and boundary condition for a set of stacked materials are given in [134, pages 295].

Relevant unsteady aero-thermo-elastic effects are examined within [6, 10]. The authors address the impact of heating on (longitudinal) structural mode frequencies and mode shapes.

Aerodynamic heating calculation details are as follows.

Recovery Factor. The ratio of the actual rise in temperature to the maximum rise in temperature that could occur is called the recovery factor. It is given by[21, page 483]:

$$r = \begin{cases} Pr^{1/3} = \left(\frac{\mu c_p}{k}\right)^{1/3} & \text{turbulent flow;} \\ Pr^{1/2} = \left(\frac{\mu c_p}{k}\right)^{1/2} & \text{laminar flow.} \end{cases} \tag{6.1}$$

where Pr is the dimensionless Prandtl number. Typical value for air is 0.71 ([21, page 292])

The valid range of Pr is between 0.7 to 0.8 for wide range of pressures(0.0001-100atm) and temperatures up to 1500°K [135, page 52,66]. During a sustained flight heating for time increment, it is calculated iteratively as the air properties (μ,c_p,k) are function of temperature. These air properties vary with time.

Stagnation or Total Temperature. The flow speed at the surface is reduced to zero. The associated hence stagnation (or total) temperature T_t is given by:

$$T_t = T_e \left(1 + \frac{(\gamma - 1)M_e^2}{2}\right) \tag{6.2}$$

where $\gamma = 1.4$ is the ratio of specific heats, T_e and M_e are temperature and Mach at the edge of boundary layer (values aft of bow shock are used).

Adiabatic or Recovery Temperature. The actual rise in temperature is the difference between the so-called recovery wall temperature T_r and the temperature at the edge of the boundary layer T_e. Given this, the adiabatic (or recovery) wall temperature associated with a near flat surface is given by [131]:

$$T_r = r(T_t - T_e) + T_e \tag{6.3}$$

Reference Temperature. The so-called reference temperature T^* (representative of a temperature within the boundary layer) is calculated using Eckert's formula [131, 132].:

$$T^* = T_e + 0.5(T_w - T_e) + 0.22(T_r - T_e) \tag{6.4}$$

where T_w is taken to be 559.67 °R initially (at $t = 0$). This temperature increases with time.

Reference Density. The associated reference density ρ^* $(lbfs^2/ft^4)$ is given by [136]

$$\rho^* = \frac{V_e}{RT^*} \tag{6.5}$$

where V_e represents the velocity at the edge of boundary layer aft of shock and R is gas constant 1716.55 (ft^2/s^2R).

Reference Viscosity. The associated reference viscosity (μ^*) $(lbfs/ft^2)$ is given by Sutherland's formula [133, page 292],[28, page 60].

$$\mu^* = \mu_0 \left(\frac{T^*}{T_0}\right)^{3/2} \left(\frac{T_0 + 198}{T^* + 198}\right) \tag{6.6}$$

where temperature is in measured in °R and $\mu_0 = 3.7372e^{-7} slug/fts$ is the reference viscosity at the temperature $T_0 = 518.688°R$. It is said from [28, page 60]For temperature below 3000 K (5400°R), the viscosity of air is independent of pressure.

Reference Reynolds Number. The associated reference Reynolds Number Re^* at the reference temperature T^* for the characteristic length l is given by [21, page 41]

$$Re^* = \frac{\rho^* V_e l}{\mu^*} \tag{6.7}$$

The associated local reference Reynolds number Re_x is given by:

$$Re_x = \frac{\rho^* V_e x}{\mu^*} \tag{6.8}$$

- There is no adequate theory to predict turbulent flow behavior hence all analysis of turbulent flow rely on experimental data only.
- The boundary layer follows a laminar growth pattern up to Critical Reynold's number ($Re_{cric} = 5 \times 10^5$) and a turbulent growth there after [131, page 245].
- When 5e5 $<$ Re $<$ 1e7, we assume that the flow is turbulent. It is noted that this is a rule of thumb - one that is valid for high speed flows on a flat plate. [131, page 261]
- Nominal calculations suggest that the flow is turbulent throughout the trimmable region.

  This assumption, of course, warrants further investigation. This will be conducted in the future.

Reference Prandtl Number. The associated reference Prandtl number Pr^* is determined using the reference temperature and a look up table [135].

Local Heat Transfer Coefficient. The associated local heat transfer coefficient $h_x(BTU/ft^sR)$ is defined by the Stanton number St_x as follows [131, page 236,253-258]:

$$St_x = \frac{h_x}{\rho^* V_e} \tag{6.9}$$

where

$$h_x = c_{p_0} Pr^{*-2/3} \rho^* V_e (0.0296) {Re_x}^{-1/5} \tag{6.10}$$

where c_p is the specific heat of air at constant pressure. Nominally, c_p = 1.009 (KJ/Kg K).

Convective Heat Flux. The associated convective heat flux $(BTU/(ft^2 s))$ is given by:

$$\dot{q}_{conv} = h_x(T_r - T_w) \tag{6.11}$$

Radiative Cooling Flux. Radiative (cooling) heat flux is given by:

$$\dot{q}_{rad} = \sigma \epsilon {T_w}^4 \tag{6.12}$$

where σ is the Stefan-Boltzman constant ($4.76 \times 10^{-13} BTU/ft^2 sR^4$ [28, page 339]) and ϵ=0.7 is the emissivity of the PM2000.

Net Heat Flux. The associated net heat flux is given by:

$$\dot{q}_{net} = \dot{q}_{conv} - \dot{q}_{rad} = \dot{q}_{conv} - \sigma \epsilon {T_w}^4 \tag{6.13}$$

Steady State Wall Temperature. At steady state $\dot{q}_{net} = 0$. Hence, after rearranging

the remaining terms one obtains the steady state wall temperature as follows:

$$T_w ss = \left(\frac{\dot{q}_{conv_{ss}}}{\sigma \epsilon} \right)^{1/4} \tag{6.14}$$

6.3 1D Heating of the Composite

Specific mathematical details now follow.

1-D Nominal Heat Equation. The 1-D heat equation with no heat generation is given by:

$$\frac{\partial^2 T_i}{\partial y^2{}_i} = \frac{1}{\alpha_i} \frac{\partial T_i}{\partial t} \tag{6.15}$$

where $\alpha_i = \frac{k_i}{\rho_i c_{p_i}}$ is the diffusivity associated with the i^{th} material, k_i is the conductivity associated with the i^{th} material, ρ_i is the density associated with the i^{th} material, $i = 1, 2, 3, ..., m$, and $m = number\ of\ materials$.

Boundary Conditions. The associated boundary conditions are as follows:

BC 1: External Skin, i=1;

$$\begin{gathered} k_1 \tfrac{\partial T_1}{\partial y_1} = \dot{q_{conv}} - \sigma \epsilon {T_1}^4 \\ where : \dot{q}_{conv} = h_1 (T_r - T_w(x_1, t)) \end{gathered} \tag{6.16}$$

BC 2: Material Interface, i=2,3...m

$$k_{i-1} \frac{\partial T_{i-1}}{\partial y_{i-1}} = k_i \frac{\partial T_i}{\partial y_i} \tag{6.17}$$

BC 3: Material Interface, i=2,3...m

$$T_{i-1}(y,t) = T_i(y,t) \tag{6.18}$$

BC 4: Innermost node, i=m+1

$$k_m \frac{\partial T_m}{\partial y_i} = 0; \tag{6.19}$$

IC: T_0 = 559.67 R (Temperature at all nodes at time t=0s)

Finite Difference Based Solution for Composite Material Heat Transfer Problem. An explicit finite difference method was utilized to study unsteady heat transfer at discrete points along the structure [6].

General 1D recursion equations (obtained from PDE discretization) for the composite layer heat transfer are given below:

(a) At the top surface of the plate:

$$T_i^{n+1} = q_{net} + T_i^n \left(1 - \frac{2\alpha_m \triangle t}{\triangle {y_m}^2}\right) + {T^n}_{i+1} \left(\frac{2\alpha_m \triangle t}{\triangle {y^2}_m}\right) \tag{6.20}$$

It should be noted that for stability, we require $\left(\triangle t_1 = \triangle t < 2\frac{\triangle {y^2}_m}{2\alpha_m}\right)$.

(b) In the interior node of a material

$$T_i^{n+1} = T_i^n \left(1 - \frac{2\alpha_m \triangle t}{\triangle {y_m}^2}\right) + ({T^n}_{i+1} + {T^n}_{i-1}) \left(\frac{2\alpha_m \triangle t}{\triangle {y^2}_m}\right) \tag{6.21}$$

for stability $\left(\triangle t_2 = \triangle t < 2\frac{\triangle {y^2}_m}{2\alpha_m}\right)$

(c) At the interface node of two different material

$$T_i^{n+1} = T_i^n \left(1 - \frac{2\triangle t}{\overline{\rho_m c_{p_m}}(\triangle y_m + \triangle y_{m+1})}\right)\left(\frac{k_m}{\triangle y_m} + \frac{k_{m+1}}{\triangle y_{m+1}}\right) \tag{6.22}$$

$$+\left(\frac{{T_{i-1}}^n k_m}{\triangle y_m} + \frac{{T_{i+1}}^n k_{m+1}}{\triangle y_{m+1}}\right)\left(\frac{2\triangle t}{\overline{\rho_m c_{p_m}}(\triangle y_m + \triangle y_{m+1})}\right)$$

for stability $\left(\triangle t_3 = \triangle t < 2\frac{\overline{\rho_m c_{p_m}}(\triangle y_m + \triangle y_{m+1})}{\left(2\frac{k_m}{\triangle y_m} + 2\frac{k_{m+1}}{\triangle y_{m+1}}\right)}\right)$

where $\overline{\rho_m c_{p_m}} = \frac{\rho_m c_{p_m} + \rho_{m+1} c_{p_{m+1}}}{2}$

(d) At inner most node (This innermost boundary is insulated)

$$T_i^{n+1} = T_i^n \left(1 - \frac{2\alpha_m \triangle t}{{\triangle y_m}^2}\right) + {T^n}_{i-1}\left(\frac{2\alpha_m \triangle t}{{\triangle y^2}_m}\right) \tag{6.23}$$

for stability $\left(\triangle t_4 = \triangle t < 2\frac{{\triangle y^2}_m}{2\alpha_m}\right)$

$\triangle t = min(\triangle t_1, \triangle t_2, \triangle t_3, \triangle t_4)$ In practice, a much smaller number is used. We used $\triangle t$=1(s)

Matrices Temperature at the particular node for next time instant is given by

$$T^{n+1} = AT^n + B \tag{6.24}$$

- T is temperature vector of the dimension (15X1). Temperatures of all the spatial nodes (number of nodes here =15) into the material is calculated together for next time instant (T^{n+1}).
- where, A is a tridiagonal matrix of dimension equal to number of nodes of the composite layers(here it is 15). Tri-diagonals are the constants for the spatial steps namely previous (${T_{i-1}}^n$), current (T_i^n) and next (${T_{i+1}}^n$) space instants for the current time instant.

$$B = \left(\frac{2\dot{q_{net}}\delta t}{\rho c_p \delta y} \right) \tag{6.25}$$

- B is the forcing term of dimension (15X1). It has the convecto-radiative heating force($\dot{q}_{net}$) at node 1 while all other values are zero. Heat is added only at the upper skin of the 3 material composite.

Thus, for a hypersonic flight, thermal design of a vehicle structure and material selection depends on the convective heating rate. [28, page 340] points that at hypersonic speeds external surface temperature is generally 0.3-0.5 of the adiabatic wall temperature as a result of the considerable radiative cooling and internal heat transfer.

Importance of the TPS

Convecto-radiative heat inout to the system for three materials namely Titanium, SiO_2 and PM2000 is shown below. Materials are exposed

Value of matrix A:

Table 6.1: Elements of A matrix in the heat input equation 6.24, for Titaniam

.9929	.0071	0	0	0	0	0	0
.0036	.9929	0.0036	0	0	0	0	0
0	.0036	.9929	0.0036	0	0	0	0
0	0	.0036	.9929	0.0036	0	0	0
0	0	0	.0036	.9929	0.0036	0	0
0	0	0	0	.0036	.9929	0.0036	0
0	0	0	0	0	.0036	.9929	0.0036
0	0	0	0	0	0	0.0071	.9929

Value of matrix B:

From table 6.4

- Titanium:8.3744, Titanium is exposed directly to the external environment without any TPS. Heat input is low initially, resulting in linear temperature

Table 6.2: Elements of A matrix in the heat input equation 6.24, for SiO2 and titanium stack

-0.2672	1.2672	0	0	0	0	0	0	0	0	0
0.6336	-0.2672	0.6336	0	0	0	0	0	0	0	0
0	0.6336	-0.2672	0.6336	0	0	0	0	0	0	0
0	0	.0010	.9853	0.0136	0	0	0	0	0	0
0	0	0	.0036	.9929	0.0036	0	0	0	0	0
0	0	0	0	.0036	.9929	0.0036	0	0	0	0
0	0	0	0	0	.0036	.9929	0.0036	0	0	0
0	0	0	0	0	0	.0036	.9929	0.0036	0	0
0	0	0	0	0	0	0	.0036	.9929	0.0036	0
0	0	0	0	0	0	0	0	.0036	.9929	0.0036
0	0	0	0	0	0	0	0	0	0.0071	.9929

Table 6.3: Elements of A matrix in the heat input equation 6.24, for PM2000, SiO2, Titanium stack

0.9725	0.0275	0	0	0	0	0	0	0	0	0	0	0	0	0
0.0137	0.9725	0.0137	0	0	0	0	0	0	0	0	0	0	0	0
0	0.0137	0.9725	0.0137	0	0	0	0	0	0	0	0	0	0	0
0	0	0.0137	0.9725	0.0137	0	0	0	0	0	0	0	0	0	0
0	0	0	0.0520	0.9466	0.0014	0	0	0	0	0	0	0	0	0
0	0	0	0	0.0036	0.9929	0.0036	0	0	0	0	0	0	0	0
0	0	0	0	0	0.0036	0.9929	0.0036	0	0	0	0	0	0	0
0	0	0	0	0	0	0.0010	0.9853	0.0136	0	0	0	0	0	0
0	0	0	0	0	0	0	0.0036	0.9929	0.0036	0	0	0	0	0
0	0	0	0	0	0	0	0	0.0036	0.9929	0.0036	0	0	0	0
0	0	0	0	0	0	0	0	0	0.0036	0.9929	0.0036	0	0	0
0	0	0	0	0	0	0	0	0	0	0.0036	0.9929	0.0036	0	0
0	0	0	0	0	0	0	0	0	0	0	0.0036	0.9929	0.0036	0
0	0	0	0	0	0	0	0	0	0	0	0	0.0036	0.9929	0.0036
0	0	0	0	0	0	0	0	0	0	0	0	0	0.0071	.9929

Table 6.4: First element of B matrix in the heat input equation 6.24

Material	Titanium	SiO_2	PM2000
B (1)	8.3744	19880	11.5432

rise over the flight time. Final temperature is very high.

- SiO2:19880, SiO2 is exposed directly to the external environment without PM2000. Heat input is exorbitantly very large, due to low conductivity and small spatial length, results in exponential temperature rise in fraction of seconds.

- PM2000:11.5432, PM2000 is exposed directly to the external environment with SiO2 and Titanium under it. Heat input is Low heat input, resulting in linear temperature rise over the flight time, initially heat input is slightly larger than the case of Titanium alone, but later the final temperature of

PM2000 is lower than saturated the external surface in above two cases. Titanium doesn't experience high temperature ranges.

6.4 TPS, Heating, and Flexibility Issues

Thermal Protection System (TPS). The thermal protection system (TPS) used was first described within [10, 137–139]. The TPS is assumed to have 3 layers:

1. an outermost honeycomb PM2000 structural metallic layer (3in), (applied as facesheets to the TPS composite),
2. a SiO2 thermal insulation (mid) layer (0.1in), (used for maximum heat insulation), and
3. a Titanium (core) load bearing (inner) structure (9.6in nominally).

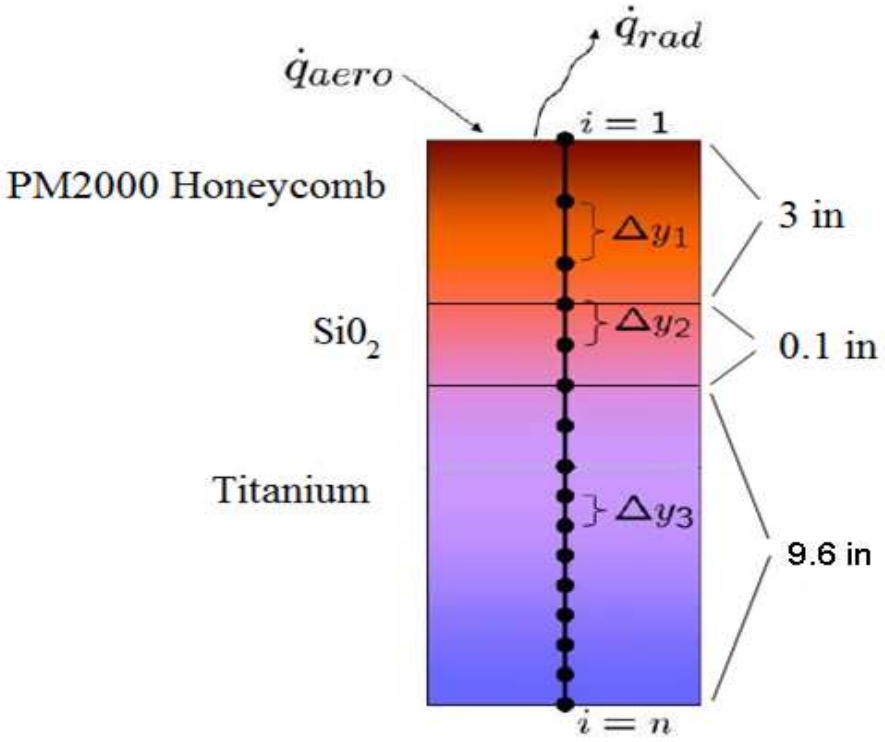

Figure 42: TPS Nodal Distribution

Bolender, et. al. modeled aerodynamic heating at a single point of an assumed stack of materials for the TPS with an aim to optimize the trajectories that mini-

mized the temperature in fuel tank. [140] gave the method to estimate structural dynamics for mode shapes of the vehicle based on mass distribution and the temperature profile over the fuselage.

Titanium . The nominal vehicle is 100 ft long. The associated beam model is assumed to be made of titanium (it acts as the structural core). It is 100 ft long, 9.6 inches high, and 1 ft wide (deep). This results in the nominal modal frequencies (at time t=0hr) $\omega_1 = 21.02$ rad/sec, $\omega_2 = 50.87$ rad/sec, $\omega_3 = 100.97$ rad/sec. When the height is reduced to 6 inches, we obtain $\omega_1 = 11.70$ rad/sec, $\omega_2 = 27.59$ rad/sec, $\omega_3 = 54.20$ rad/sec. Above values are valid for the old engine.

For new engine the fundamental modal frequencies will be as follows . $\omega_1 = 20.94$ rad/sec, $\omega_2 = 50.58$ rad/sec, $\omega_3 = 100.49$ rad/sec. When the height is reduced to 6 inches, we obtain $\omega_1 = 11.66$ rad/sec, $\omega_2 = 27.41$ rad/sec, $\omega_3 = 53.92$ rad/sec.

Future work will examine vehicle mass-flexibility-control trade studies [3].

Numerical Issues

1. Each layer has equally spaced nodes and different grid size in each material.
2. Structure is discretized into 14 layers (15 nodes).(PM2000=4; SiO_2=3; Titanium=7;)

Heating Issues. Heating issues for hypersonic vehicles are so severe that the design of hypersonic vehicles is often dictated/dominated by heating considerations [1].

Assumptions

For our purposes, the following assumptions were made:

Structural Assumptions. (1) vehicle modeled as a flat plate - 100 ft long, 0.8 ft high, 1 ft deep, (2)titanium beam is insulated at its innermost surface to maintain temperature of cryogenic fuel (adiabatic inner most wall assumption), (3) heat

Table 6.5: Material Properties

Material Property	PM2000	SiO_2	Titanium
Conductivity (k)($BTU/ft.s.R$)	$4.44 * 10^{-3}$	$5.28 * 10^{-6}$	$2.89 * 10^{-3}$
Density (ρ) (lb_m/ft^3)	449.28	6	277
Specific Heat c_p (BTU/lb_mR)	0.184	0.18	0.225
Diffusivity (α)	$0.5371 * 10^{-4}$	$0.0489 * 10^{-4}$	$0.4637 * 10^{-4}$
Emissivity	0.7	-	0.6
Max. Operating Temperature(R)	2650	2400 (melting: 3600)	1260
Thickness1 (l)(ft)	0.25	0.0083	0.8
Pole1 $-\alpha(\frac{\pi}{l})^2$	0.0085	0.6948	$7.1508 * 10^{-4}$
Settling time1 (s)	589.5	7.1	6992.2
Thickness2 (ft)(l)	0.0833	0.0083	0.5
Pole2 $-\alpha(\frac{\pi}{l})^2$	0.0763	0.6948	0.0018
Settling time2 (s)	65.5	7.1	2731.3

transfer through fasteners, spars, and stringers is neglecting, (4) thermal properties (k, c_p, ρ) within each TPS material remains constant, (5) contact resistances between layers is zero, (6) temperature of structure at time t=0 is T_0 = 559.67($^\circ R$) (100$^\circ F$), (7) PM2000 and SiO_2 portions of TPS are massless; i.e. do not impact total vehicle mass.

Propulsion Assumptions. No fuel consumption (linear fuel depletion in model not used). This will be addressed in future work.

Aero-Thermo Assumptions. (1) perfect gas behavior, (2) symmetric flow over vehicle (similar aero properties at top and bottom), (2) boundary layer is fully turbulent from the leading edge of the plate, (3) convective-radiative heat transfer occurs at outer skin of PM2000, (exposed to free stream), (5) vehicle is flying at zero AOA, (6) oblique shock results in flow turn angle of 3°, (4) skin friction formulae used for incompressible turbulent flow over flat plate, (5) stagnation heating at the nose is not taken into account.

6.5 *Heating study for Nominal Model*

The study is done for Nominal model, Nominal model has:

- the new engine (i.e. 1/0.15 ft internal nozzle area ratio, 4.5ft engine nozzle exit area per unit width, 4.5ft assume this is the height of the engine inlet, Ad 0.15ft),
- actual plume based on exit shock pressure,
- TPS structure as Ti=9.6",SiO_2=.1",PM2000=3",
- flight dependent net convective heat flux input with convecto-radiative cooling.
- Mach8, Altitude 85kft, 2hour of sustained flight.

Table 6.6: Fundamental Freq vs Time

	$\dot{q}_{conv} = var$			$\dot{q}_{conv} = 15BTU/ft^2s$		
Time,hr	ω_1	ω_2	ω_3	ω_1	ω_2	ω_3
0	20.94	50.58	100.49	20.94	50.58	100.49
0.5	20.91	50.49	100.31	20.90	50.46	100.25
1.0	20.80	50.30	99.81	20.78	50.19	99.70
2.0	20.63	49.82	98.97	20.51	49.54	98.41

Table 6.7: % drop in fundamental Freq wrt time t=0 sec.

	$\dot{q}_{conv} = var$			$\dot{q}_{conv} = 15BTU/ft^2s$		
Time,hr	% ω_1 drop	% ω_2 drop	% ω_3 drop	% ω_1 drop	% ω_2 drop	% ω_3 drop
0	0	0	0	0	0	0
0.5	-0.18	-0.18	-0.18	-0.23	-0.23	-0.23
1.0	-0.56	-0.56	-0.56	-0.78	-0.78	-0.78
2.0	-1.51	-1.51	-1.51	-2.06	-2.06	-2.06

From table 6.6, 6.7

- Time escalating heating for 2 hr forces 2% drop in the fundamental frequency.

Figure 43 shows the variation of flight dependent convective heat flux input to the system through after shock properties. TPS experiences radiative heat transmission at the skin of the composite structure.

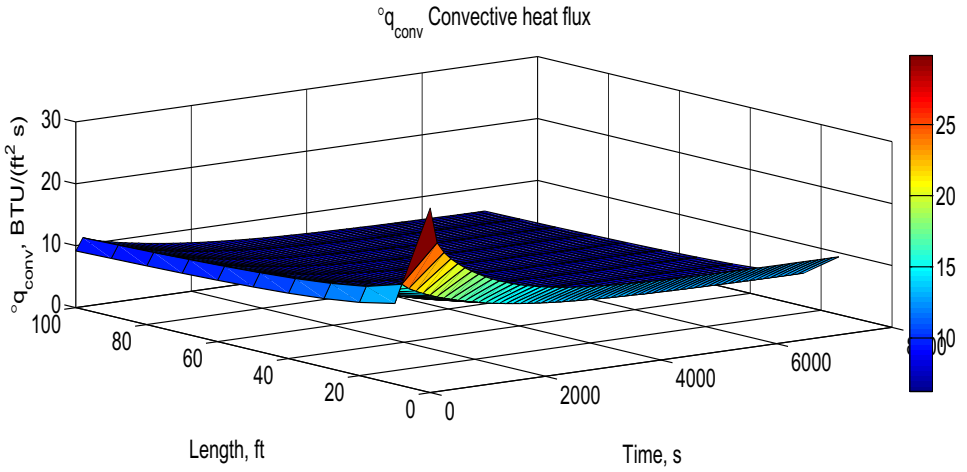

a). Convective Heat Flux vs Length and Time

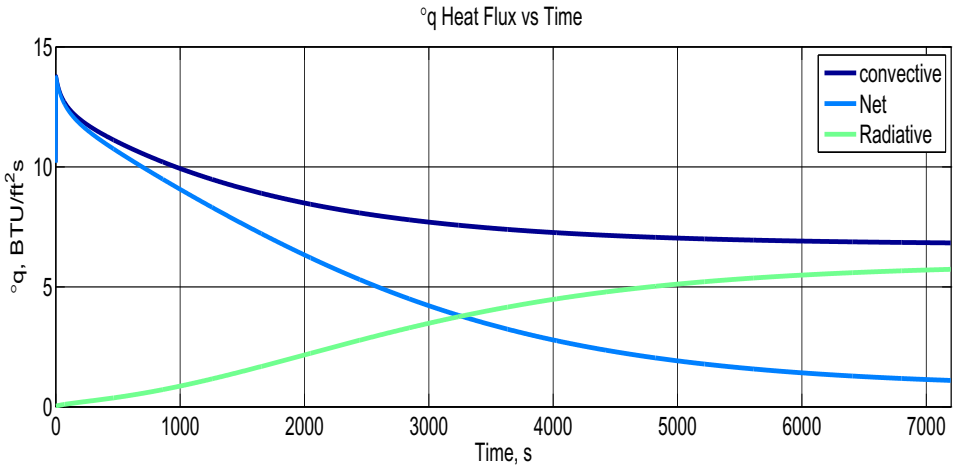

b). Heat Flux vs Time

Figure 43: Heat Flux Distribution

1. Figure 43(a), 2D heat distribution indicates peak heat input is at the nose of the vehicle,
2. Figure 43(a,b), heat flux decreases exponentially along the length of the vehicle as well as with exposure time,
3. Figure 43(b), after 2hr of flight, heat radiation and convective heat settle down to their steady state values.

In figure 44 average titanium temperature and skin temperature variation w.r.t to time and length along the beam is shown .

1. figure 44(a), sharp peak at the nose due to extreme heat flux input,

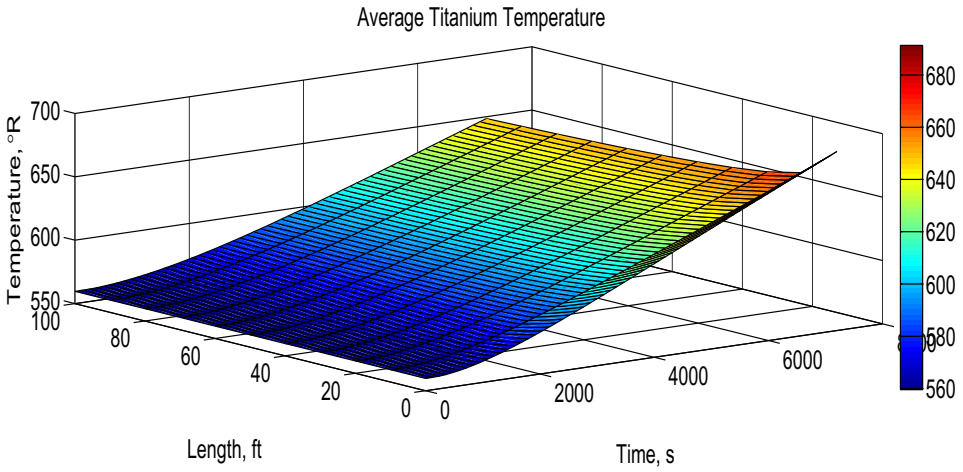

a). Average Titanium temperature

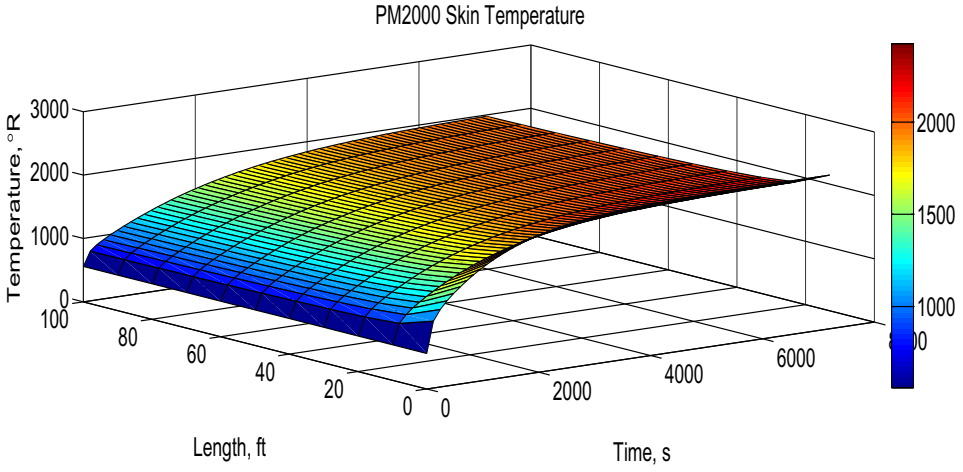

b). PM2000 Skin Temperature

Figure 44: TPS Temperature Distribution

2. figure 44(a),temperature rises uniformly along the length and with time.
3. for constant $\dot{q}_{conv}$ = 15 BTU/ft^2s, rise in average titanium temperature is 129R, outer skin temperature is 2534.2R,
4. for flight dependent $\dot{q}_{conv}$, rise in average titanium temperature is 94R, outer skin temperature is 2036.4R.

Figure 45 gives the temperature distribution along the depth of the 3 layered tps composite.

1. Figure 45, PM2000 do not experience high temperature rise, it acts as metallic

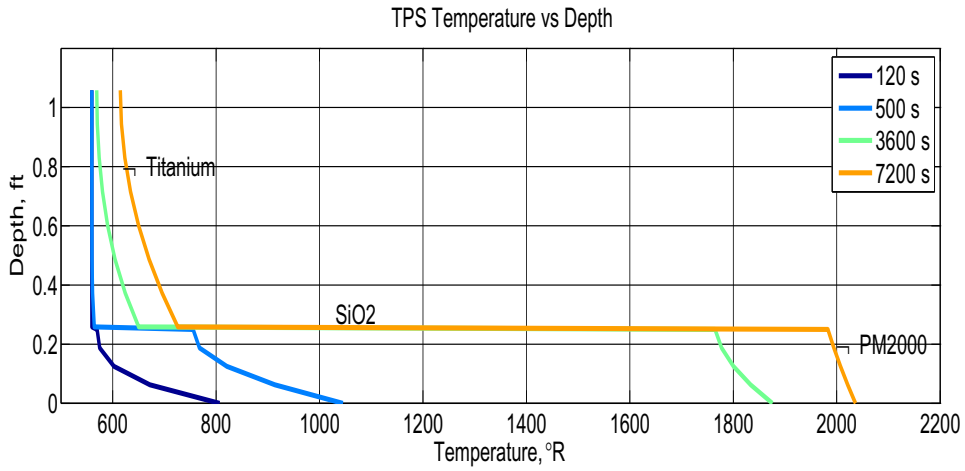

Figure 45: Temperature vs depth

conductor allowing all heat to pass through itself,

2. Figure 45, SiO_2 , provides the significant temperature drop. It is the insulation that keeps the Titanium structure under acceptable limits,
3. Figure 45, Titanium by itself is the structural core and is the thickest of all.

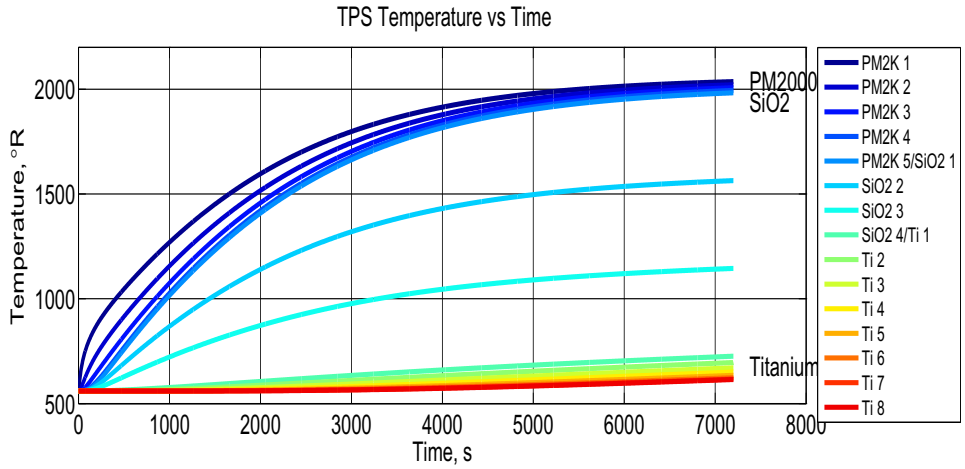

Figure 46: Temperature vs Time for TPS layers at length 50ft

Figure 46 depicts the temperature in all the layers of the tps.

6.6 Flexibility Effects

Forebody flexing can result in bow shock wave and engine inlet oscillations. This can impact the available thrust, stability and achievable performance. Flexibility can be caused by change in mass of vehicle including structure and the fuel and prolonged heating. Below is the trade study of dynamic and static properties for the variation in elasticity (EI). Reducing fundamental frequency pertains to increasing elasticity.

Summary of Elastic effects

Case 1. With TPS (PM2k 3, SiO2 0.1Titanium 9.6), Flight dependent heat flux input : [Elasticity Ratio varied from 0.3 to 1.5 , 2hr of sustained flight, Mach-8, Altitude-85kft.

6.6.1 Temperature vs Elasticity

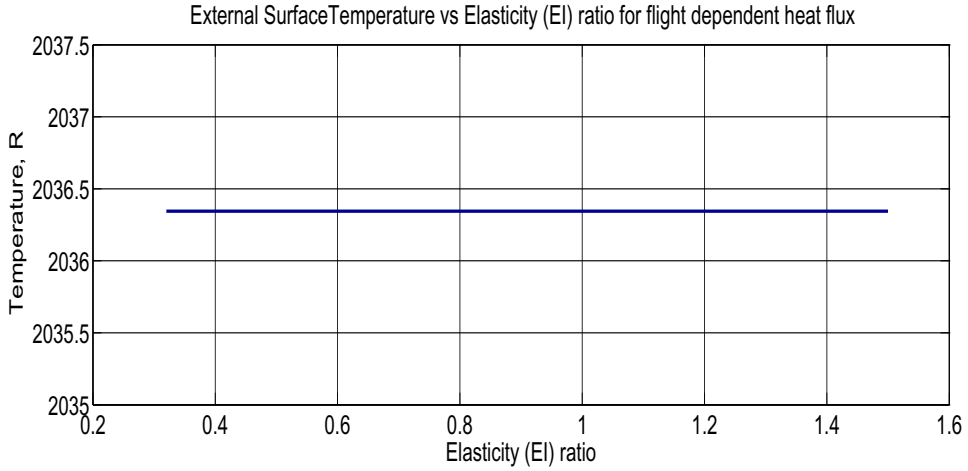

Figure 47: PM2000 Surface Temperature Vs Percent change in Elasticity (EI)

The figure 47 shows surface temperature remains unchanged for change in elasticity (EI).

The figure 48 shows average titanium temperature remains unchanged for change in elasticity (EI).

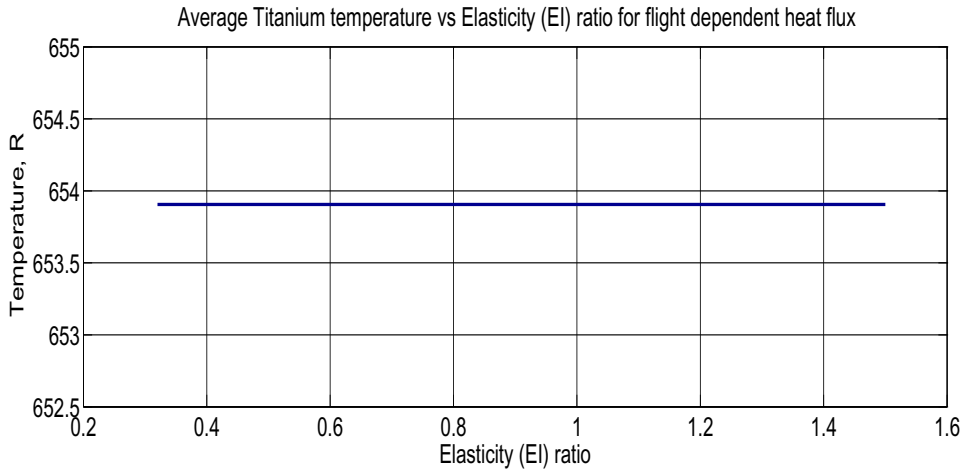

Figure 48: Average Titanium Temperature Vs Percent change in Elasticity (EI)

6.6.2 Fundamental frequency vs Elasticity

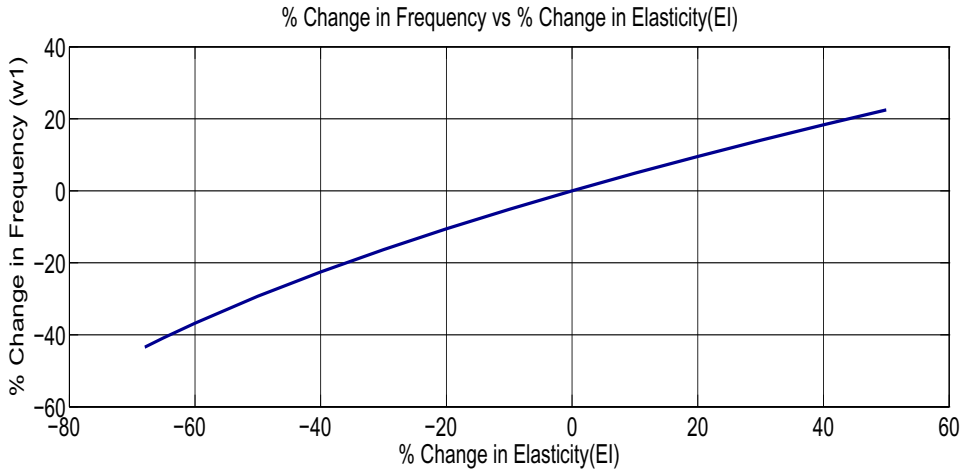

Figure 49: Percent Change in first fundamental frequency ($\omega 1$) wrt percent change in Elasticity (EI)

The figure 49 shows the variation of fundamental frequency w.r.t. the change in elasticity (EI). It is seen that:

- First fundamental frequency rises with the slope of 0.5 for EI variation,

6.6.3 Dynamic Flexibility Effects for change in EI

Following is the study for effect of elasticity variation on dynamic properties of the model. The design has Titanium=9.6", SiO_2=0.1", PM2000 = 3". The mass of TPS

is assumed to be kept constant.

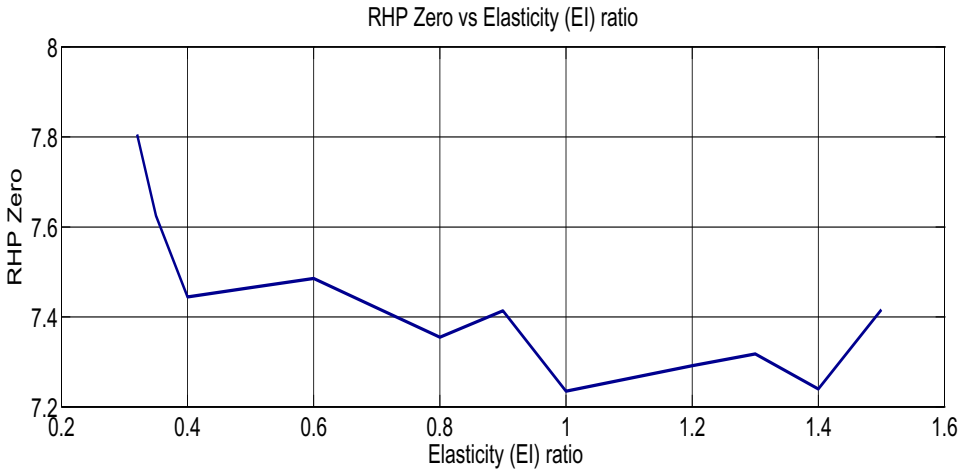

a. RHP Zero variation for change in EI (elasticity)

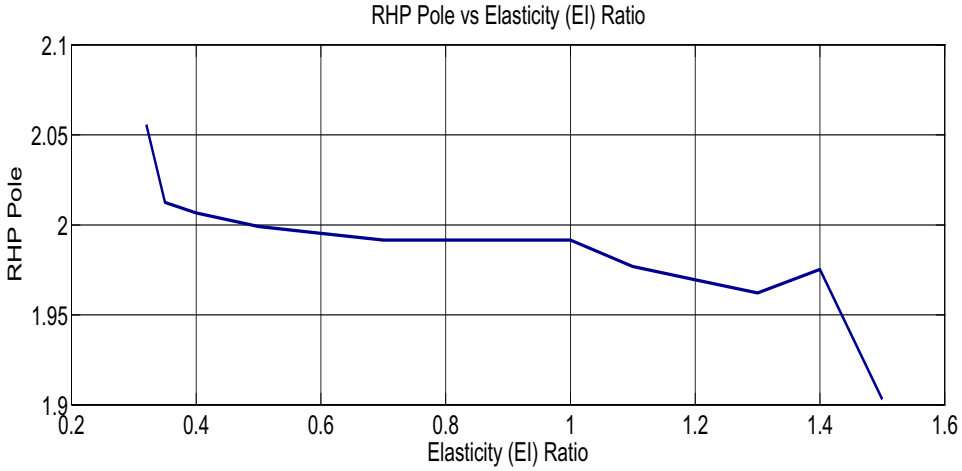

a. RHP Pole variation for change in EI (elasticity)

Figure 50: RHP Pole and Zero variation for change in EI (elasticity)

The figure 50 shows the movement of poles and zeros for change in Elasticity ratio.

- RHP poles and zeros move slowly closer to origin.
- Large variation in Elasticity brings no big change in the rhp pole and zeros.
- Dynamic properties are unaffected by Elasticity (EI).

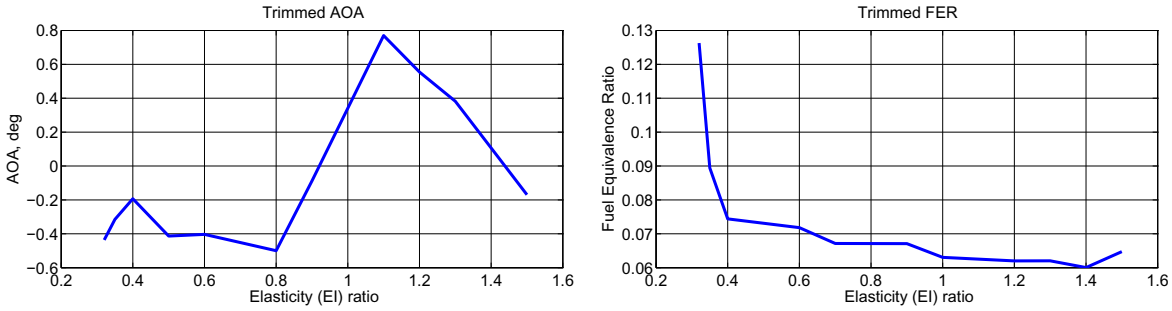

a). AOA (Angle of Attack)

b). FER (Fuel Equivalence ratio)

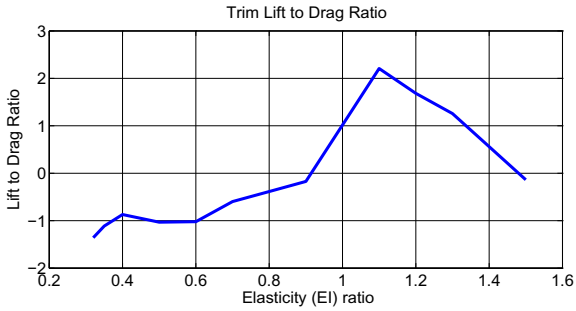

c). L2D ratio (Lift to Drag Ratio)

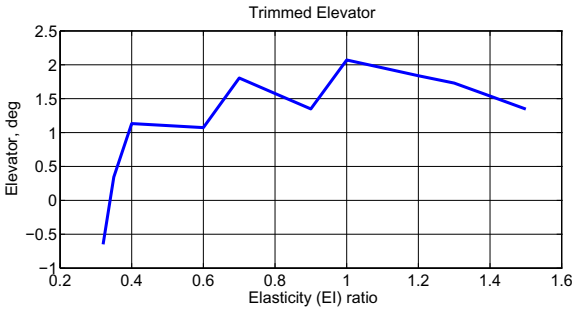

d). Elevator

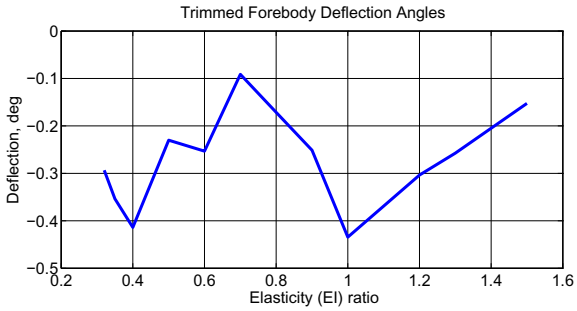

e). Forebody Deflection

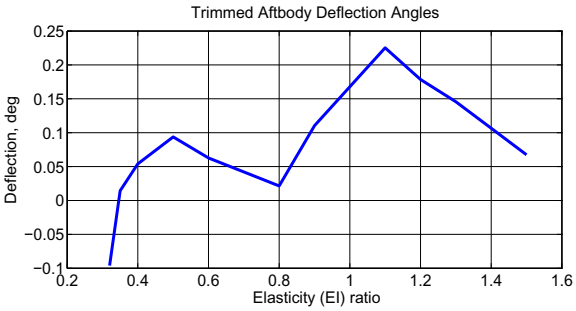

f). Aftbody Deflection

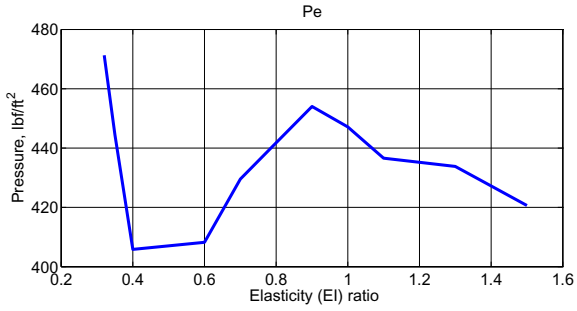

g).Engine Exit Pressure

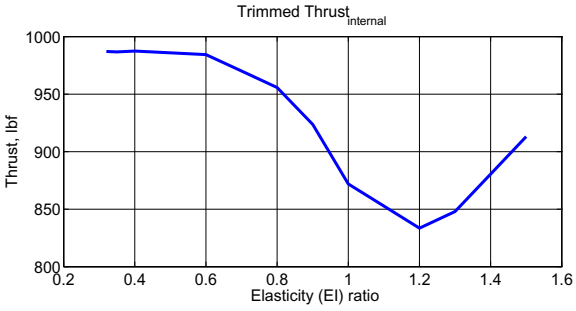

h). Internal Thrust

Figure 51: Static properties: AOA, FER, Elevator, Forebody Deflection, Aftbody Deflection, L2D Ratio, Internal Thrust, Exit Pressure, for variation of elasticity (EI)

6.6.4 Static Flexibility Effects for change in EI

From figure 51

- AOA, Aft-body deflection, Fore-body deflection, Elevator, L2D ratio : increase with increasing mass ratio greater than 0.4
- Pe, FER, External thrust decreases with increasing EI ratio (EIR greater than 0.4).
- Large variation in Elasticity brings no big change in the static properties.
- Static properties are unaffected by Elasticity (EI).

Overview of Mass fraction. TPS mass fractions for hypervelocity reentry [16, 141] table 5.1

Table 6.8: TPS Mass Fraction

Vehicle	TPS MF
Earth Re-entry	14%
Venus Re-entry	13%
Jupiter Re-entry	50%

From table 6.8

- Mass fraction is about 14% for space shuttles reentering earth's orbit at hypervelocity.
- Hypersonic vehicle always remain within atmospheric environment, hence do not experience the same heat load as done by re-entry probes.

Table 6.9: leading edge heat fluxes [1]

Vehicle	Heat Flux(Btu/ft^2s)
aerospace plane (ascent)	572
aerospace plane (reentry)	88
Space shuttle orbitor (entry)	60

$$TPSMF = 0.091 * (heatload)^{0.51575} \tag{6.26}$$

Equation 6.26 indiactes that TPS mass fraction for entry probe is the function of total heat load [16]

Aztec tsto vehicle [142] flies at mach 8, 2000psf dynamic pressure.

- A TSTO hypersonic vehicle design concept has gross lift off weight (GLOW) of 690,000lbs, with provision of TPS mass of only 6900 lbs (1% of GLOW),
- dry weight of second stage is 56000lbs hence TPS mass fraction is 12%.

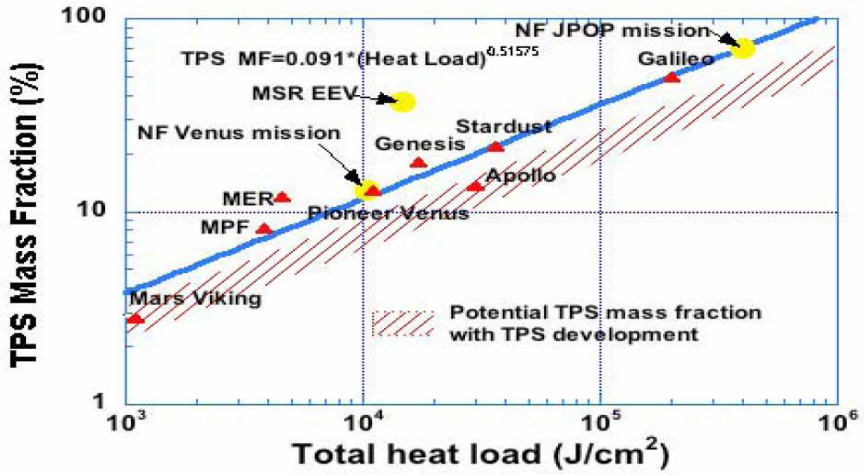

Figure 52: Ablative TPS mass fraction [16]

TPS Heat and Mass effects .

1. At 10% phase of scramjet mode mass of structure(including fuel tanks, pay-load, engine, fore-system, aft-system and load bearing titanium structure) = 193.71 slug (311,582lbs)(1 slug=32.17lbs).
2. Mass addition: mass of the vehicle is varied by 40% above and below its nominal value.

Summary of Mass variation effects

Case 2. With TPS (PM2k 3, SiO2 0.1Titanium 9.6), Flight dependent heat flux input : [Mass Ratio varied from 0.6 to 1.4 , 2hr of sustained flight, Mach-8, Altitude-85kft.]

6.7.1 Temperature vs Mass

The figure 53 shows surface temperature remains unchanged for change in Mass ratio.

The figure 54 shows average titanium temperature remains unchanged for change in Mass.

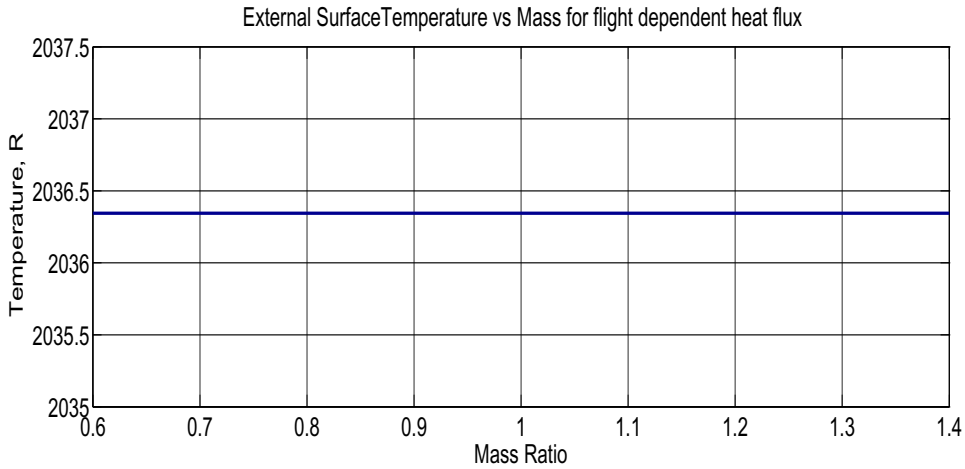

Figure 53: PM2000 Surface Temperature Vs Mass ratio

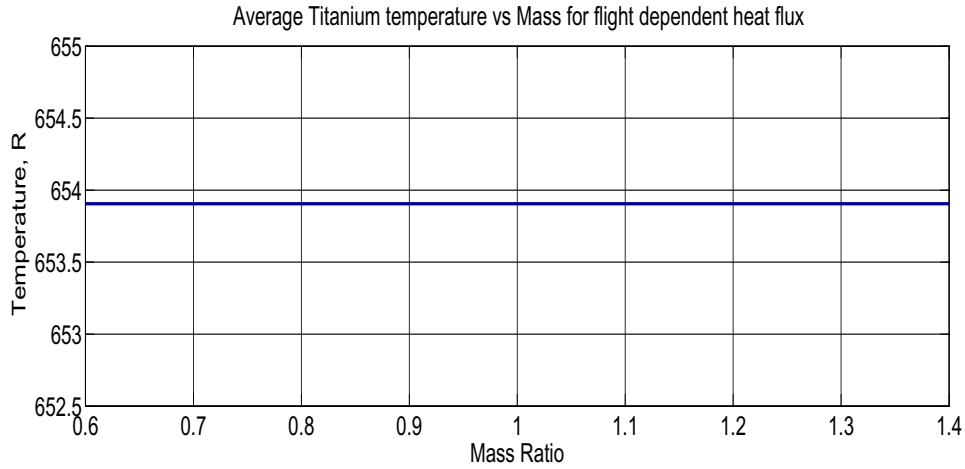

Figure 54: Average Titanium Temperature Vs Mass ratio

6.7.2 Fundamental frequency vs Elasticity for Mass Effects

The figure 55 shows the variation of fundamental frequency and percent change in elasticity (EI) w.r.t. Mass Ratio. It is seen that:

- Neither first fundamental frequency nor Elasticity is affected by structural Mass variation,

6.7.3 Dynamic Effects for change in Mass

Following is the study for effect of structural Mass variation on dynamic properties of the model.

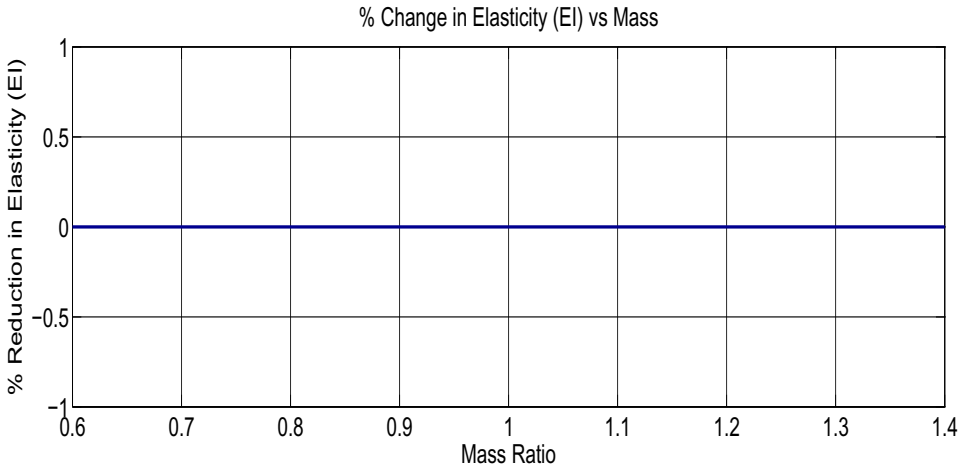

a. Percent Change in Elasticity (EI) w.r.t Mass Ratio

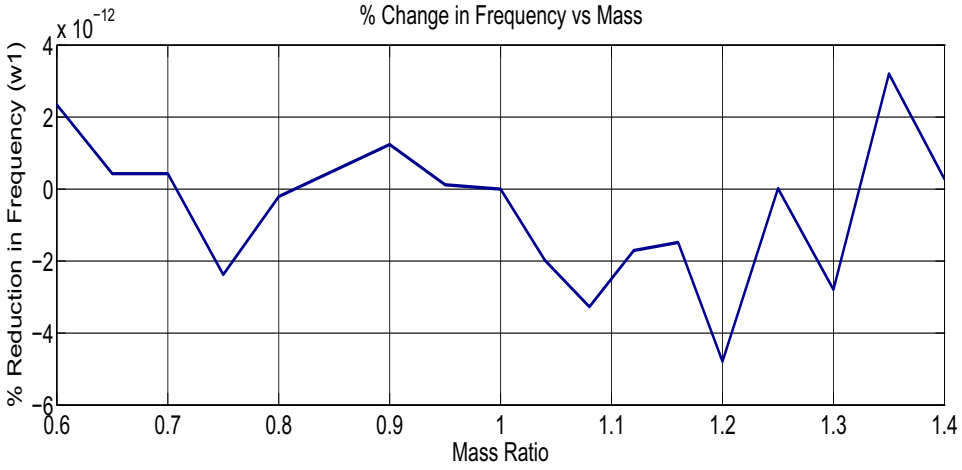

b. Percent Change in Fundamental frequency ($\omega 1$) w.r.t Mass Ratio

Figure 55: Percent Change in first fundamental frequency ($\omega 1$) and percent change in Elasticity (EI) for variation in Structural Mass

The figure 56 shows the movement of poles and zeros for change in Mass ratio.

- 10% rise in mass RHP pole moves quickly to origin,
- With 30% decrease in mass RHP pole rise by 100%,
- Increasing mass RHP zero do not change significantly,
- With 40% decrease in mass RHP zero reduces by 50%.

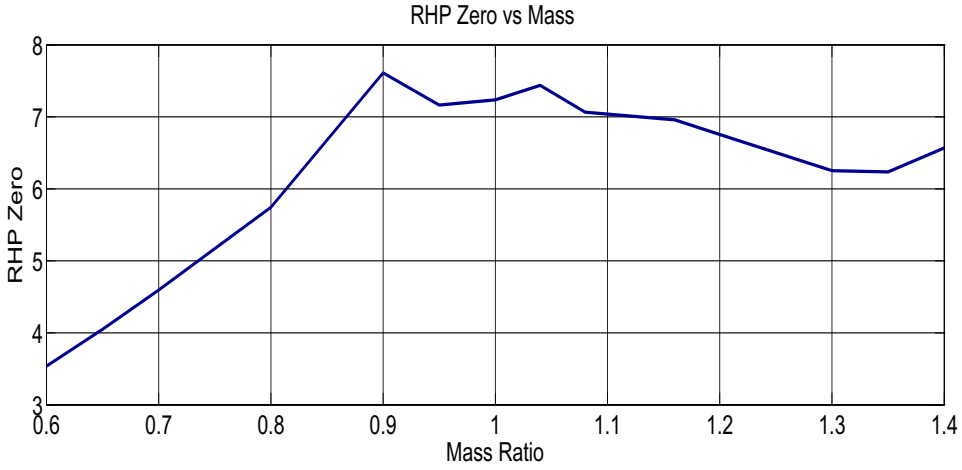

a. RHP Zero variation for change in Mass

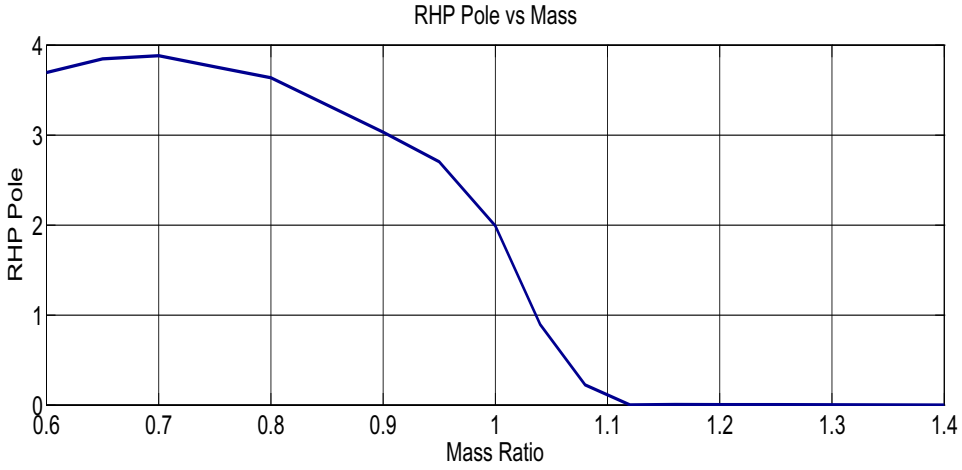

a. RHP Pole variation for change in Mass

Figure 56: RHP Pole and Zero variation for change in Mass

6.7.4 Static Effects for change in Mass

From figure 57

- AOA, FER, Aft-body deflection, Elevator, L2D ratio , exit pressure, external thrust : decrease with increasing mass ratio greater than 0.8
- Forebody deflection increases with increasing mass ratio (MR greater than 0.8).

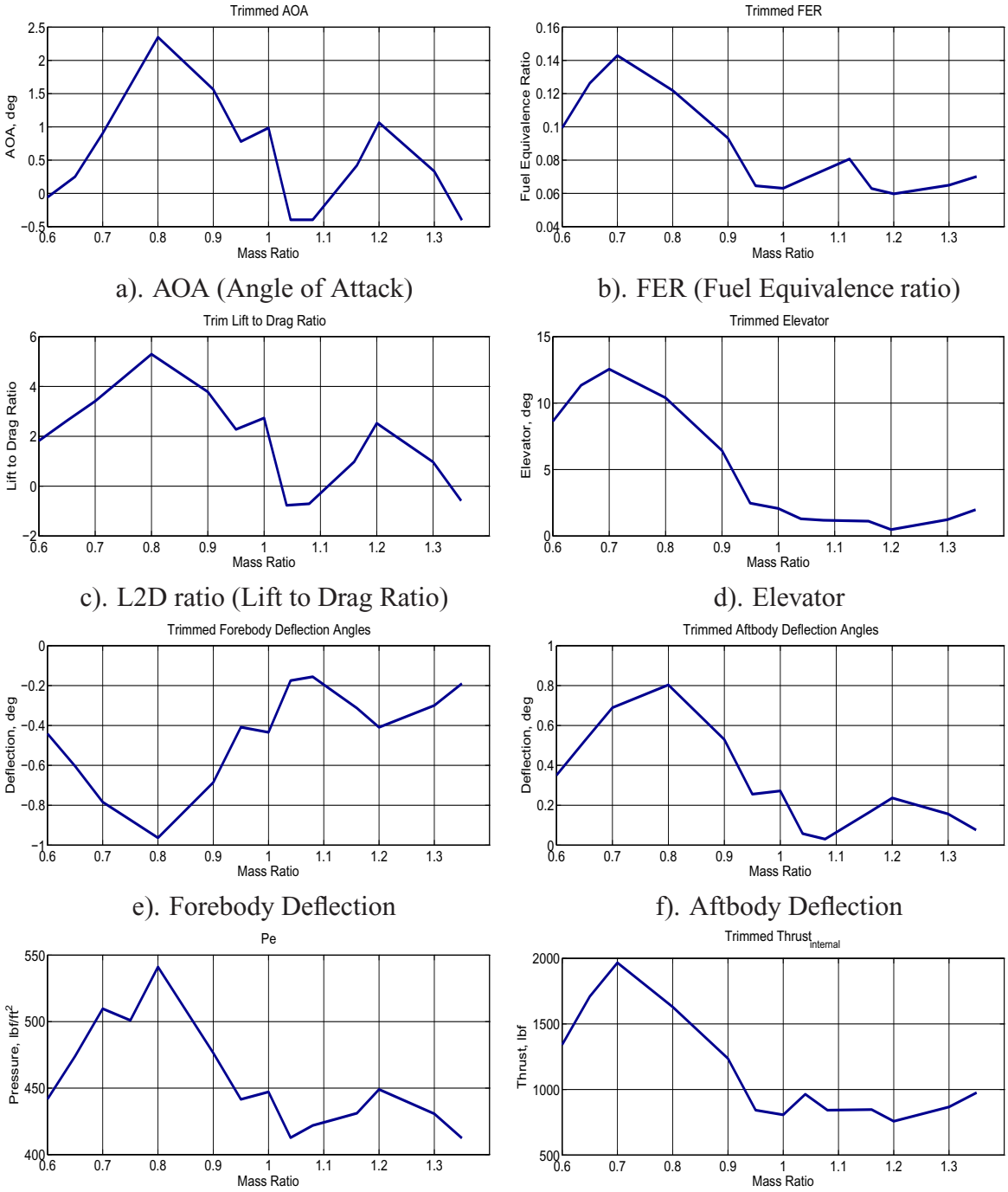

a). AOA (Angle of Attack)

b). FER (Fuel Equivalence ratio)

c). L2D ratio (Lift to Drag Ratio)

d). Elevator

e). Forebody Deflection

f). Aftbody Deflection

g).Engine Exit Pressure

h). Internal Thrust

Figure 57: Static properties: AOA, FER, Elevator, Forebody Deflection, Aftbody Deflection, L2D Ratio, Internal Thrust, Exit Pressure, for variation of Mass

6.8 Structural Prolonged Heating Effects

Prolonged Heating Effects for for upto 20hr of aerodynamic heating for PM2k 3, SiO2 0.1, Titanium 9.6:

1. With TPS, Flight dependent heat flux input.
2. Without TPS, Flight dependent heat flux input.
3. With TPS, constant heat flux input ($15 BTU/ft^2 s$).
4. Without TPS, constant heat flux input (15BTU/ft2s).

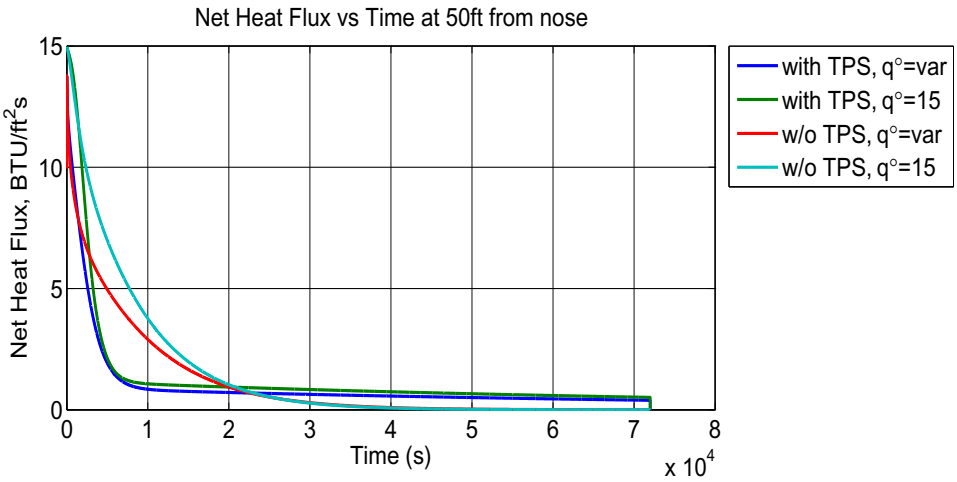

Figure 58: Net heat flux input for 20hr to the TPS surface at 50ft from nose

The figure 58 shows the flight dependent net heat flux input to the surface of TPS for 20hrs of sustained flight. Net heat flux is the function of current wall temperature Tw (radiative heat loss and convective heat input). It is seen that:

1. With TPS system involved: radiative heat flux is large and hence net heat flux drops suddenly to 0.8BTU/ft^{2}s in 2 hr and then stays steady with very low rate of decrement.
2. Without TPS, Titanium is exposed to the outer environment, taking 8hr to reach steady state value of net heat flux input of 0 BTU/ft^{2}s.
3. Peak value of heat input with TPS and without TPS is 13.8 BTU/ft^{2}s

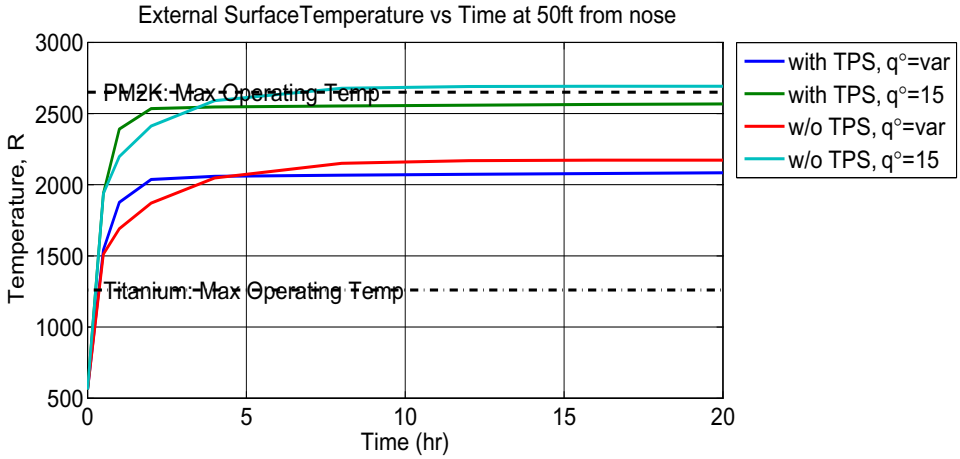

Figure 59: External surface temperature for 20hr at 50ft from nose

The figure 59 shows the surface temperature of TPS for flight dependent net heat flux input for 20hrs of sustained flight. It is seen that:

1. Titanium maximum operating temperature is 1260R, without TPS ,when Titanium is exposed to the external environment ,it takes 0.2hr (for constant heat flux) and .3hr (for flight dependent heat flux) of sustained flight to reach its limit of operability.
2. PM2000 maximum operating temperature is 2650R, with TPS ,when PM2000 is exposed to the external environment ,it never reaches its limit of operability..

The figure 60 shows the average titanium temperature distribution of TPS for flight dependent net heat flux input after 20hrs of sustained flight. It is seen that:

1. PM2000 maximum operating temperature is 2650R, with TPS ,when PM2000 is exposed to the external environment ,average titanium temperature reaches its limit of operability after 15hr (given flight dependent heat flux) and 10.5hr (given constant dependent heat flux).
2. Titanium maximum operating temperature is 1260R, without TPS ,when Titanium is exposed to the external environment given constant heat flux its takes

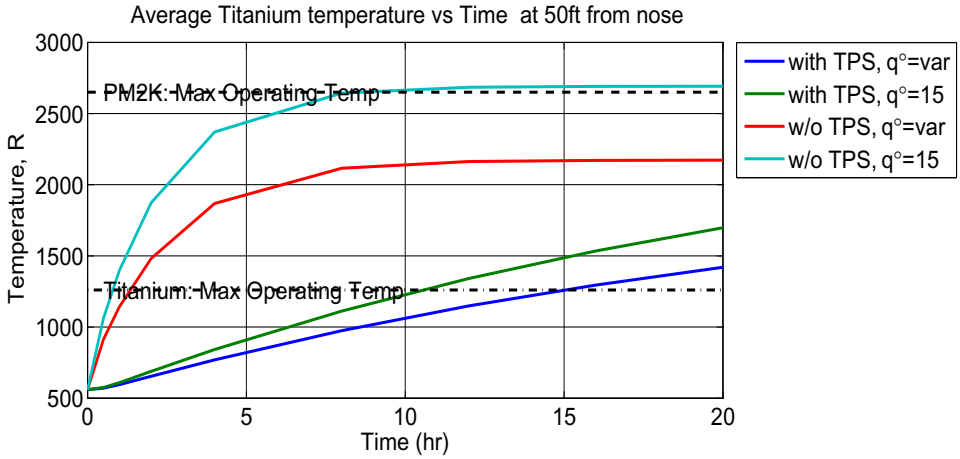

Figure 60: Average Titanium temperature for 20hr at 50ft from nose

0.8hr to reach its limit, and with flight dependent heat flux it takes 1.3hr.

6.8.1 Fundamental frequency vs Elasticity for prolonged heating

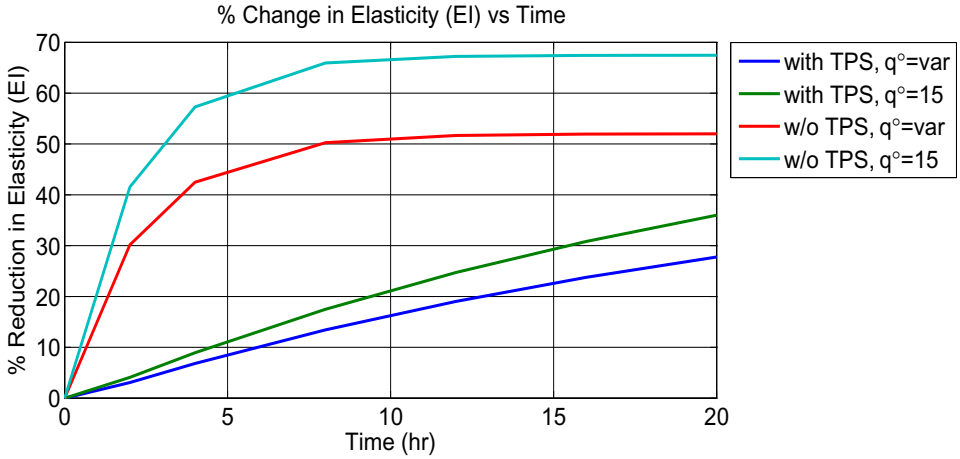

Figure 61: Percent change in elasticity (EI) for 20hr of heating

The figure 61, shows the change in elasticity EI of TPS for flight dependent net heat flux input after 20hrs of sustained flight. It is seen that:

1. w/o TPS: Titanium exposed to external aerodynamic heating, after 20hr of heating EI reduces by 27.8% for flight dependent heat flux, and by 36% for constant heat flux input.
2. With TPS: PM2000 exposed to external aerodynamic heating, after 20hr of

heating EI reduces by 52% for flight dependent heat flux, and by 67% for constant heat flux input.

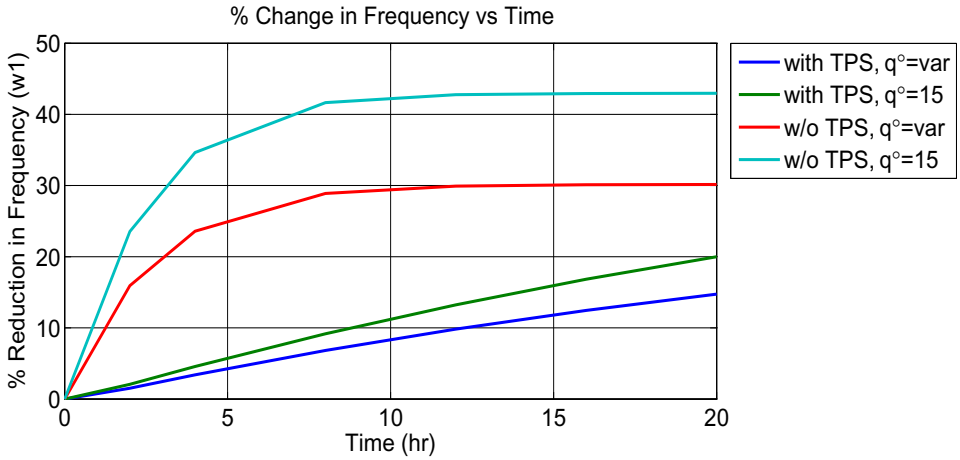

Figure 62: Percent change in fundamental frequency ($omega1$) for 20hr of heating

The figure 62, shows the change in fundamental frequency ($omega1$) of TPS for flight dependent net heat flux input after 20hrs of sustained flight. It is seen that:

1. w/o TPS: Titanium exposed to external aerodynamic heating, after 20hr of heating fundamental frequency reduces by 15% for flight dependent heat flux, and by 20% for constant heat flux input.
2. With TPS: PM2000 exposed to external aerodynamic heating, after 20hr of heating fundamental frequency reduces by 30% for flight dependent heat flux, and by 43% for constant heat flux input.

6.8.2 Dynamic Effects for Prolonged heating

Following is the study for effect of elasticity variation on dynamic properties of the model. The design has Titanium=9.6", SiO_2=0.1", PM2000 = 3". The mass of TPS is assumed to be kept constant.

The figure 63 shows the movement of poles and zeros for prolonged heating.

1. RHP zero after 20hr of flight is maximum (7.96) for constant heat flux and w/o TPS, and minimum (7.35) for constant heat flux with TPS.

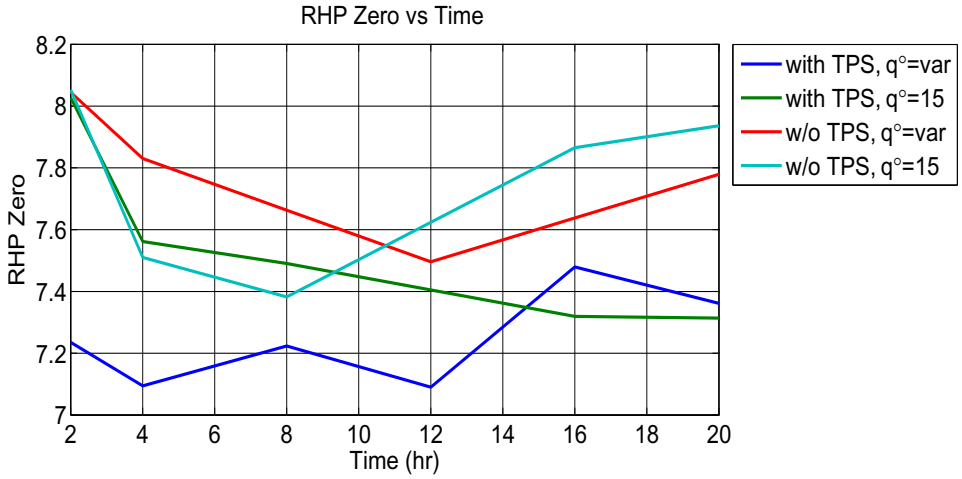

a. RHP Zero variation for prolonged heating

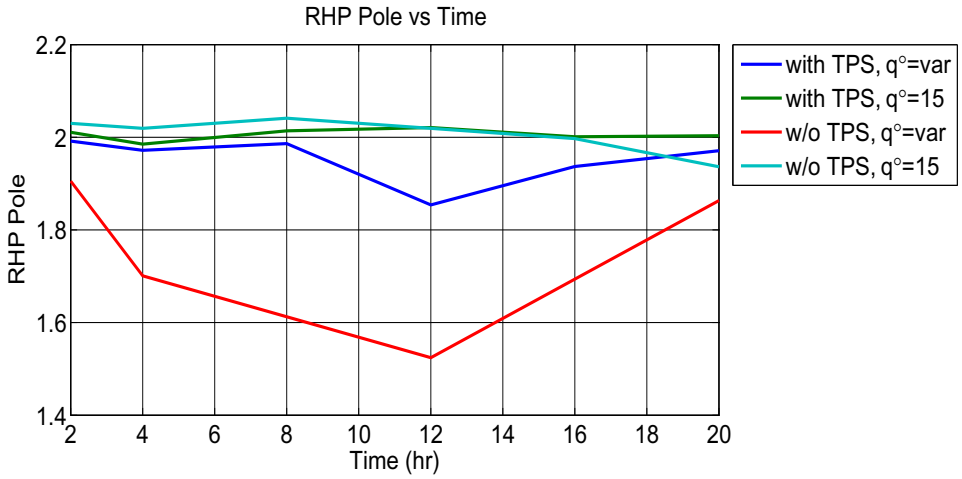

a. RHP Pole variation for prolonged heating

Figure 63: RHP Pole and Zero variation for prolonged heating

2. With TPS for both cases of heat flux input unstable zero converges closely to same value.
3. RHP pole do not change significantly over the 20hr of flight except for variable heat input without TPS.
4. RHP pole after 20hr of flight is maximum (2.12) for constant heat flux and w/o TPS, and minimum (1.58) for flight dependent heat flux w/o TPS.

The figure 64, shows the change in Zero-Pole ratio after 20hrs of sustained flight. It is seen that:

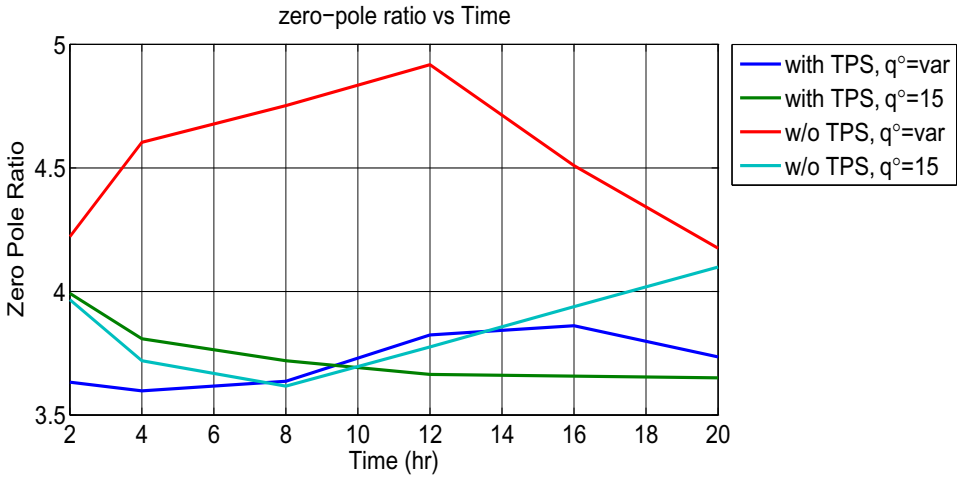

Figure 64: RHP Zero-Pole ratio for 20hr of heating

1. Z-P ratio do not change significantly over the 20hr of flight, except for variable heat input without TPS.
2. Z-P ratio, after 20hr of flight is maximum (4.25) for flight dependent heat flux w/o TPS, and minimum (3.7) for constant heat flux with TPS.

6.8.3 Static Flexibility Effects for change in EI

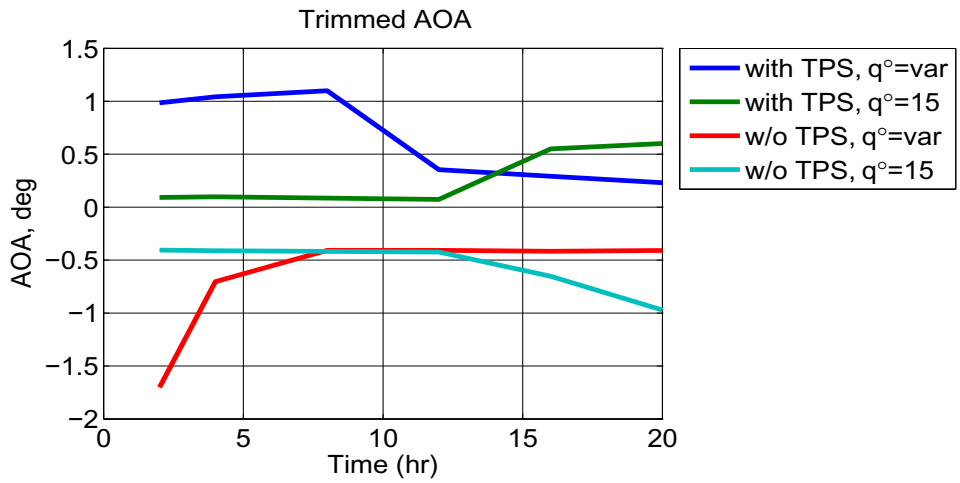

Figure 65: Angle of attack (AoA) for 20hr of heating

The figure 65, shows AoA after 20hrs of sustained flight. It is seen that:

1. AOA is negative without TPS (Titanium exposed to external environment aerodynamic high speed heating)

2. AOA is positive in case when TPS is present (PM2000 exposed to external environment aerodynamic high speed heating).

3. With TPS, variable heat input, AOA reduces by 75% (1 to .25)

4. With TPS, constant heat input, AOA rises by 140% (.25 to 0.6)

5. Without TPS, variable heat input, AOA rises by 64% (-1.7 to -0.6)

6. Without TPS, constant heat input, AOA reduces by 150% (-0.4 to -1.0)

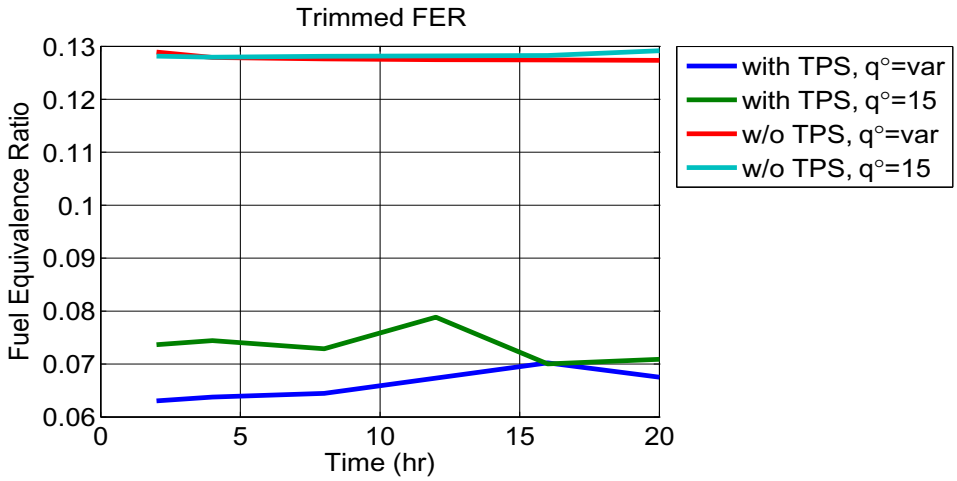

Figure 66: Fuel Equivalency Ratio (FER) for 20hr of heating

The figure 66, shows FER after 20hrs of sustained flight. It is seen that:

1. FER is high (0.13) without TPS (Titanium exposed to external environment aerodynamic high speed heating), it increases by 63% wrt w/o TPS (0.13)

2. FER is approximately 0.07 with TPS (PM2000 exposed to external environment aerodynamic high speed heating).

3. with and without TPS, FER do not change significantly over the 20hr flight.

The figure 67, shows Forebody deflection after 20hrs of sustained flight. It is seen that:

1. Forebody deflection caused by the change in fundamental mode follows decreasing pattern and is negative for all the cases after 20hr.

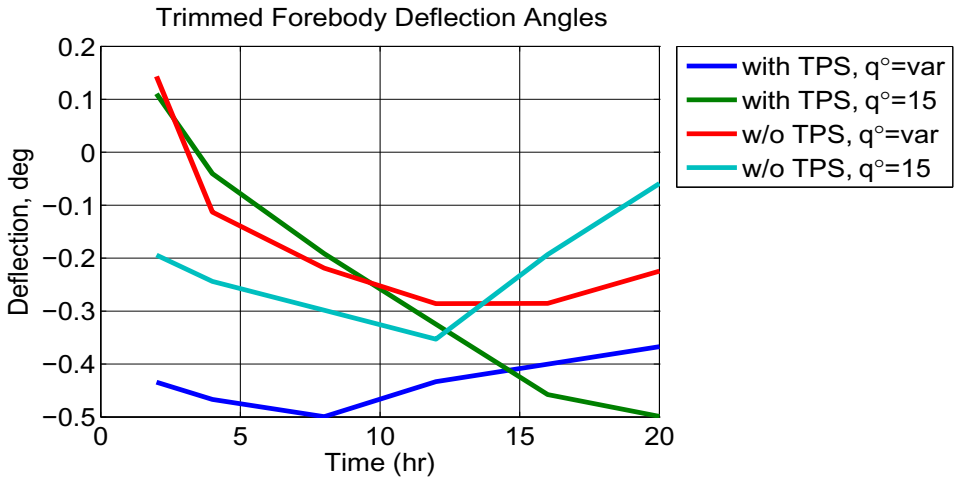

Figure 67: Forebody Deflection (Tau1) for 20hr of heating

2. For variable heat input, it follows upward trend: with TPS -0.44 to -0.38; w/o TPS 0.2 to -0.08

3. For constant heat input, it follows decreasing trend: with TPS 0.15 to -0.22; w/o TPS 0.1 to -0.5

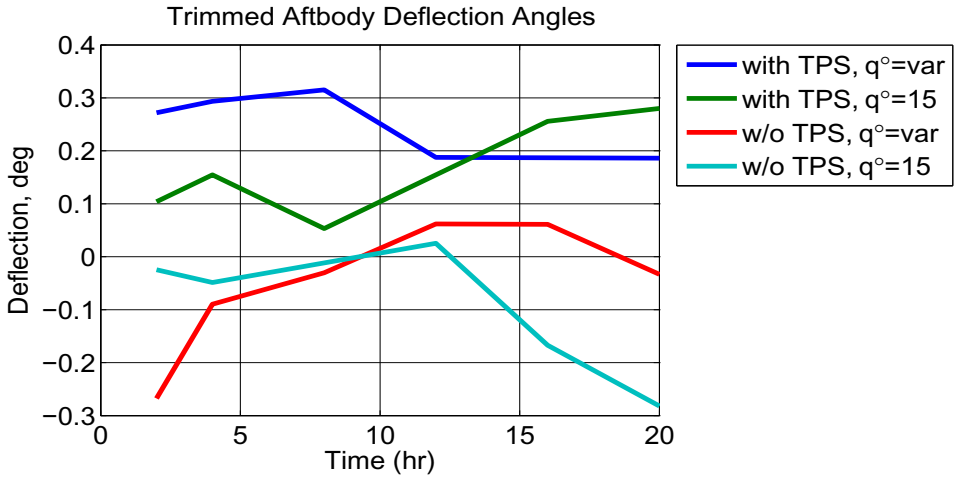

Figure 68: Aftbody Deflection (Tau2) for 20hr of heating

The figure 68, shows Aftbody deflection after 20hrs of sustained flight. It is seen that:

1. Aftbody deflection caused by the change in fundamental mode and heating decreases with increasing time for cases of flight dependent heat flux with

TPS (0.28 to 0.19); constant heat flux w/o TPS, -0.02 to -0.28

2. Aftbody deflection increases with increasing time for cases of constant heat flux with TPS (0.1 to 0.28); variable heat flux w/o TPS, -0.28 to -0.02

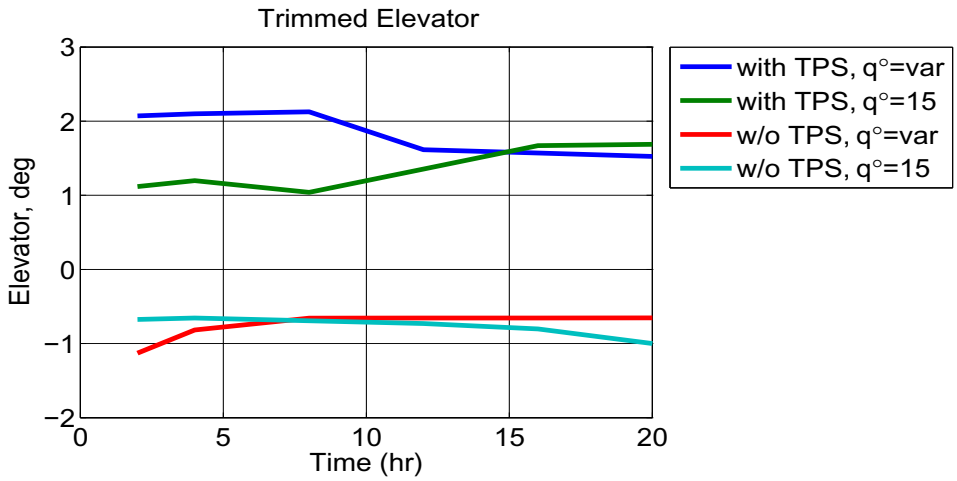

Figure 69: Elevator deflection for 20hr of heating

The figure 69, shows Elevator deflection after 20hrs of sustained flight. It is seen that:

1. Elevator control is negative (-0.7deg) without TPS, it increases by 63
2. Elevator control is 0.5deg with TPS.
3. It do not change significantly over the 20hr flight.
4. Elevator control decreases with increasing time for cases of flight dependent heat flux with TPS (2 to 1.5); constant heat flux w/o TPS, -0.65 to -1.0
5. Elevator control increases with increasing time for cases of constant heat flux with TPS (1.1 to 1.3); variable heat flux w/o TPS, -1.1 to -0.65

The figure 70, shows external thrust after 20hrs of sustained flight. It is seen that:

1. External thrust generated is low in case of TPS presence,
2. External thrust generated is high without TPS, it increases by 6.5

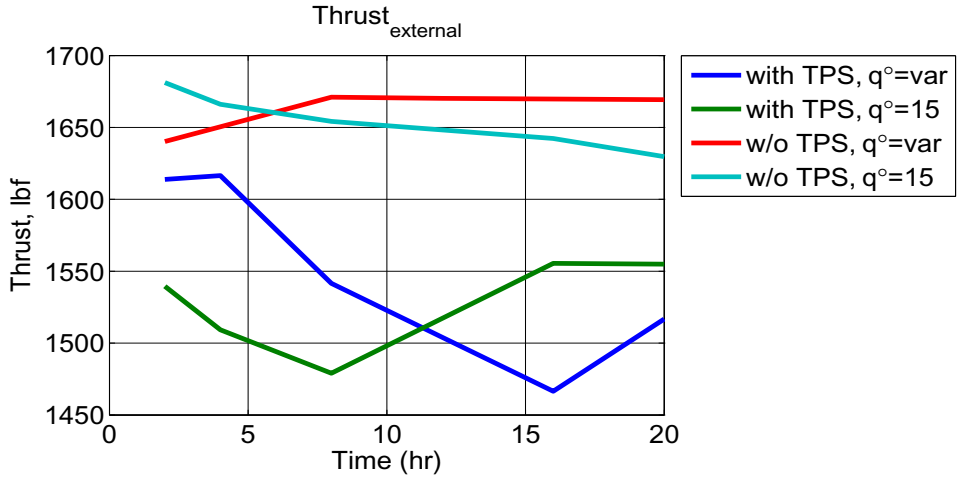

Figure 70: External Thrust for 20hr of heating

3. External thrust decreases with increasing time for cases of flight dependent heat flux with TPS constant heat flux w/o TPS.

4. External thrust increases with increasing time for cases of constant heat flux with TPS, variable heat flux w/o TPS.

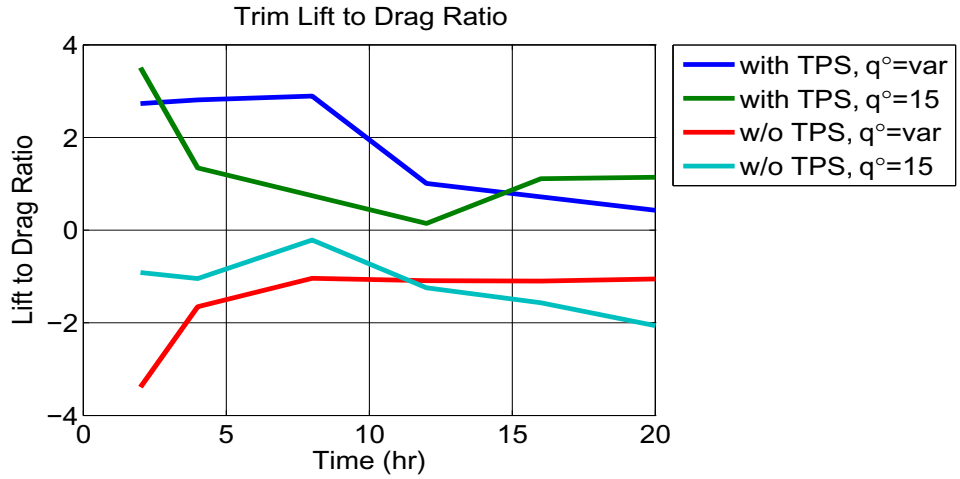

Figure 71: Lift to Drag Ratio for 20hr of heating

The figure 71, shows Lift to Drag ratio after 20hrs of sustained flight. It is seen that:

1. Lift to drag ratio is negative -1.0 when TPS is absent.

2. Lift to drag ratio is positive with TPS , it follows decreasing pattern with time . It drops by 30% after 2ohr of flight
3. Lift to drag ratio decreases with increasing time for cases of flight dependent heat flux with TPS constant heat flux w/o TPS.
4. Lift to drag ratio increases with increasing time for cases of constant heat flux with TPS, variable heat flux w/o TPS.

6.9 Structural Dimension Variation Effects

Study for reduced Titanium Thicknesses [9.6,9,8, 7,6,5,4] after 2hr of sustained flight:

1. With TPS (PM2k, SiO2, Titanium together), Flight dependent heat flux input:
2. Without TPS (only Titanium), Flight dependent heat flux input: $(15 BTU/ft^2 s)$.

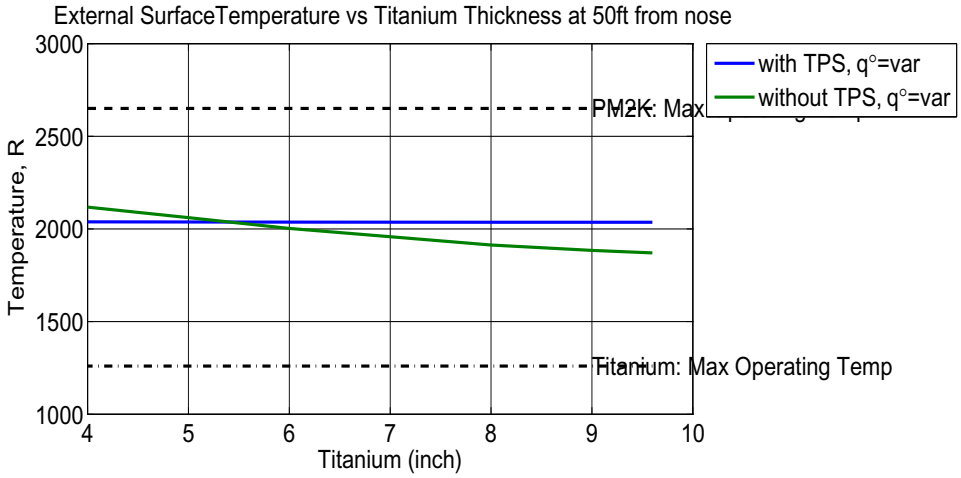

Figure 72: External surface temperature for 20hr at 50ft from nose

The figure 72 shows the surface temperature of TPS vs titanium thickness for 2hrs of sustained flight. It is seen that:

1. External Temperature with TPS (at PM2000) remains constant below its maximum operating temperature.
2. External Temperature w/o TPS (at Titanium surface) is increasing with decreasing thickness, but the temperature is always above Maximum operating temperature.

The figure 73 shows the average titanium temperature distribution vs titanium thickness of TPS 2hrs of sustained flight. It is seen that:

1. Average Titanium Temperature with TPS is below its maximum operating temperature and increases with very slow slope with decreasing thicknesses.

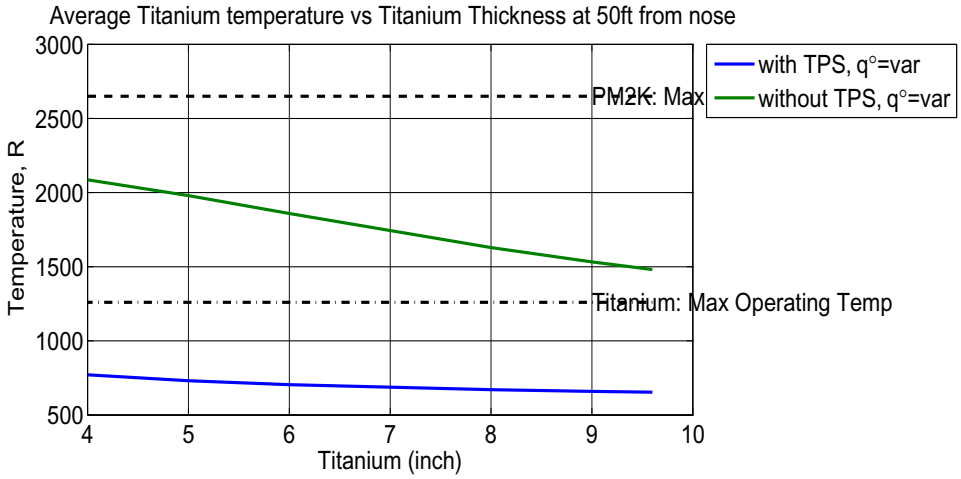

Figure 73: Average Titanium temperature for 20hr at 50ft from nose

2. Average Titanium Temperature w/o TPS is above its maximum operating temperature and increases linearly with decreasing thicknesses.

6.9.1 Fundamental frequency vs Elasticity for Titanium Thickness Variation

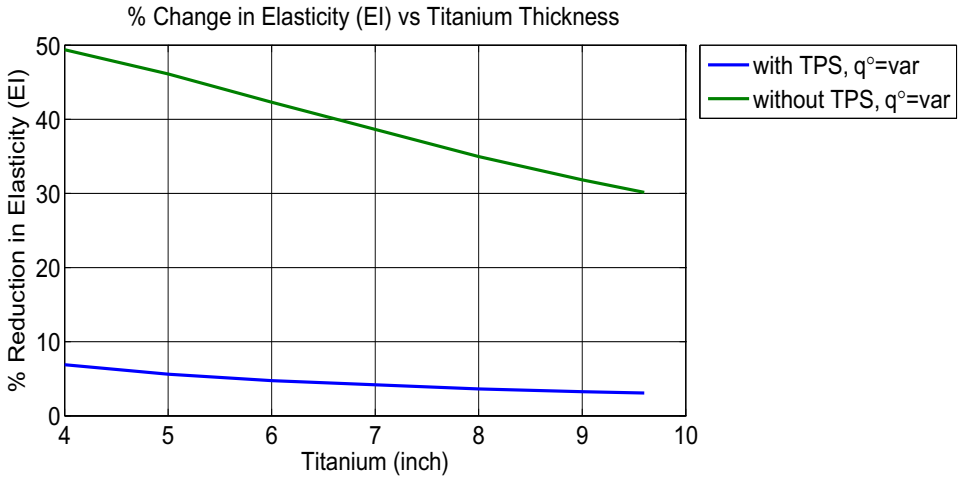

Figure 74: Percent change in elasticity(EI) vs Titanium for 2hr of heating

The figure 74, shows the change in elasticity EI of TPS vs titanium thickness for 2hrs of sustained flight. It is seen that:

1. Elasticity do not change significantly with increasing thicknesses for heating with TPS.

2. Elasticity increases linearly with decreasing thicknesses for heating without TPS.

3. It decreased by 30% without TPS at 9.6 thickness of Titanium.

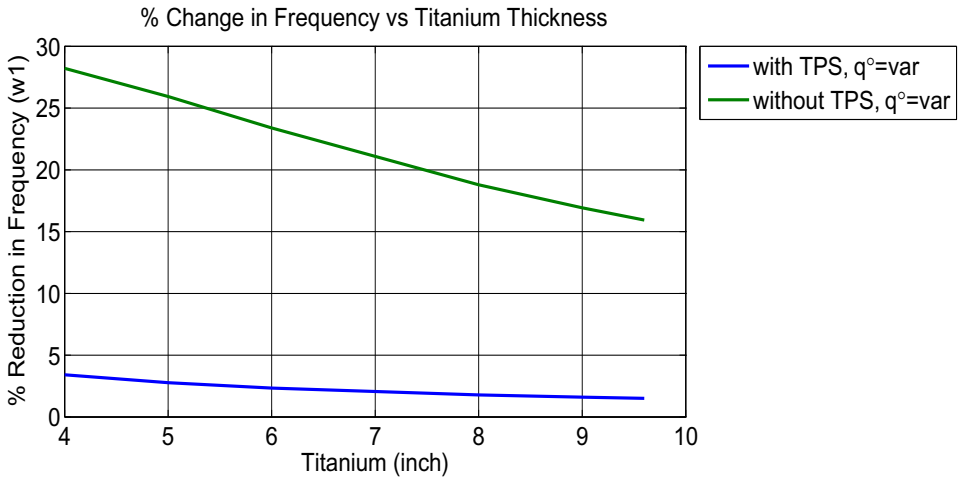

Figure 75: Percent change in fundamental frequency ($omega1$) vs Titanium thickness for 2hr of heating

The figure 75, shows the change in fundamental frequency ($omega1$) of TPS vs Titanium thickness for 2hrs of sustained flight. It is seen that:

1. Fundamental frequency do not change significantly with increasing thicknesses for heating with TPS.

2. Fundamental frequency increases linearly with decreasing thicknesses for heating without TPS.

3. It decreased by 16% without TPS at 9.6 thickness of Titanium.

6.9.2 Dynamic Effects for Prolonged heating

Following is the study for effect of elasticity variation on dynamic properties of the model. The design has Titanium=9.6", SiO_2=0.1", PM2000 = 3". The mass of TPS is assumed to be kept constant.

The figure 76 shows the movement of poles and zeros.

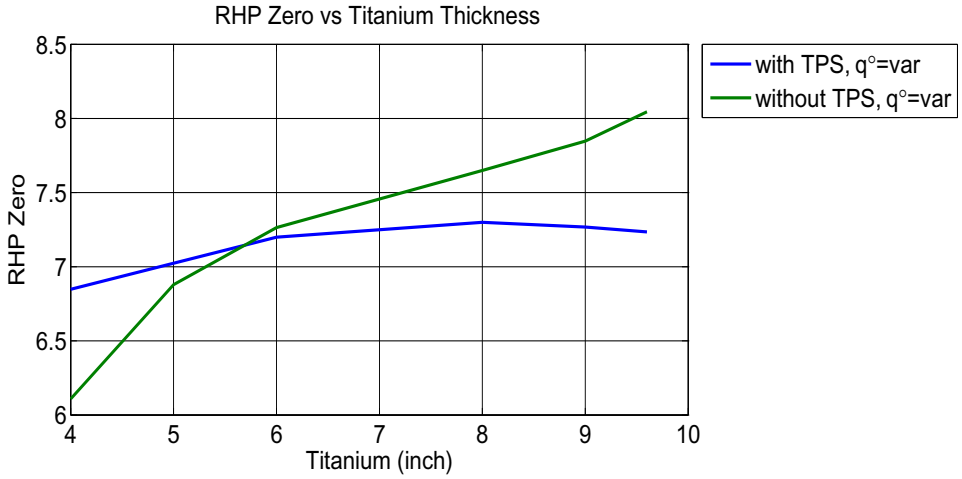

a. RHP Zero variation for prolonged heating

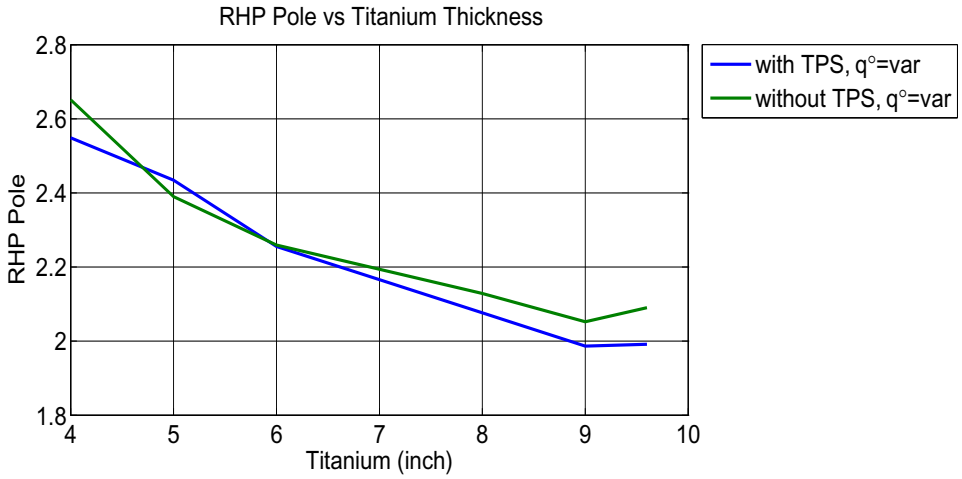

a. RHP Pole variation for prolonged heating

Figure 76: RHP Pole and Zero variation vs Titanium Thickness

1. Unstable Pole are same for both cases at each thicknesses, it increases linearly with decreasing thicknesses.
2. Unstable Zero decreases linearly with decreasing thicknesses for both cases of with and without TPS.
3. Without TPS , RHP Zero decreases significantly from 8 to 6, for titanium thickness decreased from 9.6 to 4.

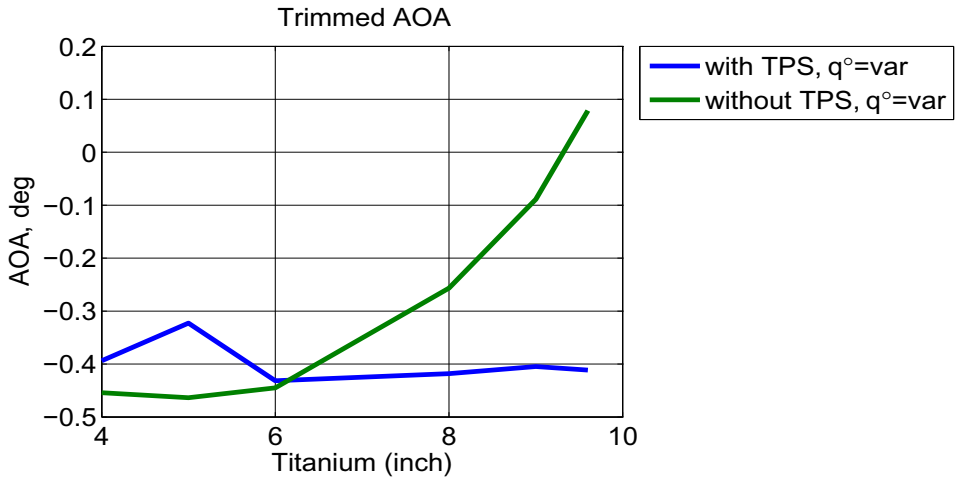

Figure 77: Angle of attack (AoA) vs Titanium

6.9.3 Static Effects against Titanium Thickness

The figure 77, shows AoA vs Titanium thickness after 2hrs of sustained flight. It is seen that:

1. AOA decreases with decreasing thickness of titanium for case without TPS.
2. AOA remains constant and does not change with decreasing thickness of titanium for case with TPS.

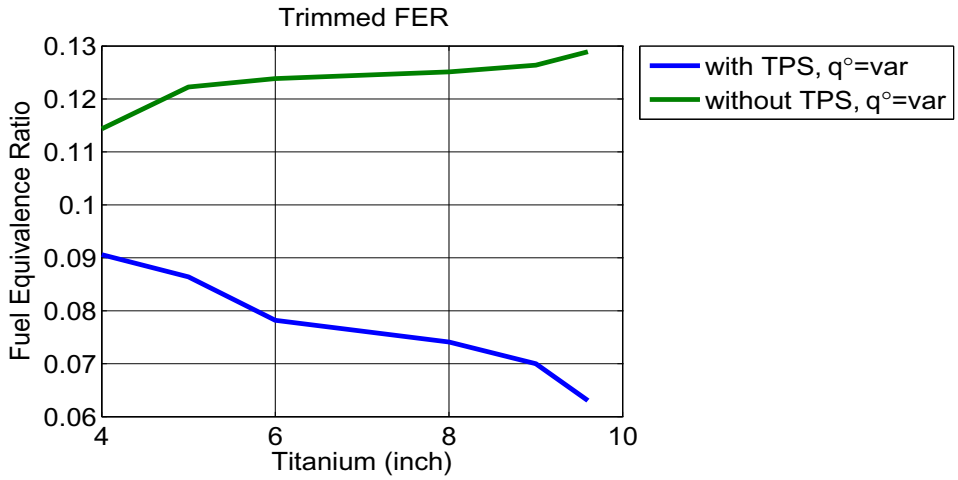

Figure 78: Fuel Equivalency Ratio (FER) against Titanium for 2hr of heating

The figure 66, shows FER vs Titanium after 2hrs of sustained flight. It is seen that:

1. FER increases with decreasing thickness of titanium for case with TPS.

2. FER decreases with decreasing thickness of titanium for case without TPS.

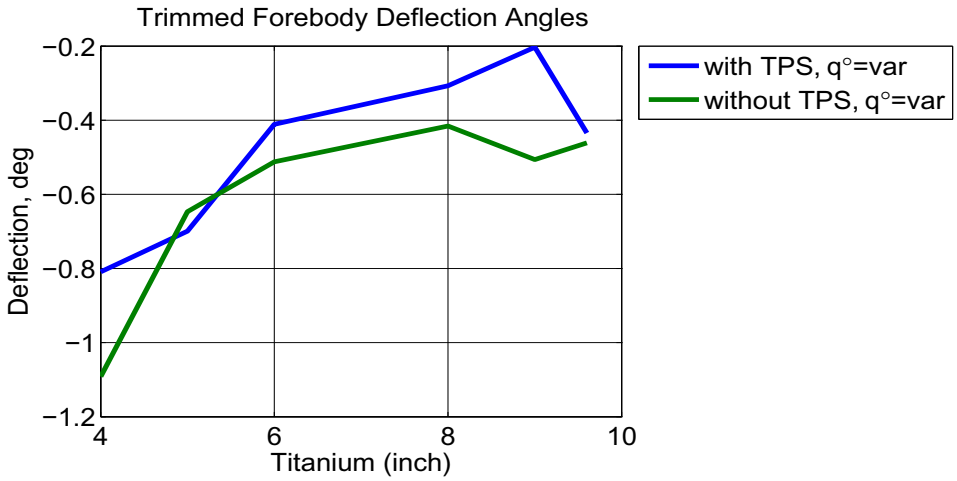

Figure 79: Forebody Deflection (Tau1) against Titanium for 2hr of heating

The figure 79, shows Forebody deflection after 2hrs of sustained flight. It is seen that:

1. With and without TPS heating, Forebody deflection decreases with decreasing thickness.

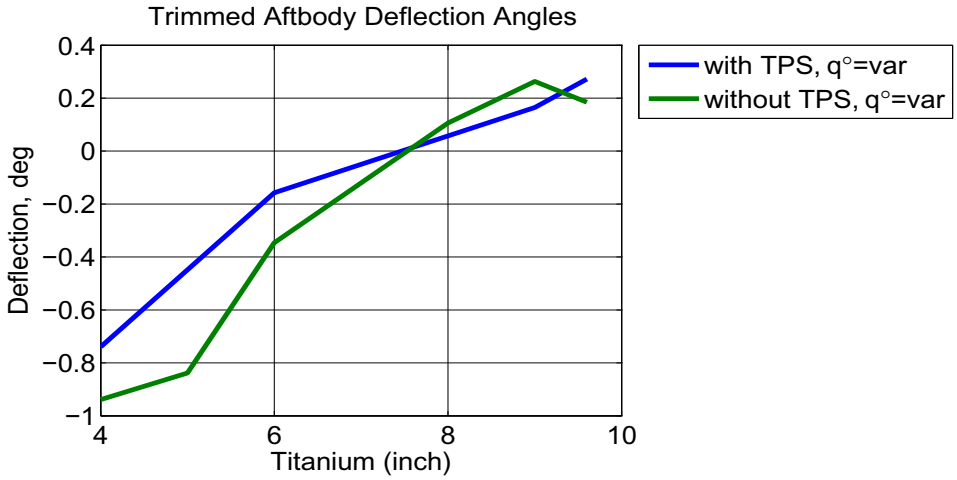

Figure 80: Aftbody Deflection (Tau2) against Titanium for 2hr of heating

The figure 80, shows Aftbody deflection vs Titanium thickness after 2hrs of sustained flight. It is seen that:

1. With and without TPS heating, Aftbody deflection decreases with decreasing thickness.

Figure 81: Elevator deflection against Titanium for 2hr of heating

The figure 81, shows Elevator deflection vs Titanium thickness after 2hrs of sustained flight. It is seen that:

1. More Negative control is required with decreasing thickness of Titanium.
2. Elevator becomes negative as titanium thickness decreases.

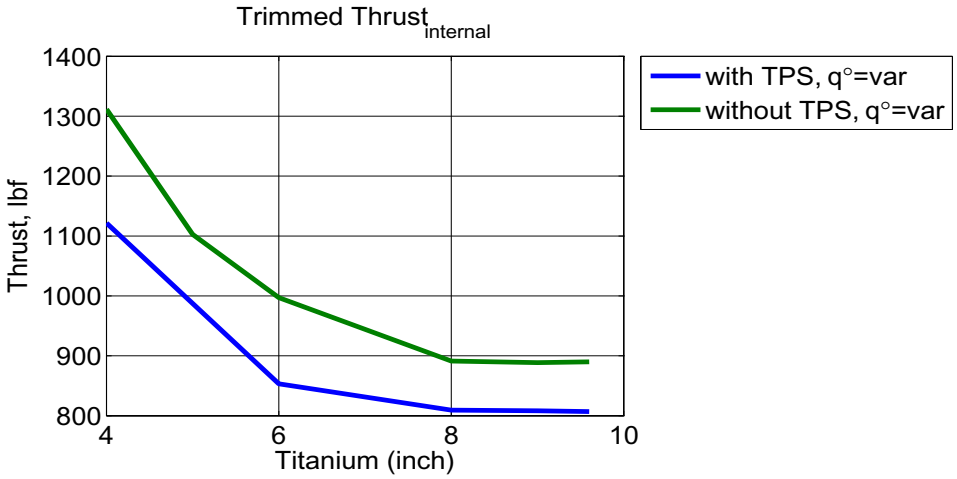

Figure 82: Internal Thrust against Titanium for 2hr of heating

The figure 82, shows internal thrust vs Titanium thickness after 2hrs of sustained flight. It is seen that:

1. With TPS heating, Internal Thrust rises with decreasing thickness from 800 lbf to 1100lbf
2. Without TPS heating, Internal Thrust rises with decreasing thickness from 900 lbf to 1300lbf.

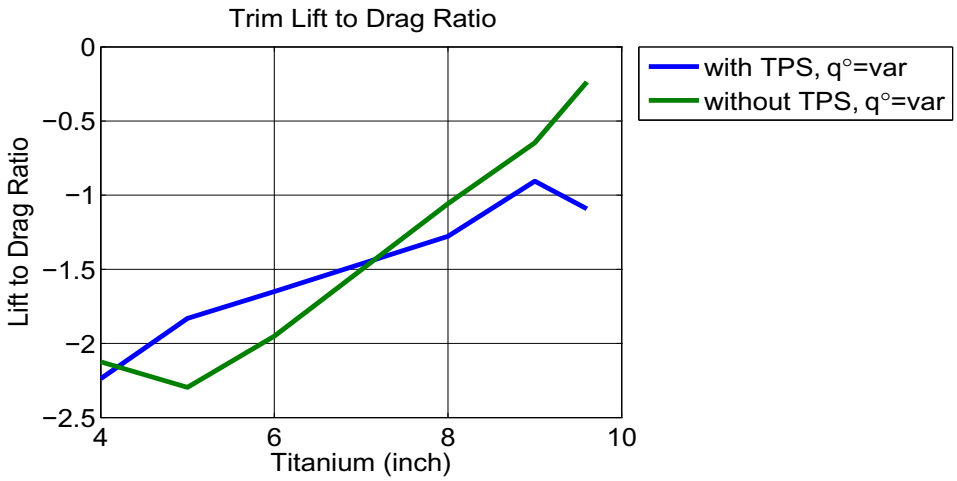

Figure 83: Lift to Drag Ratio against Titanium for 2hr of heating

The figure 83, shows Lift to Drag ratio vs Titanium thickness after 2hrs of sustained flight. It is seen that:

1. With and without TPS heating, L2D ratio decreases with decreasing thickness.

7. Control System Design

7.1 Overview

In this chapter, we consider the design of a control system for the nonlinear HSV model. We consider a two input model in this thesis (the FER and elevator are the two controls: see section 3.3 (page 44)), and we consider the FPA and velocity to be the two outputs. As seen in section 5.4 (page 111), the system is unstable and non-minimum phase. We consider some of the control challenges for the model, and present a simple control architecture to stabilize the linearized plant and track target velocity and FPA commands. We consider the changes in the controller and the trade-offs associated with different vehicle elasticity, tps mass and heating.

Fundamental Questions. This chapter considers the following control-relevant questions:

- What are the control challenges for the model?
- What amount of controller complexity is needed?
- How can control be combined with vehicle design?

This chapter is organized as follows: section 7.2 (page 167) considers the control challenges associated with the model. In section **??** (page **??**), controller design methodology and performance trade-offs associated with vehicle performance are discussed.

7.2 Control Challenges

In this section we present some of the challenges associated with the control of the HSV model. Some of the key challenges/limitations associated with the model are:

- Unstable and non-minimum phase plant with lightly damped flexible modes
- Varying Dynamic Characteristics
- Control Saturation Constraints

- Gap between the linearized plant
- Condition Number of plant

We discuss these issues in more detail below.

Linearized Plant Dynamics. In chapter 5, we considered a linearization procedure and the dynamics of the linearized model. Also, in chapter **??**, we consider the dynamic properties for a vehicle with different methods of plume computation. From these studies, we see that the linearized model has the following properties:

- RHP Pole - The long lower forebody of typical hypersonic waveriders combined with a rearward shifted center-of-gravity (CG), results in a pitch-up instability. The linearized plant is hence unstable (unless the CG is shifted forward significantly). The instability requires a minimum BW for stability [98].
- RHP zero - The non-minimum phase (inverse response) behavior is associated with the elevator to flight-path-angle (FPA) map and is characteristic of tail-controlled vehicles, unless a canard is used [124, 125]. It is understood, of course, that any canard approach would face severe heating, structural, and reliability issues. The RHP zero limits the maximum achievable bandwidth [107–109].
- Lightly damped flexible modes - The flexible modes affect the rigid body dynamics through generalized forces (see section 3.1, page 35, or [10]). Exciting the flexible modes affects the outputs and controls - structural flexing impacts the bow shock. This, in turn impacts the scramjet's inlet properties, thrust generated, aft body forces, the associated pitching moments, and hence the vehicle's attitude. Given the tight altitude-Mach flight regime - within the air-breathing corridor [21] - that such vehicle must operate within, the

concern is amplified. We see that there are significant aeroelastic-propulsive interactions. Flexible effects also impact the AOA seen by the elevator, and degrade the performance of a canard ganged to the elevator via a static gain [10]. In short, one must be careful that the control system BW and complexity are properly balanced so that these lightly damped flexible modes are not overly excited - the flexible modes limit the maximum achievable bandwidth [107–109].

Control Saturation Constraints Control saturation is of particular concern for unstable vehicles such as the one under consideration. State-dependent margins can limit the speed/size of the commands that may be followed. Two specific saturation nonlinearities are a concern for any control system implementation.

- *Maximum Elevator/Canard Deflection and Instability*. FPA is controlled via the elevator/canard combination [124]. Because these dynamics are inherently unstable, elevator saturation can result in instability [106]. Classical anti-windup methods may be inadequate to address the associated issues - particularly when the vehicle is open loop unstable. The constraint enforcement method within [106, 143] and generalized predictive control [107] have been used to address such issues. It should be noted that control surface/actuator rate limits must also be properly addressed by the control system in order to avoid instability.

- *Thermal Choking/Unity FER: State Dependent Constraint*. In section 3.7.5, we defined a instantaneous state dependent margin (FER margin) for the fuel equivalence ratio. The FER margin constraints impose BW and reference command size constraints. The FER constraint can be computed (on-line) based on the flight condition, and must be accounted for by the control law. Here, uncertainty is of great concern because of potential engine unstart is-

sues (see section 3.7.5, page 63) - issues not captured within the model. Engineers, of course, would try to "build-in protection" so that this is avoided. As such, engineers are forced to tradeoff operational envelop for enhance unstart protection. In [107], the authors consider GPC-based constraint enforcement to address thermal choking, unity FER, and elevator saturation constraint issues in a systematic non-conservative manner. Other papers addressing saturation include: saturation prevention [8, 106, 144], and thermal choking prevention[105, 144].

Varying Dynamic Characteristics. Within [105], it is shown that the nonlinear model changes significantly as a function of the flight condition. Specifically, it is shown that the vehicle pitch-up instability and non-minimum phase zero vary significantly across the vehicle's trimmable region. In addition, the mass of the vehicle can be varied during a simulation in order to represent fuel consumption. Several methods have been presented in the literature to deal with the nonlinear nature of the model. Papers addressing modeling issues include: nonlinear modeling of longitudinal dynamics [14], heating effects and flexible dynamics [6, 10, 145], FPA dynamics [124], unsteady and viscous effects [2, 5], and high fidelity engine modeling [114, 146, 147]. Papers addressing nonlinear control issues include: control via classic inner-outer loop architecture[108], nonlinear robust/adaptive control [148], robust linear output feedback [149], control-oriented modeling [3], and linear parameter-varying control of flexible dynamics [150].

7.3 Controller Design

In this section, a simple, classical control based methodology is considered. The HSV model presented in chapter **??** (i.e. new engine design) is linearized at Mach 8, 85kft. This is considered as the nominal plant.

More specifically, the following questions are considered:

- What performance/robustness properties can be achieved using decentralized controller (decoupled 1st order single-input single-output control) structure?
- How does Controller performance: FER to FPA step response, Singular values for sensitivities and complimentary sensitivities changes.
- When does controller fails for changes in Elasticity (EI), Mass heating and structural dimension?

An inner-outer loop feedback structure is used to alleviate limitations imposed by the small RHP zero-pole ratio [151].

7.3.1 Design Assumptions and Approximations

Plant Assumptions and Approximations. The following assumptions and approximations are made for the linearized plant:

- The altitude state is removed to provide controllability (it is included in all nonlinear simulations)
- The flexible states are not directly measurable
- The plant is approximately diagonal at high frequencies

7.3.2 Control Architecture

The inner-outer feedback loop controller is shown here.

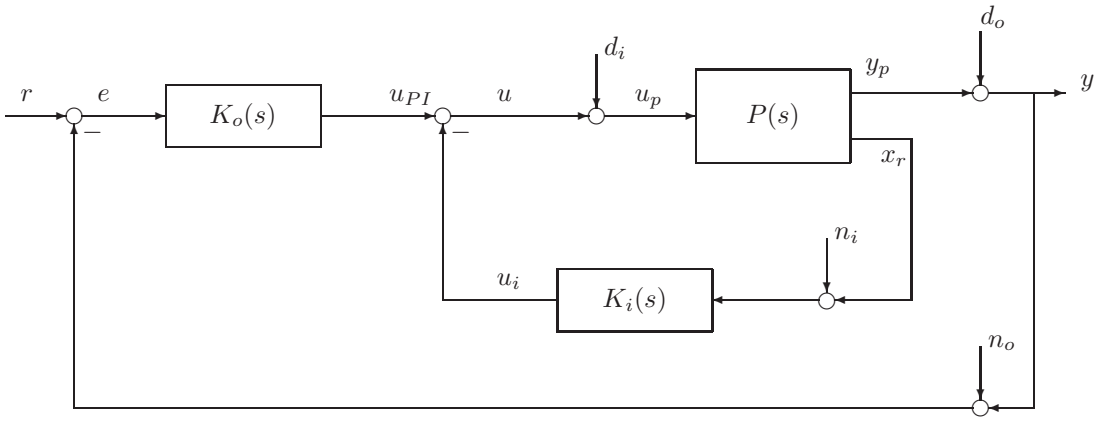

Output vector: $y_p = [\ y_1\ y_2\ ]^T = [\ v\ \gamma\ ]^T$

Control vector: $u = [\ u_1\ u_2\ ]^T = [\ FER\ \delta_e\ ]^T$

$x_r = [\ \theta\ q\ ]^T$

The nominal controllers $K_i(s)$ and $K_o(s)$ are given in equation 7.1

$$K_i(s) = \begin{bmatrix} 0 & 0 \\ -g_i z_i & -g_i \end{bmatrix} \tag{7.1}$$

$$K_o(s) = \begin{bmatrix} \frac{g_v(s+z_v)}{s}\left[\frac{20}{(s+20)}\right]^3 & 0 \\ 0 & \frac{g_o(s+z_o)}{s}\left[\frac{20}{(s+20)}\right]^2 \end{bmatrix} \tag{7.2}$$

From Equation 7.1, we observe the following:

- The inner controller has two parameters associated with it (z_i, g_i)
- The outer controller has four parameters associated with it (g_v, z_v, g_o, z_o)
- The modified plant (P_{mod}) is defined as the transfer function matrix from $u_{PI} \rightarrow y_p$

$K_i(s)$ can be re-written as in Equation 7.3:

$$K_i(s) = \frac{\delta_e(s)}{\theta(s)} = -g_i(s + z_i) \tag{7.3}$$

We augment $K_i(s)$ with a high frequency roll off. The modified $K_i(s)$ is given in Equation 7.4. In what follows, we shall omit the roll-off for convenience.

$$K_i(s) = -\frac{50g_i(s + z_i)}{(s + 50)} \tag{7.4}$$

Two useful transfer function are given by Equations 7.5 and 7.6

$$\hat{P}_\theta = \frac{\theta(s)}{\delta_e(s)} = \frac{g_\theta(s + z_\theta)}{s(s - p_1)(s + p_2)} \tag{7.5}$$

$$\frac{\gamma(s)}{\theta(s)} = \frac{g_\gamma(s - z)(s + z)}{g_\theta(s + z_\theta)} \tag{7.6}$$

- The open loop transfer function for the inner loop is given by Equation 7.7

$$L_{c,i}(s) = \hat{P}_\theta(s)K_I(s) = \frac{\theta(s)}{\delta_e(s)} = \frac{-g_\theta g_i(s + z_\theta)(s + z_i)}{s(s - p_1)(s + p_2)} \tag{7.7}$$

- The BW of Equation 7.7 is given by $|L_{c,i}(\omega_{g,i})| = 1$
- Finally, the FPA component of the modified plant can be written as

$$\hat{P}_{mod} = \frac{\hat{P}_\theta(s)}{1 + K_i(s)\hat{P}_\theta(s)} \frac{\gamma(s)}{\theta(s)} \tag{7.8}$$

$$= \frac{g_\gamma(s - z)(s + z)}{s^3 + (p_2 - p_1 + g_i g_\theta)s^2 + (g_i g_\theta z_i + g_i g_\theta z_\theta - p_1 p_2)s + g_i g_\theta z_i z_\theta} \tag{7.9}$$

- The modified plant (u_{p_I}-to-γ) should possess approx 3rd order (PI friendly) phase ($0°$ to $-270°$ modulo leading negative gain)
- A "good" modified plant contributes minimal lag to outer PI controller at frequencies of interest

RHP Zero/Pole Limitations One major benefit of the inner-outer loop structure is to avoid robustness limitations imposed by the ratio of the RHP zero and the RHP pole. For SISO output feedback, the following limitation applies [151]:

$$\overline{\sigma}[S],\ \overline{\sigma}[T] \geq \frac{|z+p|}{|z-p|} \tag{7.10}$$

For elevator-to-FPA system, this would mean

$$\overline{\sigma}[S],\ \overline{\sigma}[T] \geq 6.5\ dB \tag{7.11}$$

This rule does not apply to our inner-outer loop structure [152, 153].

7.4 Control Methodology

- The two inner loop parameters (g_i , z_i) can be utilized to P_{mod} look like Equation 7.12

$$P_{mod}(s) = \begin{bmatrix} \frac{b_v}{s} & 0 \\ 0 & -b_\gamma \left(\frac{a_\gamma}{s+a_\gamma}\right) \end{bmatrix} [1 + \Delta_m(s)] \tag{7.12}$$

- As $\omega_{g,initial}$ increases, $b_v \to 0.03887$, $a_\gamma \to z_\theta$, $b_\gamma \to \frac{1}{g_i z_i} \frac{g_\gamma z^2}{g_\theta z_\theta}$
- $\Delta_m(j\omega)$ should be small (less than -10 dB) for $\omega <$ BW at the Error
- Outer loop control can be designed using standard second order system ideas

Rules of Thumb (FPA)

- BW at the Control > 10 BW at the Error (fast IL dynamics)
- BW at the Control $> 2 \times p_{rhp}$ (instability)
- BW at the Control $< \frac{3}{4} \times \omega_{n_{\eta 1}}$ (1st flexible mode freq) for a single lead-lag notch to suppress vehicle flexing
- BW at the Error $< \frac{1}{10} \times z_{rhp}$ (non-invertible RHP zero)
- Increasing BW at the Error relative to the BW at the Control requires a more complicated outer loop control structure
- Increasing BW at the Error $> \frac{1}{10} \times z_{rhp}$ requires a more complicated outer loop control structure
- Increasing BW at the Control $> \frac{3}{4} \times \omega_{n_{\eta 1}}$ requires a more complicated inner loop control structure

Rules of Thumb (V)

- Velocity response is primarily dictated by FERM
- Velocity appears like a filtered input disturbance to FPA loop
- Velocity BW at the Error $< \frac{1}{10}$ FPA BW at the Error $< \frac{1}{10} z_{rhp}$

7.4.1 FPA Outer Loop Design Method

- FPA Design Plant: $\hat{P}_\gamma = -b_\gamma \left(\frac{a_\gamma}{s + a_\gamma} \right)$
- Assume $a_\gamma = z_\theta$, $b_\gamma = \frac{1}{g_i z_i} \frac{g_\gamma z^2}{g_\theta z_\theta}$
- The FPA control system design method will make the closed loop response have the following form

$$\hat{T}_{ry} = \frac{\omega_n^2}{s^2 + 2\zeta w_n s + \omega_n^2} \tag{7.13}$$

1. Choose a desired settling time (t_s) and overshoot (M_p)

2. Calculate $\zeta = \frac{|lnM_p|}{\sqrt{(lnM_p)^2+\pi^2}}$ and $\omega_n = \frac{5}{\zeta t_s}$
3. Calculate $g_o = \frac{2\zeta\omega_n - a_\gamma}{b_\gamma a_\gamma}$ and $z_b = \frac{\omega_n^2}{g_o b_\gamma a_\gamma}$
4. Formulate the controller $K_o(s) = \frac{g_o(s+z_o)}{s}\left[\frac{20}{(s+20)}\right]^3$
5. Formulate the command pre-filter $W(s) = \frac{z_o}{s+z_o}$

- In general, robustness properties (Sensitivities, Margins, etc) will be worse than those associated with the target $\hat{T}_{ry}$
  - Very slight for BW at the Error $< \frac{1}{10}z_{rhp}$
  - For BW at the Error $> \frac{1}{5}z_{rhp}$, the robustness properties worsen severely

7.4.2 Velocity Design Method

- Velocity Design Plant: $\hat{P}_V = \frac{b_v}{s}$
- The velocity control system design method will make the closed loop response have the following form

$$\hat{T}_{ry} = \frac{\omega_n^2}{s^2 + 2\zeta w_n s + \omega_n^2} \tag{7.14}$$

1. Choose a desired settling time (t_s) and overshoot (M_p)
2. Calculate $\zeta = \frac{|lnM_p|}{\sqrt{(lnM_p)^2+\pi^2}}$ and $\omega_n = \frac{5}{\zeta t_s}$
3. Calculate $g_v = \frac{2\zeta\omega_n}{b_v}$ and $z_v = \frac{\omega_n}{2\zeta}$
4. Formulate the controller $K(s) = \frac{g_v(s+z_v)}{s}\left[\frac{10}{(s+10)}\right]^3$
5. Formulate the command pre-filter $W(s) = \frac{z_v}{s+z_v}$

It should be noted that z_v, the zero of the FER-Velocity controller is only depends on the closed loop specifications (and not the plant). However, the achievable velocity bandwidth is constrained by the FER margin (defined in section 3.7.5, 63) [108].

7.4.3 Flexible mode attenuation

In [108], the authors examine the use of an increased complexity controller to improve sensitivity properties via the use of additional lead-lag. Based on results presented in [108], a lead-lag structure was added to the inner loop. The new $K_i(s)$ is given below:

$$K_i(s) = \begin{bmatrix} 0 & 0 \\ -g_i z_i & -g_i \end{bmatrix} \frac{50}{s+50} \left[\frac{s^2 + b_1 s + b_o}{s^2 + a_1 s + a_o} \right] \frac{a_o}{b_o} \tag{7.15}$$

The values for the lead-lag elements were selected as:

$$b_1 = 15 \quad b_o = 250$$

$$a_1 = 30 \quad a_o = 1800$$

The variation in lead-lag design with geometry will be examined in future work.

7.4.4 Advantages

The advantages of the above controller structure is multi-fold:

1. *Implementation.* The structure is simple to implement since it consists of integrators, summers, command pre-filters, and gains that can be readily scheduled.

2. *Low Frequency Command Following.* Because of the PI structure on the error signal, we expect to have zero steady state error to step reference commands. More generally, this structure will assist in following low frequency reference commands and attenuating low frequency output disturbances. It must be emphasized that our capability to follow rapid commands is limited by the plant RHP (transmission) zero and by control constraints (e.g. FERM, elevator saturation levels).

3. *Addressing Control Tradeoffs.* $K_i(s)$ can be used to stabilize the unstable plant and hence lessen sensitivity tradeoffs at the error that are associated with having a RHP pole and RHP zero. In our case, this sensitivity tradeoff would be quite formidable (without the inner-outer feedback structure), given the small RHP zero to RHP pole ratio - even if we used a controller much more complex than the PI structure on the error [151].

7.4.5 Saturation Nonlinearities

FER saturation. FER saturation was initially considered in section 3.7.5 (page 63). Excessive heat addition might result in unstart, a highly undesirable condition. A control-relevant FER margin was also presented earlier. In the control methodology presented in this section, FER saturation does not affect stability - FER acts on the modified plant, which is stabilized via state feedback into the elevator. As a result, adequate performance might be achieved via a simple anti-windup techniques [108]. FER saturation, however, dictates the velocity channel bandwidth [108].

Elevator saturation. Since stabilization in the inner loop is achieved via state-feedback into the elevator, elevator saturation can lead to instability [106]. Classical anti-windup methods may be inadequate to address the associated issues. The effects of elevator saturation will be considered in future work.

The new $K_i(s)$ after roll off is given below:

$$K_i(s) = \begin{bmatrix} 0 & 0 \\ \frac{-283.8143(s+20)}{s+200} & \frac{-212.1877(s+20)(s^2+15s+250)}{(s+200)(s^2+30s+1800} \end{bmatrix} \tag{7.16}$$

The new $K_o(s)$ after roll off is given below:

$$K_o(s) = \begin{bmatrix} \frac{-783414.5038(s+.05249)}{s(s+20)^3} & 0 \\ 0 & \frac{-230827.7104(s+.7019)}{s(s+20)^2} \end{bmatrix} \tag{7.17}$$

7.5 Elasticity (EI) effects on Controller Performance

De-centralized Controller performances for variation in the elasticity(EI).

7.5.1 Time Responses for EI variation

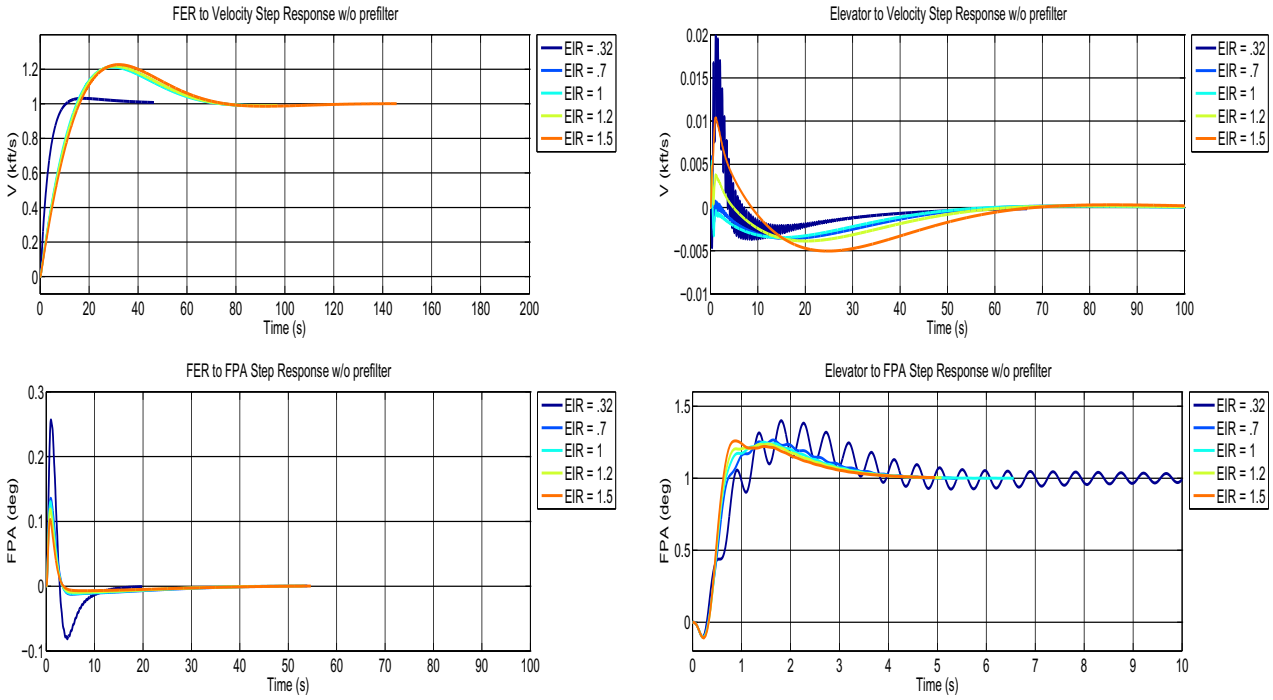

Figure 84: Step responses without prefilter for flexible Controller with changes in elasticity

From fig 85,

- Elevator to FPA step response is unaffected by the elasticity (EI) reduction.
- Elevator to FPA step response ripples get larger with increasing EI ratio for without pre-filter

7.5.2 Frequency Responses for EI variation

From fig 86,

- Sensitivities for first fundamental frequency experience hiked peaking for reduced EI ratio.

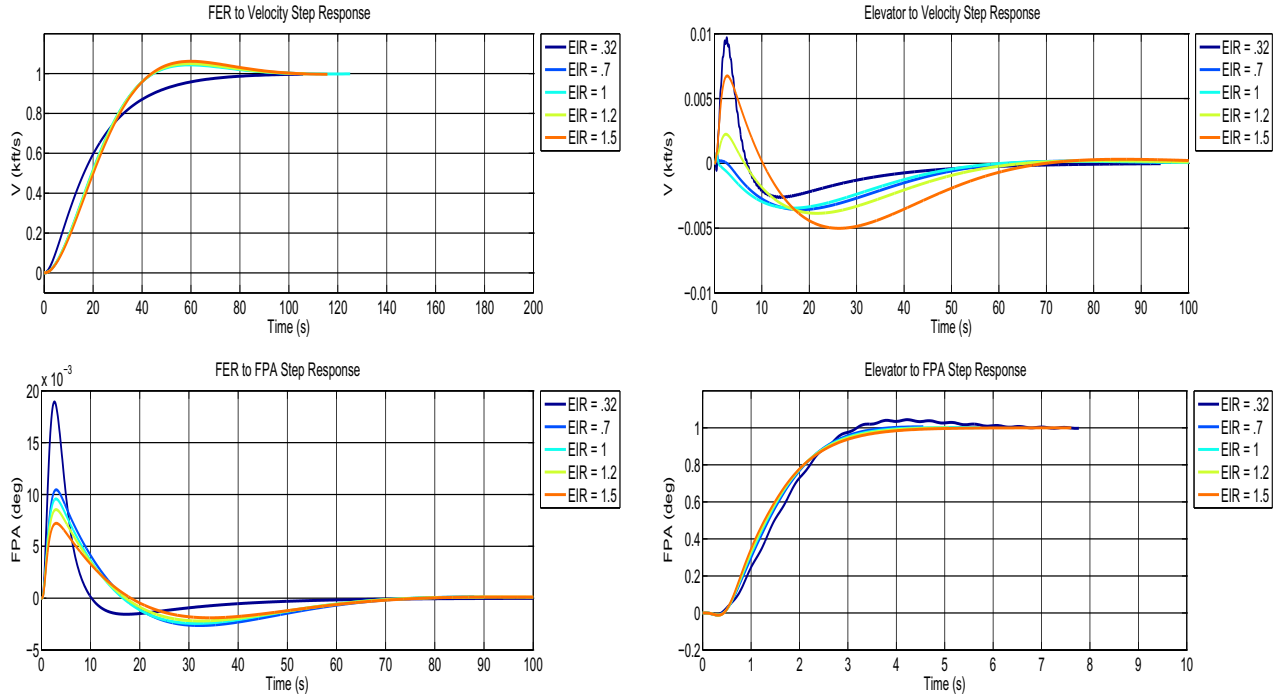

Figure 85: Step responses with prefilter for flexible Controller with changes in elasticity

- Plant experiences increased peaking at phugoid mode for lower EI ratio.

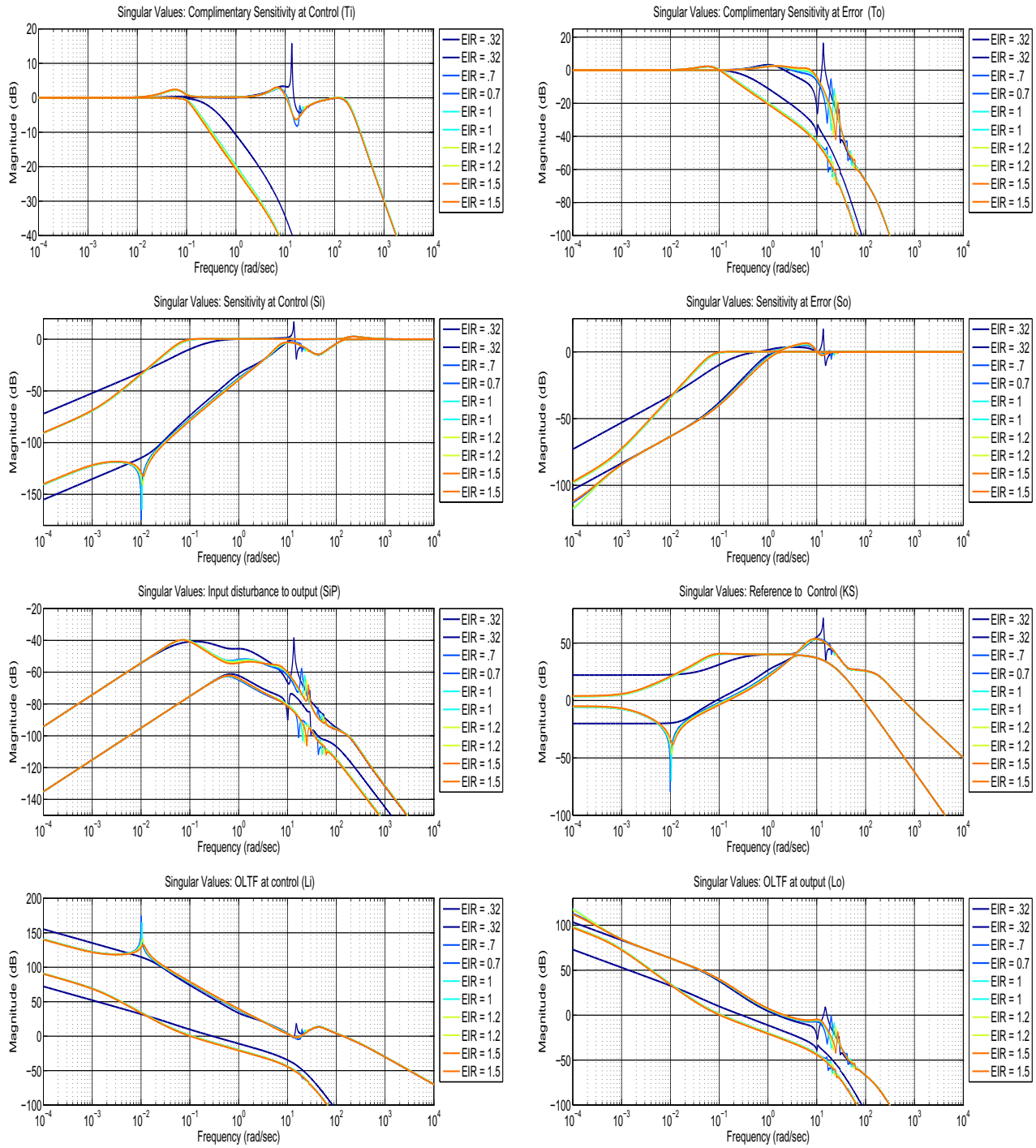

Figure 86: Singular values for flexible Controller with changes in elasticity

7.6 Mass effects on Controller Performance

De-centralized Controller performances for change in mass. Nominal Control Looses controllability at 25% mass reduction

7.6.1 Time Responses for EI variation

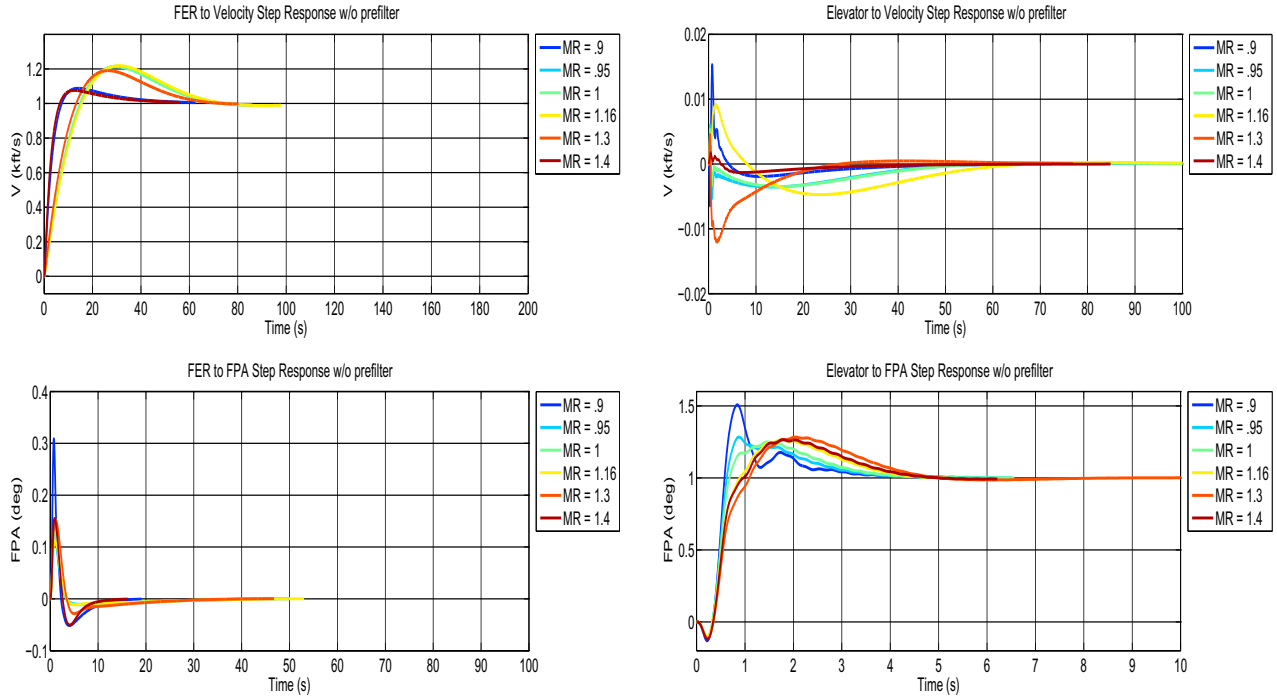

Figure 87: Step responses without prefilter for flexible Controller with changes in Mass

From fig 88, 87

- Elevator to FPA step response is unaffected by changes in mass.
- Elevator to FPA step response ripples get larger with decrease in Mass for without pre-filter

7.6.2 Frequency Responses for Mass variation

From fig 89,

- Sensitivities for first fundamental frequency experience hiked peaking for re-

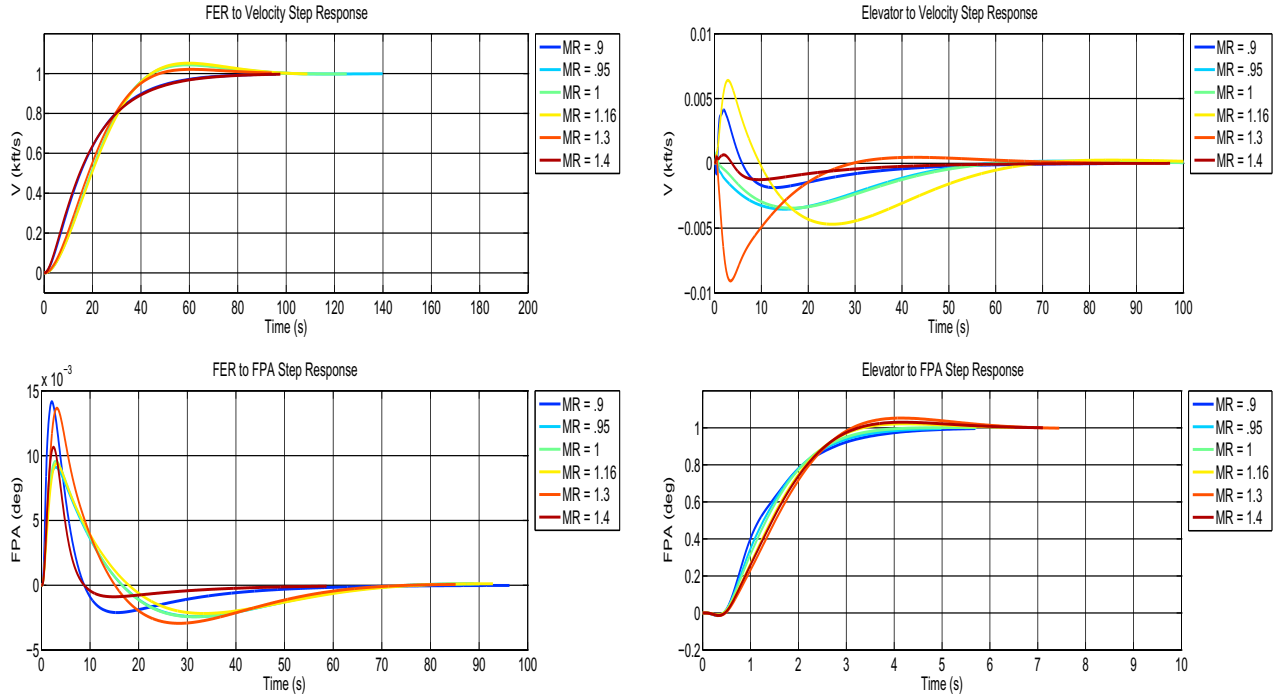

Figure 88: Step responses with prefilter for flexible Controller with changes in Mass

duced mass ratio.

- Mass do not have significant effect over the control performance.

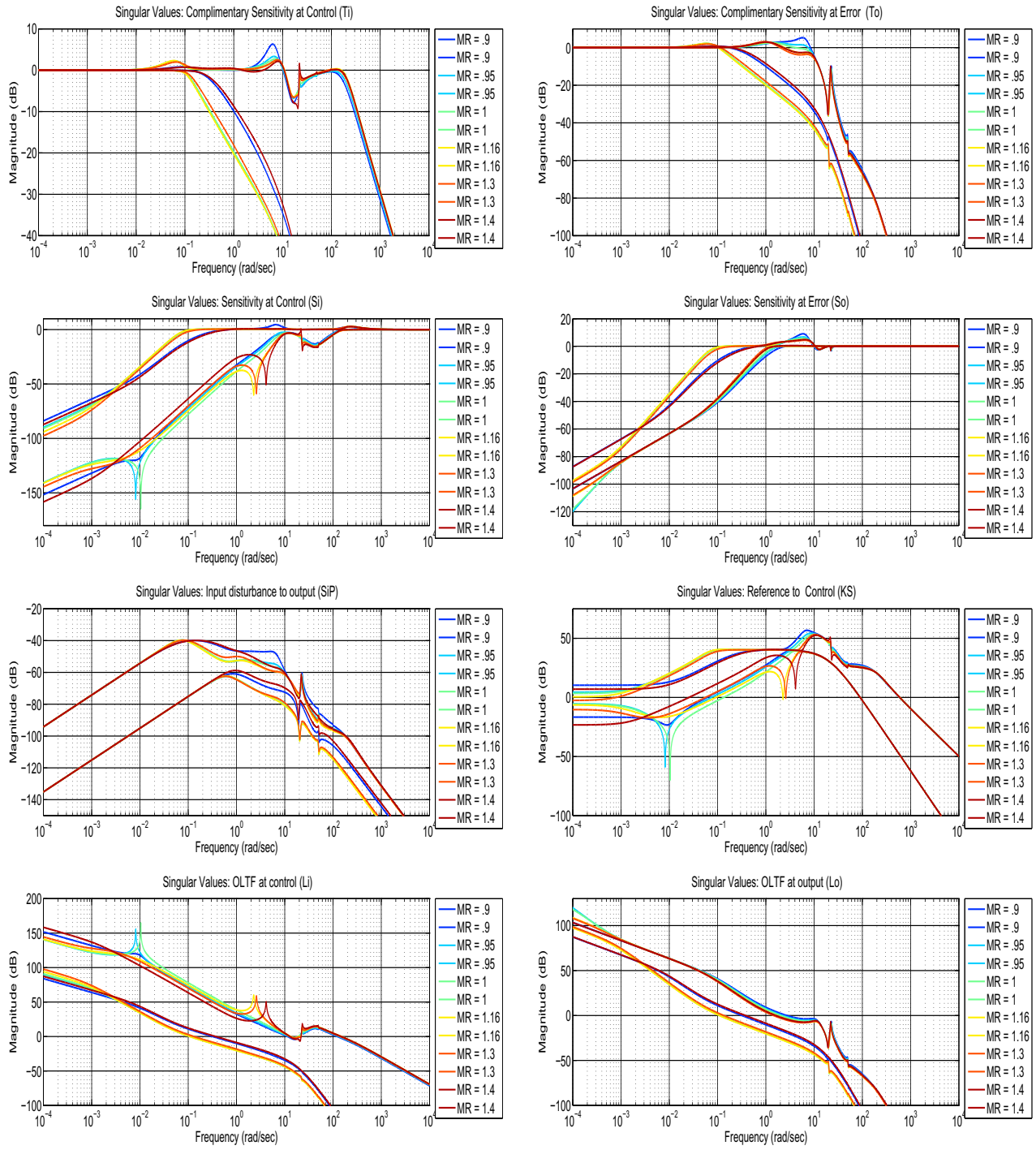

Figure 89: Singular values for flexible Controller with changes in Mass

7.7 Prolonged Heat effects on Controller Performance

De-centralized Controller performances for prolonged heating for 4 cases namely:

1. With TPS, flight dependent heat flux (PM2k 3, SiO2 0.1, Titanium 9.6)
2. w/o TPS, flight dependent heat flux (PM2k 3, SiO2 0.1, Titanium 9.6)
3. With TPS, Constant heat flux (PM2k 3, SiO2 0.1, Titanium 9.6)
4. w/o TPS, Constant heat flux (PM2k 3, SiO2 0.1, Titanium 9.6)

7.7.1 Case1: With TPS, flight dependent heat flux (PM2k 3, SiO2 0.1, Titanium 9.6)

1. With TPS, flight dependent heat flux at Mach8, Altitude85kft , Control Designed for nominal model after 2hr of heating is also valid for Plant obtained after 20hr of flight.
2. Elevator to FPA step response is also unaffected by the heating with time.
3. Sensitivities do not experience increased peaking due to heating with time.
4. Peaking at first fundamental frequency becomes higher (though hike is not significant) with increased flight duration.
5. Peaking at phugoid mode frequencies dominate over the peaking at fundamental frequency frequencies.

Time Responses

From fig 91, 90

- Elevator to FPA step response do not experience change in peaking or steady state time.

Frequency Responses

From fig 92,

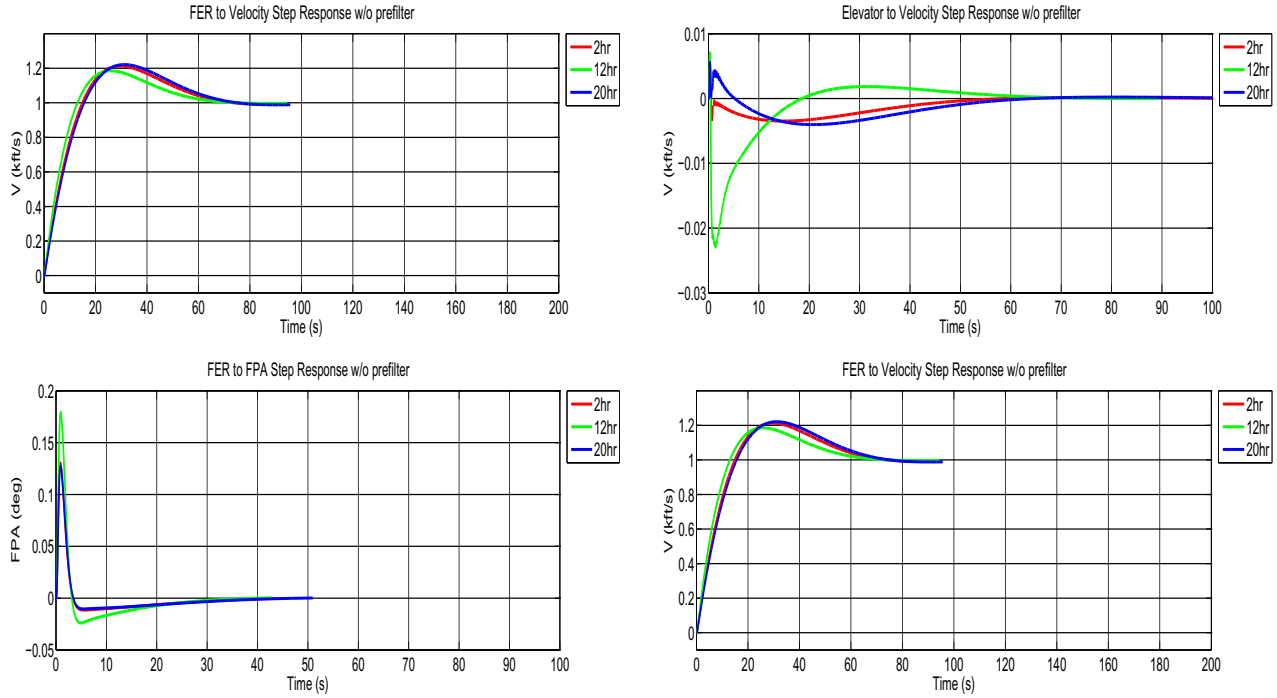

Figure 90: Step responses without prefilter for flexible Controller for prolonged heating at structure surface with TPS, flight dependent net heat flux input

- Complimentary sensitivity / Sensitivities at Error have no severe peaking
- Complimentary sensitivity / Sensitivities at Control have no severe peaking
- Phugoid mode peaking are dominant over the first fundamental frequency based peaking.
- Singular Values of OLTF has lowered peaking with increased heating
- Other singular values do not experience any severe peaking

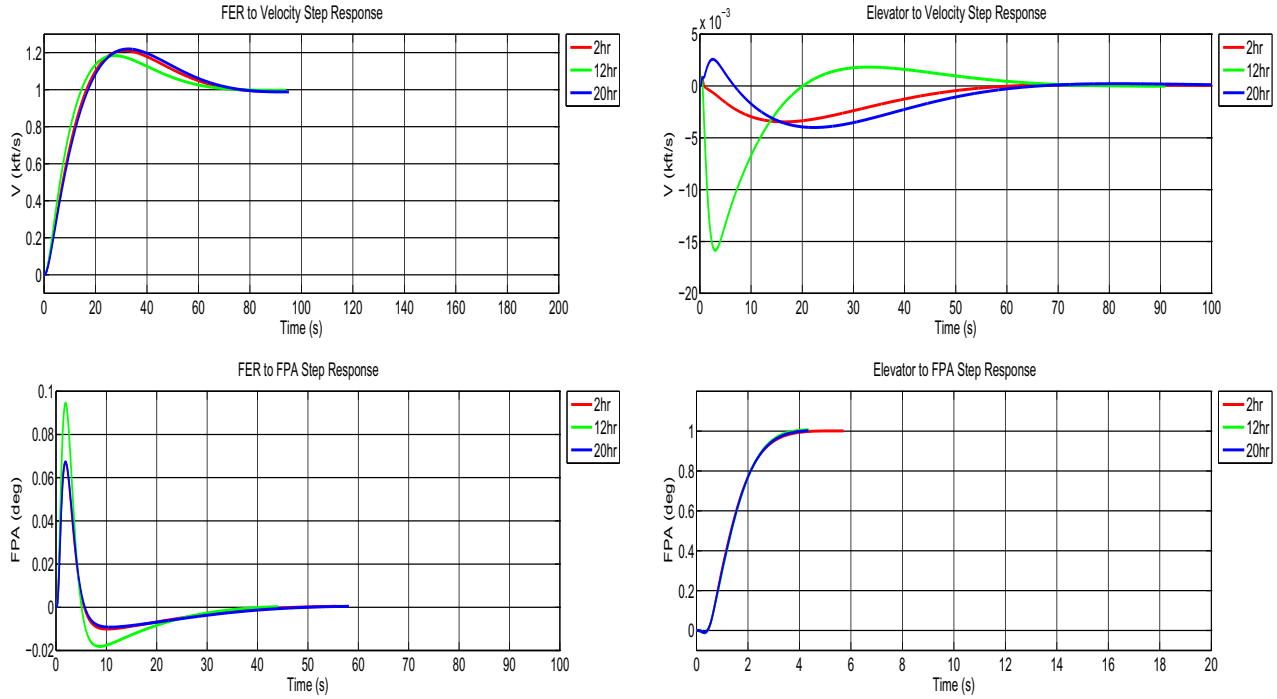

Figure 91: Step responses with prefilter for flexible Controller for prolonged heating at structure surface with TPS, flight dependent net heat flux input

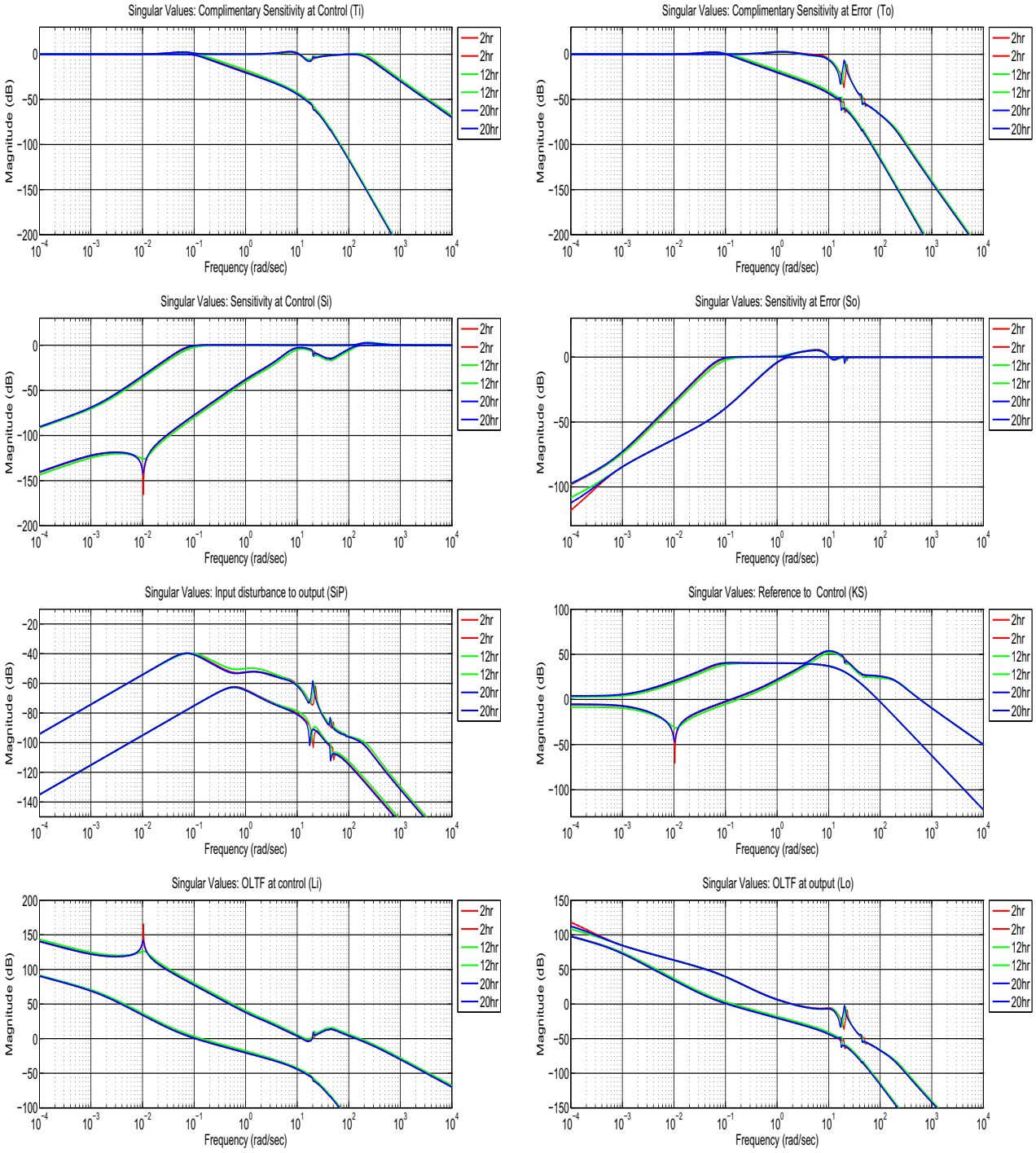

Figure 92: Frequency response with flexible Controller for prolonged heating at structure surface with TPS, flight dependent net heat flux input

7.7.2 Case2: w/o TPS, flight dependent heat flux (PM2k 0, SiO2 0, Titanium 9.6)

1. Without TPS, flight dependent heat flux at Mach8, Altitude85kft , Control Designed for nominal model after 2hr of heating is also valid after 20hr of flight.
2. Elevator to FPA step response is also unaffected by 20hr heating.
3. Sensitivities do not experience peaking due to 20 hr of heating

Time Responses

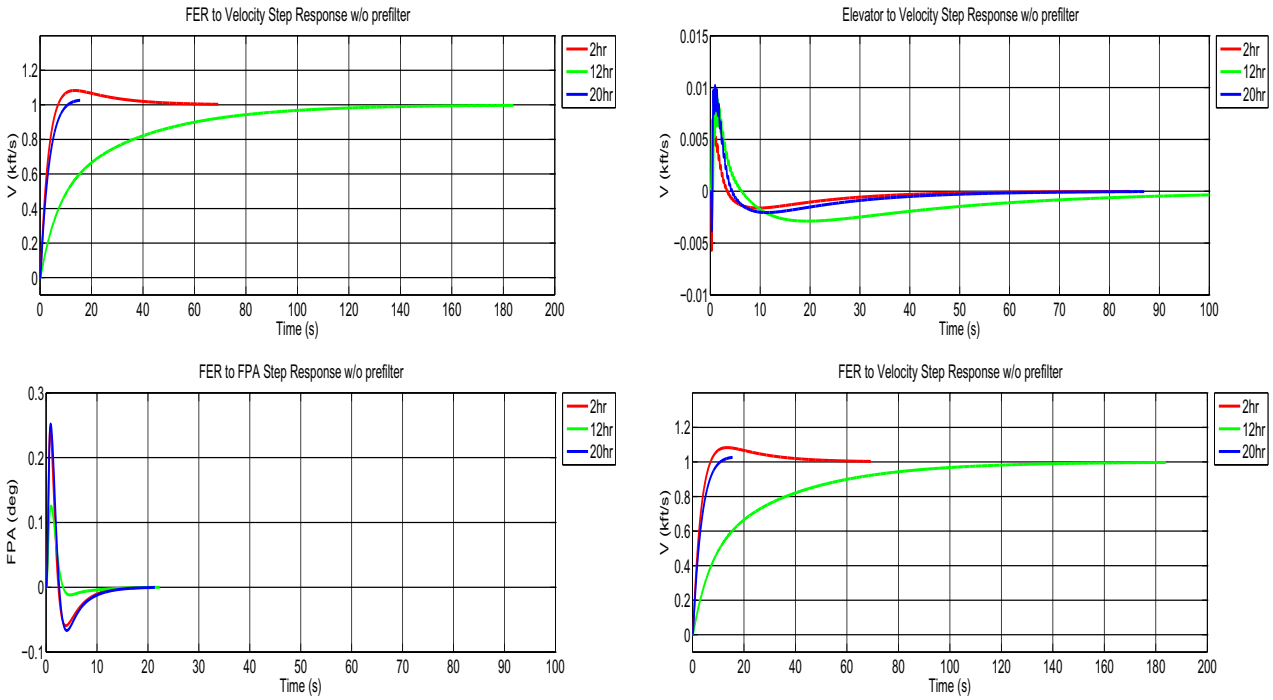

Figure 93: Step responses without prefilter for flexible Controller for prolonged heating at structure surface without TPS, flight dependent net heat flux input

From fig 94, 93

- Elevator to FPA step response with pre-filter do not experience change in peaking or steady state time.

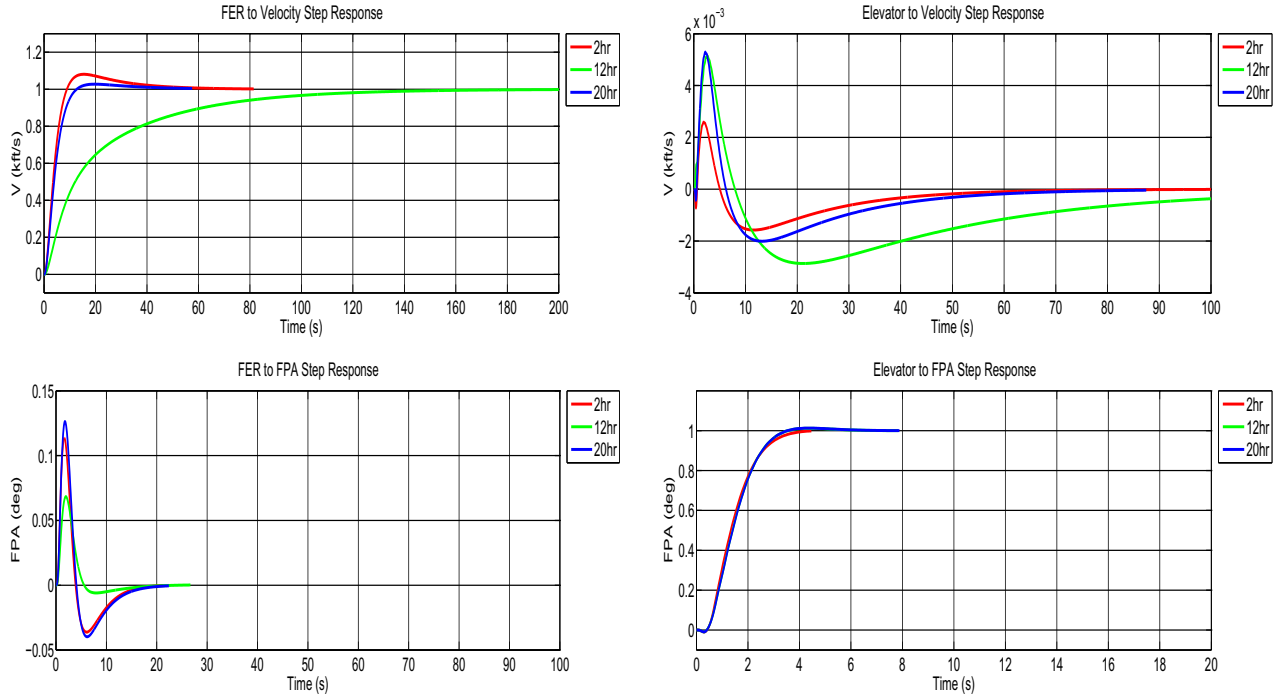

Figure 94: Step responses with prefilter for flexible Controller for prolonged heating at structure surface without TPS, flight dependent net heat flux input

- Ripples start to develop with increased heating for Elevator to FPA step response without pre-filter

Frequency Responses

From fig 95,

- Sensitivity at Error has no severe peaking for 20hr of sustained flight.
- Sensitivities has no severe peaking for 20hr of sustained flight.
- Singular values for OLTF Plant experience lowered peaking at phugoid mode but increased for first fundamental frequency.

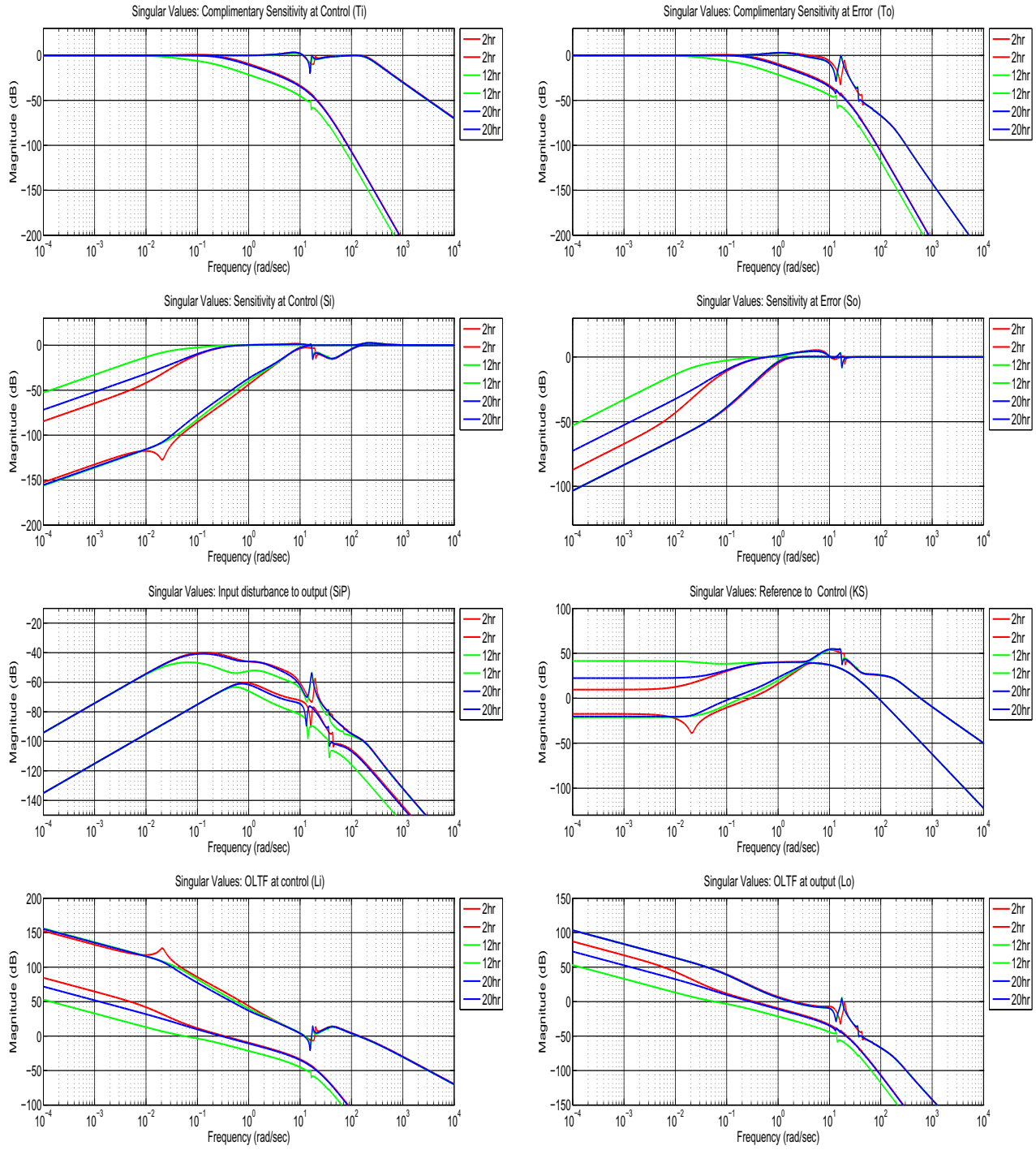

Figure 95: Frequency response with flexible Controller for prolonged heating at structure surface without TPS, flight dependent net heat flux input

7.7.3 Case3: With TPS, Constant heat flux (PM2k 3, SiO2 0.1, Titanium 9.6)

1. With TPS, constant heat flux at Mach8, Altitude85kft , Control Designed for nominal model after 2hr of heating is also valid after 20hr of sustained flight.
2. Elevator to FPA step response is unaffected by the 20hr heating.
3. Sensitivities do not experience peaking due to 20hr heating

Time Responses

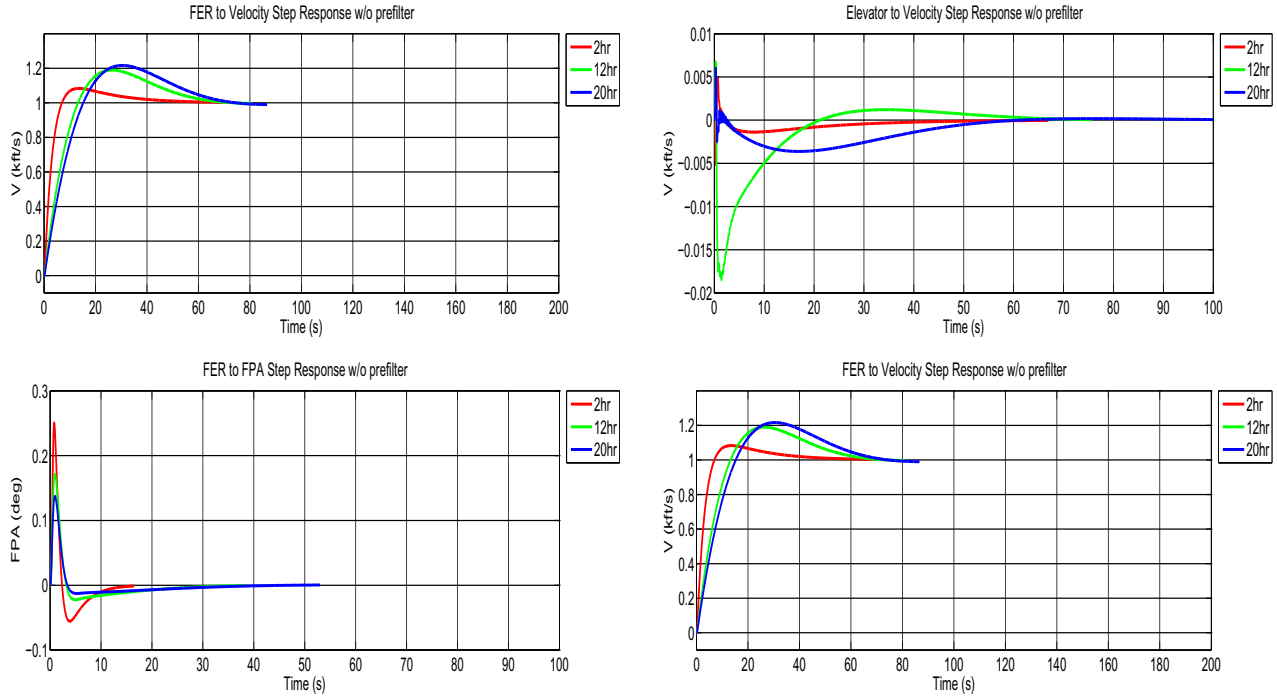

Figure 96: Step responses without prefilter for flexible Controller provided prolonged heating at structure surface with TPS, constant net heat flux input of 15BTU/ft^{2}s

From fig 97, 96

- Elevator to FPA step responses for increased hours of heating with TPS causes peak overshoot to increase and reduce the settling time.
- Ripples start to develop with increased heating for Elevator to FPA step response without pre-filter

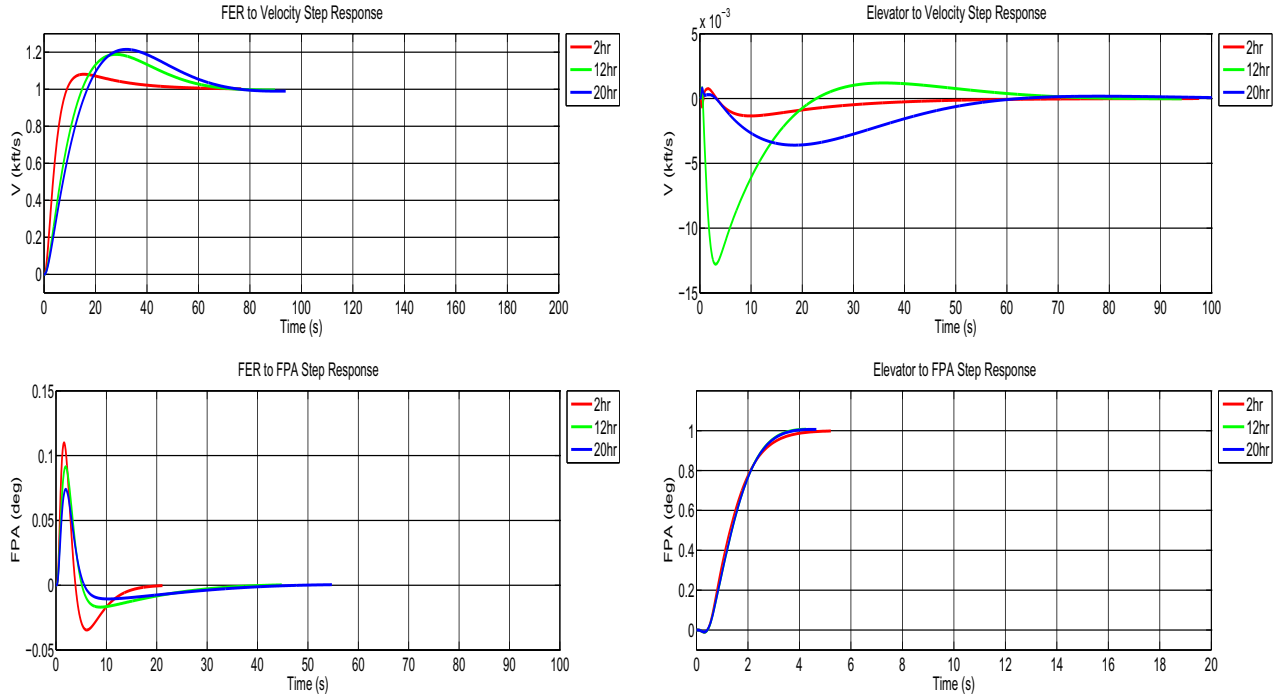

Figure 97: Step responses with prefilter for flexible Controller for prolonged heating at structure surface with TPS, flight dependent net heat flux input

Frequency Responses

From fig 98,

- Sensitivities experience peaking moving toward lower frequency.
- Sensitivity at Error and Control has no severe peaking even after 20hr of flight.
- Sensitivities experience peaking of first fundamental frequency moving toward lower frequency for increased heating.
- OLTF Plant singular value experiences hiked peaking for phugoid mode frequencies after 20hr of flight.

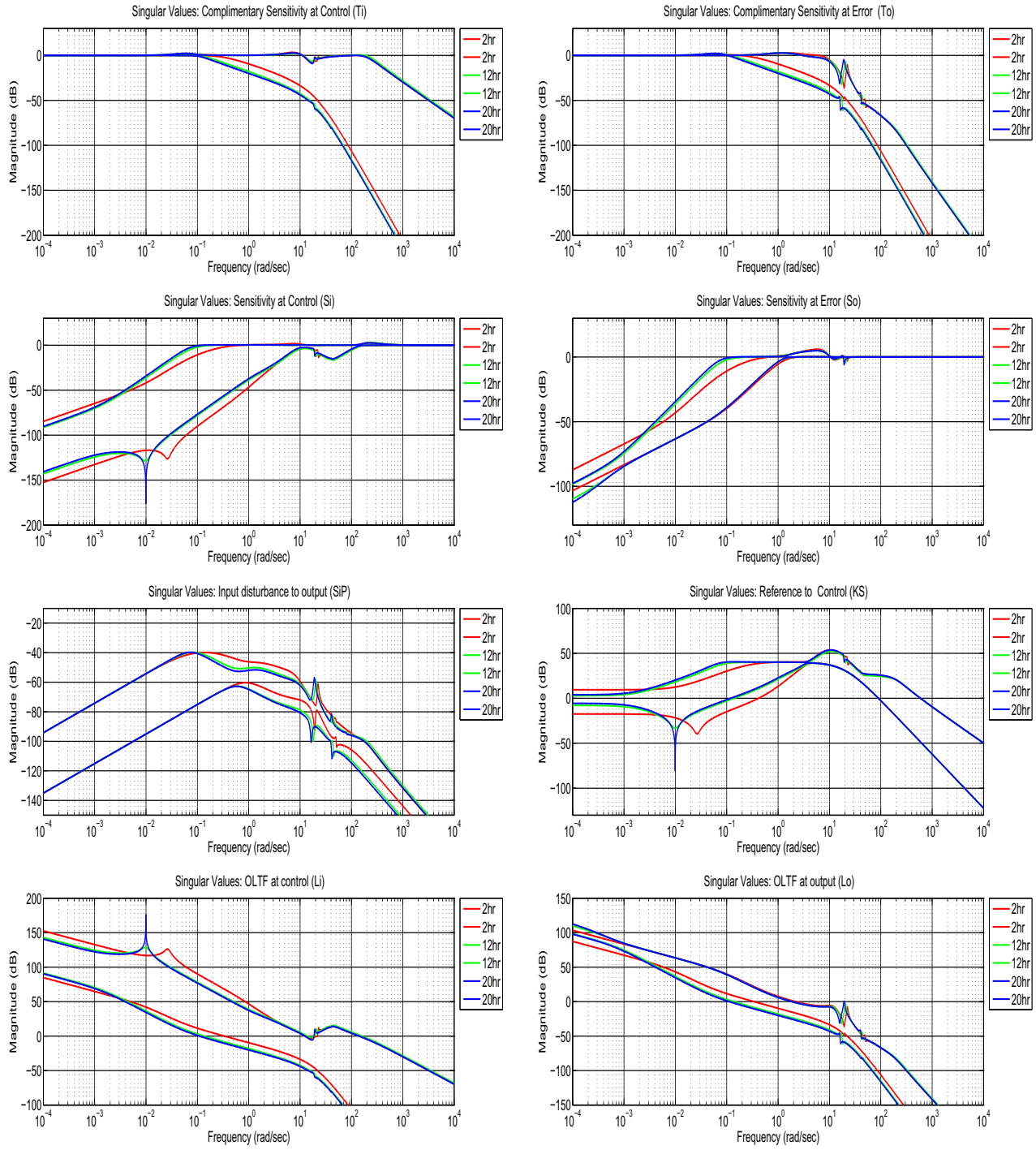

Figure 98: Frequency response with flexible Controller for prolonged heating at structure surface with TPS, constant net heat flux input of 15BTU/ft^{2}s

7.7.4 Case4: Without TPS, Constant heat flux (PM2k 0, SiO2 0, Titanium 9.6)

1. Without TPS, constant heat flux (15BTU/ft2s) at Mach8, Altitude85kft , Control Designed for nominal model after 2hr of heating is also valid after 20hr of flight.
2. Elevator to FPA step response is unaffected by the 20hr heating.
3. Sensitivities do not experience peaking due to 20hr heating
4. Sensitivity peaking at first fundamental frequency becomes dominant (greater than phugoid mode frequencies)

Time Responses

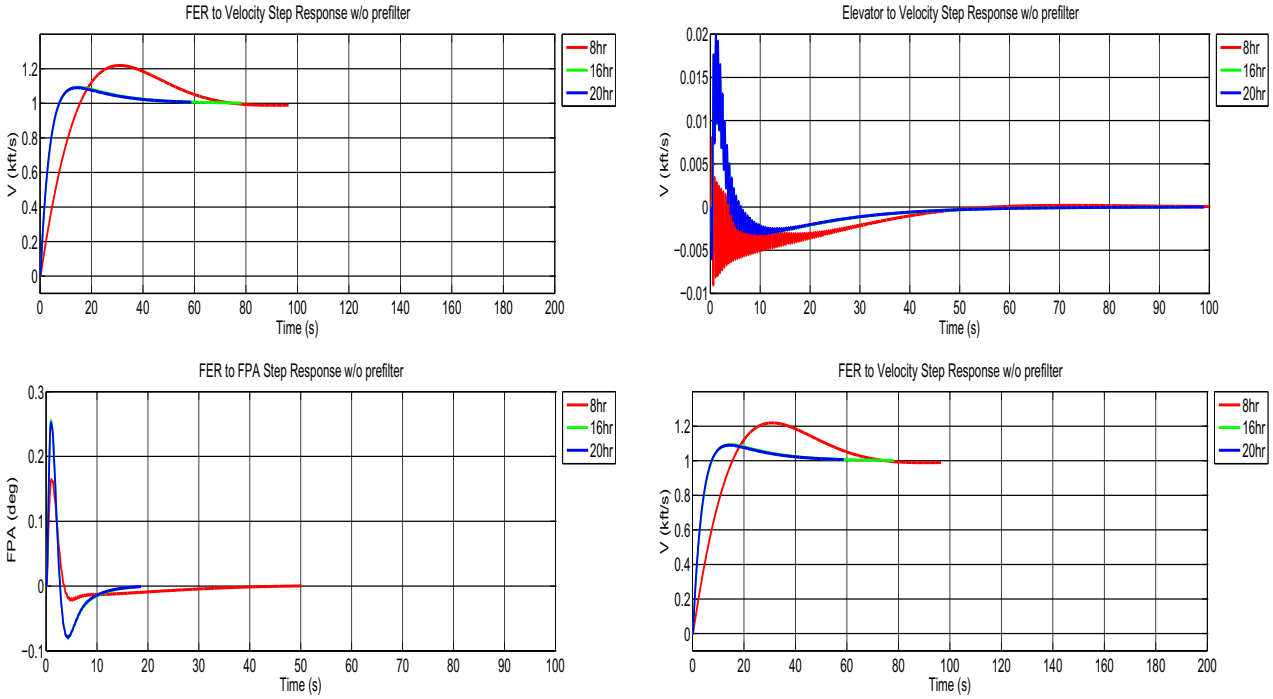

Figure 99: Step responses without prefilter for flexible Controller provided prolonged heating at structure surface with TPS, constant net heat flux input of 15BTU/ft^{2}s

From fig 100, 99

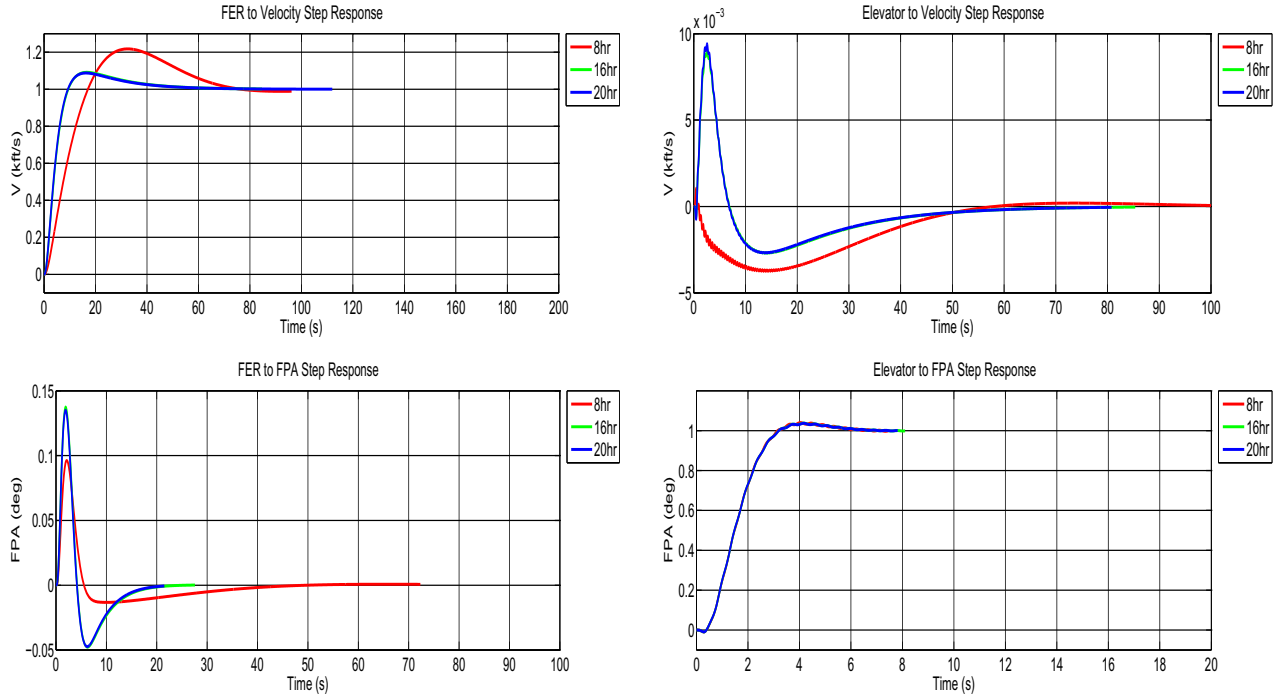

Figure 100: Step responses with prefilter for flexible Controller for prolonged heating at structure surface without TPS, flight dependent net heat flux input

- Elevator to FPA step responses for increased hours of heating with TPS causes peak overshoot to decrease and reduce the settling time.
- Ripples gets lowered with increased heating duration for Elevator to FPA step response without pre-filter

Frequency Responses

From fig 101,

- Sensitivities experience hiked peaking of first fundamental frequency with longer heating duration.
- Sensitivity at Error and Control have reduced peaking with large heating hours.
- Sensitivity have reduced peaking with large heating hours.

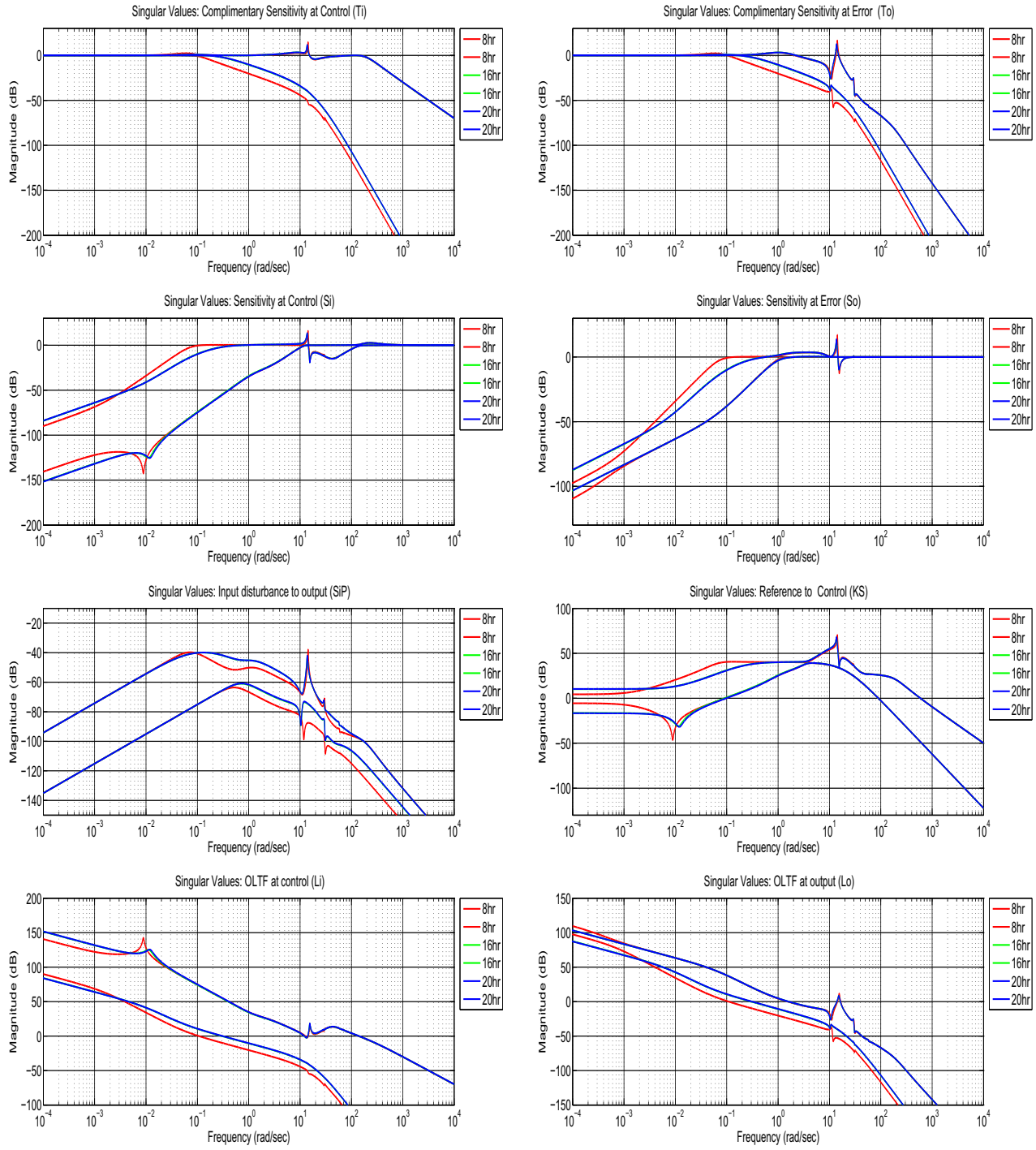

Figure 101: Frequency response with flexible Controller for prolonged heating at structure surface without TPS, constant net heat flux input of 15BTU/ft^{2}s

7.8 Structural Dimension effects on Controller Performance

De-centralized Controller performances for variable thickness of titanium are two cases namely with and without TPS.

7.8.1 w/o TPS, flight dependent heat flux (PM2k 0, SiO2 0, Titanium 4 to 9.6)

1. Without TPS, flight dependent heat flux at Mach8, Altitude85kft , Control Designed for nominal model after 2hr of heating is applied to other plants with decreasing Titanium thicknesses.
2. Control fails to stabilize titanium thickness below 7.
3. Elevator to FPA step response exhibits increased peak overshoot by the titanium thickness reduction.
4. Singular values experience peaking due to titanium thickness reduction.

Time Responses

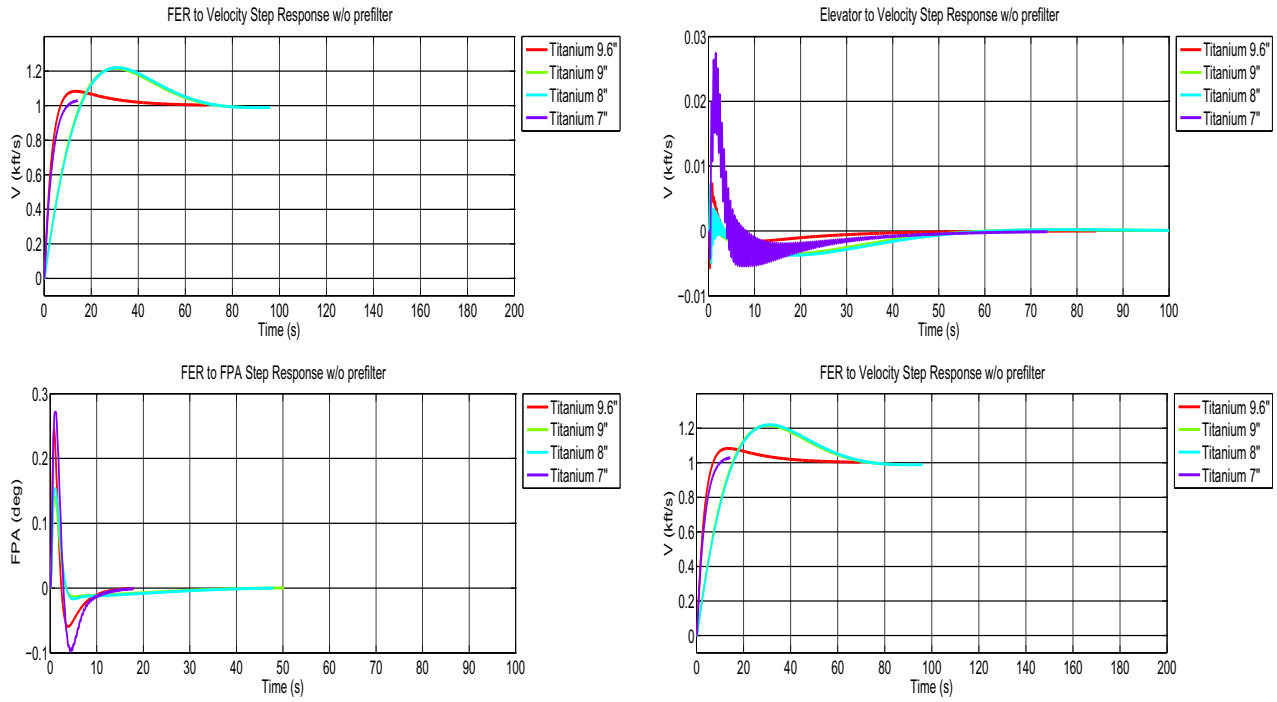

Figure 102: Step responses without prefilter for flexible Controller at structure surface without TPS, flight dependent net heat flux input, Titanium thickness variable

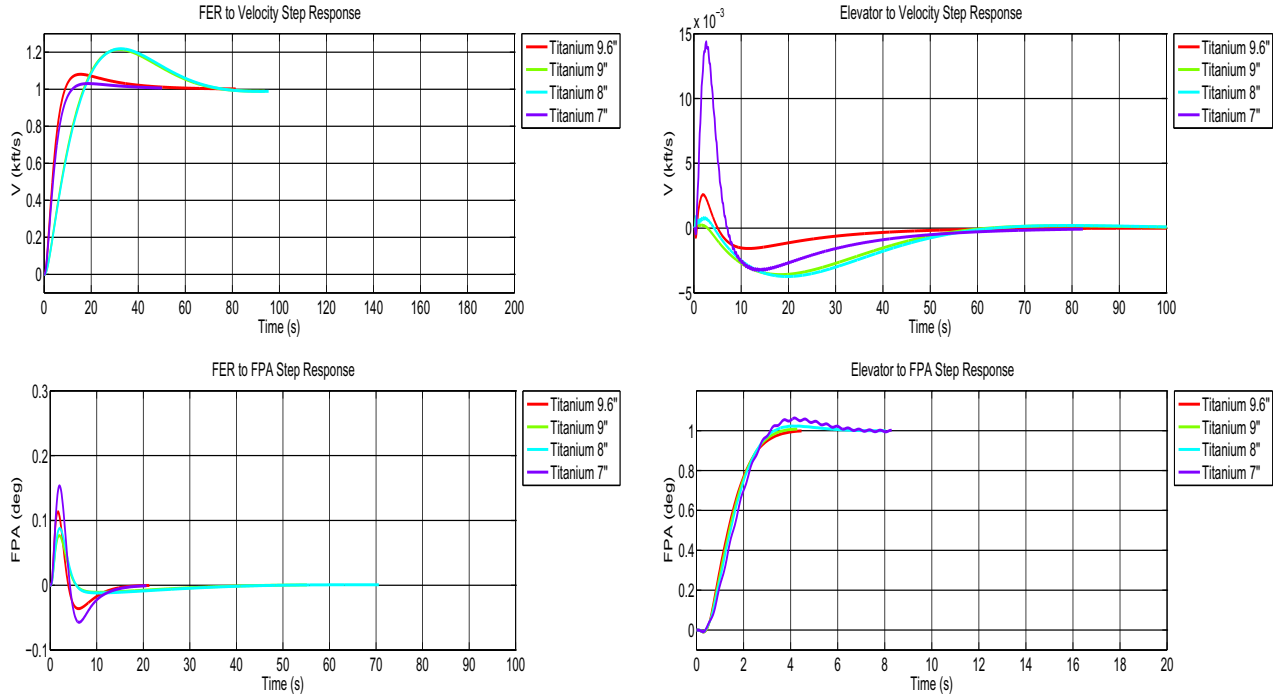

Figure 103: Step responses with prefilter for flexible Controller at structure surface without TPS, flight dependent net heat flux input, titanium thickness vary

From fig 103, 102

- Elevator to FPA step response exhibits increased peak overshoot by the titanium thickness reduction.
- Ripples start to develop with reduced Titanium thickness for Elevator to FPA step response without pre-filter.

Frequency Responses

From fig 104,

- Sensitivities peaking for the fundamental frequency experience hike for reduced Titanium thickness.
- Sensitivities are dominant as compared to phugoid mode frequency peaking.

- Sensitivities peaking for the fundamental frequency experience hike for reduced Titanium thickness.

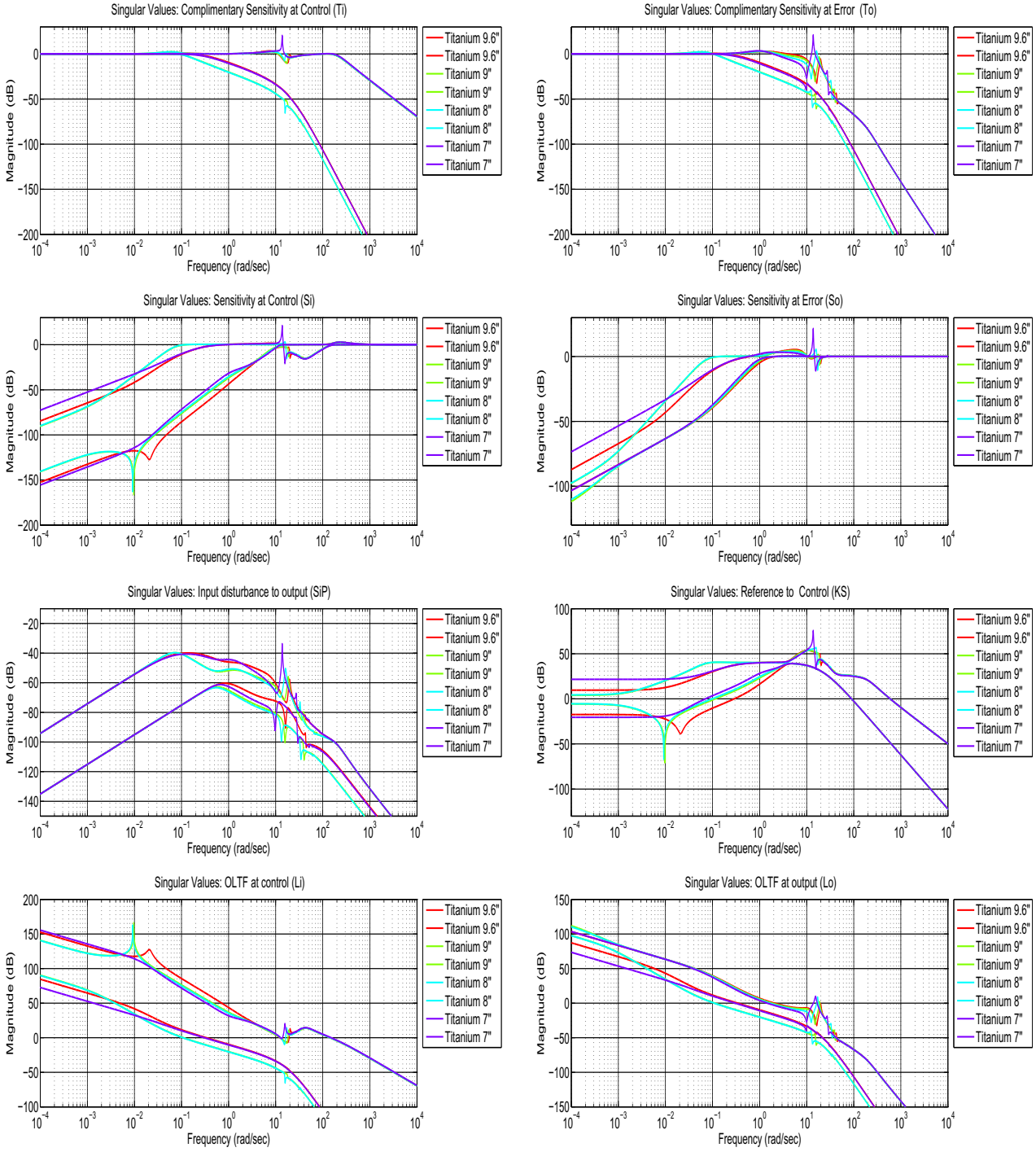

Figure 104: Frequency response with flexible Controller for structure surface without TPS, flight dependent net heat flux input, Titanium thickness varied

7.8.2 With TPS, flight dependent heat flux (PM2k 3, SiO2 0.1, Titanium 4 to 9.6)

1. With TPS, flight dependent heat flux at Mach8, Altitude85kft , Control Designed for nominal model after 2hr of heating is applied to other plants with decreasing Titanium thicknesses.
2. Nominal Control designed fails to stabilize Plants for titanium thicknesses below 8.
3. Elevator to FPA step response is unaffected by the titanium thickness reduction.
4. Sensitivities experience peaking due to titanium thickness reduction

Time Responses

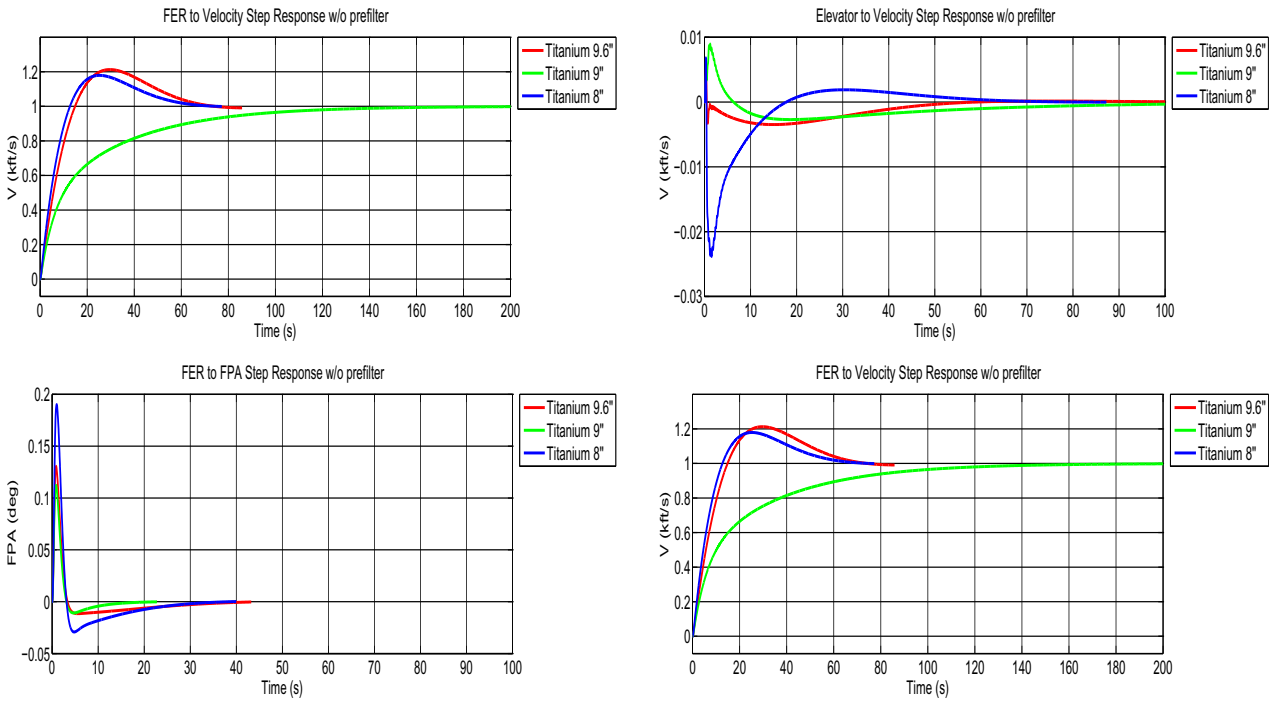

Figure 105: Step responses without prefilter for flexible Controller at structure surface including TPS, flight dependent net heat flux input, Titanium thickness variable

From fig 106, 105

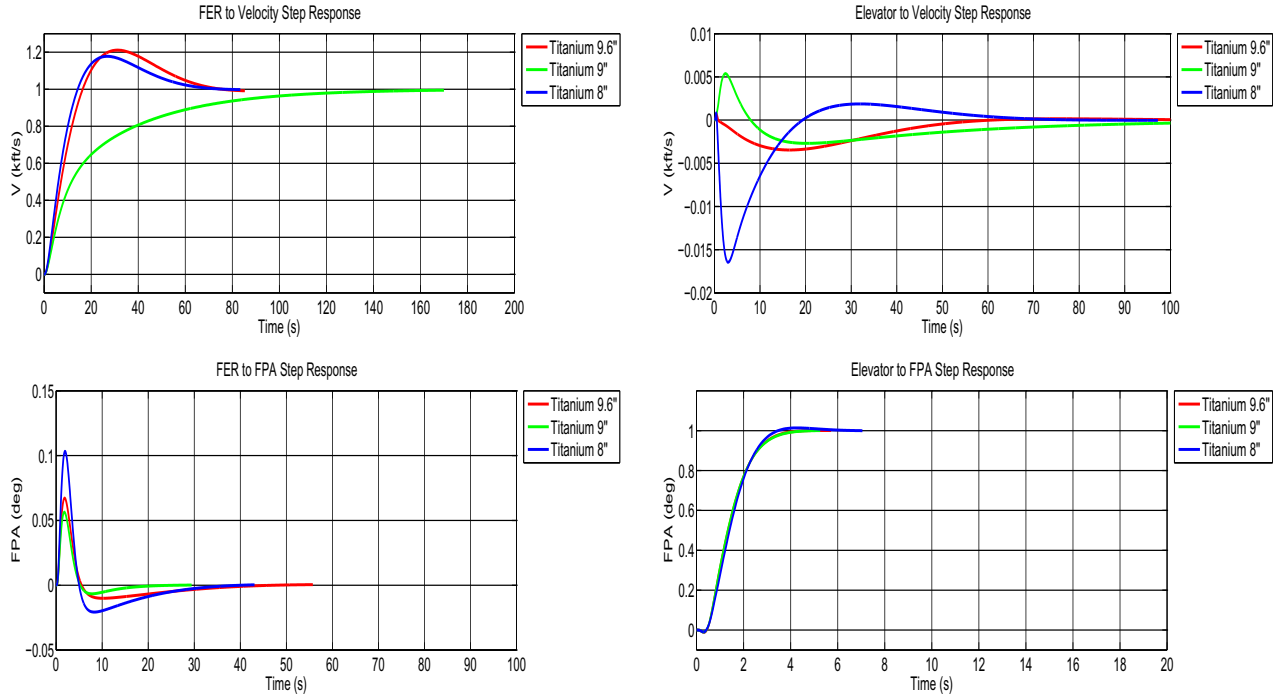

Figure 106: Step responses with prefilter for flexible Controller at structure surface with TPS, flight dependent net heat flux input, titanium thickness vary

- Elevator to FPA step response is unaffected by the titanium thickness reduction.
- Ripples get larger with decreased Titanium thickness for Elevator to FPA step response without pre-filter

Frequency Responses

From fig 107,

- Sensitivities for first fundamental frequency experience hiked peaking for reduced Titanium thickness.
- Phugoid mode frequencies are not effected by Titanium thinning with TPS and flight dependent heat flux.
- Sensitivities experience peaking moving toward lower frequency with lower titanium thickness.

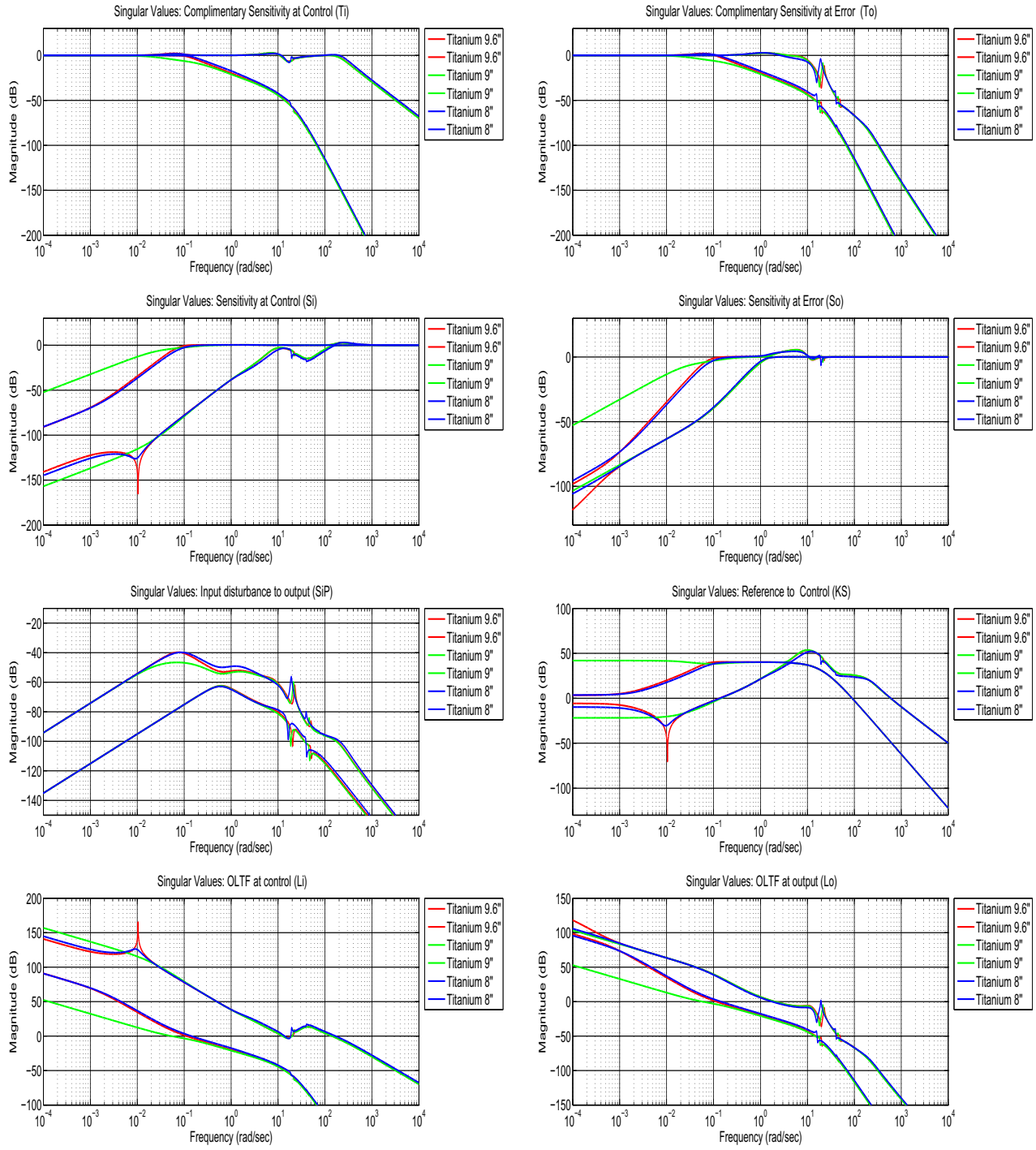

Figure 107: Frequency response with flexible Controller for structure surface with TPS, flight dependent net heat flux input, Titanium thickness varied

7.9 Summary

In this chapter, controller design for the hypersonic vehicle as well as the nominal performance of the controller were presented. It is shown that, the peak frequency-dependent (singular value) conditioning of the two-input two-output plant (FER-elevator to speed-FPA) does not change significantly due to prolonged heating, or change in titanium structure thicknesses. For the vehicle under consideration (with a very aggressive engine and no coupling), it is shown that a large FPA settling time (5sec) is needed in order to obtain reasonable (performance/robustness) properties at the plant input. The results in this section offer insight into control-relevant vehicle design.

Table 7.1: Sensitivities(dB) for Nominal Plant as well as the its application to other cases namely Elastic Ratio (ER), Mass ratio(MR), Prolonged heating with-without TPS, Titanium thickness variation with-without TPS

Max SV (dB)	Nominal Plant	ER 0.32	MR 0.9	20hrs Heat w TPS	20hrs Heat w/o TPS	8" Titanium w TPS	7" Titanium w/o TPS
So	5.70	17.13	9.04	5.25	4.51	4.39	21.69
To	2.65	16.34	5.31	2.67	3.03	2.94	21.21
Si	2.68	16.88	4.57	2.59	2.56	3.11	21.25
Ti	2.73	15.71	6.31	2.77	3.26	2.05	20.54
KS	53.27	71.64	56.76	53.72	54.94	52.12	75.91
SiP	-39.73	-38.37	-39.91	-39.73	-40.73	39.78	33.42

1. Nominal Controller is designed for Nominal Plant and then applied to several other cases.
2. Nominal Control fails to stabilize ER for and below 0.30
3. Nominal Control fails to stabilize MR for and below 0.8
4. Controller is robust for prolonged heating of 20hr.
5. Controller is robust for structural variation(titanium thickness decrease) with TPS upto 8". But fails to stabilize 7" and below.
6. Controller is robust for structural variation(titanium thickness decrease) without TPS upto 7". But fails to stabilize 6" and below.

8. Conclusions

8.1 Summary

This thesis examines heat modeling, analysis, vehicle design, and control system design issues for scramjet-powered hypersonic vehicles. A nonlinear 3DOF (degree of freedom) longitudinal model which includes aero-propulsion-elasticity effects is used for all analysis. The model is based upon classical compressible flow and Euler-Bernouli structural concepts.

The model is used to examine the vehicle's static and dynamic characteristics over the vehicle's trimmable region. The vehicle is characterized by unstable non-minimum phase dynamics with significant (approximately lower triangular) longitudinal coupling between fuel equivalency ratio (FER) or fuel flow and flight path angle (FPA).

The scope of this thesis is to analyze the flexibility, mass, heat and structural dimension effects on static and dynamic properties of the resultant model. With nominal control design when can we improve the performance of the model when vehicle become more flexible. Original model with Bolender's assumptions on plume centralized and de-centralized control design both had comparable performances. With the introduction of new plume and heating, de-centralized controller gave good performances.

Vehicle's structural Flexibility cause little or nor effect on the static properties while for 68% reduction in elasticity (EI) nominal controller looses it controllability. For 68% decrease in EI(elasticity) there is 43% decrease in fundamental frequency ω.

Mass Fraction of the TPS is about 10% of the total mass of the vehicle. It was seen that mass impacts static properties significantly while has little impact on dynamic properties. Controller for nominal model can no longer stabilize plants generated for 25% reduction in mass.

Addition of aerodynamic heat modeling had very little effect on the parameters. It was observed that after 2hr of sustained flight at mach 8, alt 85kft fundamental frequency dropped by 1.5%, surface temperature rose to steady state value of 2000R. Aerodynamic heating has very little impact on static and dynamic properties of linearized plant.

Changes in structural dimension of Titanium had very little effect on the static and dynamic parameters.

Without PM2000 (SiO2 0.1 Titanium 9.6), Flight dependent heat flux input: 2hr of sustained flight, Direct exposure of SiO2 to external environment cause tremendous heat addition to the surface. Temperature rises rapidly and gets past the maximum operating temperature within seconds.

8.2 Ideas for Future Research

The work presented in this thesis provides motivation for conducting comprehensive trade studies using higher fidelity vehicle models;i.e. 6DOF + flexibility [154]. As such, the work motivates the development of general 6DOF tools that adequately address control-relevant modeling, analysis, and design issues for hypersonic vehicles during the early vehicle conceptualization/design phases. One specific concern will be to assess when conclusions obtained from a 3DOF model may be misleading.

Future work would include the design and analysis of reasonable TPS structure and its effect on the static-dynamic properties of the vehicle. TPS designs based on mass and dimensional feasibility for the extreme environmental conditions such as large heat flux and high heat load. Attention would be towards a better control design and comparison of the H-inf based loop shaping centralized control structure to other design methods. Future work will also involves comparing these analytical solutions with higher fidelity CFD (computational fluid dynamics) solutions.

REFERENCES

[1] J. Anderson, *Hypersonic and High-Temperature Gas Dynamics*. Second Edition. AIAA, 2006.

[2] M. A. Bolender, M. W. Oppenheimer, and D. B. Doman, "Effects of unsteady and viscous aerodynamics on the dynamics of a flexible air-breathing hypersonic vehicle," in *AIAA 2007-6397*, 2007.

[3] J. T. Parker, A. Serrani, S. Yurkovich, M. A. Bolender, and D. B. Doman, "Control-oriented modeling of an air-breathing hypersonic vehicle," *AIAA J. Guidance, Control, and Dynamics, Accepted for publication*, 2007.

[4] M. A. Bolender and D. B. Doman, "A Non-Linear Longitudinal Dynamical Model of an Air-Breathing Hypersonic Vehicle," *J. Spacecraft and Rockets*, vol. 44 no. 2, pp. 373 – 387, 2007.

[5] M. W. Oppenheimer, D. B. Doman, M. A. Bolender, and T. Skujins, "A flexible hypersonic vehicle model developed with piston theory," in *AIAA 2007-6396*, 2007.

[6] M. Bolender and D. Doman, "Modeling unsteady heating effects on the structural dynamics of a hypersonic vehicle," in *AIAA-2006-6646*, 2006.

[7] D. Doman, M. Oppenheimer, and M. Bolender, "Progress in guidance and control research for space access and hypersonic vehicles," Air Force Research Laboratory (AFRL), Wright Patterson Air Force Base, pp. 1 – 18, Tech. Rep., 2006.

[8] D. Sigthorsson, A. Serrani, S. Yurkovich, M. Bolender, and D. Doman, "Tracking control for an overactuated hypersonic air-breathing vehicle with steady state constraints," in *AIAA Guidance, Navigation and Control Conf., Paper No. AIAA-2006-6558,*, 2006.

[9] T. Adami, J. Zhu, M. Bolender, D. Doman, and M. Oppenheimer, "Flight control of hypersonic scramjet vehicles using a differential algebraic approach," in *AIAA Guidance, Navigation and Control Conf., Paper No. AIAA-2006-6559,*, 2006.

[10] T. Williams, M. A. Bolender, D. Doman, and O. Mortaya, "An Aerothermal Flexible Mode Analysis of a Hypersonic Vehicle," Airforce Research Laboratory (AFRL), Wright Patterson Air Force Base, pp. 1 – 25,, Tech. Rep., 2006.

[11] J. T. Parker, A. Serrani, S. Yurkovich, M. Bolender, and D. Doman, "Approximate feedback linearization of an air-breathing hypersonic vehicle," Air

Force Research Laboratory (AFRL), Wright Patterson Air Force Base, pp. 1 – 20, Tech. Rep., 2005.

[12] K. Groves, D. Sigthorsson, A. Serrani, S. Yurkovich, M. Bolender, and D. Doman, "Reference command tracking for a linearized model of an air-breathing hypersonic vehicle," in *AIAA Guidance, Navigation and Control Conf. and Exhibit, Paper No. AIAA-2005-6144*, 2005.

[13] K. P. Groves, A. Serrani, S. Yurkovich, M. Bolender, and D. Doman, "Anti-windup control for an air-breathing hypersonic vehicle model," Air Force Research Laboratory (AFRL), Wright Patterson Air Force Base, pp. 1 – 27, Tech. Rep., 2005.

[14] M. A. Bolender and D. B. Doman, "A Non-Linear Model for the Longitudinal Dynamics of a Hypersonic Air-Breathing Vehicle," in *Proceedings of the 2005 Guidance, Navigation and Control Conf., Paper No. 2005-6255*, 2005.

[15] ——, "Flight Path Angle Dynamics of Air-Breathing Hypersonic Vehicles," Airforce Research Laboratory (AFRL), Wright Patterson Air Force Base, pp. 1 – 37, Tech. Rep., 2005.

[16] E. Kolawa, "Extreme environment technologies for future space science missions," NASA, Sept 2007.

[17] E. Baumann, C. Bahm, B. Strovers, R. Beck, and M. Richard, "The X-43A Six Degree of Freedom Monte Carlo Analysis," in 46^{th} *AIAA Aerospace Sciences Meeting and Exhibit, Paper No. 2008-203*, 2008.

[18] C. Peebles, *Road to Mach 10: Lessons Learned from the X-43A Flight Research Program*. AIAA, 2008.

[19] C. R. McClinton, "X-43 Scramjet Power Breaks the Hypersonic Barrier Dryden Lectureship in Research for 2006," 44^{th}*AIAA Aerospace Sciences Meeting and Exhibit, Paper No. 2006-1*, 2007.

[20] V. L. Rausch, C. R. McClinton, and J. L. Crawford, "Hyper-X Flight Validation of Hypersonic Airbreathing Technology," Technical Report, NASA Hyper-X Program Office, pp. 1 – 7, 1997.

[21] W. H. Heiser, D. T. Pratt, D. Daley, and U. Mehta, *Hypersonic Airbreathing Propulsion*. AIAA, 1994.

[22] M. Davis and J. White, "X-43A Flight-Test-Determined Aerodynamic Force and Moment Characteristics at Mach 7.0 ," *J. of Spacecraft and Rockets*, vol. 45, no. 3, pp. 472–484, 2008.

[23] E. A. Morelli, S. D. Derry, and M. S. Smith, "Aerodynamic Parameter Estimation for Flight 2 of the X-43A," *Joint Army Navy NASA Air Force JANNAF Conf.*, 2005.

[24] S. D. Holland, W. C. Woods, and W. C. Engelund, "Hyper-X Research Vehicle Experimental Aerodynamics Test Program Overview," *J. Spacecraft and Rockets*, vol. 38, no. 6, pp. 828–835, 2001.

[25] Q. Wang and R. F. Stengel, "Robust nonlinear control of a hypersonic vehicle," *J. Guidance, Control, and Dynamics*, pp. 577 – 585, 2000.

[26] B. Cobleigh, "Development of the X-33 Aerodynamic Uncertainty Model," NASA/TP-1998-206544, April 1998.

[27] H. Buschek and A. J. Calise, "Uncertainty Modeling and Fixed-Order Controller Design for a Hypersonic Vehicle Model," *J. Guidance, Control and Dynamics*, pp. 42 – 48, 1997.

[28] J. J. Bertin, *Hypersonic Aerothermodynamics*. AIAA Education Series, 1994.

[29] H. Buschek and A. J. Calise, "Robust control of hypersonic vehicles considering propulsive and aeroelastic effects," *Paper No. AIAA-1993-3762*, pp. 1 – 11, 1993.

[30] J. J. Bertin, J. Periaux, and J. Ballmann, *Advances in Hypersonics: Defining the Hypersonic Environment, Volume 1*. Birkhauser Boston, 1992.

[31] ——, *Advances in Hypersonics: Modeling Hypersonic Flows, Volume 2*. Birkhauser Boston, 1992.

[32] ——, *Advances in Hypersonics: Computing Hypersonic Flows, Volume 3*. Birkhauser Boston, 1992.

[33] J. Young and J. Underwood, "Development of Aerodynamic Uncertainties for the Space Shuttle Orbiter ," *J. of Spacecraft and Rockets*, vol. 20, no. 6, pp. 513–517, 1983.

[34] J. Heeg, T. A. Zieler, A. S. Potozky, C. V. Spain, and W. C.Englend, "Aerothermoelastic Analysis of a NASP Demonstrator Model, Report No. NAS 1.15109007," NASA, Tech. Rep., 1993.

[35] D. Johnson, C. Hill, S. Brown, and G. Batts, "Natural Environment Application for NASP-X-30 design and mission planning ," in 31^{st} *Aerospace Sciences Meeting and Exhibit, Paper No. 1993-851*, 1993.

[36] D. Johnson, "Beyond the X-30 - Incorporating mission capability ," in 3^{rd} *Int. Aerospace Planes Conf., Paper No. 1991-5078*, 1991.

[37] J. D. Shaughnessy, S. Z. Pinckney, J. D. McMinn, C. I. Cruz, and M. L. Kelley, "Hypersonic Vehicle Simulation Model: Winged-Cone Configuration, No. 102610," NASA, Tech. Rep., 1990.

[38] J. J. McNamara and P. P. Friedmann, "Aeroelastic and Aerothermoelastic Analysis of Hypersonic Vehicles: Current Status and Future Trends," 48^{th} *AIAA/ASME/ASCE/AHS/ASC Structures, Structural Dynamics, and Materials Conference, Paper No. 2007-2013*, 2007.

[39] P. P. Friedmann, J. J. McNamara, B. Thuruthimattam, and I. Nydick, "Aeroelastic Analysis of Hypersonic Vehicles," *J. Fluids and Structures*, pp. 681 – 712, 2004.

[40] J. McNamara, P. Friedmann, K. Powell, B. Thuruthimattam, and R. Bartels, "Aeroelastic and Aerothermoelastic Vehicle Behavior in Hypersonic Flow ," in *AIAA/CIRA* 13^{th} *International Space Planes and Hypersonics Systems and Tech. Conf., Paper No. AIAA-2005-3305*, 2005.

[41] B. Pamadi, G. Brauckmann, M. Ruth, and H. Fuhrmann, "Aerodynamic Characteristics, Database Development, and Flight Simulation of the X-34 Vehicle," *J. of Spacecraft and Rockets*, vol. 38, pp. 334–344, 2001.

[42] C. Bahm, E. Baumann, J. Martin, D. Bose, R. E. Beck, and B. Strovers, "The X-43A Hyper-X Mach 7 Flight 2 Guidance, Navigation, and Control Overview and Flight Test Results," in *AIAA/CIRA International Space Planes and Hypersonic Systems and Technologies Conference*, 2005, pp. 682 – 704.

[43] J. Hank, J. Murphy, and R. Mutzman, "The X-51A Scramjet Engine Flight Demonstration Program ," in 15^{th} *AIAA International Space Planes and Hypersonic Systems and Technologies Conf, Paper No. AIAA-2008-2540*, 2008.

[44] S. Walker, M. Tang, S. Morris, and C. Mamplata, "Falcon HTV-3X - A Reusable Hypersonic Test Bed," in 15^{th} *AIAA International Space Planes and Hypersonic Systems and Tech. Conf., Paper No. AIAA-2008-2544*, 2008.

[45] S. Walker, J. Sherk, D. Shell, R. Schena, J. Bergmann, and J. Gladbach, "The DARPA/AF Falcon Program: The Hypersonic Technology Vehicle 2 (HTV-2) Flight Demonstration Phase," in 15^{th} *AIAA International Space Planes and Hypersonic Systems and Technologies Conf., Paper No. 2008-2539*, 2008.

[46] S. H. Walker and F. Rodgers, "Falcon Hypersonic Technology Overview," *AIAA/CIRA* 13^{th} *International Space Planes and Hypersonics Systems and Technologies, Paper No. 2005-3253*, 2005.

[47] B. Fidan, M. Mirmirani, and P. Ioannou, "Flight Dynamics and Control of Air-Breathing Hypersonic Vehicles: Review and New Directions," in 12^{th} *AIAA/AHI Space Planes and Hypersonic Systems and Technologies Conf. Paper No. 2003-7081*, 2003.

[48] R. T. Voland, L. D. Huebner, and C. R. McClinton, "X-43A Hypersonic Vehicle Technology Development," Technical Report, NASA Langley Research Center, Hampton, VA, Report No. IAC-05-D2.6.01, 2005.

[49] A. Kumar, J. P. Drummond, C. R. McClinton, and J. L. Hunt, "Research in Hypersonic Airbreathing Propulsion at the NASA Langley Research Center," National Aeronautics and Space Administration (NASA), Report No. ISABE-2001-4, Tech. Rep., 2001.

[50] J. Heeg, M. G. Gilbert, and A. S. Pototzky, "Active control of aerothermoelastic effects for a conceptual hypersonic aircraft," *J. of Aircraft*, pp. 453 – 458, 1993.

[51] M. G. Gilbert, J. Heeg, A. S. Potozky, C. V. Spain, D. L. Scistmann, and H. J. Dunn, "The Application of Active Controls Technology to a Generic Aircraft Configuration," National Aeronautics and Space Administration (NASA), Report No. NAS 1.15101689, Tech. Rep., 1990.

[52] J. Heeg, M. G. Gilbert, and A. S. Pototzky, "Active control of aerothermoelastic effects for a conceptual hypersonic vehicle," in *AIAA Guidance, Navigation and Control Conf., Paper No. AIAA-1990-3337, pp. 200 – 208*, 1990.

[53] A. S. Potozky, C. V. Spain, D. L. Spain, and T. E. Noll, "Application of Unsteady Aeroelastic Analysis Techniques on the National Aerospace Plane," National Aeronautics and Space Administration (NASA), Report No. NAS 1.15100648, Tech. Rep., 1988.

[54] D. Glass, "Ceramic Matrix Composite (CMC) Thermal Protection Systems (TPS) and Hot Structures for Hypersonic Vehicles ," in 15^{th} *AIAA International Space Planes and Hypersonic Systems and Technologies Conf/*, 2008.

[55] [Online]. Available: http://www.uq.edu.au/hypersonics/index.html?page=19501

[56] M. Smart, N. Hass, and A. Paull, "Flight Data Analysis of the HyShot 2 Scramjet Flight Experiment," *AIAA Journal*, vol. 44, Issue 10, pp. 2366–2375, 2006.

[57] S. Walker, F. Rodgers, A. Paull, and D. V. Wie, "HyCAUSE Flight Test Program," in 15^{th} *AIAA International Space Planes and Hypersonic Systems and Technologies Conf., Paper No. 2008-2580*, 2008.

[58] X-43A Mishap Investigation Board, "Report of Findings: X-43A Mishap," Technical Report, pp. 1 – 33, 2003.

[59] D. E. Reubush, L. T. Nguyen, , and V. L. Rausch, "Review of X-43A Return to Flight Activities and Current Status," *12th AIAA International Space Planes and Hypersonic Systems and Technologies, Paper No. 2003-7085*, 2003.

[60] L. Marshall, G. Corpening, and R. Sherrill, "A Chief Engineer's View of the NASA X-43A Scramjet Flight Test," in *AIAA/CIRA* 13^{th} *International Space Planes and Hypersonics Systems and Tech. Conf., Paper No. AIAA-2005-3332* , 2005.

[61] C. Bahm, E. Baumann, J. Martin, D. Bose, R. Beck, and B. Strovers, "The X-43A Hyper-X Mach 7 Flight 2 Guidance, Navigation, and Control Overview and Flight Test Results," in *AIAA/CIRA* 13^{th} *International Space Planes and Hypersonics Systems and Technologies Conf., Paper No. AIAA-2005-3275*, 2005.

[62] S. M. Ferlemann, C. R. McClinton, K. E. Rock, and R. T. Voland, "Hyper-X Mach 7 Scramjet Design, Ground Test and Flight Results," Technical Report, NASA Langley Research Center, Hampton, VA, pp. 1 – 9, 1999.

[63] C. E. Cockrell, W. C. Englelund, R. D. Bittner, T. N. Jentink, A. D. Dilley, and A. Frendi, "Integrated Aeropropulsive Computational Fluid Dynamics Methodology for the Hyper-X Flight Experiment," *J. of Spacecraft and Rockets*, pp. 836 – 843, 2001.

[64] L. Marshall, C. Bahm, G. Corpening, and R. Sherril, "Overview With Results and Lessons Learned of the X-43A Mach 10 Flight," in *AIAA/CIRA* 13^{th} *International Space Planes and Hypersonics Systems and Technologies Conf., 2005-3336*.

[65] R. C. Rogers, A. T. Shih, and N. E. Hass, "Scramjet Engine Flowpath Development for the Hyper-X Mach 10 Flight Test," National Aeronautics and Space Administration (NASA), Report No. ISABE-2005-1025, Tech. Rep., 2005.

[66] J. Davidson, F. Lallman, J. D. McMinn, J. Martin, J. Pahle, M. Stephenson, and J. Selmon, "Flight Control Laws for NASA's Hyper-X Research Vehicle," *AIAA Guidance, Navigation, and Control Conference and Exhibit,*

Paper No. 1999-4124, 1999.

[67] E. Morelli, S. Derry, and M. Smith, "Aerodynamic Parameter Estimation for the X-43A (Hyper-X) from Flight Data," in *AIAA Atmospheric Flight Mechanics Conf. and Exhibit, Paper No. AIAA-2005-5921*, 2005.

[68] D. Dolvin, "Hypersonic International Flight Research and Experimentation (HIFiRE) Fundamental Science and Technology Development Strategy ," in 15^{th} *AIAA International Space Planes and Hypersonic Systems and Technologies Conf., Paper No. 2008-2582*, 2008.

[69] B. H. M. Tang and R. Chase, "The Quest for Hypersonic Flight with Air-Breathing Propulsion," in 15^{th} *AIAA International Space Planes and Hypersonic Systems and Technologies Conf., Paper No. 2008-2546*, 2008.

[70] "Blackswift Program Solicitation," Defense Advanced Research Projects Agency, Tech. Rep., February, 2008.

[71] M. D. Salas, "DIGITAL FLIGHT: the last CFD aeronautical grand challenge," *J. Scientific Computing*, pp. 1 – 63, 2004.

[72] J. J. McNamara, "Aeroelastic and Aerothermoelastic Behavior of Two and Three Dimensional Lifting Surfaces in Hypersonic Flow," Ph.D. dissertation, University of Michigan, 2005.

[73] M. Maughmer, L. Ozoroski, D. Straussfogel, and L. Long, "Validation of Engineering Methods for Predicting Hypersonic Vehicle Control Forces and Moments," *J. of Guidance, Control and Dynamics*, vol. 16, pp. 762–769, 1993.

[74] S. Keshmirir, "Nonlinear and Linear Longitudinal and Lateral-Directional Dynamical Model of Air-Breathing Hypersonic Vehicle," in 15^{th} *AIAA International Space Planes and Hypersonic Systems and Technologies Conf.*, 2008.

[75] S. Keshmiri, "Modeling and Simulation of a Generic Hypersonic Vehicle," Ph.D. dissertation, University of Kansas, 2007.

[76] S. Keshmiri, R. Colgren, and M. Mirmirani, "Modeling and Simulation of a Generic Hypersonic Vehicle using Merged Aerodynamic Models," in 14^{th} *AIAA/AHI Space Planes and Hypersonic Systems and Technologies Conf., Paper No. 2006-8087*, 2006.

[77] ——, "Six-DOF Modeling and Simulation of a Generic Hypersonic Vehicle for Control and Navigation Purposes," in *AIAA Guidance, Navigation and Control Conf., Paper No. 2006-6694*, 2006.

[78] S. Keshmiri, R. Colgren, S. Farokhi, and M. Mirmirani, "Ramjet and Scramjet Engine Cycle Analysis for a Generic Hypersonic Vehicle," in 14^{th} *AIAA/AHI Space Planes and Hypersonic Systems and Technologies Conf., Paper No. 2006-8158*, 2006.

[79] S. Keshmiri, R. Colgren, and M. Mirmirani, "Development of an Aerodynamic Database for a Generic Hypersonic Air Vehicle," in *AIAA Guidance, Navigation and Control Conf., Paper No. 2006-6257*, 2005.

[80] ——, "Six-DOF Modeling and Simulation of a Generic Hypersonic Vehicle for Conceptual Design Studies," in *AIAA Modeling and Simulation Technologies Conf., Paper No. 2004-4805*, 2004.

[81] P. Lohsoonthorn, E. Jonckheere, and S. Dalzell, "Eigenstructure vs constrained $\mathcal{H}^{\infty}$ design for hypersonic winged cone," *J. Guidance, Control and Dynamics*, pp. 648 – 658, 2001.

[82] F. R. Chavez and D. K. Schmidt, "Analytical Aeropropulsive/Aeroelastic Hypersonic-Vehicle Model with Dynamic Analysis," *J. Guidance, Control and Dynamics*, pp. 1308 – 1319, 1994.

[83] J. D. Anderson, *Modern Compressible Flow,* 3^{rd} *Edition*. McGraw-Hill, 2002.

[84] A. Clark, C. Wu, M. Mirmirani, and S. Choi, "Development of an Airframe Integrated Generic Hypersonic Vehicle Model," in *AIAA Aerospace Conference and Exhibit,Paper No. 2006-6560*, 2006.

[85] A. Clark, M. Mirmirani, S.Choi, C. Wu, and K. Mathew, "An Aero-Propulsion Integrated Elastic Model of a Generic Airbreathing Hypersonic Vehicle," in *AIAA Guidance, Navigation, and Control Conf., Paper No. 2006-6560*, 2006.

[86] R. Starkey and M. Lewis, "A Simple Analytical Model for Parametric Studies of Hypersonic Waveriders ," in 8^{th} *AIAA International Space Planes and Hypersonic Systems and Technologies Conf. Paper No. 1998-1616*, 1998.

[87] I. Blankson, "Airbreathing Hypersonic Cruise: Prospects for Mach 4-7 Waverider Aircraft," in *ASME Int. Gas Turbine and Aerospace Congress and Exposition, Paper No. 92-GT-437*, June 1992.

[88] D. Capriotti, K. Bowcutt, and J. Anderson, "Viscous Optimized Hypersonic Waveriders," in *AIAA* 25^{th} *Aerospace Sciences Meeting, Paper No. 1987-272*, 1987.

[89] T. Nonwiler, "Aerodynamic Problems of Manned Space Vehicles," *J. of the*

Royal Aeronautical Society, vol. 63, pp. 521–528, 1959.

[90] R. Starkey, D. Liu, R. Chang, and P. Chem, "Rapid Conceptual Design and Analysis of a Hypersonic Air-Breathing Missile ," in 15^{th} *AIAA International Space Planes and Hypersonic Systems and Technologies Conf., 2008-2590*, 2008.

[91] K. Bowcutt, G. Kuruvila, T. Grandine, and E. Cramer, "Advancements in Multidisciplinary Design Optimization Applied to Hypersonic Vehicles to Achieve Performance Closure," in 15^{th} *AIAA International Space Planes and Hypersonic Systems and Technologies Conf, Paper No. AIAA-2008-2591*, 2008.

[92] P. Moses, K. Bouchard, R. Vause, S. Pinckney, S. Ferlemann, C. Leonard, L. Taylor, J. Robinson, J. Martin, D.H.Petley, and J. Hunt, "An airbreathing launch vehicle design with trubine-based low-speed propulsion and dual mode scramjet high-speed propulsion," in 21^{st} *International Space Planes and Hypersonic Systems and Technologies Conference*, 1999.

[93] J. Robinson, J. Martin, J. Bowles, U. Mehta, and C. Snyder, "An overview of the role of systems analysis in nasa's hypersonics project," in 14^{th} *AIAA/AHI Space Planes and Hypersonic Systems and Technologies Conf. Paper No. AIAA-2006-8013*, 2006.

[94] J. Pittman and P. A. Bartolotta, "Fundamental aeronautics hypersonics project reference document," National Aeronautics and Space Administration (NASA), Tech. Rep., 2006.

[95] C. McClinton, "High Speed Hypersonic Aircraft Propulsion Technology Development," NASA Hypersonics GNC Kickoff Workshop Presentation, NASA Glenn, 84 slides, April 2007.

[96] D. McRuer, "Design and Modeling Issues for Integrated Airframe/Propulsion Control of Hypersonic Flight Vehicles," in *American Control Conf., pp. 729 – 734*, 1991.

[97] J. C. E. Cockrell, A. H. Auslender, R. W. Guy, C. R. McClinton, and S. S. Welch, "Technology Roadmap for Dual-Mode Scramjet Propulsion to Support Space-Access Vision Vehicle Development," in *AIAA/AAAF International Space Planes and Hypersonic Systems and Technologies Conf., pp. 1 – 14*, 2002.

[98] G. Stien, "Respect the unstable," IEEE Control Systems Magazine, August 2003, pp. 12 - 25.

[99] A. A. Rodriguez, *Analysis and Design of Multivariable Feedback Control Systems*, Control3D, Ed. Control3D, LLC, 2004.

[100] R. Lind, "Linear parameter-varying modeling and control of structural dynamics with aerothermoelastic effects," *J. Guidance, Control, and Dynamics*, pp. 733 – 739, 2002.

[101] M. W. Oppenheimer and D. B. Doman, "Control of unstable, nonminumum phase hypersonic vehicle," in *IEEE Aerospace Conf., pp. 5782 – 5787*, 2006.

[102] J. Khatri, "Modeling, analysis, and control of a hypersonic vehicle with significant aero-thermo-elastic-propulsion interactions and thermo-elastic uncertainty," Master's thesis, Arizona State University, 2010.

[103] M. W. Oppenheimer and D. B. Doman, "A hypersonic vehicle model using developed with piston theory," in *AIAA 2006-6637*, 2006.

[104] M. Oppenheimer and D. Doman, "A Hypersonic Vehicle Model Developed with Piston Theory," Airforce Research Laboratory (AFRL), Wright Patterson Air Force Base, pp. 1 – 26, Tech. Rep., 2006.

[105] A. Rodriguez, J. Dickeson, R. McCullen, A. Kelkar, and J. Vogel, "Control System Tradeoffs for a Scramjet-Powered Hypersonic Vehicle," in *to be submitted to 2008 GNC*, 2008.

[106] K. Groves, A. Serrani, S. Yurkovich, M. Bolender, and D. Doman, "Anti-Windup Control for an Air-Breathing Hypersonic Vehicle Model," in *AIAA Guidance, Navigation, and Control Conf. and Exhibit, Paper No. AIAA 2006-6557*, 2006.

[107] D. Soloway, A. Rodriguez, J. Dickeson, O. Cifdaloz, J. Benavides, S. Sridharan, A. Kelkar, and J. Vogel, "Constraint Enforcement for Scramjet-Powered Hypersonic Vehicles with Significant Aero-Elastic-Propulsion Interactions," in *2009 American Control Conference, Accepted for Publication*, 2009.

[108] J. Dickeson, A. Rodriguez, S. Sridharan, J. Benavides, D. Soloway, A. Kelkar, and J. Vogel, "Decentralized control of an airbreathing scramjet-powered hypersonic vehicle," in *AIAA Conf. on Guidance, Navigation and Control, AIAA-2009-6281*, 2009.

[109] A. A. Rodriguez, J. J. Dickeson, S. Sridharan, A. Khorad, J. Khatri, J. Benavides, D. Soloway, A. Kelkar, and J. M. Vogel, "Control-Relevant Modeling, Analysis, and Design for Scramjet-Powered Hypersonic Vehicles," in *16th AIAA/DLR/DGLR International Space Planes and Hypersonic Systems and Technologies Conference*, 2009.

[110] C. Breitsamter, T. Cvrlje, B. Laschka, M. Heller, and G. Sachs, "Lateral–Directional Coupling and Unsteady Aerodynamic Effects of Hypersonic Vehicles," *J. Spacecraft and Rockets*, pp. 159 – 167, 2001.

[111] M. E. Tauber and G. P. Menees, "Aerothermodynamics of transatmospheric vehicles," *Journal of Aircraft*, vol. 24, No. 9, pp. 594 – 602, 1986.

[112] S. Berry, K. Daryabeigi, K. Wurster, and R. Bittner, "Boundary Layer Transition on X-43A ," in 38^{th} *Fluid Dynamics Conf. and Exhibit, Paper No. 2008-3736*, 2008.

[113] S. A. Berry, A. H. Auslender, A. D. Diller, and J. F. Calleja, "Hypersonic Boundary-Layer Trip Development for Hyper-X," *J. Spacecraft and Rockets*, pp. 853 – 864, 2001.

[114] S. Torrez, N. Scholten, J. Driscoll, M. Bolender, M. Oppenheimer, and D. D. Doman, "A Scramjet Engine Model Including Effects of Precomubstions Shocks and Dissociation," in 44^{th} *AIAA/ASME/SAE/ASEE Joint Propulsion Conference and Exhibit, Paper No. 2008-6386*, 2008.

[115] D. H. Baldelli, R. Lind, and M. Brenner, "Nonlinear Aeroelastic/Aeroservoelastic Modeling by Block-Oriented Identification," *J. Guidance, Control and Dynamics*, pp. 1056 – 1064, 2005.

[116] R. Lind and M. Brenner, *Robust Aeroservoelastic Atability Analysis: Flight Test Applications*. Springer, 1999.

[117] "Aiaa guide to reference and standard atmosphere models (g-003b-2004)," 2004.

[118] D. L. Johnson, B. C. Roberts, and W. W. Vaughan, "Reference and Standard Atmosphere Models," in *10th Conference on Aviation, Range, and Aerospace Meteorology*, 2002.

[119] M. W. Oppenheimer and D. B. D. B. Doman, "Viscous effects for a hypersonic vehicle model," in *In preperation for submittal to the 2008 AIAA Atmospheric Flight Mechanics Conference*, 2008.

[120] C. R. McClinton, J. L. Hunt, R. H. Ricketts, P. Reukau, and C. L. Peddie, "Airbreathing Hypersonic Technology Vision Vehicles and Development Dreams," in *AIAA International Space Planes and Hypersonic Systems and Technologies Conf., Paper No. 1999-4978*, 1999.

[121] A. Khorad, "Modeling, analysis, and control of a hypersonic vehicle with significant aero-thermo-elastic-propulsion interactions and propulsion uncertainty," Master's thesis, Arizona State University, 2010.

[122] D. K. Schmidt, "Dynamics and Control of Hypersonic Vehicles- The integration Challenge for the 1990's," in rd *Intl. Aerospace Planes Conf., Paper No.1991-5057*, 1991.

[123] W. J. S. J. P. Weidner and J. A. Penland, "Scramjet Integration on Hypersonic Research Airplane Concepts," *J. Aircraft*, vol. 14, no. 5, pp. 460–466, May 1977.

[124] M. Bolender and D. Doman, "Flight Path Angle Dynamics of Air-Breathing Hypersonic Vehicles," AIAA Guidance Navigation and Control Conf and Exhibit, Paper No. 2006-6692, Tech. Rep., 2006.

[125] R. J. McCullen, "Modeling and control of scramjet-powered-hypersonic vehicles with aero-thermo-elastic-propulsive effects." Master's thesis, Arizona State University, 2008.

[126] A. A. Rodriguez, *Linear Systems, Analysis and Design*, Control3D, Ed. Control3D, LLC, 2004.

[127] R. C. Nelson, *Flight Stability and Automatic Control*, Second, Ed. McGraw Hill, 1998.

[128] K. G. Bowcutt, "A perspective on the future of aerospace vehicle design," in *12th AIAA International Space Planes and Hypersonic Systems and Technologies, Paper No. AIAA 2003-6957*, 2003.

[129] ——, "Multidisciplinary optimization of airbreathing hypersonic vehicles," *Journal of Propulsion and Power*, vol. Vol. 17, No. 6, pp. 1184–1190, 2001.

[130] W. Hankey, *Re-entry Aerodynamics*. AIAA Education Series, 1988.

[131] J. P. Holman, *Heat Transfer*, 6th ed. McGraw-Hill Book Company, 1986.

[132] J. H. H.A. Simon, C.S. Liu, "The eckert reference formulation applied to high-speed laminar boundary layers of nitrogen and carbon dioxide," University of Delaware, Washington, D.C., NASA Contractor report NASA CR-420, April 1966.

[133] J. John D. Anderson, *Fundamentals of Aerodynamics*. McGraw-Hill Book Company, 1984.

[134] M. N. Ozisik, *Heat Conduction*. John Wiley and Sons, 1980.

[135] C. F. Hansen, "Approximations for the thermodynamic and transport properties of high temperature air," Ames Aeronautical Laboratory, Moffett Field, California, Technical note NACA TN 4150, March 1958.

[136] D. B. D. Michael A. Bolender, Michael W. Oppenheimer, "Effects of unsteady and viscous aerodynamics on the dynamics of a flexible air-breathing hypersonic vehicle," in *AIAA Atmospheric Flight Mechanics Conference and Exhibit*, no. AIAA-2007-6397, Hilton Head, South Carolina, Aug. 20-23 2007.

[137] M. Dinkelmann and G. Sachs, "Trajectory optimization for reducing unsteady heat input of aerospace craft," in *AIAA Atmospheric Flight Mechanics Conference*, no. AIAA-2000-3994. Denver, CO: AIAA, Aug. 14-17 2000.

[138] G. S. M. Dinkelmann, M. Wachter, "Modelling and simulation of unsteady heat transfer for aerospacecraft trajectory optimization," in *Mathematics and Computers in Simulation*, ser. 2000, vol. 53, no. 4-6, 2000, pp. 389–394.

[139] G. S. M. Wachor, R.C.E. Tan and O. da Costa, "Optimizing fuel consumption and reducing thermal load for a hypersonic vehicle," in *AIAA/CIRA 13th International Space Planes and Hypersonics Systems and Technologies Conference*, no. AIAA-2005-3273. Capua, Italy: AIAA, May 16-20 2005.

[140] T. Williams, M. A. Bolender, D. Doman, and O. Mortaya, "An aerothermal flexible mode analysis of a hypersonic vehicle," Airforce Research Laboratory (AFRL), Wright Patterson Air Force Base, Conference paper postprint AFRL-VA-WP-TP-2006-331, 2006.

[141] E. V. B. Laub, "Thermal protection system technology and facility needs for demanding future planetary missions," NASA Ames Research Center, Tech. Rep., 2003.

[142] V. H. J. R. T. Kokan, J.R. Olds, "Aztec: A tsto hypersonic vehicle concept utilizing tbcc and hedm propulsion technologies," in *40th AIAA/ASME/SAE/ASEE Joint Propulsion Conference And Exhibit*, no. AIAA 2004-3728, 2004.

[143] A. Teel and N. Kapoor, "The $\mathcal{L}_2$ anti-windup problem: Its definition and solution." in *Proc. of the European Control Conf.*, 1997.

[144] A. Zinnecker, A. Serrani, M. Bolender, and D. Doman, "Combined reference governor and anti-windup design for constrained hypersonic vehicles models," in *AIAA Guidance, Navigation, and Control Conference 2009, Paper No. 2009-6283*, 2009.

[145] A. Culler, T. Williams, and M. Bolender, "Aerothermal modeling and dynamic analysis of a hypersonic vehicle," in *AIAA Atmospheric Flight Mechanics Conference and Exhibit 2007 Paper. No. 2007-6395*, 2007.

[146] S. Torrez, J. Driscoll, M. Bolender, M. Oppenheimer, and D. Doman, "Effects of Improved Propulsion Modeling on the Flight Dynamic of Hypersonic Vehicles," in *AIAA Atmospheric Flight Mechanics Conf. and Exhibit, Paper No. 2008-6386*, 2008.

[147] S. Torrez, J. Driscoll, D. Dalle, M. Bolender, and D. Doman, "Hypersonic vehicle thrust sensitivity to angle of attack and mach number," in *AIAA Atmospheric Flight Mechanics Conference 2009, Paper No. 2009-6152*, 2009.

[148] L. Fiorentini, A. Serrani, M. Bolender, and D. Doman, "Nonlinear Robust/Adaptive Controller Design for an Air-breathing Hypersonic Vehicle Model," in *AIAA Guidnace Navigation and Control Conf. and Exhibit, Paper No. 2007-6329*, 2007.

[149] D. Sigthorsson, P. Jankovsky, A. Serrani, S. Yurkovich, M. Bolender, and D. Doman, "Robust Linear Output Feedback Control of an Airbreathign Hypersonic Vehicle," *J. of Guidnace, Control and Dynamics*, vol. 31, pp. 1–15, 2008.

[150] S. Bhat and R. Lind, "Control-oriented analysis of thermal gradients for a hypersonic vehicle," in *Proc. ACC '09. American Control Conference*, 10–12 June 2009, pp. 2513–2518.

[151] S. Skogestad and I. Postlethwaite, *Multivariable Feedback Control: Analysis and Design*, 2^{nd}, Ed. Wiley-Interscience, 2005.

[152] A. Isidori and L. Marconi, "A note on the design of the robust regulator for non-minimum phase linear systems," in 43^{rd} *IEEE Conf. on Decision and Control, Atlantis, Paradise Island, Bahamas*, Decenber 2004.

[153] V. Marcopoli, J. Freudenberg, and R. Middleton, "Nonminimum phase zeros in the general feedback configuration," in *Proceedings of the American Control Conf.*, May 2002.

[154] V. J. W. C. S. A. Kelkar, A. and A. Rodriguez, "Modeling and Analysis Framework for Early Stage Studies in Scramjet-Powered Hypersonic Vehicles," in 16^{th} *AIAA/DLR/DGLR International Space Planes and Hypersonic Systems and Technologies Conf., Paper No. 2009-7325*, 2009.